

# Light Scattering Flow Cytometry for the Characterization and Quantification of Circulating Breast Cancer Cells

A thesis submitted by  
**Michael M Polmear**

in partial fulfillment of the requirements for the degree of

Master of Science  
in  
Biomedical Engineering

TUFTS UNIVERSITY  
Medford, MA, USA

February 2014

Research Committee  
**Professor Irene Georgakoudi**  
Department of Biomedical Engineering, Tufts University

**Professor David Kaplan**  
Stern Family Professor of Engineering, Chair, Department of Biomedical Engineering,  
Tufts University

**Professor Gail Sonenshein**  
Department of Developmental, Molecular & Chemical Biology, Sackler, Tufts University

## Abstract

Circulating tumor cells (CTC) in patient blood samples correlate with poor disease-free survival. CTCs derive from a tumor, invade the bloodstream, and colonize secondary tissue sites as key agents in the metastatic cascade. Current CTC detection modalities use cell surface antigen-antibody affinity but suffer from high antibody costs and poor yield due to multiple blood sample processing steps. The objective of this thesis project was to develop a peripheral blood CTC detection method using microfluidic confocal flow cytometry to discriminate cell types based on differences in backscattered light intensity. Characteristic light scattering signatures originate from variable cell morphologies and densities of intracellular organelles, and such differences are used routinely in clinical complete blood cell counts.

The proof of concept of this endogenous light scattering detection method was explored in three ways. Firstly, the scattering profiles of cultured breast cancer cells were compared to enriched populations of the two major leukocyte classes, mononuclear cells and granulocytes, isolated from non-cancerous peripheral blood. We determined that cultured cancer cells scattered in a unique, intermediate space relative to the two leukocyte classes. This result motivated the second set of experiments, where fluorescently labelled cultured cancer cells were mixed into hemolysed leukocyte suspensions. The purpose was to develop classification algorithms to detect unlabeled CTCs in cancer patient blood samples. However, classification performance was reduced relative to the enriched sample comparison due to the attenuating effects of residual erythrocytes.

The third set of experiments involved detection of green fluorescent protein-expressing (GFP<sup>+</sup>) human breast cancer cells following orthotopic implantation into the mouse mammary fat pad. This animal work was conducted in collaboration with a

therapeutic target project investigating ADAM8, a member of the ADAM (a disintegrin and metalloprotease domain) family. CTC concentration and scattering characteristics of leukocytes and GFP<sup>+</sup> CTCs were acquired for two studies. In a one-month tumor induction time course study, cells with ADAM8-knockdown had significantly reduced circulating tumor cell concentrations and brain metastases. In the second study, anti-ADAM8 antibody treatment of resected tumors decreased metastases and significantly increased a rare population of autofluorescent leukocytes implicated in an immune response. A group of cells with unique light scattering characteristics was identified in metastatic mice.

This confocal flow cytometry approach to cancer cell enumeration and light scattering characterization was useful in both in vitro method development and animal blood sample assessment. Optimizations in signal processing, blood sample preparation, and discriminate analysis are ongoing efforts to enhance the sensitivity and specificity performance.

## Acknowledgments

It has been my pleasure to learn from and work alongside talented and helpful individuals during my time at Tufts University.

All members of our lab group were instrumental in helping me to overcome various challenges, especially Tyler Chang, Dr. Joanna Xylas, Antonio Varone, and Dr. Dimitra Pouli. In particular, Drs. Martin Hunter and Carlo Alonzo provided insight into optical system design and alignment. Dr. Kyle Quinn graciously offered signal-processing vision. Undergraduate students Brad Napier and Nedda Sanayei were enthusiastic contributors to the project. Milva Ricci and Keleigh Sanford were inestimable strategists and supporters. Recently, I have had the gratification of transitioning the project to a new graduate student, Joe Lyons, over the past seven months, and his burgeoning expertise in the multi-faceted aspects of the project bode well for his progress.

This work also included a host of collaborators, all of whom offered their time and knowledge to propel the project. Drs. Mathilde Romagnoli and Nora Mineva in Professor Gail Sonenshein's group at Tufts' Sackler provided blood samples for the animal studies and co-authored our paper on a potential therapeutic target for inhibiting breast cancer metastasis. Dr. Devin Rosenthal in Professor Charlotte Kuperwasser's group at Tufts' Sackler conducted collaborative studies on leukocyte autofluorescence, which remains an ongoing thrust in our work. Dr. Rachel Buchsbaum of Tufts' Sackler and Medical Center coordinated breast cancer patient blood sample acquisition, and her dual commitment to her patients and our research was inspirational. Kris Goldizen of MIT Lincoln Laboratory was instrumental in system alignment. Professor Jeffrey Guasto, Professor Robert White, and Mark Brenckle provided invaluable technique on microfluidic design and fabrication. Professor Francisca Rius Díaz of the University of



Málaga, Spain was appreciated for her biostatistics acumen and collaborative spirit. I would also like to acknowledge the Lab Services personnel at the Tufts Health Services, particularly Mina Levitsky, for drawing my blood so often.

I am grateful to members of my research committee. Not only did Professor Sonenshein provide vision and leadership in the breast cancer therapeutic target work, she was also a diligent courier between campuses for the numerous blood samples. Professor Kaplan strengthened my understanding of the biotechnology field and provided a resourceful graduate student experience. It was an honor to work with Professor Georgakoudi for her technical expertise and guidance. Her willingness to discuss data and experimental design matched her keen insight into biomedical optics.

Finally, I thank my parents and siblings for their long-distance but perennial support. My deepest gratitude lies with my wife, Stephanie, for her encouragement and help. She was also vital in my alignment and sample processing sessions.

## Table of Contents

Abstract.....	2
Acknowledgments.....	4
Abbreviations.....	9
2 Chapter: Clinical significance and review of current techniques for the enumeration of cancer cells in blood .....	11
2.1 Motivation.....	11
2.2 In Vitro Techniques for Detecting and Enumerating Cancer Cells in Blood Samples.....	14
2.2.1 Physical Property-Based Detection Techniques .....	14
2.2.2 Biological Properties Detection Techniques .....	16
2.2.3 Nucleic Acid-Based Detection Techniques .....	21
2.2.4 In Vivo Flow Cytometry (IVFC) .....	22
2.3 In Vitro Flow Microfluidic Flow Cytometry .....	27
2.4 Thesis Outlook .....	28
3 Chapter: Background .....	31
3.1 Biology.....	31
3.1.1 Metastatic Pathway including ADAM8 .....	31
3.1.2 Morphological Differences among Differentiated Blood Cells and Epithelial-Derived Circulating Cancer Cells .....	33
3.2 Cancer Immune Response.....	41
3.3 Elastic Scattering of Biological Molecules.....	42
3.4 Fluorescence .....	50
3.5 Confocal Flow Cytometry.....	52
3.6 Microfluidic Design and Processing.....	55
3.7 Statistical Analysis.....	56
4 Chapter: Flow Cytometry Instrumentation and Analytical Tools.....	61
4.1 Introduction.....	61
4.2 Instrumentation .....	61
4.2.1 Illumination Parameters .....	64
4.3 Flow Measurement Details .....	70
4.3.1 Cell Culture Preparations.....	70
4.4 Data Analysis .....	74
4.4.1 Single Channel Peak Detection Method .....	74

4.4.2	Cumulative Channel Peak Detection Method .....	79
4.4.3	Fluorescence intensity as a standard marker in mixed populations .....	81
4.5	Effect of Channel Depth .....	84
4.5.1	Conclusion and Discussion .....	86
5	Chapter: Light Scattering Measurements of Isolated Leukocyte Populations and In Vitro Breast Cancer Cells .....	87
5.1	Introduction.....	87
5.2	Methods .....	87
5.3	Results.....	88
5.4	Statistical Analysis.....	90
5.5	Conclusion and Discussion .....	92
6	Chapter: Light Scattering Measurements of Lysed Leukocyte Populations Spiked With In Vitro Breast Cancer Cells .....	94
6.1	Introduction.....	94
6.2	Methods – Leukocyte Preparations.....	94
6.3	Results.....	97
6.4	Statistical Analysis.....	99
6.5	Conclusion and Discussion .....	102
7	Chapter: Fluorescence and Scattering Detection of Circulating Tumor Cells in Murine Model .....	104
7.1	Introduction.....	104
7.2	Methods .....	104
7.2.1	Tumor Induction Studies.....	105
7.2.2	Tumor Induction, Resection and Antibody Treatment Study .....	107
7.3	Results.....	109
7.3.1	Tumor Induction .....	109
7.3.2	Scattering-Based Measurements in Tumor Resection Study .....	118
7.4	Conclusions and Discussion .....	131
8	Chapter: Future Research Directions .....	134
8.1	Microfluidics.....	134
8.2	Forward and Side Scatter-Based Detection of Cancer Cells.....	134
8.3	Density Centrifugation for Enhanced Erythrocyte Depletion.....	136
8.4	Leukocyte Library for Negative Selection of CTCs in Patient Samples.....	137
8.5	In Vivo Imaging of Tumor Body and Periphery .....	139

8.6	Leukocyte Autofluorescence .....	141
8.7	Concluding Remarks .....	146
9	References .....	149
10	Appendix .....	162
10.1	Chapter: Background .....	162
10.1.1	Microfluidic Device Fabrication .....	162
10.1.2	Discriminant Analysis .....	166
10.2	Chapter: Flow Cytometry Instrumentation and Analytical Tools .....	168
10.2.1	Optical Components .....	168
10.2.2	System Alignment Procedure .....	170
10.2.3	Cell Suspension Flow Protocol .....	172
10.2.4	Instructions for Individual Channel Threshold Approach in MATLAB .....	172
10.3	Effect of Channel Depth Statistical Analysis - 10- $\mu$ m Window Centered on the Middle of the Channel .....	178
10.4	Chapter: Light Scattering Measurements of Isolated Leukocyte Populations and In Vitro Breast Cancer Cells .....	181
10.4.1	All Three Enriched Cell Populations – PBMC, PMN, and SUM1315 ...	182
10.4.2	PMN vs. SUM1315 .....	188
10.4.3	PBMC vs. SUM135 .....	190
10.5	Appendix – Chapter: Light Scattering Measurements of Lysed Leukocyte Populations Spiked With In Vitro Breast Cancer Cells .....	192
10.5.1	Ammonium Chloride Lysis Protocol .....	192
10.6	Chapter: Fluorescence and Scattering Detection of Circulating Tumor Cells in Murine Model .....	<b>Error! Bookmark not defined.</b>
10.6.1	Tumor Induction Time Course Study Discriminant Analysis .....	193
10.6.2	Tumor Induction, Resection, and Antibody Treatment Study .....	196

## Abbreviations

4',6-diamidino-2-phenylindole: DAPI

A disintegrin and metalloprotease: ADAM

Acetomethoxy: AM

ADAM8: A8

Ammonium chloride:  $\text{NH}_4\text{Cl}$

Circulating tumor cell(s); tumor cells in blood: CTC(s)

Cluster of Differentiation: CD

Coherent anti-stokes Raman scattering spectroscopy: CARS

Collagen adhesion matrix: CAM

Common myeloid progenitors: CMP

Data acquisition board: DAQ

DiD, DiR: types of dialkylcarbocyanines fluorescent dyes

Dielectrophoresis: DEP

Disintegrin/cysteine-rich/EGF-like domains: DCE

Disseminated metastatic tumor cell(s); micrometastases; tumor cells in blood, lymphatic system, and bone marrow: DTC(s)

Epithelial cell adhesion molecule: EpCAM

EPithelial ImmunospOT assay: EPISPOT

Epithelial-to-mesenchymal transition: EMT

Erythrocyte(s); red blood cell(s): RBC(s)

Extracellular matrix: ECM

False Negative: FN

False Positive: FP

Flavin adenine dinucleotide: FAD

Fluorescence-activated cell sorting (FACS)

Fluorescence-activated cell sorting: FACS

Forward-scattered light: FSC

Full width at half-maximum: FWHM

Green fluorescent protein (GFP)

Hematopoietic stem cells: HSC

Human epidermal growth factor receptor 2: HER2

Human immunodeficiency virus infection / acquired immunodeficiency syndrome: HIV/AIDS

In vivo flow cytometry: IVFC

Leukocyte(s); white blood cell(s): WBC(s)

Minimal residual disease; presence of DTCs

Multipotent progenitors: MPP

Multivariate analysis of variance: MANOVA

Natural killer T leukocyte; primary cytotoxic targets virus-infected and tumor cells: NKT

Negative predictive value: NPV

Neutrophil extracellular traps: NETs

Numerical aperture: NA

Peripheral blood mononuclear cell(s), leukocytes: PBMC(s)

Photothermal/Photoacoustic: PT/PA

Phycoerythrin (PE)

Polydimethylsiloxane: PDMS

Polymorphonuclear cell(s), leukocytes; PMN(s)

Positive predictive value: PPV

propylene glycol monomethyl ether acetate: PM acetate

Reduced nicotinamide adenine (phosphate) dinucleotide: NAD(P)H

Short hairpin: sh

Side-scattered light: SSC

Signal-to-noise ratio: SNR

Traditional and real-time polymerase chain reaction: PCR and RT-PCR

Traditional and real-time polymerase chain reaction: PCR and RT-PCR

Triple-negative breast cancer - negative for estrogen receptor, progesterone receptor, and HER2: TNBC

True Negative: TN

True Positive: TP

Vascular endothelial growth factor: VEGF

# **Light Scattering Flow Cytometry for the Characterization and Quantification of Circulating Breast Cancer Cells**

## **1 Chapter: Clinical significance and review of current techniques for the enumeration of cancer cells in blood**

The primary objective of our research is the development of a minimally invasive and efficient detection technique to discriminate circulating tumor cells (CTCs) from normal blood cells for clinical diagnostic and therapeutic monitoring purposes. CTCs are defined as tumor cells shed from a solid tumor and in transit within the circulatory system<sup>1</sup>. A blood sample is minimally invasive relative to a bone marrow aspirate where disseminated tumor cells (DTCs) were initially found and sparked clinical interest in the hematological spread of cancer<sup>2</sup>. Although DTC concentration was demonstrated to be prognostically significant, the very low detection rate of tumor cells within only 3% of bone marrow aspirates from early stage breast cancer patients prompted renewed interest in CTC enumeration within blood<sup>3</sup>. The purpose of this thesis project was to assess potential of light scattering-based microfluidic flow cytometry to detect breast cancer CTCs as a diagnostic and therapeutic monitoring tool.

### **1.1 Motivation**

Epithelial solid tumors are responsible for 90% of the 1.6 million new cancer diagnoses in the US, with breast, prostate, lung, and colon cancer constituting the majority of cases<sup>4</sup>. Current tumor staging protocols use local tumor extension, sentinel lymph node involvement, serum cancer marker analysis, and computed tomography evidence of metastasis. Despite ongoing enhancements in these staging modalities, metastases are the cause of 90% of the 572,000 annual cancer deaths<sup>5</sup>. Moreover, despite recent advances in cancer treatment, the American Cancer Society reports that over 40,000 women die yearly in the United States of metastatic breast disease. Therefore,

there is a clinical need for development of detection technologies with increased sensitivity. Hematological spread is an integral step in the metastatic pathway, thus CTC concentration monitoring represents one such strategy and has been coined a “liquid biopsy”<sup>6</sup>.

Although the presence of CTCs in an autopsy was first documented in 1869, the rarity and heterogeneity of these cells have hindered our understanding of their role in cancer pathology<sup>7</sup>. CTCs are extraordinarily rare; current estimates are one CTC per billion blood cells in the circulation of patients with advanced cancer<sup>8</sup>. CTCs are a heterogeneous population, a fraction of which is viable metastatic precursors capable of initiating a clonal metastatic lesion<sup>8</sup>. Recent technological advances beginning in the early 2000s have enabled researchers to characterize and enumerate CTCs. Several studies with large cohorts have shown that the detection of circulating cancer cells has prognostic value for individual patient disease progression, survival, and therapeutic response particularly in breast, prostate and colorectal cancer cases<sup>9</sup>. The majority of these prospective multi-center studies of newly diagnosed metastatic cancer patients used CellSearch™ (Veridex/J&J), the first FDA-cleared immunomagnetic bead capture assay for CTC detection<sup>10</sup>. Seminal studies found that a CTC concentration of  $\geq 5$  cells for breast and prostate and  $\geq 3$  for colorectal cancer patients in 7.5 mL of peripheral blood prior to treatment and at first follow-up correlated with shorter progression free and overall survival<sup>1,10-14</sup>. Subsequent studies demonstrated sensitivity of 27-57% and specificity of 93-99% based on type of malignancy<sup>15-19</sup>. The CellSearch™ CTC detection platform demonstrated the monitoring efficacy of CTC concentration to improve prognosis when individual patient CTC concentrations decreased up to 50% in response to therapy<sup>20</sup>. There was a correlated increase or no change in CTC concentrations in the cases where individual patients did not respond favorably to therapy. These preliminary



findings motivated a major ongoing clinical trial that seeks to incorporate CTC monitoring into the standard of care for risk-management and economical purposes<sup>21</sup>.

Although prognostic and monitoring capacities emerged from these studies, CTCs were only detected in approximately half of the metastatic cancer patients using as much as 50 milliliters of blood<sup>21</sup>. Moreover, recent results from CTC screening in early-stage breast cancer patients demonstrated a less than expected CTC concentration of only  $>1$  cell/7.5 ml of blood using the CellSearch™ assay<sup>22</sup>. Compared to the present standard of  $\geq 5$  CTCs/7.5 ml of blood, this small average of  $>1$  CTC/7.5 ml was insignificantly higher than normal (i.e. non-cancerous) levels and was of limited prognostic value to the care of early-stage breast cancer patients.

Therefore, ongoing research, including the work presented here, has focused on increasing the sensitivity of a detection assay. Subsequent studies using other CTC detection systems have demonstrated similar correlations between CTC concentration and patient survival. For example, a microfluidic epithelial antibody-based CTC capture device tracked decreasing CTC concentration in metastatic lung, prostate, and breast cancer patients in response to effective chemotherapy, hormonal therapy, and targeted kinase inhibition<sup>23-25</sup>. Of the samples assayed, approximately 60% were positive for CTCs with concentration values ranging from 14 to 5000 CTCs per milliliter of blood. The increased sensitivity of a microfluidic approach motivated the pursuit of a minimally invasive enumeration technique on a similar blood sample-processing platform.

Rather than using epithelial-specific antigens for CTC isolation, our detection method exploited endogenous differences in light scattering characteristics among CTCs and blood cells. Our approach centers on microfluidic-based flow cytometry using multiple interrogative visible light wavelengths to detect differences in backscattering light intensity that originate from a variety of cell morphologies and densities of

intracellular organelles. The excitation wavelengths of 405, 488, and 633 nm were first used in our research group to discriminate leukemic from normal blood cells<sup>26</sup>. Specific performance attributes of the leukemia study will be discussed in 1.3, and this promising technique motivated this thesis work to extend backscattered light-based detection to CTCs deriving from solid tumors.

The following section provides an overview of more established in-vitro detection techniques using a range of blood volumes, an overview of current developments in minimally invasive and non-invasive alternatives, and advantages and limitations of each technique.

## **1.2 In Vitro Techniques for Detecting and Enumerating Cancer Cells in Blood Samples**

Accurate assessments of CTC concentration are expected to improve risk-adapted therapy, which is tailoring individual treatment to the patient's present risk<sup>21</sup>. Recent advances have focused on two endpoints of CTC analysis: isolation with minimal cell disruption for pathological understanding and detection with maximal cell recovery for prognosis. While this thesis describes a detection-centered method, alternative approaches address one or both endpoints. Discussed in this section are in-vitro techniques based on physical properties, cell surface biological properties, and nucleic acid analysis. Additionally, techniques using in vivo flow cytometry and intrinsic light scattering will also be discussed. Prior to cell quantification, most in-vitro detection techniques rely on enrichment of samples to increase CTC concentration relative to more abundant blood cells. The most commonly used enrichment techniques involve isolation of cancer cells by physical properties or affinity to specific antibodies.

### **1.2.1 Physical Property-Based Detection Techniques**

Physical differences among CTCs and normal blood cells include size<sup>27</sup>, density<sup>28</sup>, deformability<sup>29</sup>, and membrane capacitance<sup>30</sup>. Although not absolute, these

differences have been used to enrich blood samples for enumeration and further assessment, such as molecular characterization of gene products. The broad advantage is a label-free approach, whereas the broad disadvantage is decreased specificity owing to overlapping density distributions<sup>31</sup>. An intermediate density reagent such as Ficoll-Paque ( $1.077 \text{ g ml}^{-1}$ ) separates lower density peripheral blood mononuclear cells (PBMC; i.e. lymphocytes, monocytes and macrophages) from higher density polymorphonuclear leukocytes (PMN, granulocytes; i.e. neutrophils, eosinophils, and basophils) and erythrocytes (Figure 1-1)<sup>32</sup>.



Figure 1-1 Separated blood cell sub-populations following density centrifugation with Ficoll-Paque ( $1.077 \text{ g ml}^{-1}$ ). PMNs constituted the thin pink layer above the dark red erythrocyte layer.

CTCs sediment within the PBMC layer, and the fewer residual erythrocytes decreases the cell suspension viscosity for ease of further processing<sup>28</sup>.

Size-based filtration methods exploit the larger size of epithelial tumor cells relative to normal blood cells. Cancer and blood cells are different sizes due to differences in cell volume related to transport phenomena and metabolic demands<sup>27</sup>. One such embodiment of a detection approach is the Isolation by Size Epithelial Tumor Cells (ISET) method that employs eight-micrometer-diameter cylindrical filtration pores<sup>33</sup>. The sensitivity threshold for reproducible cancer cell detection was determined to be one spiked carcinoma cell per milliliter of normal blood using established cell lines deriving from liver,

breast, cervical, or prostate cancer patients. By transitioning the size-based discrimination approach to microfluidics, an alternative method used a pinched flow device to retain larger tumor cells while smaller blood cells flowed through the channel<sup>34</sup>. Owing to differences in size and deformability, CTCs have been captured in a microfluidic device studded with physical structures that allowed for passage of smaller and more deformable normal blood cells. The optically transparent device facilitates further antibody-based microscopic detection and analysis<sup>29</sup>. Although the low cost and high sensitivity in spiked samples of these methods are promising, rigid pore sizing, pinched width parameters, and physical structure spacing are not dynamically adaptable to smaller diameter CTCs that have been observed in clinical cancer samples<sup>35</sup>.

Differences in cell membrane capacitance and conductance have been used via dielectrophoresis (DEP) to isolate CTCs<sup>36</sup>. Total cell capacitance is proportional to plasma membrane area and cell size, though ruffles, folds, and microvilli also augment discrimination power<sup>30</sup>. Cells flowing through a channel responded to an applied electric field, and resultant forces were either attractive or repulsive, thus allowing cells with different membrane capacitance properties to be in the fast-flowing center or slow-flowing boundary of the channel. This approach isolated 90% of spiked breast cancer cells at concentrations of one tumor cell in one thousand PBMCs in volumes less than 4.5 milliliters<sup>36</sup>. The primary drawback to this method was the requirement for quick sample processing times in less than 15 minutes to mitigate changes in membrane capacitance due to ion leakage.

### **1.2.2 Biological Properties Detection Techniques**

Differences between CTCs and blood cells in surface and intracellular protein expression, viability in culture, and invasion capacity have been used for CTC isolation. The primary advantage of these approaches was versatility in method design using

antibody affinity, whereas the drawbacks were high antibody cost, irreversible antibody affinity, slow processing times, and large sample volume requirements<sup>37</sup>. The most widely used techniques relied on antibody-based capture of CTCs expressing epithelial cell surface markers or rejection of CTCs not expressing leukocyte common antigens, such as cluster of differentiation antigen CD45, a pan-leukocyte marker. Antibodies against human epidermal growth factor receptor 2 (HER2) served a similar purpose for CTC detection in approximately 30% of breast cancer patients<sup>38</sup>. The nearly universal, albeit variable, expression of epithelial cell adhesion molecule (EpCAM) in cells of epithelial origin and contrasting absence in blood cells has motivated the majority of monoclonal antibody-based CTC capture systems. Fluorochrome-labeled antibodies against EpCAM have been conjugated to magnetic beads<sup>17</sup>, microfluidic posts<sup>39</sup>, magnetic stir bars<sup>40</sup>, directly to cells for flow cytometry analysis<sup>41</sup>, and 3D-structured silicon-nanowires<sup>42</sup>.

The CellSearch™ system, the only FDA-approved method for CTC detection, employed ferrofluidic nanoparticles coated with antibodies against EpCAM to magnetically separate CTCs from other blood cells in a 7.5-milliliter sample. Captured cells were further identified as epithelial via affinity for antibodies against cytokeratins CK8, CK18, and CK19 or as leukocytes via anti-CD45 antibody affinity<sup>43</sup>. Due to contaminating issues where cells express affinity for both antibody types, all nuclei were stained with DAPI (4',6-diamidino-2-phenylindole) for microscopic visual inspection. The semi-automated method used a four-color fluorescence microscope to discriminate epithelial cells from blood cells based on cell size, roundness, nucleation, positive cytokeratin staining, positive EpCAM staining, and negative CD45 staining<sup>44</sup>. An operator made the final decision on CTC identity from the potential cells found by the program. This platform is the most advanced to date and has propelled the CTC

detection field; however, the method is subject to operator discretion, primarily based on perceived fluorescence intensity threshold indicating marginal staining<sup>15,37,45</sup>. Specific ongoing efforts to automate this CTC selection process are discussed in 2.1.2.

As previously mentioned in 1.1, an emerging microfluidic device with anti-EpCAM antibody-coated microposts has already demonstrated improved sensitivity and reduced sample volume requirement relative to the CellSearch™ assay<sup>6</sup>. The first generation device relied on microposts to facilitate mixing, and generated promising results. Whole blood was flowed through a microfluidic chip, and cells interacted with 78,000 microposts. EpCAM-expressing cells attached to the posts were inspected by staining with antibodies against cytokeratins, similar to the CellSearch assay. Following imaging for enumeration purposes, on-chip lysis allowed for DNA and RNA extraction and molecular analyses. The investigators attributed the increased sensitivity of a median 50 CTCs per milliliter of blood in cancer patients to the minimally disruptive one-step processing that retained the rare CTC population<sup>23</sup>. This platform demonstrated clinical utility in longitudinally monitoring patients for both CTC concentration and molecular characteristics. The second generation of the device used a herringbone to generate microvortex mixing, thereby increasing the number of cell-micropost interactions to increase sensitivity theoretically<sup>39</sup>. The design of this chip was also less complex than that of the first generation making it more amenable to manufacturing in terms of cost, consistent antibody coating, and visualization of adhered cells. This microfluidic platform was one of the most sensitive approaches; however, the relatively increased number of detected false-positive cells in nonmetastatic patients and healthy controls warranted further investigations on assay specificity.

A second microfluidic platform, Ephesia, used columns of biofunctionalized superparamagnetic beads conjugated to anti-EpCAM antibodies to capture CTCs<sup>46</sup>. The

beads self-assembled along microcontact-printed magnet traps, thus enhancing the ease of manufacturing of a microfluidic chip platform over the technical hurdles inherent to coating antibodies on microposts. A third microfluidic platform, “Fly Paper,” used an anti-EpCAM antibody-coated silicon-nanowire array<sup>42</sup>. The reduced structural dimension to the nanoscale theoretically reduced variability encountered due to collision frequency and contact duration. Validation experiments are underway, and microfluidic approaches continue to show potential for their heightened sensitivity in blood volumes of less than 1 milliliter.

Although microfluidic approaches require less initial sample volume, the rarity of CTC abundances motivates innovative approaches to enrich CTCs from large blood volumes with fewer processing steps than the current standard of the CellSearch™ assay<sup>43</sup>. A new immunomagnetic separation technology, MagSweeper, used a magnetic stir bar to enrich gently epithelial cells bound to anti-EpCAM antibody-coated magnetic particles<sup>40</sup>. By assaying nine milliliters of blood in less than hour, the system found  $12 \pm 23$  circulating epithelial cells per patient with metastatic disease (n=47) and none in healthy control samples (n=5). CTCs were detected in all 47 metastatic patients assayed, and the large standard deviation was attributed to one outlying patient where 100 CTCs were detected.

As the workhorse for clinical CBCs, investigators have adapted flow cytometry applications for CTC detection. With the capability to process large sample volumes, assaying  $10^4$ - $10^5$  events per second, flow cytometry remains a promising platform for enumerating rare cells. Commercial flow cytometers contain multiple excitation wavelengths and 10 detection channels, including forward and side scatter intensities, which produce real-time scatter plots and histograms, thus allowing the operator to define regions of interest. Within the fluorescence-activated cell sorting (FACS) field, regions of

interest can be further defined as gates to allow for collection and further analysis of specific cell populations. Investigators initially started with anti-EpCAM and anti-cytokeratin antibody staining approaches but found that variable detection fluorophore intensities amidst high background levels of cell and buffer autofluorescence produced a surplus of positive counts. In many cases, the number of detected CTCs from the same sample was 50 to  $3 \times 10^5$  higher than observed with other approaches<sup>6</sup>. A new method, MAINTRAC<sup>TM</sup>, used specialized laser scanning cytometry to provide additional information on the morphological properties of positively identified cells, which was similar to the way operators scrutinized each cell microscopically in the CellSearch<sup>TM</sup> system<sup>41</sup>.

Other assays have been developed to reject false-negatives. The functional EPISPOT assay (for EPithelial ImunnoSPOT) is non-destructive and assessed secreted protein products during 24-48 hours of short-term culture<sup>47</sup>. This assay has been applied to blood and bone marrow samples of breast and prostate cancer patients, thus providing the first indication that cytokeratins can be released by viable isolated cells and used as markers for positive CTC identification<sup>48</sup>. A second cell viability method was the collagen adhesion matrix (CAM) assay, which assessed CAM ingestion and epithelial immunostaining<sup>49</sup>. In vitro, isolated CTCs from breast, prostate, and ovarian cancer patients have demonstrated this invasive capability to thrive in a collagen matrix. A more thorough discussion on the invasive properties of tumor cells follows in 2.1.1. In addition to surface antigen and invasive biological properties of CTCs, molecular characteristics provide insight on cell identity, disease pathology, and the influence of the microenvironment on the circulating cell.



### 1.2.3 Nucleic Acid-Based Detection Techniques

In addition to harboring CTCs, blood also contains cell-free tumor DNA and, to a lesser extent, RNA. DNA from intact cells and cell-free DNA are emerging as complementary biomarkers to CTCs and DTCs for metastatic spread of solid tumors<sup>6</sup>. Probable origins include direct shedding from necrotic cells in tumor deposits, tumor-derived exosomes, and cellular fragments of lysed tumor cells associated with an immune response. Nucleic acid analysis provided evidence for an epithelial-mesenchymal transition (EMT) where the changing microenvironment influenced variable gene expression as the cell transitioned from solid tumor to a shear flow regime in circulating blood to a distant site. This phenomenon will be further discussed in 2.1.1, and is typified by genetic expression of cancer stem cell properties, namely downregulation of E-cadherin and some cytokeratins and upregulation of vimentin and N-cadherin<sup>50</sup>.

Traditional and real-time polymerase chain reaction (PCR and RT-PCR) techniques verified the presence of gene products unique to epithelial cells relative to blood cells. Blood sample collection and sample enrichment was followed by nucleic acid extraction, cDNA synthesis, and marker gene cDNA amplification. In addition to the previously described gene products associated with EMT, other targets included proto-oncogenes, tumor suppressor genes, loss of heterozygosity, and microsatellite instabilities. Collectively, these gene products were unique to epithelial cells and indicated metastatic cancer<sup>51</sup>. In assessing metastatic stage in breast cancer patients, DNA concentration/integrity in the forms of allelic imbalance, and evidence of HER2 amplification were measured in patients with indeterminate early or metastatic disease<sup>52</sup>. The most sensitive methods for identifying tumor-specific DNA aberrations relied on using multiple gene product probes with established cut-off thresholds.

Advantages of nucleic acid analysis centered on method specificity of a primer-product match, whereas drawbacks included initial identification of marker genes, high

blood volume requirement due to variable abundance of gene products, and observed discrepancies between blood-borne and tumor-biopsied nucleic acid sequences<sup>53</sup>. Primers designed for specific gene products established preliminary abundance cutoff limits for markers indicative of metastatic disease in prostate and breast cancer<sup>53</sup>. These molecular characterization techniques have elucidated gene expression aspects of the metastatic pathway. Nonetheless, selected primers represented an initial guess of gene products indicative of metastasis, and false-positive and false-negatives were observed<sup>51,54</sup>. Moreover, primer development was confounded by microenvironment changes that influenced gene expression. Blood-borne nucleic acid in plasma and detected CTCs differed from primary tumor gene expression, as observed in HER2 status in breast cancer patients<sup>22</sup>. Both cell-free tumor DNA and CTC DNA were extraordinarily rare. Although next-generation sequencing allows for increased sensitivity, interpretation of a negative result cannot be discerned from insufficient amounts of tumor-derived nucleic acid in the final sample preparation<sup>8</sup>.

#### **1.2.4 In Vivo Flow Cytometry (IVFC)**

Of particular interest to our group, in vivo flow cytometry (IVFC) used narrow, superficial blood vessels to acquire light scattering and fluorescence signals from flowing cells. White and red blood cells<sup>55</sup>, stem cells<sup>56</sup>, leukemic cells<sup>57,58</sup>, breast<sup>56,59</sup>, ovarian<sup>58</sup>, and prostate cancer cells<sup>60</sup> have all been detected using IVFC<sup>61</sup>. Primary aims of IVFC were to monitor CTC concentration for metastatic progression and for treatment response. Four principal approaches to in vivo assessment have used intrinsic sources of contrast, exogenous fluorescent labeling of native cancer cells via surface antigen binding, mutated cancer cells capable of fluorescent protein production, and delivery methods of venous injection, orthotopic implantation, or ectopic implantation in animal models. Intrinsic sources that enabled label-free CTC assessment were coherent anti-

stokes Raman scattering spectroscopy (CARS) IVFC and photothermal/photoacoustic signal detection (PT/PA).

CARS is a third-order nonlinear optical process that amplifies molecular vibrational signatures that are observed in Raman scattering spectroscopy, such as those produced by lipids with symmetrical CH<sub>2</sub> stretch vibrations. One IVFC application exploited accumulation of lipids in primary, circulating, and metastasized lung cancer cells in mice following subcutaneous injection<sup>62</sup>. Without use of high signal-to-noise ratio (SNR) fluorescence signals, this study demonstrated potential for one source of intrinsic contrast in IVFC; however, assay volumes characterized by single cell flow, such as narrow veins with low flow rates, currently limit the technology by extending assay time.

While both PT and PA emanate from non-radiative relaxation of absorbed laser energy, PT signal indicates thermoelastic collision and PA signal indicates photoacoustic waves<sup>63</sup>. PT IVFC techniques were based on irradiation of flowing cells in microvessels with a spectrally tunable laser pulse and on detection of temperature-dependent variations of refractive index with a second continuous probe laser beam<sup>64</sup>. PT signal characteristics emanated from intracellular absorbing molecules and included amplitude, rise time for cell heating, decay from cell cooling, and local concentration. In the context of blood cells, uniform distribution of hemoglobin in erythrocytes yielded a contrasting signal to locally distributed absorbing cytochromes in leukocytes and breast cancer cells that produced larger PT amplitudes and faster signal decays<sup>65</sup>.

Similar to PT, PA IVFC techniques used endogenous chromophores, such as hemoglobin and melanin, and were susceptible to high background signals in fast-flowing blood. The physical mechanism of PA IVFC was thermoelastic sound generation detected by an ultrasound transducer<sup>63</sup>. CTCs deriving from a melanoma were enumerated following subcutaneous injection using PA detection<sup>66</sup>. Both PT and PA were also

adapted for nanoparticle detection with conjugated biological affinity for CTCs<sup>65</sup>. As toxicity levels for both PT/PA nanoparticles and exogenous fluorophores used in fluorescence-based detection decrease to clinically safe levels, detection modalities have already demonstrated efficacy in animal models<sup>66</sup>.

Fluorescence-based CTC detection systems employed single photon confocal excitation, multiphoton excitation, or diffuse tomography. Confocal detection used focused illumination at the sample plane and a pinhole in the conjugate plane in front of the detector to block out-of-focus light. As in confocal microscopy, tissue scattering, absorption, and autofluorescence effects limited imaging depths to less than 200 micrometers of medium<sup>67</sup>. Nevertheless, superficial capillaries in the human lip<sup>68</sup> and mouse ear<sup>55</sup> were found 70-100 micrometers below the skin surface. IVFC investigations have been used alone and in tandem with in vivo imaging modalities.

Alternatively, multiphoton microscopy evolved to provide optical sectioning resolution to depths of 500-1000 micrometers<sup>69,70</sup>. Multiphoton excitation utilized a localized, non-linear probabilistic event where a fluorophore absorbed multiple photons simultaneously. The subsequent emission spectrum was equivalent to that of single photon excitation; however, the diminished probability of such an event occurring outside of the focal volume eliminated the need for a confocal pinhole. Two- and three-photon excitation are commonly employed to excite the same fluorophores of interest that emit in the visible region. The greater penetration depth was attributed to longer excitation wavelengths in the near infrared region where medium attenuation effects were decreased relative to those occurring with visible light excitation<sup>69</sup>. Despite these advantages, multiphoton approaches had practical limitations relative to single photon excitation approaches. Multiphoton excitation required expensive lasers capable of delivering necessary peak power in short pulses to achieve sufficient photon flux to cause a

fluorophore to absorb two or more photons simultaneously. Moreover, sub-cellular resolution of multiphoton excitation limited the focal volume to within a cross-section of a blood vessel where flowing cells steadily traversed for consistent excitation efficiency<sup>60</sup>.

The differences in depletion kinetics of two prostate cancer cell lines were observed following tail vein injection of fluorescently DiD-labeled cells<sup>60</sup>. By shaping the excitation light into a slit and focusing on narrow arteries in ears of mice and rats, the decreasing concentration of circulating cells were enumerated over time as they settled in specific organs, such as lungs, liver, spleen, kidneys, and lymph nodes.

In a separate study, epithelial linings of blood vessels were fluorescently tagged with a Cy5-conjugated anti-platelet/endothelial cell adhesion molecule monoclonal antibody beginning 24 hours prior to inoculum injection. The imaging technique used a video-rate confocal scanning laser microscope, first described by Rajadhyaksha et al<sup>71</sup>. In a separate study, the homing propensity of tail vein-injected leukemia cells to bone marrow vasculature of the skull was assayed to elucidate the mechanism<sup>57</sup>. The inoculum cells were fluorescently stained with DiD or DiR and were further imaged within bone marrow using a multiphoton fluorescence microscope.

Two tumor induction studies used two distinct fluorescent sources to assess CTC concentration following injection. In the first study, cells in circulation were detected following intravenous infusion and subcutaneous inoculation<sup>58</sup>. Leukemia cells were injected intravenously and followed 15 minutes later by a fluorescently conjugated anti-folate receptor antibody. In contrast to normal tissues that lack folate receptors or express a site that is inaccessible to parenterally administered drugs, some leukemic cells overexpressed the receptor. In this way, circulating cancer cells were detected in ear vasculature using nonconfocal, confocal, and multiphoton microscopy. Multiphoton was

determined to be superior to other modalities, due to improved sensitivity with increased penetration depth and reduced propensity to photodamage. Secondly, murine lung cancer cells were implanted subcutaneously to induce tumor formation. Using the same folate receptor labeling method, CTCs were detected as early as two weeks following implantation with subsequent exponential growth in CTC concentration at three and four weeks. Micrometastases were observed in necropsied lung sections.

In the second tumor induction study, GFP-expressing human breast cancer cells were orthotopically implanted in mice to observe the time course of CTC concentration alongside development of metastatic lesions<sup>61</sup>. The concentration of CTCs and autofluorescent red cells were observed in mouse vasculature using a single photon confocal optical system. Shaped into slits and focused on a blood vessel, excitation wavelengths were 488 nm for green autofluorescence and GFP-positive CTCs and 488 or 633 nm light for red autofluorescent cells. Three fluorescent cell types were of interest in this study: (1) red autofluorescent leukocytes; (2) green autofluorescent leukocytes; and (3) GFP<sup>+</sup> CTCs. Both red and green autofluorescent leukocytes were observed in non-tumor-bearing mice with a range of intensity levels and at respective concentrations of less than five cells per microliter of blood. In mice that developed metastases, green fluorescent cells, e.g. GFP<sup>+</sup> CTCs and green autofluorescent cells, peaked approximately ten days after implantation with an average concentration of  $20 \pm 7$  cells per microliter of blood. The increased abundance of green fluorescent cells in metastatic mice relative to wild type mice suggested that the detected cells were GFP<sup>+</sup> CTCs. However, the integral number of detected green cells less accurately predicted formation of metastases than the ratio of the number of green fluorescent peaks to the ratio of green to red fluorescent peaks. Therefore, mice with an increase in green fluorescent cells coupled with a decrease in red autofluorescent cells had a greater prevalence of metastatic lesions. This

ratio was most accurate within the first seven days following cell implantation. The identity of red autofluorescent cells spanned multiple leukocyte lineages.

Diffuse tomography flow cytometry was a separate imaging approach that detected fluorescence light using a high-sensitivity fiber-optic detection ring centered on a mouse limb (e.g. forelimb, hindlimb, or tail<sup>72</sup>). The optical sectioning capability and increased sensitivity to the isotropic nature of fluorescence emission allowed for analysis of larger blood vessels than previous IVFC approaches. Specifically, this technique enumerated fluorescently labeled multiple myeloma cells within relatively large blood vessels with flow rates from  $0.2 - 0.5 \text{ ml min}^{-1}$ , which was two orders of magnitude greater than vessels assayed in confocal IVFC approaches<sup>56</sup> and theoretically allowed for total mouse blood volume analysis within 10 minutes<sup>72</sup>.

In adapting flow cytometry principles from in-vitro to in-vivo settings, IVFC systems offer a unique opportunity to investigate cells flowing in their natural states. The previously described approaches have made progress in overcoming technical design challenges attributed to light scattering and absorption from blood vessels and surrounding tissue, variations in blood vessel cross section and flow, and presence of many normal cells surrounding just a few cancer cells.

### **1.3 In Vitro Flow Microfluidic Flow Cytometry**

The final circulating cancer cell enumeration method discussed in this section is a combination of microfluidics, flow cytometry, and intrinsic contrast. Elastic light scattering is another intrinsic source of signal contrast beyond photothermal and photoacoustic sources. At the tissue level, several light scattering spectroscopy studies have shown the sensitivity to morphological differences that occurred during neoplastic transformation, thus allowing for discrimination of normal from cancerous cells<sup>73</sup>. Prior to this thesis work, our group developed a confocal backscattering-based detection

system for flowing cells. The hypothesis was that morphological differences among circulating cancer cells and blood cells formed a basis for discrimination of various cell types.

Using Nalm-6 cells, a pre-B acute lymphocytic leukemia cell line, as a model, cancer cells were discriminated from erythrocytes and leukocytes by varying backscattering intensities of three interrogative wavelengths, specifically 405, 488, and 633 nm<sup>74</sup>. These wavelengths were chosen based on white light scattering spectroscopy measurements<sup>26</sup>. By spiking cultured leukemia cells into PBMC or PBMC plus PMN leukocyte suspensions at varying concentrations from 0.01-20% of leukocytes, a discriminant analysis framework was developed for mixed populations. Statistical results from training and validation data sets demonstrated similar performance levels. As expected, sensitivity and specificity of the classification of leukemic cells decreased when both PMNs and PBMCs were included in the flowing samples. Specifically, while the sensitivity and specificity achieved in the validation set were on average  $45.2 \pm 2.1\%$  and  $99.6 \pm 0.1\%$ , respectively, for samples containing PBMCs and leukemic cells, they decreased to  $39.5 \pm 2.58\%$  and  $91.6 \pm 1.5\%$  when PMNs were also present. Given that no labeling or expensive reagents were needed for this method, these results were promising. The instrumentation, microfluidic design, and data analysis within these studies formed the foundation of this thesis work and will be discussed in Chapter 3.

#### 1.4 Thesis Outlook

The purpose of this thesis work was to extend the detection platform from circulating leukemia cells to CTCs originating from solid tumors. An outline of the thesis is presented in Figure 1-2. Two breast cancer cell lines were used: (1) SUM 1315 deriving from a patient with skin metastasis of infiltrating ductal carcinoma who had prior chemotherapy and (2) SUM 159 deriving from a patient with an anaplastic



carcinoma who did not have prior chemotherapy<sup>75</sup>. The light scattering characteristics of these cells were compared to those of blood cells in enriched and mixed populations. The blood cells were separated by gradient centrifugation or enriched by ammonium chloride erythrocyte lysis. Cultured cancer cells were fluorescently stained with calcein AM, a vital dye, to identify positively the cells in the flow cytometry experiments. In this way, a complementary aim was to develop a sample handling protocol to assay blood samples from breast cancer patients. In recognizing the limitations of using cultured cancer cells to classify native CTCs, murine tumor induction studies were conducted. These experiments were performed in collaboration with a project centered on assessing a new therapeutic target to effectively block breast cancer dissemination. The clinical motivation is to improve the overall survival of patients with limited therapeutic options, such as women with triple-negative (TN) breast tumors (negative for estrogen receptor, progesterone receptor, and HER2)<sup>76</sup>. GFP<sup>+</sup> CTCs detected in murine tumor induction experiments were used to optimize sample processing and define light scattering characteristics of native CTCs. A rare population of green autofluorescent leukocytes was observed in the wild type mouse cohort. Thus, a second study was conducted to enhance resolution in scattering properties of non-fluorescent leukocytes, autofluorescent leukocytes, and GFP<sup>+</sup> CTCs. A sub-population of green fluorescent cells consisting of either autofluorescent leukocytes or GFP<sup>+</sup> CTCs was discriminated from non-fluorescent leukocytes.

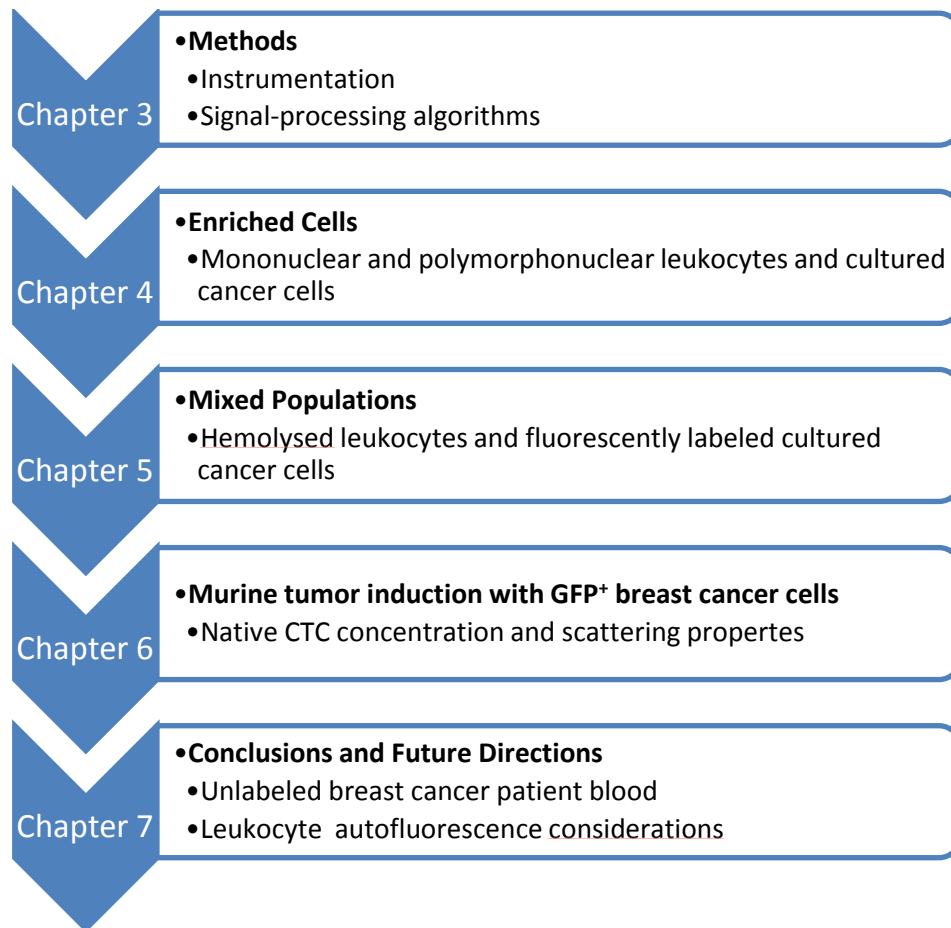


Figure 1-2 Thesis outlook and outline

## 2 Chapter: Background

This chapter begins with a discussion of relevant biological principles of solid tumor metastasis, the role of the immune system in cancer, and morphological differences among blood and epithelial cells. The second section discusses the optical interrogation method of elastic light scattering based on cellular structures. The third section discusses exogenous and endogenous sources of fluorescence contrast. The fourth section introduces confocal flow cytometry as a means of collecting scattering signals from flowing cells. The fifth section illustrates the microfluidic design process. The final section summarizes the theory of discriminant analysis as an analytical tool for comparing populations with multiple components.

### 2.1 Biology

Biological concepts that intersected with this thesis centered on physical and biological differences among blood and epithelial cells. Solid tumor metastatic pathway, immune response to cancer, and pertinent blood cell morphologies will be discussed. Although a myriad of signaling pathways are implicated in cancer metastasis, a collaboration within this thesis work focused on the therapeutic potential of interrupting a specific membrane-anchored protein, and the role of this target will be discussed in this section.

#### 2.1.1 Metastatic Pathway including ADAM8

Cancer metastasis results from a multistep process that selects for invasive tumor cells capable of escaping from the primary site and colonizing distant organs<sup>77</sup>. Early in the tumorigenesis process, the hypoxic stress that characterizes the low tissue oxygen microenvironment of a solid tumor stimulates tumor-induced angiogenesis. The increased nutrient and oxygen supply prevents tumor dormancy, supports tumor growth, and provides routes for tumor cell dissemination<sup>78,79</sup>. Secretion of proangiogenic mediators by tumor cells, most notably vascular endothelial growth factor (VEGF), promotes

endothelial migration and proliferation<sup>80</sup>. The resulting neovascularization of the surrounding stroma facilitates the dissemination of tumor cells into the blood stream and lymphatic vessels, a process which involves adherence to and transmigration through the endothelium, in particular via processes involving integrins<sup>81,82</sup>. Depending on conditions in the microenvironment at secondary sites, a proportion of these single cells or cell aggregates is capable of reinitiating tumor growth in distant organs. Such cells are collectively referred to as disseminated tumor cells, occult metastases, micrometastases, or minimal residual disease. Chambers et al. reviewed various studies that elucidated the barriers to metastatic spread including vascular impingement in capillaries of large CTCs, organ homing, and CTC adaptation to a flow regime<sup>83</sup>.

Upon identification of the primary tumor, carcinoma patient prognosis currently relies on imaging technologies that determine the extent of metastasis in distant organs, such as lymph nodes, bone marrow, liver, lungs, or brain, and subsequent outgrowth of these cells in their new microenvironment<sup>54,77</sup>. Even after localized treatment and resection of the tumors, DTCs can remain in a dormant state for many years before giving rise to macrometastases<sup>84,85</sup>. The same previously described cytometric and immunological detection strategies have been applied to characterizing DTCs from bone marrow, lymph nodes, and circulating blood. Bone marrow, acquired through aspirates of the iliac crest, was a common homing organ for DTCs derived from carcinomas of different organs<sup>86</sup>.

Although the metastatic pathway involves a plethora of genes and gene products, the ADAM (a disintegrin and metalloprotease) family is relevant to this thesis work for its role as a potential therapeutic target<sup>87</sup>. ADAM8 (A8) is a transmembrane protein and mediates cell adhesion, cell migration, and proteolysis of a variety of substrates, including cytokine receptors or their ligands, cell adhesion molecules and extracellular

matrix components<sup>87</sup>. Synthesized as a proform, ADAM8 can dimerize or multimerize and autocatalytically clip off its prodomain, leaving an active membrane-anchored metalloprotease. Active ADAM8 can be further processed by release of the metalloprotease domain into the extracellular matrix, which leaves a remnant form within the membrane. Both active and remnant forms mediate cell adhesion through their disintegrin/cysteine-rich/EGF-like (DCE) domains<sup>88</sup>, notably by direct binding to integrins<sup>89</sup>. ADAM8 was found to be non-essential under physiological conditions, as evidenced by the normal development and lack of pathological defects in ADAM8 deficient mice<sup>90</sup>, despite its expression in a variety of immune cells<sup>91,92</sup>. Interestingly, ADAM8 expression was detected under several pathological conditions characterized by inflammation and extracellular matrix remodeling, including cancer<sup>87</sup>. ADAM8 levels were induced under hypoxia in breast cancer cells<sup>93</sup>. Therefore, in collaboration with investigators seeking to identify ADAM8 as a therapeutic antibody target, this thesis work enumerated and characterized light scattering properties of CTCs in tumor induction and resection studies.

### **2.1.2 Morphological Differences among Differentiated Blood Cells and Epithelial-Derived Circulating Cancer Cells**

Morphological differences among constituent blood cell types are the basis for light scattering discrimination and are used in routine complete blood cell counts with flow cytometric analysis. In a clinical blood draw, CTCs may constitute less than one percent of nucleated cells; therefore, a discussion on peripheral blood components is pertinent. Human blood typically consists of 55% plasma (90% water and 10% protein) and 45% cells (>90% of which are erythrocytes) by volume. All normal blood cells derive from bone marrow but have different purposes within the circulatory and immune systems. Erythrocytes are responsible for oxygen transport, thrombocytes play a key role in blood clotting, and various leukocyte sub-populations are primary defenders within the

immune system. Normal concentration ranges and percentages of the main circulating blood cell types are shown in Table 2-1.

Table 2-1 Peripheral blood constitutive cell types with normal frequencies and percentages<sup>94</sup>.

Cell Type	Frequencies (X 10 <sup>6</sup> cells/mL)	Percent
<b>Erythrocytes</b>	3800 – 6200	93 – 96% of blood cells
<b>Platelets</b>	140 – 450	4 – 7% of blood cells
<b>Leukocytes</b>	4.1 – 10.9	0.1 – 0.2% of blood cells
<b>Lymphocytes</b>	1.1 – 3.5	14 – 47% of leukocytes
T Cells	0.54 – 1.79	7 – 24% of leukocytes
B Cells	0.07 – 0.53	1 – 7% of leukocytes
Natural killer	0.08 – 0.43	1 – 6% of leukocytes
<b>Myeloid</b>	3.9 – 6.5	53 – 86% of leukocytes
Dendritic cells	0.02 – 0.06	0.3 – 0.9% of leukocytes
Plasmacytoid dendritic cells	0.01 – 0.04	0.2 – 0.6% of leukocytes
Monocytes	0.2 – 0.9	2 – 12% of leukocytes
Granulocytes	2.13 – 6.35	35 – 80% of leukocytes
Neutrophils	2.09 – 5.97	30 – 80% of leukocytes
Eosinophils	0.03 – 0.3	0 – 7% of leukocytes
Basophils	0.01 – 0.08	0 – 2% of leukocytes
<b>Hematopoietic stem and progenitor cells (CD34<sup>+</sup>)</b>	0.001 – 0.007	0.03 – 0.09% of leukocytes

Morphological differences among cell types and corresponding scattering signatures of leukocytes are evident in the images shown in Figure 2-1. Mature erythrocytes<sup>95</sup>, displayed among single leukocytes, are anucleated, flat and biconcave disks, 6-8  $\mu\text{m}$  in diameter, 2-3  $\mu\text{m}$  in thickness, and have a mean volume of 90  $\mu\text{m}^3$ . Optimized for oxygen transport, erythrocytes exist in circulation for approximately 100 days, lack mitochondria, and are abundant in hemoglobin, which constitutes 90% of the cell by volume with approximately 270 million molecules<sup>95</sup>. Hemolysis using ammonium chloride ( $\text{NH}_4\text{Cl}$ ) is a common erythrocyte depletion method that was used in this thesis work<sup>96</sup>. First used in the 1940s, the mechanism of action is a rapid influx of  $\text{NH}_4^+$  ions via

exchange with hydroxide ( $\text{OH}^-$ ), bicarbonate ( $\text{HCO}_3^-$ ), or chloride ( $\text{Cl}^-$ ) to cause cell swelling and hemolysis<sup>96</sup>. The abundance of these channels in erythrocytes relative to leukocytes predominantly spares leukocytes within the first 10 minutes of exposure. However, the efficacy of lysis diminishes and leukocyte destabilization ensued after two 10-minute ammonium chloride exposure rounds<sup>96</sup>.

Platelets result from fragmentation of precursor megakaryocytes, are even smaller than erythrocytes at 2-3  $\mu\text{m}$  in diameter, and have an average lifespan of only five to nine days<sup>97</sup>.

Among leukocytes, there is a close link for roles within the immune system, lineages, and cell morphologies. Consisting of two broad groups, the innate and adaptive systems follow separate hematopoietic lineages and elicit the broad purposes of resisting and eliminating potentially harmful foreign materials and mutant cells<sup>98</sup>. The innate immune system is the first line of defense against infection and consists of soluble factors, such as complement proteins, and diverse cellular components including granulocytes (neutrophils, eosinophils, and basophils), mast cells, macrophages, and dendritic cells<sup>98</sup>. These cells derive from common myeloid progenitor cells in bone marrow. Granulocytes and mononuclear cells constitute the two broad morphological leukocyte sub-types. Granulocytes contain prominent and numerous cytoplasmic secretory granules and were first demarcated as polymorphonuclear cells due to the presence of a single but multi-lobed nucleus<sup>98</sup>.

Neutrophils stain a neutral pink with hematoxylin and eosin and contain a nucleus divided into two to five lobes with highly condensed chromatin<sup>98</sup>. With a primarily antimicrobial purpose, neutrophils respond to cytokines released by activated endothelium cells, mast cells, and macrophages. Neutrophils have an abundance of intracellular contractile proteins actin and myosin alongside microtubules for ease of

extravasation and intracellular transport. Neutrophils phagocytose using intracellular reactive oxygen species and hydrolytic enzymes, undergo degranulation to release soluble anti-microbial proteins, and generate neutrophil extracellular traps (NETs) composed of web-like structures of DNA to quarantine infection<sup>99</sup>.

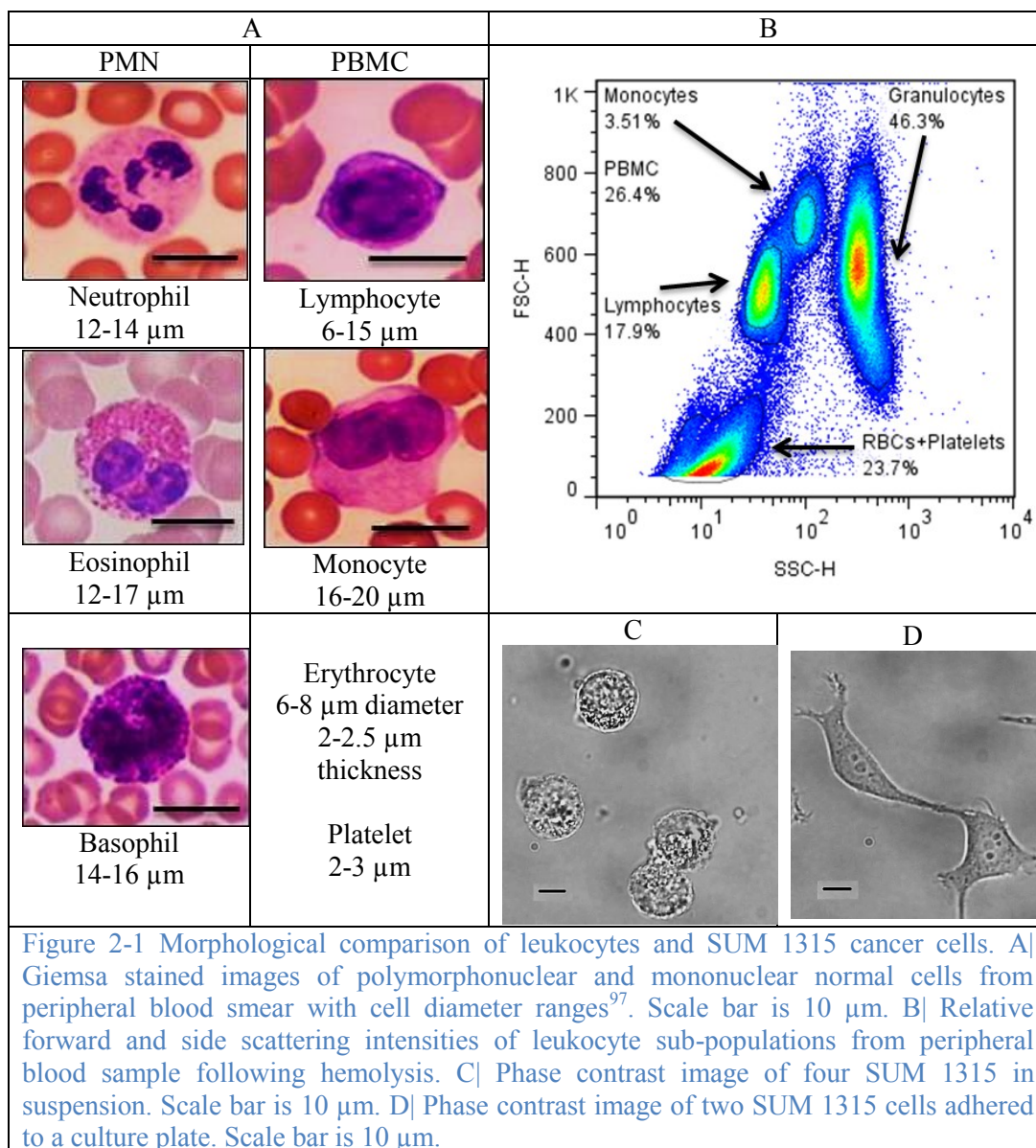
Eosinophils stain a deep red with eosin and are characterized by an abundance of ellipsoid cytoplasmic granules, and have a bi-lobed nucleus. These cells undergo degranulation and are implicated in anti-parasitic, anti-viral, infection chemokine chemotaxis, and allergy response, including asthma<sup>100</sup>. The contents of granules are cationic granule proteins, reactive oxygen species, lipid mediators, enzymes, growth factors, RNases, and cytokines.

Basophils stain a deep blue with basic dyes and contain an abundance of cytoplasmic granules that visually obscure the bi-lobed nucleus. Like eosinophils, basophils respond to inflammatory reactions caused by parasites and allergies<sup>101</sup>. However, their granules contain histamine to further trigger inflammation and heparin to reduce localized blood clotting.

Monocytes constitute the final component of the innate immune system. Their role is to differentiate into macrophages upon extravasation at damaged tissue sites based on chemotaxis. In circulation, monocytes, alongside lymphocytes, are one of two cell types that constitute peripheral blood mononuclear cells, which is the other morphological category outside of granulocytes. For both mononuclear cell types, the primary differentiating factor from granulocytes is the presence of a non-segmented smooth nucleus. Monocytes are the largest of leukocytes and contain a large, eccentrically placed bean-shaped nucleus. Macrophages are highly mobile and mature into dendritic cells, thus linking the innate and adaptive systems by processing material and presenting antigens on the cell surface for recognition by other cells<sup>98</sup>.



If the innate immune system fails to neutralize a threat then inflammation ensues and either of the two components of the adaptive immune system, humoral and cell-mediated, responds with increased antigenic specificity. These cells derive from common lymphoid progenitor cells in bone marrow and are composed of lymphocytes. The humoral component targets bacteria and consists of antibodies produced by B-lymphocytes. The cell-mediated immunity component targets virus-infected and cancer cells and consists of activated T lymphocytes. Both types of lymphocytes are characterized by a round nucleus with condensed chromatin. In contrast to monocytes, lymphocytes have fewer intracellular organelles such as lysosomes and vacuoles and a less developed Golgi apparatus. Similar in structure to lymphocytes but also containing cytotoxic granules, natural killer (NK) cells straddle the innate and adaptive roles by lacking immunological memory and nonspecifically lysing target cells, including cancer cells. This mechanism of action follows cytokine release from the tumor microenvironment<sup>102</sup>. The complex role of the immune response in cancer mitigation and progression will be discussed further in 2.2.



A flow cytometric representation of leukocyte sub-populations (Figure 2-1) demonstrates how cell diameter and refractive organelle abundance correlate to relative scattering intensity. In general, larger diameter cells scatter more light in the forward direction while increasing concentrations of smaller intracellular refractive organelles increase side scatter<sup>103</sup>. Elastic light scattering yields the observed differences among leukocytes and the underlying theory will be discussed in 2.3. Beyond light scattering signatures, leukocytes can be subtyped polychromatically using fluorescently labeled

antibodies against specific CD cell surface molecules<sup>103</sup>. This is a common enrichment and analytical technique that was introduced in 1.2.2. Noting the light scattering differences among leukocyte sub-populations due to morphological differences, a discussion on CTC morphological characteristics is pertinent to understand the basis for CTC light scattering-based detection.

The epithelial-mesenchymal yields new, albeit heterogeneous, morphological characteristics that distinguish CTCs from blood cells. Within a solid tumor, malignant cells are characterized broadly by acceleration of the cell cycle, increased cell motility, chemotaxis, changes in surface protein composition, and genomic alterations<sup>104</sup>. These characteristics present morphologically with a large, irregular nucleus, prominent nucleoli, and scarce cytoplasm. Irregularities within the nucleus reflect the increased rate of mitosis and arise from segmentation, invaginations, changes in chromatin organization, and increased porosity. Accumulation of ribosomal RNA and messenger RNA make the cytoplasm basophilic<sup>97</sup>. Each intracellular organelle experiences morphological changes as metabolic demand favors cell division over growth-related metabolisms. The granular endoplasmic reticulum undergoes degranulation to enhance protein production from free and polysomic ribosomes<sup>98</sup>. The Golgi apparatus is poorly developed due to the emphasis on proliferation, rather than differentiation. Mitochondria generally decrease in volume, but high variability has been observed, especially in cells where fermentation dominates aerobic respiration, which is known as the “Warburg phenomenon.” Intracellular glycogen increases have been observed in peripheral cells, while intra-carcinoma cells have decreased glycogen and increased lipid content<sup>105</sup>.

As mentioned before in relation to CTC enrichment techniques, the presence of cytokeratins distinguishes epithelial cells as these structures enhance cell-to-cell adhesion<sup>47</sup>. Although cytokeratins continue to exist in CTCs, the intravasation process

disrupts these adhesions with desmosomes and links to the basal membrane. Surface molecular changes reflect the enhanced invasive capacity of some cells while other changes tag different cells for apoptosis and immune cell destruction<sup>83</sup>. In the case of increased motility, proteins and carbohydrates that acted as enzymes on the cell surface receptors diminish and no longer react with corresponding ligands, thereby causing reduction in cell-to-cell adhesion contacts, detachment from the basal membrane, and evasion from the immune system. The enhanced activity and abundance of ADAM8 is one such example of a surface protein in a malignant cell that augmented invasiveness.

Once in circulation, CTCs are exposed to a flow and shear regime that sharply contrasts the relatively static nature of the extracellular matrix of the epithelium<sup>83</sup>. The understanding of CTC morphology has improved alongside enrichment techniques; however, artifacts from ex vivo manipulation inherently alter morphological aspects to some degree. Apoptosis and immune cell destruction persist in circulation, thus reducing the population of CTCs capable of the second transition, extravasation, from mesenchymal to epithelial traits in a secondary metastatic site. As previously discussed in the FDA-approved CellSearch™ CTC enumeration assay, an operator manually selects CTCs from a range of isolated cells. Efforts to standardize and automate this process uncovered distinctive morphological characteristics, in addition to immunohistochemical EpCAM and cytokeratin positivity, that were used to identify CTCs<sup>44</sup>. Using image analysis algorithms on known metastatic and control patient data sets, minimum thresholds were established for nuclear to cytokeratin ratio and roundness. Conversely, maximum thresholds were set for CD45 intensity. However, leukocytes and CTCs shared a size range of 35-900  $\mu\text{m}^2$  (in pixels).

## 2.2 Cancer Immune Response

The interaction between the immune system and cancer, as manifested by rogue leukocytes in leukemia, was first discovered in the mid-19<sup>th</sup> century by the German pathologist Rudolf Virchow<sup>106</sup>. Over the past 200 years, a wide body of literature has emerged that supports numerous relationships between the immune system and cancer. The implications of this immune response to tumor-specific cytokines range from inhibiting to promoting tumor growth and are collectively known as immunoediting<sup>107</sup>. The predominant evidence for immunoediting derives from genetically mutated mice with absent, dysfunctional, or altered immune system components. A comprehensive review published in 2011 referred to dozens of such studies<sup>108</sup>. In brief, mice lacking components of the adaptive immune system including T cells, B cells, and NKT cells were more susceptible to carcinogen-induced sarcomas. In contrast, mice with upregulated T cells and eosinophils had reduced carcinogenesis. Additional studies have also been conducted on immunocompromised mice where tumorigenesis was observed to develop spontaneously in the absence of mitigation mechanisms inherent to the immune system<sup>107</sup>. The typical immune response to unchecked tissue growth is direct infiltration by cytotoxic T cell and indirect modulation of angiogenesis factors by humoral and cytokine signaling<sup>107</sup>.

Animal studies have illuminated the activation mechanisms of these responses and suggested cofactors that have been subsequently investigated for several cancers to determine prognosis<sup>109</sup>. NKT cells abundant in human gastric or colorectal carcinoma elicited a favorable prognosis<sup>110,111</sup>. On the other hand, infiltration of other immune cell components, such as mast cells, was unfavorable in lung adenocarcinoma<sup>112</sup>. Epidemiological evidence based on immunosuppression due to infection (e.g. AIDS) or organ transplant medication corroborated the animal data with corresponding increases in

cancer prevalence<sup>113,114</sup>. Functional impairment of T cells and accumulation of myeloid suppressor cells in circulation elicited the ability to evade anti-tumor regulation<sup>115-117</sup>.

Recent cancer immunotherapy developments reflect our growing understanding of the role of the immune system in cancer<sup>118</sup>. Current approaches either activate or suppress molecules and cells of the immune system to reject cancer. Immunization is one example of immune system activation, and the first therapeutic cancer vaccine to receive US FDA approval (2010) was Sipuleucel-T, indicated for castration-resistant prostate cancer<sup>119</sup>. The vaccine contains autologous PBMCs activated with a recombinant antigen that is prostate specific and stimulates therapeutic granulocyte-macrophage formation. Monoclonal antibodies constitute a second therapeutic class<sup>118</sup>. Alemtuzumab (Campeth-1H) typifies an activation approach that targets CD52<sup>+</sup> blood lymphocytes to initiate an augmented immune response and is indicated for leukemia. Conversely, Bevacizumab (Avastin) exemplifies a suppression approach that binds vascular endothelial growth factor (VEGF) to inhibit angiogenesis and is indicated for colon, kidney, lung, ovarian, and breast cancers. The potential therapeutic role of an inhibitory antibody against ADAM8 was introduced in 2.1.1, and the early animal studies constituted a major component of this thesis work and will be presented in Chapter 6.

## 2.3 Elastic Scattering of Biological Molecules

Differences in elastic light scattering intensity are the basis for our cell type discrimination approach. The general theory, relevant scattering regimes, and the refractive index ranges of biological molecules will be discussed in this section.

Light scattering phenomena arise from the wave nature of light. Interaction of a propagating wave with a substance of different refractive index than the surrounding medium yields a scattering event with a new propagation vector. In the case of elastic scattering, there is not an overall energy transfer but only a possible change in the

direction of the momentum vector; therefore, the incidence and propagation vectors have equal magnitude, and the wave retains the same frequency. Conversely, inelastic scattering increases or decreases the frequency of the scattered wave<sup>120</sup>.

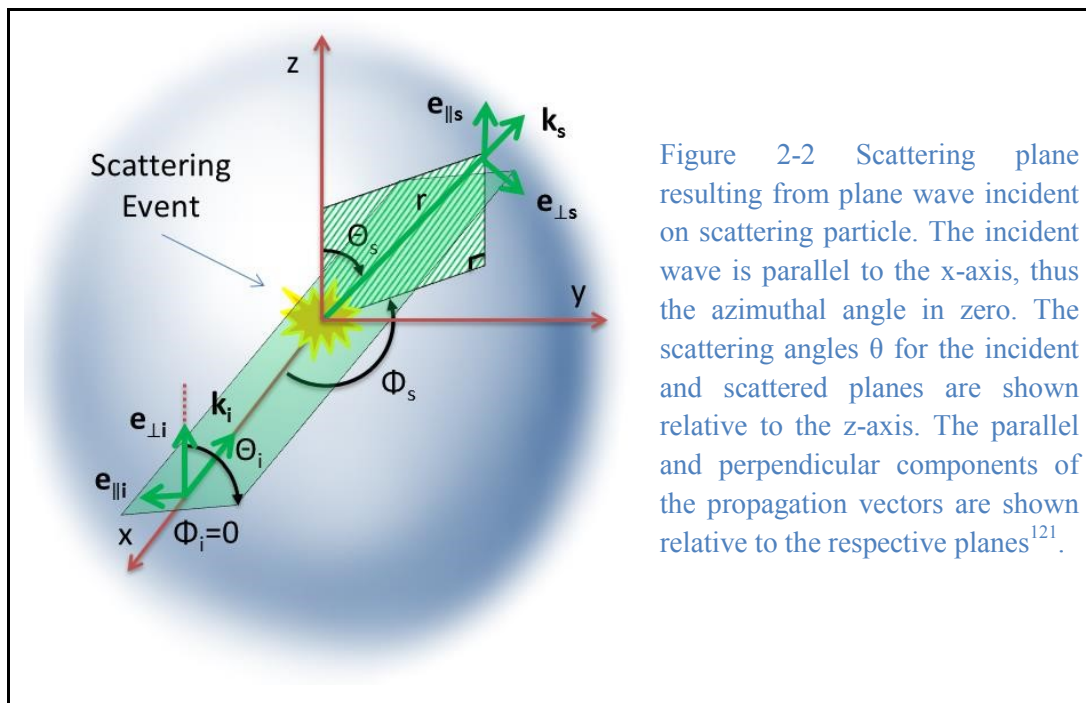
In the case of elastic scattering, the plane electric field of the incident wave induces dipoles in the electrons of the substance. The oscillations of these induced dipoles re-radiate the new scattered spherical waves or ‘wavelets’, which our detection system, in the far field, perceives as a superposition of scattered light. The induced dipoles oscillate in a space constrained by the dimensions of the particle. If the particle is small relative to the incident wavelength, then the dipoles are exposed to equal intensities of energy and the oscillations are in phase. As the particle size increases, however, there is a greater probability for non-uniform dipole induction, and interference occurs among the re-radiated wavelets with variable magnitude at different angles of observation. Three scattering regimes mathematically approximate the relationship between scattering intensity and incident wavelength: Rayleigh, Rayleigh-Gans, and van de Hulst. There is a fourth approach, Mie theory, which provides exact numerical solutions by applying Maxwell’s equations to plane waveforms incident on any size sphere.

Consider a particle illuminated by a plane electromagnetic wave described as  $\mathbf{E} = \mathbf{E}_0 e^{-i(\mathbf{k}\mathbf{r} - \omega t)}$  where  $E_0$  is the wave amplitude,  $i$  is the imaginary unit, wavenumber  $k = |\mathbf{k}| = 2\pi/\lambda$ ,  $\lambda$  is the wavelength,  $\mathbf{r}$  is the position vector from the scattering event to the point of observation, angular frequency  $\omega = 2\pi f$ , and  $f$  is the frequency<sup>121</sup>. The incident and scattered fields are transverse to the scattering plane<sup>121</sup>. Thus, these fields can be decomposed into two orthogonal components, one parallel, and the other perpendicular to the scattering plane defined by the incident and scattered fields. The decomposition of the scattering field for incident ( $E_i$ ) and scattered ( $E_s$ ) fields is a combination of the parallel ( $\parallel$ ) and perpendicular ( $\perp$ ) components as follows in Equation 2-1<sup>122</sup>.

## Equation 2-1 General formulation for scattering event

$$\begin{pmatrix} E_{\parallel s} \\ E_{\perp s} \end{pmatrix} = \frac{e^{-i(\mathbf{k}\mathbf{r}-\omega t)}}{-i\mathbf{k}\mathbf{r}} \begin{pmatrix} S_2 & S_3 \\ S_4 & S_1 \end{pmatrix} \begin{pmatrix} E_{\parallel i} \\ E_{\perp i} \end{pmatrix}$$

The scattered electric field with complex amplitudes is the product of three terms. The first term represents the scattered wave in the far field as a spherical, outgoing wave. In spherical coordinates, the position vector  $\mathbf{r}$  is defined in terms of scattering angle  $\theta$  and azimuthal angle  $\phi$ , as shown in Figure 2-2.



The amplitude of the wave is inversely proportional to the magnitude of the direction vector. The second term is the scattering amplitude or Jones matrix  $S$ . For all three scattering regimes and for Mie theory, the elements of the  $S$  matrix are solved for appropriate boundary conditions of electromagnetic field continuity. For example, in the case of scattering sphere, the  $S_3$  and  $S_4$  elements are zero. The third term is the complex amplitudes of the incident electric field. Working from this general formulation, the respective solutions are functions of the wavelength, characteristic dimension of scattering particle, and refractive indices of particle and medium.



The size of a scattering particle is parameterized by the ratio  $x = \frac{2\pi r}{\lambda}$  where  $r$  is the characteristic dimension, such as diameter for a sphere, and  $\lambda$  is the wavelength of incident light<sup>121</sup>. Measured as a scattering system, a cell produces an aggregate signature that is a combination of the individual regimes of the cell itself and variable-sized intracellular components. The refractive indices and size ranges of representative subcellular components are shown in Table 2-2.

Table 2-2 Refractive index and size ranges of blood cell components.

Biological Component	Refractive Index	Size Range
<b>Extracellular fluid</b>	1.35-1.36 <sup>123</sup>	Surrounding cells
<b>Cytoplasm</b>	1.34-1.375 <sup>123</sup>	Contains proteins and solutes (<100nm)
<b>Nucleus</b>	1.38-1.41 <sup>123</sup>	3-10 $\mu\text{m}$ containing chromatin <sup>124</sup>
<b>Mitochondrion</b>	1.38-1.42 <sup>123</sup>	Length: 1-4 $\mu\text{m}$ and Width: 0.3-0.7 $\mu\text{m}$ <sup>124</sup>
<b>Lysosome</b>	1.6 <sup>125</sup>	0.2-0.5 $\mu\text{m}$ <sup>124</sup>
<b>PMN Leukocyte Granules</b>	1.47-1.6 <sup>126</sup>	0.1-1.2 $\mu\text{m}$ <sup>127,128</sup>
<b>Lymphocyte</b>	1.36 <sup>129</sup> 1.36 <sup>130</sup>	6-15 $\mu\text{m}$ <sup>97</sup>
<b>Monocyte</b>	1.35 <sup>130</sup>	16-20 $\mu\text{m}$ <sup>97</sup>
<b>Erythrocyte</b>	1.41 <sup>131</sup>	6-8 $\mu\text{m}$ <sup>97</sup>

Noting the dimensions and parameters in Table 2-2, the first regime, Rayleigh, applies to particles much smaller than the incident light wavelength, such as components of the cytosol. The fundamental assumption of this regime is that all scatters experience the same magnitude of induced dipole and are in phase. The elements of the scattering matrix take the form shown in Equation 2-2 for a scattering sphere<sup>121</sup>.

Equation 2-2 Jones matrix for Rayleigh scattering approximation from a sphere

$$\begin{pmatrix} S_2 & S_3 \\ S_4 & S_1 \end{pmatrix} = ik^3 \alpha \begin{pmatrix} \cos \theta & 0 \\ 0 & 1 \end{pmatrix}$$

The polarizability  $\alpha = \frac{(m-1)V}{2\pi}$  is a function of volume  $V$  and relative refractive index  $m$  between the particle and the surrounding medium<sup>121</sup>. Upon substitution of the Jones matrix into the general formulation in Equation 2-1, Rayleigh scattering is characterized

by a  $\lambda^{-4}$  inverse power law. When using visible light for scattering measurements, proteins and small granules with a size of approximately 100 nm scatter light according to this regime.

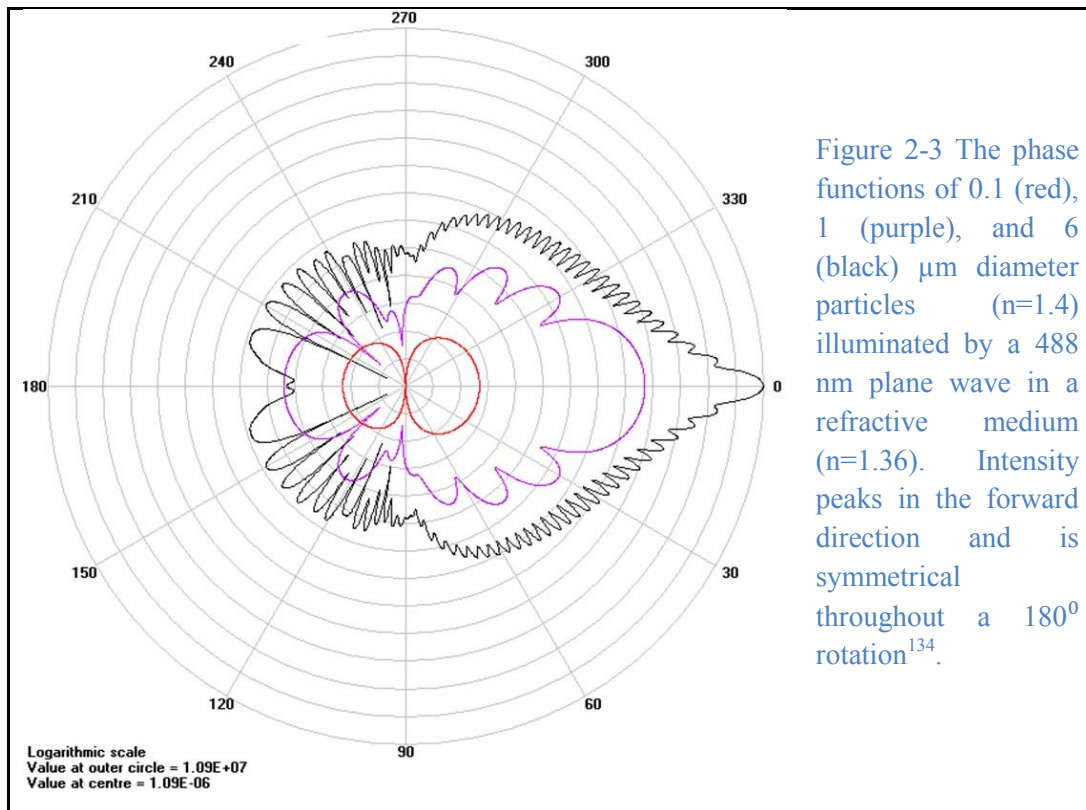
The second regime, Rayleigh-Gans, pertains to particles with a size comparable to the incident light wavelength. The assumptions of this regime are that infinitesimal volume elements within the scatterer behave as induced dipoles (Rayleigh scatterers); however, their cumulative far field interference follows the superposition principle, which allows for phase variability. This variability manifests as oscillations in a log-log plot of scattering intensity versus wavelength. In the case of incident visible light on a mitochondrion with size of approximately one micrometer, oscillations occur in the purple and blue wavelengths before the scattering intensity decays according to the Rayleigh inverse power law<sup>132</sup>.

The final regime, van de Hulst, is relevant to particles much bigger than the incident wavelength<sup>122</sup>. The approximate solutions are most accurate in the forward scattering direction assuming a spherical scatterer with center-emanating wavelets. Furthermore, this approximation uses the total scattering cross-section and is valid up to a relative refractive index of two. Cell nuclei and whole cells with diameters greater than one micrometer interrogated with visible light produce oscillations throughout the visible spectrum. Light scattering spectroscopy has been used to differentiate cancerous from normal tissue regions as a function of the increased nuclear size observed in cancerous tissues<sup>132</sup>.

In contrast to the three regimes that vary according to the size of the scatterer for a given interrogative wavelength, Mie theory numerically applies Maxwell's solutions and is valid for a sphere of any diameter (relative to scattered light wavelength) and relative refractive index. As before, spherical polar coordinates defined in Figure 2-2 are

used with appropriate boundary conditions at the surface of the sphere. Although original solutions applied to scattering generated from a plane wave, generalized Lorenz-Mie theory parameterizes Jones matrix elements for scattering generated from a focused Gaussian beam<sup>133</sup>.

The phase function of scattering is anisotropic and a polar plot generated using Mie theory demonstrates the augmented relative intensity in the forward direction and frequency of oscillations for larger particles. The phase functions of 0.1 (red), 1 (purple), and 6 (black)  $\mu\text{m}$  diameter particles with a refractive index of 1.4 in a surrounding medium of 1.36 illuminated with 488 nm plane wave light are shown in Figure 2-3<sup>134</sup>. With increasing particle size, there is a proportional increase in isotropic intensity and frequency of oscillations, as approximated by van de Hulst. For all three particles, forward-scatter ( $0^\circ$ ) intensity is the most intense; however, the relative difference between forward and backward intensity is greatest for larger particles.



In addition to influencing the oscillatory behavior of scattered light, particle size also affects the scattering angle, as measured relative to the incident vector. The intensity of forward-scattered light (FSC) is proportional to particle size<sup>135</sup>. Light diffracts from the interface of changing refractive indexes; therefore, a greater surface area yields a greater intensity in forward-scattered light<sup>136</sup>. The intensity of side-scattered light (SSC) is proportional to internal complexity and granularity<sup>135</sup>. Light refracts and reflects at any refractive index differential interface. As applied to complete blood cell counts, flow cytometry discerns granulocytes from agranulocytes within white blood cell subpopulations based on increased intensity of SSC due to the presence of intracellular granules containing refractive cytotoxic agents, as seen in Figure 2-1 B<sup>137</sup>. The reduced scattering intensity observed from erythrocytes is a function of the relationship between scattering and absorption. Although the constituent hemoglobin of erythrocytes is highly refractive ( $n=1.4$ ), the imaginary component representing absorption dominates and erythrocytes are highly colored (red) relative to leukocytes<sup>131</sup>.

As predicted by the three scattering regimes and Mie theory, light scattering intensity is sensitive to incident wavelength, in addition to particle size. This additional level of discrimination is the basis for our multi-wavelength backscattering flow cytometry system. The interrogative wavelengths of 405, 488, and 633 nm light were determined in light scattering spectroscopy measurements using white light illumination<sup>26</sup>. The backward-direction ( $150-180^\circ$ ) Mie theory phase functions of one- and six-micrometer diameter particles ( $n=1.4$ ) within a surrounding medium ( $n=1.36$ ) illuminated by plane wave light are shown in Figure 2-4<sup>134</sup>. As before in Figure 2-3, the phase functions of the larger particle (6  $\mu\text{m}$ , primary axis) have oscillations while the smaller particle (1  $\mu\text{m}$ , secondary axis) follows a power law. Furthermore, the maximum

amplitude of the phase function of the larger particle is approximately one to two orders of magnitude greater than that of the smaller particle. The aggregate measured scattering signal is a superposition of all individual scattering wavelets, such as those emanating from small intracellular organelles, the nucleus, and the membrane of the cell.

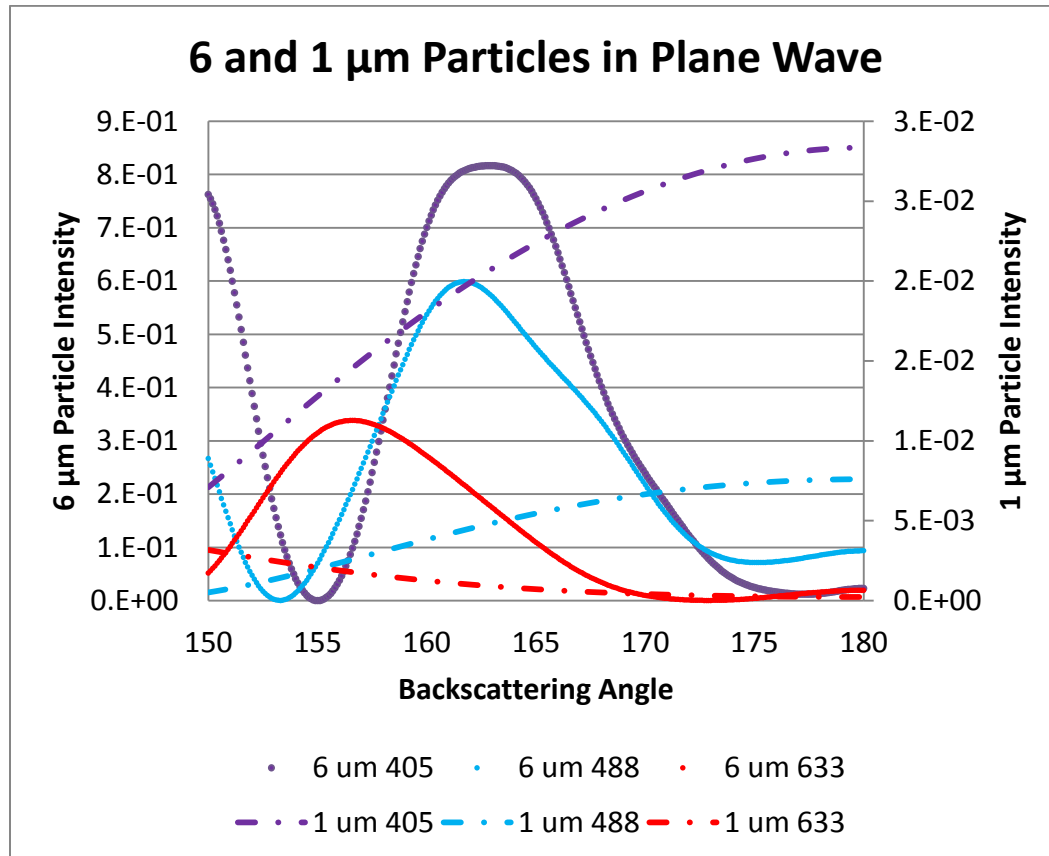


Figure 2-4 Backscattering intensity plot from 150-180 $^{\circ}$  for particles of one (secondary axis) and six (primary axis) micrometers in diameters for the three interrogative wavelengths of 405, 488, and 633 nm. In both cases of particles diameter, the refractive index of the particle was 1.6 and that of the surrounding medium was 1.4.

The backward detection direction was chosen for purposes of system design, translation to in vivo assessment, and supporting studies demonstrating the ability to resolve scattering from intracellular structures<sup>138-142</sup>. In general, backscattering from cells and tissues follows an inverse power as a function of interrogative wavelength. Different cell types have characteristic power law exponents, thus suggesting that differences in cellular composition produce variable aggregate scattering signatures. Although Mie

theory accurately describes phase functions from single particles, even more nuanced approaches are required to model the cumulative effect of multiple scattering events and interfering wavelets. Whereas photons emanating from multiple scattering events exhibit phase changes and are rejected with a polarizer in the detection pathway, interference effects constitute the final detected signal. Finite Difference Time Domain (FDTD) is a grid-based differential modeling method that allows for refractive index changes in the space and time domains<sup>143</sup>. By switching between solving for the electric and magnetic fields in a given grid unit with variable refractive indices and boundary conditions, the approach leapfrogs across the space to develop a transient or steady state model. A second approach to modeling scattering contributions from multiple sources is based on fractal organization of continuous refractive index fluctuations<sup>140,141,144-146</sup>. Fractal organization has been observed in nuclear and cell membranes, nuclear chromatin, and mitochondrial networks<sup>146,147</sup>. Primary purposes of these analyses are to more accurately characterize the high-frequency power spectral density and provide insight into the topography of dominant scatterers.

## 2.4 Fluorescence

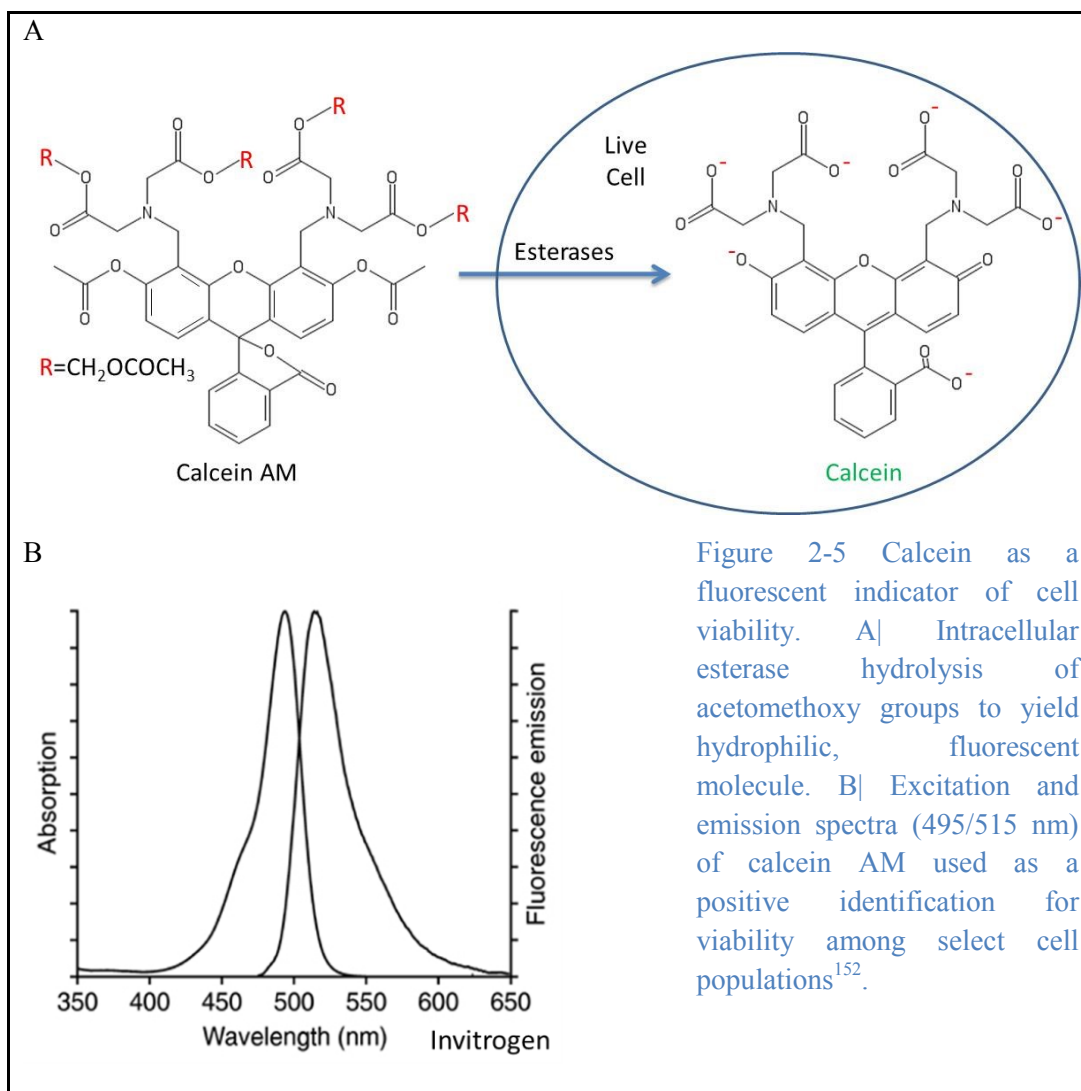
Fluorescence signal was used in this thesis work as a positive identification of labeled cells and as a marker of rare autofluorescent cells. The two fluorescence molecules were calcein AM and green fluorescent protein (GFP).

A fluorescence event starts with absorption and it is followed by radiative relaxation<sup>148</sup>. Incident light excites a ground state electron to a vibrational level in an excited singlet electronic state. The energy of the incident wave must be sufficient to excite the electron, which is equal to the energy difference between the two electronic states as determined by principal quanta levels in atoms and molecular orbitals in molecules. Non-radiative internal conversion reduces the position of the electron to the

lowest vibrational level in the excited electronic state. Fluorescence occurs when the electron returns to any vibrational level within the ground state. The internal conversion process elicits the Stokes shift where the fluorescent photon has a longer wavelength than the incident excitation light<sup>148</sup>.

Biological fluorophores are endogenous and exogenous. In both cases and in the context of visible light, the molecules contain extensive conjugated systems that possess an energy gap of approximately two eV between the bonding and anti-bonding molecular orbitals. Amino acids, enzymes and coenzymes, and proteins are endogenous fluorescence sources. Tryptophan, tyrosine, and phenylalanine are aromatic amino acids. Flavin adenine dinucleotide (FAD) and reduced nicotinamide adenine (phosphate) dinucleotide (NAD(P)H) are cytosolic and intra-mitochondrial metabolic factors<sup>149</sup>. Both molecules have extensively conjugated aromatic structures. GFP is a beta barrel structure protein that undergoes a proton transfer when exposed to blue light with peak excitation and emission at 473 and 508 nm, respectively. The fluorescence process emits a green photon upon relaxation. GFP was first isolated from jellyfish and is now used extensively as a reporter molecule for transfection and transduction experiments<sup>150</sup>.

Exogenous calcein AM (acetomethoxy) is a cell-permeant dye that is commonly used to determine eukaryotic cell viability<sup>151</sup>. In live cells, intracellular esterases hydrolyze the acetomethoxy group of the non fluorescent dye, thus generating a hydrophilic molecule, which is trapped inside the cell and fluoresces via binding  $\text{Ca}^{2+}$ , as shown in Figure 2-5.



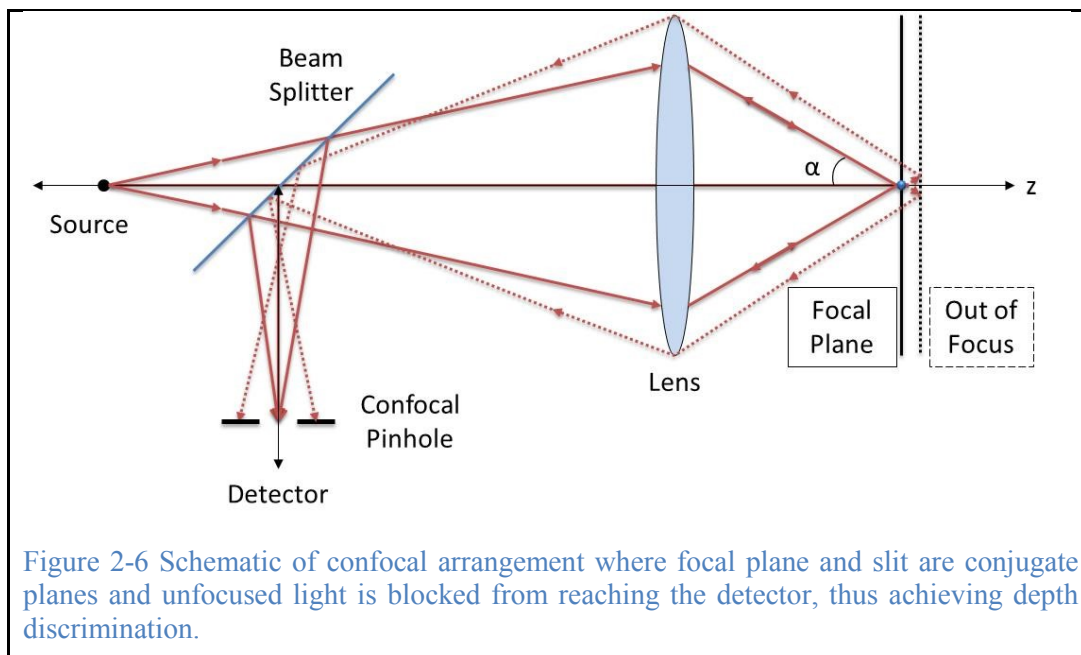
In contrast, dead cells lack active esterases, have compromised cell membranes, and do not fluoresce via calcein. Having established the basis for biological scattering and fluorescent events, the following section on confocal reflectance microscopy discusses the optical techniques used for detecting such events.

## 2.5 Confocal Flow Cytometry

The confocal design of the backscattering light detection system minimizes scattering signal from out-of-focus light in the flowing samples. Whereas standard detection systems collect scattered and fluorescent light inside and outside of the focal plane, confocal detection systems achieve depth resolution by blocking out-of-focus light from the detectors. As illustrated in Figure 2-6, the light source transmits through a beam



splitter and is focused into a point on the sample by an objective lens. Scattering and fluorescent photons propagating within the collection angle of the lens are reflected by the beam splitter and focused onto a conjugate plane that aligns with a pinhole in front of the detector. Our flow system continuously measures signal intensity passing through the confocal pinhole.



In our optical system, the objective is responsible for illumination and collection. The lateral resolution,  $r$ , and axial resolution,  $z$ , of the light microscope are described by the Abbe equation, as shown in Equation 2-3 and Equation 2-4, as functions of emission wavelength  $\lambda$ , refractive index of the sample  $n$ , and numerical aperture (NA) of the objective<sup>148</sup>.

Equation 2-3 The xy-resolution of an objective as a function of the emission wavelength and numerical aperture (NA) of the objective.

$$r = 0.61 \frac{\lambda}{NA}$$

Equation 2-4 Axial resolution near the focal plane of the slit as a function of the emission wavelength, refractive index of the sample, and NA of the objective.

$$z = 0.95 \frac{\lambda}{n \left[ 1 - \sqrt{1 - \left( \frac{NA}{n} \right)^2} \right]}$$

The numerical aperture is defined as  $NA = n \cdot \sin \alpha$  where  $n$  is the refractive index of the sample and  $\alpha$  is half of the acceptance angle. Although a higher NA allows for additional light collection over a wider angular range, the size of the confocal slit is a practical limitation that balances transmitting focused light while blocking unfocused light. The optimal diameter of a slit,  $D$ , is equal to the full width at half maximum of the Airy figure and can be approximated by Equation 2-5<sup>148</sup>.

Equation 2-5 Optimal diameter of confocal slit as a function of emission wavelength, system magnification, and NA of the objective.

$$D = \frac{1.2\lambda M}{NA}$$

The magnification  $M$  is specified for each objective from the sample to the imaging plane. The NA of our objective was selected to allow sufficient working distance to interrogate the middle of a 30-70  $\mu\text{m}$  (height) channel above a millimeter of microscope slide glass. Our mid-range 40x 0.6 NA objective has a working distance of 2.7-4 mm. The theoretical resolution and slit diameter values are shown in Table 2-3 for the three-wavelength system.

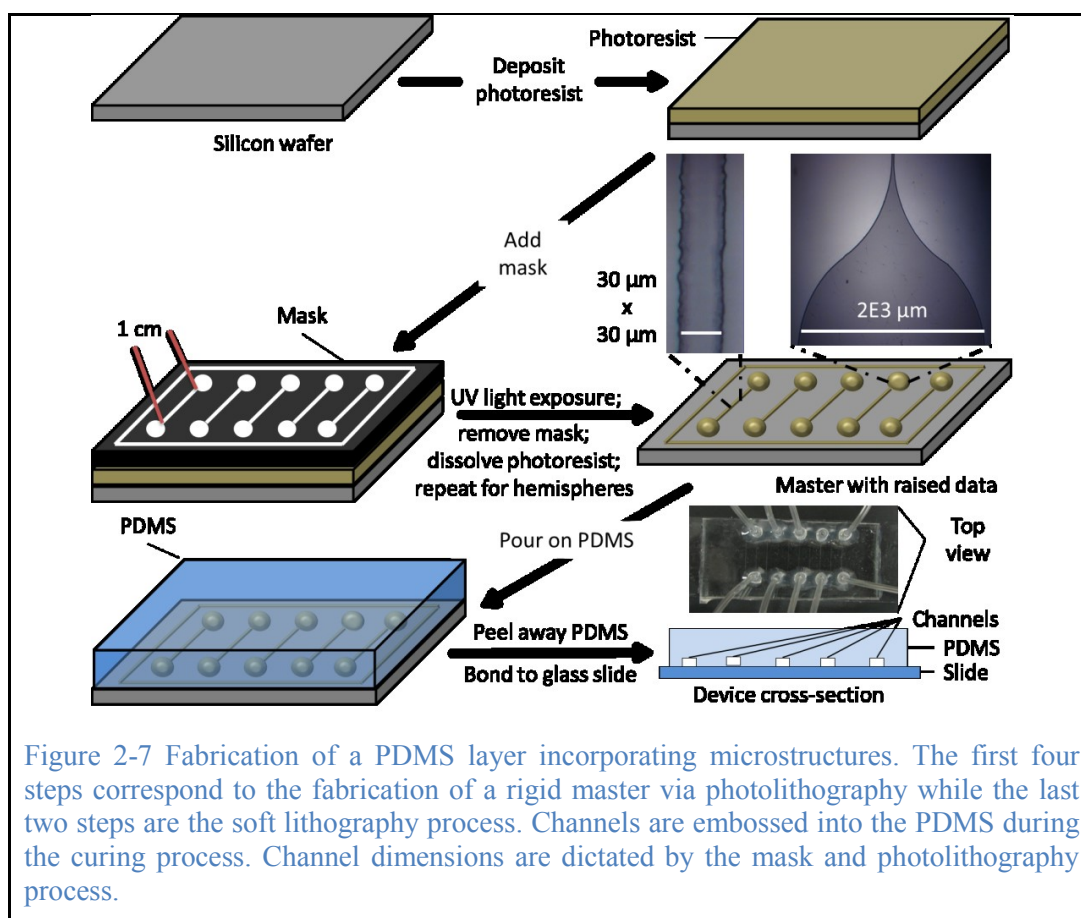
Table 2-3 Theoretical resolution and slit diameter values for the three-wavelength system using a 40x 0.6 NA objective.

Parameter		Wavelength (nm)	405	488	633
Resolution	Lateral	$r$ ( $\mu\text{m}$ )	0.411	0.496	0.644
	Axial	$z$ ( $\mu\text{m}$ )	2.6	3.2	4.1
Slit Diameter		$D$ ( $\mu\text{m}$ )	45.0	54.2	70.3

Experimental measurements of these same parameters are discussed in Chapter 3. The primary design goal of a confocal system is to minimize out-of-focus light. Sources of noise include ambient light, spherical aberrations arising from refractive index mismatches between objective glass and biological molecules, and absorption events that attenuate scattering intensity.

## 2.6 Microfluidic Design and Processing

The microfluidic devices used in this work were created using soft lithography and fusion bonding techniques, which have roots in the microelectronics industry but are now widespread in microbiology and flow applications<sup>153</sup>. The fabrication process is illustrated in Figure 2-7 with images of the final device.



The materials of silicon, photoresist, and glass reflect the microelectronics origin of the technology. The first four steps entail the photolithography process wherein a

master mold contains raised data while the last two steps use soft lithography techniques to generate the final device. In the first step, SU8-2025 photoresist is spin-coated onto a polished silicon wafer to create the height dimension of the raised data, here 30  $\mu\text{m}$ . A photomask (Advance Reproductions, North Andover, MA) created in CAD with transparent data is applied in contact with the photoresist. The lateral dimensions of the transparent areas dictate the lateral dimensions of the final data. Dimensions used in this work were 1 cm (length) x 30  $\mu\text{m}$  (width) x 30  $\mu\text{m}$  (height), which is illustrated in Figure 2-7, and 1 cm (length) x 50  $\mu\text{m}$  (width) x 70  $\mu\text{m}$  (height). Upon exposure to ultraviolet light, the photoresist polymerizes and bonds to the silicon substrate. The unexposed photoresist is dissolved and washed away using propylene glycol monomethyl ether (PM) acetate, thus leaving a bas-relief master data, which is silanized for low affinity embossing. Polydimethylsiloxane (PDMS) is then poured onto the master to a desirable height and allowed to cure with embossed structures before being cut out and peeled away. PDMS is a preferable material for numerous reasons, including negligible toxicity, low cost, optical transparency for 240-1100 nm light, and capable of curing in two hours at 65  $^{\circ}\text{C}$ <sup>154</sup>. The final step entails plasma cleaning the to-be adjoined surfaces of the embossed PDMS and microscope slide where the bottom surface of the channel is the glass slide. Dangling bonds formed by Si-O-Si between the plasma-exposed surfaces constitute the covalent bond<sup>155</sup>. A complete procedure is provided in the Appendix section 9.1.1.

## 2.7 Statistical Analysis

Discriminant analysis was employed to compare scattering profiles among various cell types. In the development of classification functions, fluorescence intensity emanating from calcein-labeled cultured cancer cells or GFP<sup>+</sup> CTCs in tumor induction studies served as positive identification for epithelial cells among a background of blood cells. However, a fluorescent standard will be absent in future clinical applications;

therefore, discriminant analysis was used to derive classification functions using linear combinations of scattering parameters. The objective of linear discriminant analysis is to identify two or more groups (i.e. cell populations) defined by their centroids and variance. In this way, a multivariate analysis of variance (MANOVA) first identified discriminating values among groups to elucidate whether significant differences exist that could be leveraged for classification purposes. The second step was to apply the discriminant function through cross-validation or training and validation sets to predict group membership of individual cells<sup>156</sup>.

Discriminant analysis was chosen for the application of developing classification functions based on training data sets. The suitability of MANOVA and discriminant analysis for this application relates to assumptions of the methods. First, the cell types (groups) must be independent of one another. The present application of measuring scattering from individual cells as samples from independent populations fulfils this assumption. Second, population distributions according to discriminating variables must be continuous and normal. Third, the discriminating variables must not be linear combinations of one another. We used scattering intensities and ratios thereof, which demonstrated minimal skewness toward the high-intensity direction in approximately 10% of the cell populations. This aspect of potential non-normality was mitigated by increasing the sample size and consistently analyzing the homogeneity of covariance matrices to confirm that the error variance of each interval of dependent variable was similar<sup>157,158</sup>.

MANOVA tests the differences in the centroid (vector) of means of the multiple interval dependents (cell types), for various categories of the discriminating variables (scattering intensities). Analyses were performed using SPSS (Statistical Product and Service Solutions, IBM) and `manova1` and `classify` functions within MATLAB. The

complete discriminant algorithms are provided in the technical help sections of SPSS<sup>159</sup>. A detailed discussion of discriminant analysis theory is provided in Appendix section 9.1.2.

In addition to providing canonical functions, statistical software packages also define test statistics for interpreting the classification at overall, individual variable, and individual canonical function levels. SPSS provides exact P-values when the test statistic is significant above 0.0005. Complete classification outputs for key results are provided in the appendix and definitions of those outputs are provided here to complement the interpretations.

The first test statistic is Wilks' lambda ( $\Lambda$ ), which is calculated as a value between 0 and 1, where  $1-\Lambda$  or  $1-\Lambda^2$  (partial  $\eta^2$ ) is interpreted as the overall degree of variation among the groups<sup>160</sup>. A second test statistic, Pillai's Trace, also quantifies the overall differences among centroid means and variances and is used when homogeneity of variance-covariance (e.g. normal distributions) is in question, thus indicating a more conservative evaluation of group differences<sup>160</sup>. For both test statistics, smaller values indicate a greater degree of difference among group centroids. The test of equality of group means measures the potential of each independent variable, as defined by their means, to discriminate before the model is created. Overlapping means are not a promising start for discriminating cell types. In general, model robustness increases by avoiding over-specification, e.g. using the fewest discriminant variables and using canonical functions that account for the greatest amount of observed variance among cell type populations<sup>158</sup>.

Each test displays the results of a one-way ANOVA for the independent variable using the grouping variable as the factor. If the significance value is greater than  $p=0.10$ , the variable has negligible contribution to the model. Insignificant variables complicate

and detract from models. The discrimination powers of individual variables are also assigned a Wilks' lambda value. As before in terms of overall classification, smaller values indicate that the variable is better at discriminating among groups. Box's M tests the assumption of equality of covariances across groups and is preliminary indicator of violations in population distribution normality. A significant result violates this test and prompts additional analysis into effects of sample size and magnitudes of covariances. Once the degree of separation among the groups has been assessed, the algorithms generate a series of canonical functions to cross-validate or use a validation set to assess model fit<sup>161</sup>.

When there are two groups, the canonical correlation is the most useful measure, and it is equivalent to Pearson's correlation between the discriminant scores and the groups. As an extension to the overall Wilks' lambda for the MANOVA, individual Wilks' lambda values for each function measure how well the function separates cases into groups. It is equal to the proportion of the total variance in the discriminant scores not explained by differences among the groups. Smaller values of Wilks' lambda indicate greater discriminatory ability of the function. The associated chi-square statistic tests the hypothesis that the means of the functions listed are equal across groups. This separation is the driving factor for generating the canonical functions, so a significant value indicates that the discriminant function does better than chance at separating the groups. The standardized coefficients allow for comparison of variables measured on different scales. Coefficients with large absolute values correspond to variables with greater discriminating ability. For each case, a classification score is computed for each function. The classification functions are used to assign cases to groups where a chi-square distance from each centroid provides a probability of group membership. The discriminant model assigns the case to the group whose classification function obtained

the highest score. Following classification, metrics of sensitivity, specificity, positive predictive value (PPV), and negative predictive value (NPV) provide an overall quality and robustness of the method. These metrics are commonly used to compare the performance of a new diagnostic test to a standard test result or known condition. In the case of fluorescently labeled cultured cancer cells mixed into leukocyte suspensions, fluorescence signal served as the positive identification of cancer cells. The performance of the model was assessed based on the percentage of cancer cells that had statistically different scattering properties relative to leukocytes.

As the project developed from comparing scattering characteristics among cultured cancer and blood cells to detecting GFP<sup>+</sup> cancer cells from murine samples, the presence of autofluorescent blood cells compromised the gold standard of fluorescence signal. The autofluorescent cells in wild type mouse samples were detected at the same order of magnitude as GFP<sup>+</sup> counts in metastatic mice. Unlike the case of spiking experiments where fluorescently labeled cultured cancer cells served as a gold standard, an isolated population of native CTCs was unavailable. In the absence of this gold standard, an alternative statistical approach was taken to quantify CTC concentration. Mahalanobis distance of individual counts relative to a reference population provided a metric for delineating a unique population of fluorescently green cells (i.e. GFP<sup>+</sup> CTCs) based on differences in scattering properties relative to those of autofluorescent cells. Represented as a dendrogram, the Mahalanobis distances among centroids also denote relative similarities.



### **3 Chapter: Flow Cytometry Instrumentation and Analytical Tools**

#### **3.1 Introduction**

Although light scattering occurs radially in varying intensities, near-backscattering angles were chosen for this investigation to build upon preceding work that focused on the development of an in vivo system where the forward ( $0^\circ$ ) and side ( $90^\circ$ ) are not accessible. This chapter illustrates the instrumentation, signal-processing approach, and pertinent cell culture techniques used to define system parameters.

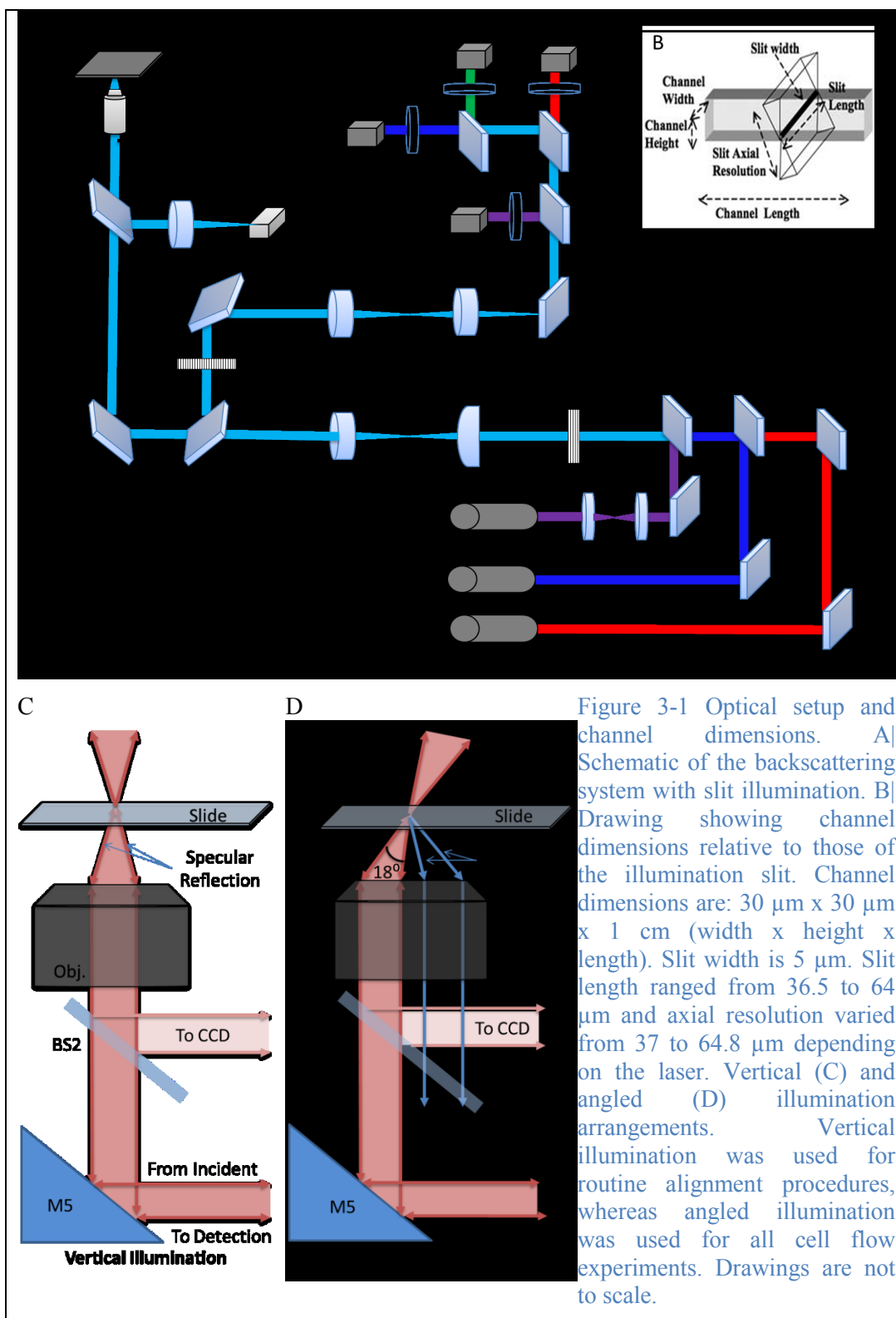
#### **3.2 Instrumentation**

The optical technique used in this work was introduced in 2.5 and was chosen to minimize out-of-focus light and discriminate scattering differences among cell types. The schematic of the system is shown in Figure 3-1 A with a table of components in 9.2.1 of the Appendix. Building on the preceding leukemia work<sup>26</sup>, 405, 488 and 633 nm lasers were combined into a single illumination path by mirrors (M1-M4) and dichroic filters (D1 and D2). Following transmission through a linear polarizer (Pol1), all three incident beams, circular in size, were shaped into a slit using a 150 mm cylindrical lens (Cyl Lens) and 150 mm achromatic lens (L3). The line was re-imaged unto the sample plane by the achromatic lens (L3) and an infinity-corrected 40x (0.6 NA) microscope objective.

The mirror underneath the objective cube (M5) was translated laterally to steer the incident beams in vertical or angled illumination modes. In vertical illumination mode, incident light filled the center of the objective aperture and was used for routine alignment purposes. However, to reduce noise in the form of specular reflection from the bottom surface of the glass slide during cell suspension flow experiments, M5 was translated laterally by 2.5 mm to angle the illumination slit, thus allowing for the collection of scattered and fluorescent light between 0 and  $18^\circ$ , where  $0^\circ$  was the optical axis in vertical illumination mode. The reflected light in angled illumination mode was

intercepted by a razor blade beam block covering the half of the back of the objective aperture opposite to the incident and scattered light, as shown in Figure 3-1 C, D.

Approximately 10% of the scattered and fluorescent light collected by the objective was directed to a CCD in the trans-illumination imaging path via a beam splitter (BS2) and 150 mm achromatic lens (L6) in the objective cube. An overhead 530 nm LED was used to align the illumination slit across the channel cross-section via visualization onto the CCD. The remaining scattered and fluorescent light was directed towards the detection path, by a 50/50 splitter (BS1). By configuring the incident polarizer (Pol1) and linear detection analyzer (Pol2) in the same transmission orientation, scattered light polarized in the same direction as the input polarization was acquired.



Elastically-scattered light maintains the original polarization contributing mainly to detected light along the same polarization as that of the incident light ( $I_{\parallel}$ )<sup>121</sup>. Light that was transmitted through the analyzer (Pol2) was then focused by a 150 mm achromatic lens (L4) onto a confocal slit to reject scattered light emanating from outside the focal volume. Based on the illumination slit width, the longest illumination slit length, and commercially available apertures, we selected a 150 x 3000  $\mu\text{m}^2$  slit aperture for confocal detection. Backscattered and fluorescent light that passed through the slit was re-focused by a 150 mm achromatic lens (L5) and spectrally separated by dichroic filters (D3–D5).

Light was detected by four photomultiplier tubes (PMTs; Hamamatsu), each placed behind a 405/10 nm (center wavelength/bandpass width), 488/10 nm, 633/10 nm, or 545/45 nm bandpass filter to detect scattered light at each one of the illumination wavelengths and fluorescent light in the green region. This fluorescent region corresponded with the emission spectrum of a fluorescent dye, calcein-AM, used experimentally to mark specific cells and that of GFP. The scattered and fluorescence light intensities from each PMT were digitally sampled at 25 KHz and recorded onto a computer for analysis using Measure Foundry software (Data Translation, Marlboro, MA). The System Alignment Procedure is provided in the Appendix section 9.2.2.

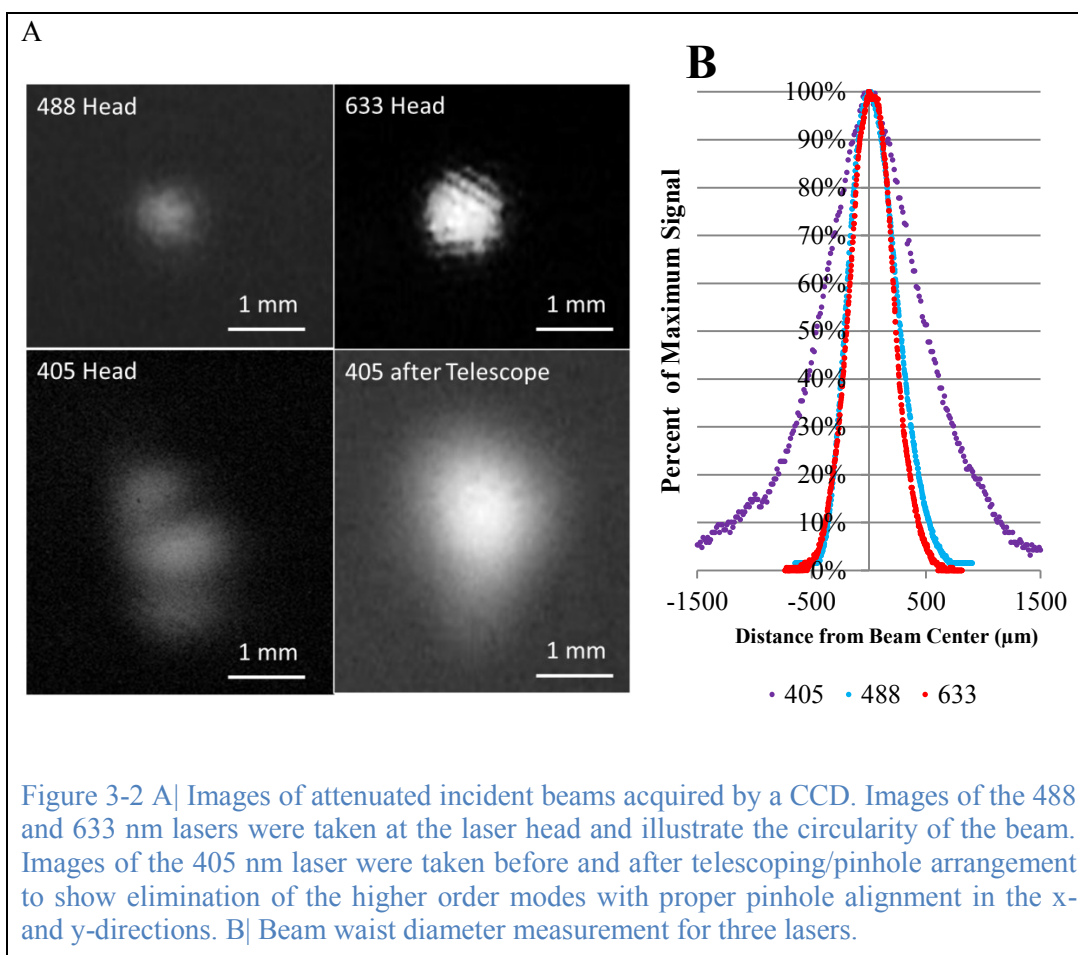
### 3.2.1 Illumination Parameters

Illumination parameters included quantification of excitation beam waist diameters and illumination slit dimensions.

#### 3.2.1.1 Beam Waist Diameters

The beam waists of all three lasers were measured with a profilometer (Ophir, on loan from Clemens Alt) and oscilloscope at the laser head, except for the 405 nm laser, which was measured after the pinhole designed to eliminate the higher order modes. The divergence of 405 nm beam was modified by a pair of plano-convex lenses (L1 and L2,

35 mm focal length), near the laser head so that the central mode of the 405 nm beam would be focused at the same axial location as the 488 and 633 nm lasers. This was required to compensate for the chromatic aberrations of the cylindrical lens. Optimal alignments of the 405 nm laser telescope and pinhole were periodically confirmed by visualizing the transmitted beam using a CCD. The images of all three lasers are shown in Figure 3-2 A to demonstrate the circular shape of the 488 and 633 nm beams and utility of the pinhole in removing the higher order lobes of the 405 nm beam. The profiles for the three lasers were acquired by scanning the intensity of the laser cross-section perpendicularly with respect to the optical axis. The measured beam diameters according to a standard  $\frac{1}{e^2} \approx 13.5\%$  intensity cutoff<sup>162</sup> were 2107, 825, and 758  $\mu\text{m}$  for the 405, 488, and 633 nm lasers, respectively (Figure 3-2 B).



### *3.2.1.2 Illumination Slit Dimensions and Axial Resolutions in Angled Illumination Mode*

The illumination slit widths were approximately five  $\mu\text{m}$  as measured by a graticule. This value was greater than the theoretical axial resolution values of 2.6, 3.2, and 4.1  $\mu\text{m}$  for the 405, 488, and 633 nm lasers, respectively. The increase in actual relative to theoretical values was attributed to beam divergence throughout the optical system.

The slit lengths were 57.2, 36.5 and 64.1  $\mu\text{m}$  for 405, 488 and 633 nm lasers, respectively, which were estimated from the 10% - 90% power from knife-edge measurements at the focus of the objective as shown in Figure 3-3. Power measurements were acquired as the knife-edge was moved incrementally in the x-axis direction of the illumination angle. Orienting axes and experiment schematic are shown in Figure 3-4. Illumination slit length was determined by a third-order polynomial fit<sup>163</sup> (solid lines) to the measurements bounding the 10th and 90th percentiles of the maximum power value, which were acquired in the absence of the blade<sup>163</sup>. The polynomial parameters are shown in Table 3-1. The variation in the slit lengths among the lasers was attributed to the differences in beam diameter at the cylindrical lens and differences in the beam divergence. The confocal slit, with 150 x 3000  $\mu\text{m}^2$  dimensions, allowed for complete transmission of the slit image at the focal plane of the objective.

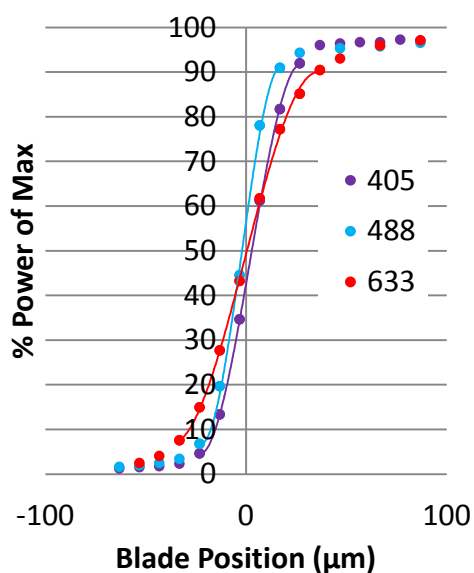


Figure 3-3 Normalized knife-edge measurements in angled illumination determining slit lengths at the focal plane.

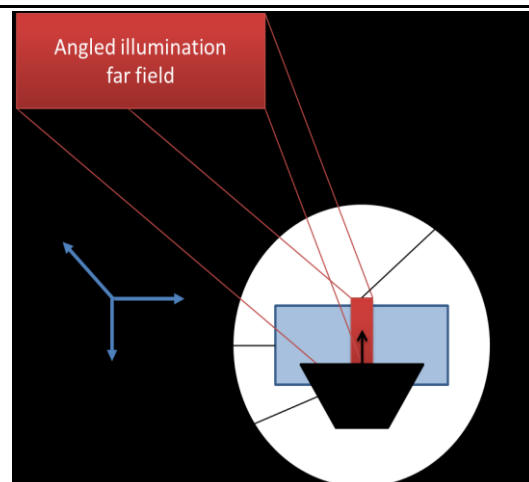


Figure 3-4 Schematic of knife-edge measurements taken in angled illumination to determine the slit lengths. In a flow experiment, the illuminated slit length spanned the 30- $\mu\text{m}$  channel while cells traversed the overlapping  $\sim 5$   $\mu\text{m}$ -slit widths.

Table 3-1 Polynomial parameters and slit length values for knife-edge measurements acquired in the x-axis direction of the symmetrical slit.

Laser	$x^3$	$x^2$	$x$	constant	Slit Length ( $\mu\text{m}$ )
405	-1.00E+06	9011.8	2583.8	42.464	57.21
488	-3.00E+06	-18406	3156.7	56.301	36.50
633	-437046	-578.43	1719.4	49.201	64.07

The focus location corresponded to the axial position for which the highest signal was detected from axially scanning a spectralon (Labsphere, North Sutton, NH) at the sample plane in angled illumination. The spectralon provides a reproducibly high diffuse reflective surface (>99%) for assessing system throughput. In angled illumination mode with installed beam block arrangement, the full width at half-maximum (FWHM) values of the slits were determined. At constant PMT gain settings and spectralon placement, signal values were acquired in the two cases of translating the stage downward and upward from the focal point where signals were at maximum values. The three incident wavelengths had maximum reflective values, and thus focal points, within a two-micrometer axial space. Signal values above and below the focal point were separately fit with third-order polynomials<sup>163</sup>, as shown in Figure 3-5. Polynomial parameters are

shown in Table 3-2 and Table 3-3 for the two cases of translating the spectralon above and below the focal points, respectively. FWHM values were determined for the displacement where the signal dropped to half the maximum value. The axial resolutions are provided in Table 3-4 and were 64.8, 37.0, and 52.6  $\mu\text{m}$  for the 405, 488, and 633 nm lasers, respectively. The two-fold asymmetry in measured FWHM values arose from the asymmetry of the angled illumination with respect to the center of the objective lens. The slit lengths and axial resolutions encompassed the entire cross-sectional area of a 30x30  $\mu\text{m}^2$  channel.



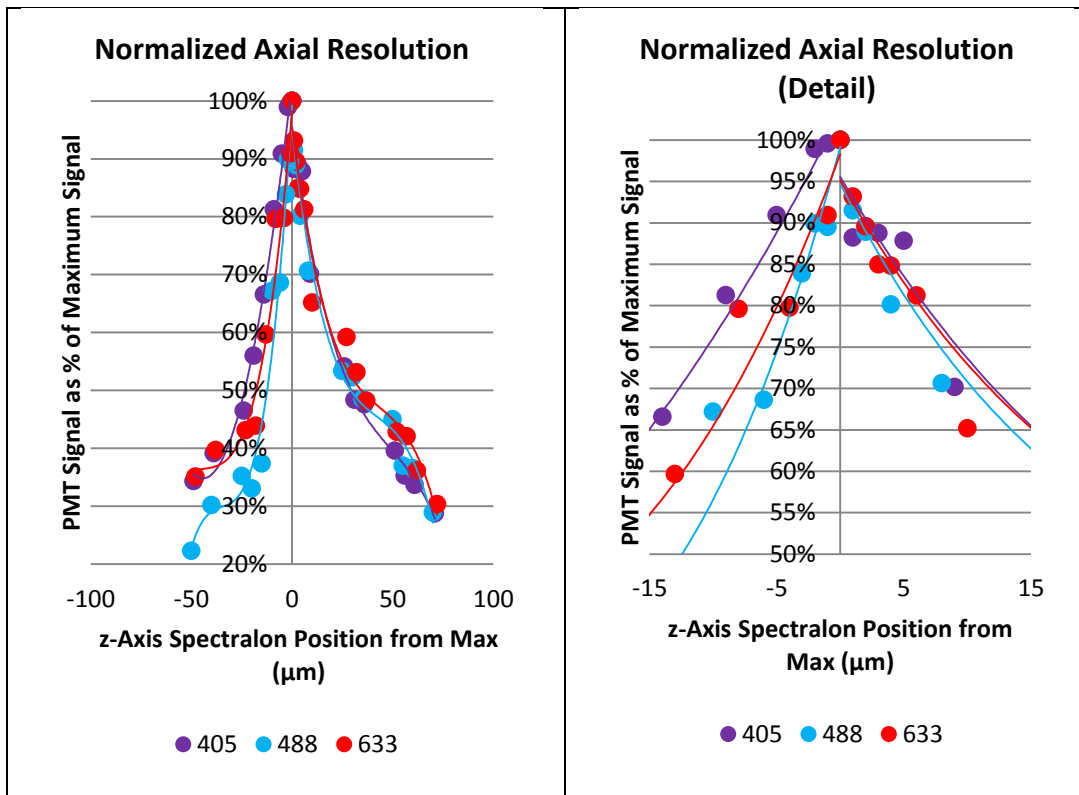


Figure 3-5 Normalized axial resolution using spectralon reflectance in angled illumination. Solid line is third-order polynomial fit used to determine FWHM.

Table 3-2 Axial resolution obtained by translating spectralon upward

Laser	$x^3$	$x^2$	$x$	constant	FWHM
405	-3.00E-07	0.0003	0.0302	1.0312	-22.9
488	2.00E-05	0.0016	0.057	0.9918	-12.1
633	7.00E-06	0.0009	0.0414	0.9828	-17.3

Table 3-3 Axial resolution obtained by translating spectralon downward

Laser	$x^3$	$x^2$	$x$	constant	FWHM
405	-3.00E-06	0.0005	-0.0261	0.9555	41.9
488	-5.00E-06	0.0006	-0.0298	0.9468	24.9
633	-4.00E-06	0.0006	-0.0274	0.9513	35.3

Table 3-4 Maximum signal location along optical axis corresponding to focal points of three incident beams and total axial resolution about the focal points.

Laser (nm)	405	488	633
Max PMT Signal Position (mm)	10.599	10.6	10.598
Translate Spectralon Downward Component	41.9	24.9	35.3
Translate Spectralon Upward Component	22.9	12.1	17.3
Total FWHM	64.8	37.0	52.6

### 3.3 Flow Measurement Details

To flow cells in a microfluidic channel for light scattering measurements, the outlet tubing (McMaster Carr, #5114K11) was placed into 2 mL Eppendorf tubes and a syringe pump (Harvard Apparatus) set at a flow rate of three- $\mu\text{L min}^{-1}$  drew the constantly stirred cell suspension, unless otherwise specified. The concentration of the cell suspension was  $50\text{E}4 \text{ cells mL}^{-1}$ , unless otherwise specified. This concentration minimized clogging due to cellular accumulation and allowed for sufficiently frequent cell counts for real-time monitoring. For each sample, a new microfluidic channel was used to avoid contamination. Once flow stabilized as indicated by a stable baseline, data were taken in 100-second intervals for varying numbers of runs depending on the experimental purpose, i.e. characterizing rare cells at a concentration of 1% of the total cells necessitated as many as 50 runs. Signal traces were recorded in all four PMT channels. The cell suspension flow protocol is provided in the Appendix section 9.2.3.

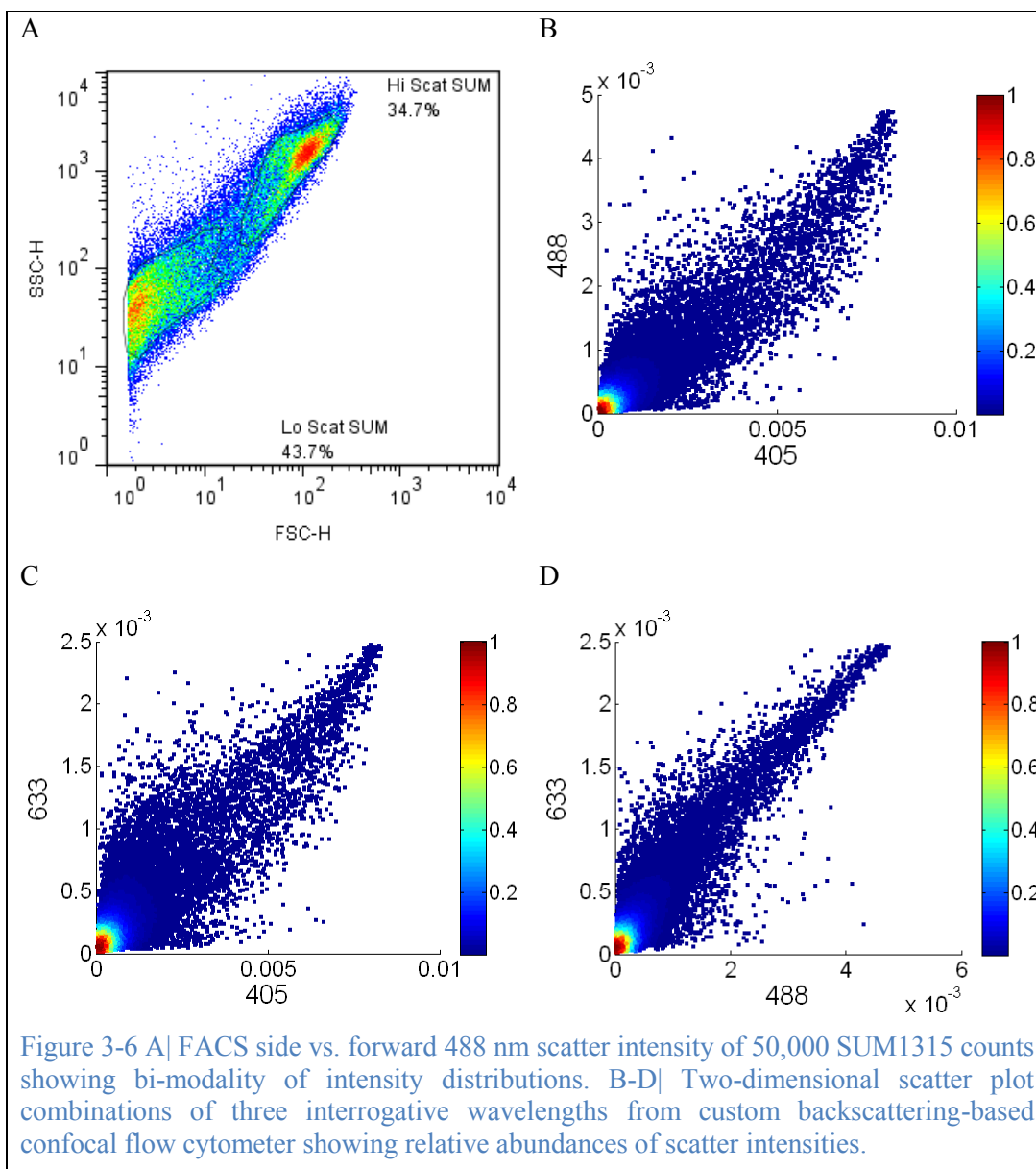
At the end of the experiment, the backscattering from a spectralon on a microscope slide was measured as a calibration standard 10 times for the angular and spectral dependence of the system. Due to the highly reflective property of the surface, it was necessary to use neutral density filters to attenuate the illumination power for spectralon measurements to prevent PMT saturation. Therefore, illumination power during cell sample and spectralon measurements were recorded and accounted for during calibration. Unless otherwise specified, independent flow measurements of each type of isolated and mixed cell sample were repeated at least three times, on different days, to assess reproducibility. Mouse and human blood samples were processed on the same day as collection.

#### 3.3.1 Cell Culture Preparations

SUM159 and SUM1315 cells were grown in culture medium consisting of Ham's F12 (Invitrogen, 11765-054) with five v/v% fetal bovine serum (FBS), one v/v%

penicillin/streptomycin/fungi zone (PSF, Invitrogen, 15240-062), 0.5 w/v% insulin (Sigma, I9278), and 0.1% epidermal growth factor (Sigma, E9644)<sup>164</sup>. The cells were incubated at 37°C, 5% CO<sub>2</sub>, 85% humidity, and split twice a week. These cells were adherent and were routinely passaged (1:3-1:5) at less than 90% confluence using 0.05 v/v% trypsin.

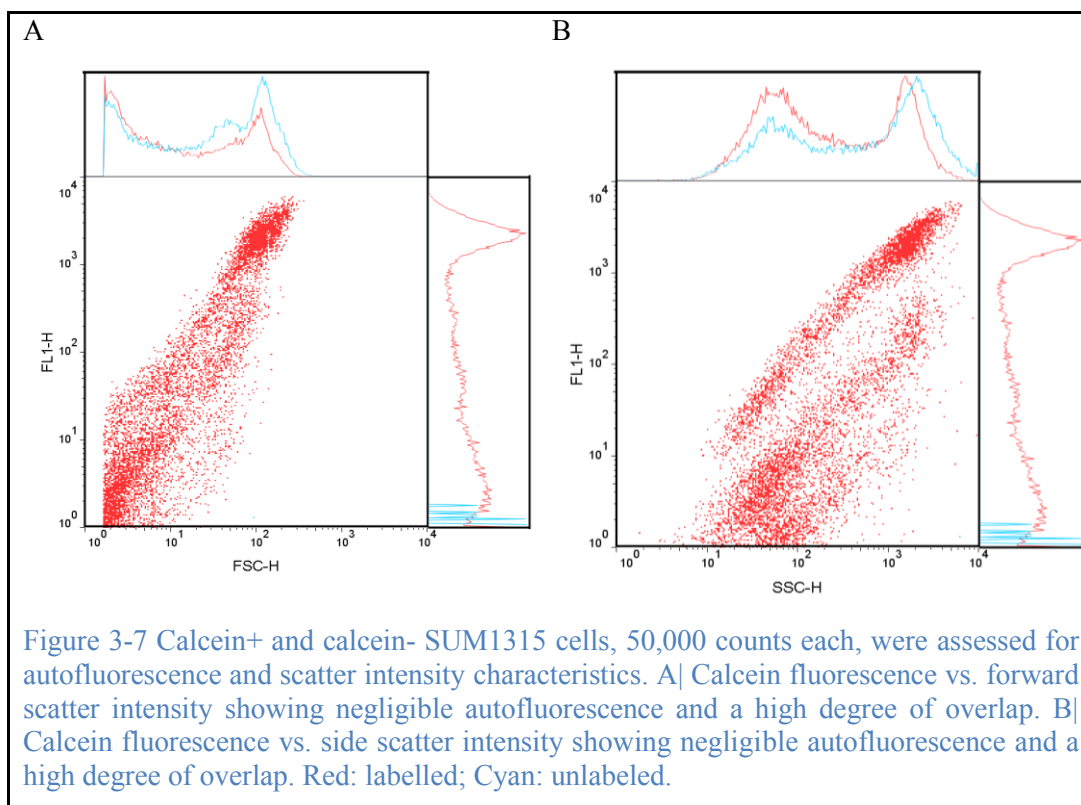
Standard flow cytometry characteristics of 488 nm forward and side scatter intensities were acquired to assess SUM1315 size and granularity distributions. Cultured cells exhibited a bi-modality in both scattering intensities, as shown in Figure 3-6 A for 50,000 cells (BD FACSCalibur). Two distinct populations of low (43.7%) and high (34.7%) scattering intensity emerged surrounding an intermediate gradient. Scatter plots of the three combinations of interrogative wavelengths used in the custom backscattering-based confocal flow cytometer in two-dimensions illustrate the same continuum with a relatively decreased abundance of cells scattering in the high intensity regions (Figure 3-6 B-D). Regardless of whether this bi-modal property was an artifact of cell culture passaging or an intrinsic attribute of the primary cell line, the continuum was consistently observed and accounted for in discriminant analysis.



For all flow measurements, cultured cancer cells were stained with a dye solution of 1 mg calcein AM dissolved in 1 mL of anhydrous DMSO (Invitrogen #C3099). The peak excitation and emission of calcein AM are 492 and 514 nm, respectively, thus allowing for excitation by the 488 nm laser and detection in the 500-590 nm channel. Briefly, cultured cells were harvested, centrifuged (five minutes, 800 x g, room temperature), and re-suspended in 500  $\mu$ L of RPMI-1640 without FBS. To this solution,

five  $\mu\text{L}$  of calcein AM solution was added to every one million cells for 30 minutes at  $37^{\circ}\text{C}$ , and then washed three times with 1.5 mL RPMI-1640 to remove excess dye. These same centrifugation parameters were used for all concentrating steps, unless otherwise specified.

The calcein-labelling protocol did not appreciably affect forward and side scatter intensities, as illustrated in Figure 3-7. With fluorescence intensity plotted along the ordinate, scatter histograms indicate overlap while fluorescence histograms indicated negligible autofluorescence among unlabeled cells. The clear variability in fluorescence intensity is a limitation of the staining protocol and will be discussed further in section 3.4.3.



### 3.4 Data Analysis

#### 3.4.1 Single Channel Peak Detection Method

To analyze flow measurements, we used a previously developed peak counting MATLAB program to detect and characterize scattering and fluorescence signals from flowing cells<sup>26,55</sup>. Following data acquisition, each channel time trace was smoothed in the forward and reverse directions using a second-order lowpass digital Butterworth filter with normalized cutoff frequency of 0.2. Once smoothed, peaks from each channel and each run were sorted in ascending order to determine the mean and standard deviation of the constitutive noise of each channel for each 100-second run. We modified the intensity threshold values until the cumulative FWHM values of detected cells constituted 1% of the data stream for a cell suspension of 50E4 cells mL<sup>-1</sup> at a flow rate of three-μL min<sup>-1</sup>. Therefore, the noise comprised the lower 99% of the smoothed data, unless otherwise noted. Cell peaks were demarcated by intensity values four to seven standard deviations above the mean of the noise, which yielded a total detection count matching the anticipated value based on acquisition time, flow rate, and cell concentration in suspension.

Detected peaks from all the PMTs were compared to determine time-correlated peaks, which were peaks that occurred within a time tolerance of 6.5E-4 seconds (approximately half of the typical FWHM). Correlated peaks from the entire data trace were calibrated by the average light scattering signal from the spectralon and ratio of the illumination power between the cell and spectralon measurements, to calculate the calibrated scattering intensity at each wavelength (Equation 3-1).

Equation 3-1 Scattering intensity normalization method for detected light with the same parallel polarization as the excitation light.

$$I_{cells_{\lambda(l)}} = \frac{I_{measured_{\lambda(l)}} - I_{media_{\lambda(l)}}}{I_{spectralon_{\lambda(l)}}} \times \frac{P_{cells_{\lambda(l)}}}{P_{spectralon_{\lambda(l)}}}$$

$I_{cells_{\lambda(l)}}$  were final baseline-corrected and power normalized cell scattering intensities.  $I_{measured_{\lambda(l)}}$  were the smoothed peak values from the acquired data stream.  $I_{media_{\lambda(l)}}$  were the lower 99% of smoothed peak values from the acquired data stream.  $I_{spectralon_{\lambda(l)}}$  was the average spectralon intensity value over 10 trials that provided a normalization parameter for day-to-day throughout variability.  $P_{cells_{\lambda(l)}}$  was the illumination power value during cell flow measurements ( $\mu$ W).  $P_{spectralon_{\lambda(l)}}$  was the illumination power value during spectralon measurements, which was reduced relative to cell measurements to avoid PMT saturation due to the highly reflective (99%) surface the spectralon ( $\mu$ W).

In our experiments, time correlated peaks in all three scattering wavelengths with no corresponding fluorescence signal (“3 $\lambda$ -correlated peaks”) were considered to be those from PBMCs, PMNs, or erythrocytes. However, correlated peaks in all three scattering wavelengths with associated fluorescence peaks (“4 $\lambda$ -correlated peaks”) were attributed to autofluorescent leukocytes, calcein labeled cancer cells, or GFP<sup>+</sup> cells. Other combinations of 2 $\lambda$  and 3 $\lambda$  correlated peaks occurred where one or two time-correlated peak values was insufficiently intense to exceed the standard deviation threshold above the noise. Uncorrelated peaks occurring in just one channel were denoted as 1 $\lambda$ .

Standard deviation thresholds were iteratively manipulated toward the convergence of three endpoints based on the expected number of cells, which was calculated as a function of cell concentration, flow rate, and sampling time:

1. Total number of detected cells from all channels equals total number of expected cells
2. Total number of detected cells in each channel be greater than 100% of the expected count

3. Total number of correlated cells in among channels equal the expected number of cells

However, this hard line threshold approach yielded uncorrelated peaks, thus the total number of detected cells was typically greater than the expected number to achieve a high percentage of correlated peaks. This limitation detracted from the overall sensitivity of this peak-finding method, as seen for a sample of calcein-stained SUM1315 flow experiment outlined in Table 3-5 with a time trace and detail in Figure 3-8.

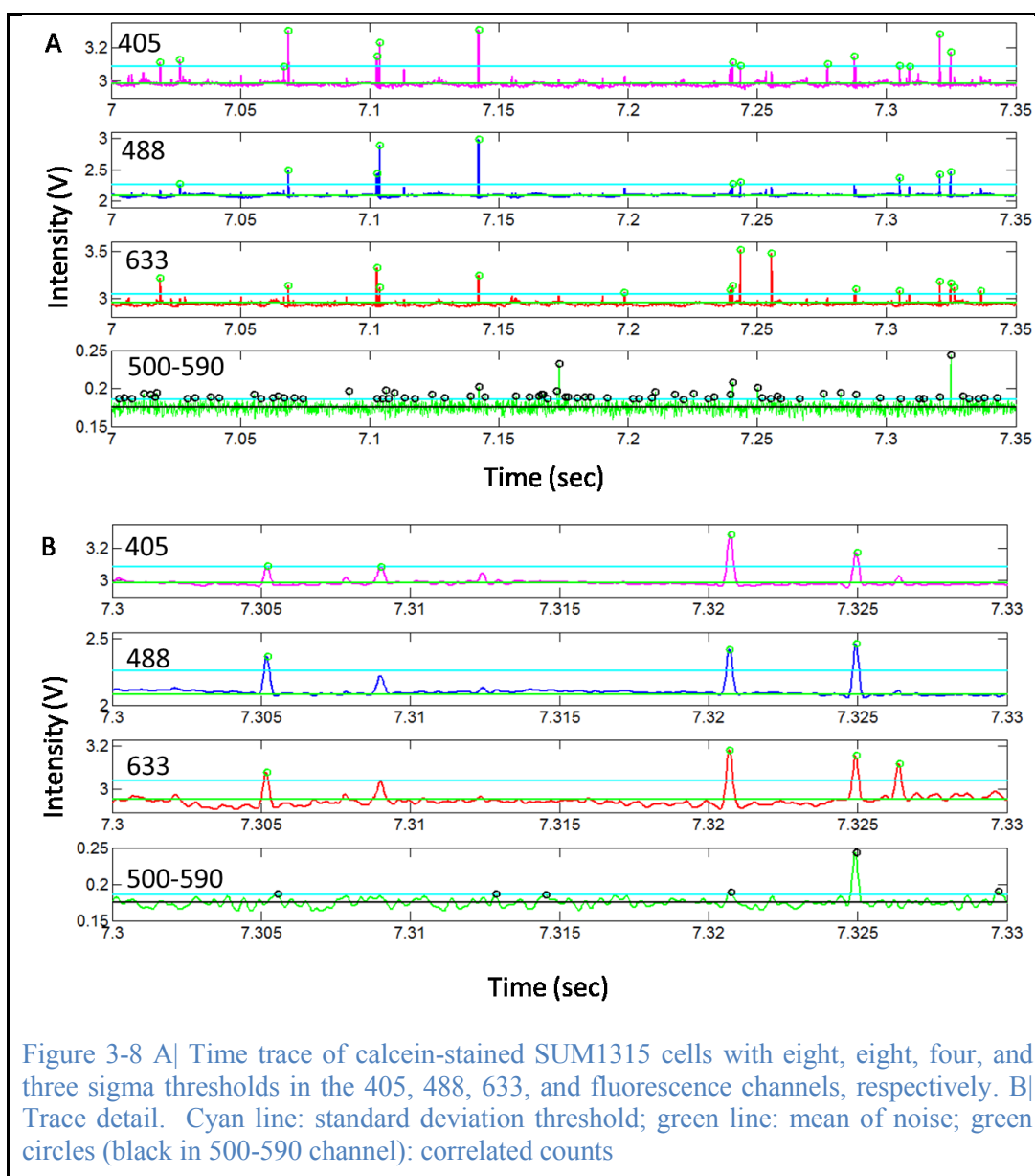


Table 3-5 Correlated peaks for two standard deviation threshold combinations for calcein-stained SUM1315 cells. Standard deviation threshold are shown as  $n\sigma$  above the mean of the noise in each channel, as [405 488 633 Green Flr]. % Exp Count: percentage of the expected concentration detected in each correlation sub-category. % Count: percentage of the total number of detected cells in each correlation sub-category.

Peak Correlation	[8 8 5 3]			[8 8 4 2]		
	Count	% Exp Count	% Count	Count	% Exp Count	% Count
<b>405 + 488</b>	10674	20	18	5122	10	7
<b>405 + 488 + Green</b>	4706	9	8	6194	12	8
<b>405 + 633</b>	3475	7	6	3320	6	4
<b>405 + 633 + Green</b>	922	2	2	2923	6	4
<b>405 + Green</b>	3120	6	5	5636	11	8
<b>488 + 633</b>	4006	8	7	4005	8	5
<b>488 + 633 + Green</b>	651	1	1	2515	5	3
<b>488 + Green</b>	1536	3	3	3926	7	5
<b>633 + Green</b>	1472	3	2	7996	15	11
<b>405 + 488 + 633 (3<math>\lambda</math>)</b>	16961	32	29	12398	24	17
<b>405 + 488 + 633 + Green (4<math>\lambda</math>)</b>	11850	23	20	20477	39	27
<b>All 405</b>	62025	118	104	62025	118	83
<b>All 488</b>	60937	116	103	60937	116	82
<b>All 633</b>	50516	96	85	68211	130	92
<b>All Green</b>	89166	170	150	430591	820	578
<b>Uncorr. 405</b>	10317	20	17	5955	11	8
<b>Uncorr. 488</b>	10553	20	18	6300	12	8
<b>Uncorr. 633</b>	11179	21	19	14577	28	20
<b>Uncorr. Green</b>	64909	124	109	380924	726	511
<b>Corr. 405</b>	51708	98	87	56070	107	75
<b>Corr. 488</b>	50384	96	85	54637	104	73
<b>Corr. 633</b>	39337	75	66	53634	102	72
<b>Corr. Green</b>	24257	46	41	49667	95	67
<b>Total (Corr.) Cells</b>	<b>5.94E+04</b>	<b>113</b>	<b>100</b>	<b>7.45E+04</b>	<b>142</b>	<b>100</b>

At a concentration of 50E4 cells ml<sup>-1</sup> and a flow rate of three- $\mu$ l min<sup>-1</sup> for 21 100-second runs, the expected number of cells was 5.3E4. Two standard deviation threshold combinations are presented to illustrate the low 4 $\lambda$  counts, 23 and 39%, of the expected

count for higher and lower threshold combinations, respectively. As expected, decreasing a standard deviation threshold resulted in an increased total number of detected peaks; however, the fluorescence channel time trace visually suggested a proportional increase in uncorrelated fluorescence peaks (Figure 3-8 A). In this case of calcein-staining,  $3\lambda$  scattering peaks indicated weak fluorescence signals from counts with scattering signals (exemplified at  $\sim 7.31$  seconds in Figure 3-8 B). This particular limitation of calcein will be further addressed within this section.



By following the previously described threshold approach and convergence priorities, the inherent bias toward high-scattering peaks composing  $3\lambda$  and  $4\lambda$  counts was applied consistently in the analyses presented in Chapter 4. An alternative method for increasing sensitivity to  $4\lambda$  peaks entailed iteratively decreasing the individual channel standard deviation thresholds. However, the subsequent increase in total number of detected cells above the number of expected cells called into question the validity of the final  $4\lambda$  population containing counts with minimal SNRs. This limitation motivated an improved approach, presented in the following section, and was used to analyze cancer cell and leukocyte mixed samples presented in Chapter 5.

### 3.4.2 Cumulative Channel Peak Detection Method

By setting a hard standard deviation threshold in each detection channel, the previous method limited the total number of detected cells by implementing a bias toward cells exhibiting high signals in all three scattering channels. For example, the previous method classifies a cell as  $2\lambda$  when two out of the four channels have high time-correlated scattering peaks while the other two channels have low scattering peaks. This is useful for setting intensity thresholds; however, we are interested in unstained leukocytes and fluorescently labeled cancer cells, each of which are  $3\lambda$  and  $4\lambda$ , respectively. Complete scattering property information derives from extracting all time-correlated intensity values for each cell. The new approach adds individual channel signals and detects peaks within this cumulative stream, thus leveraging the additive property of time-correlated signals to increase the SNR (Equation 3-2).

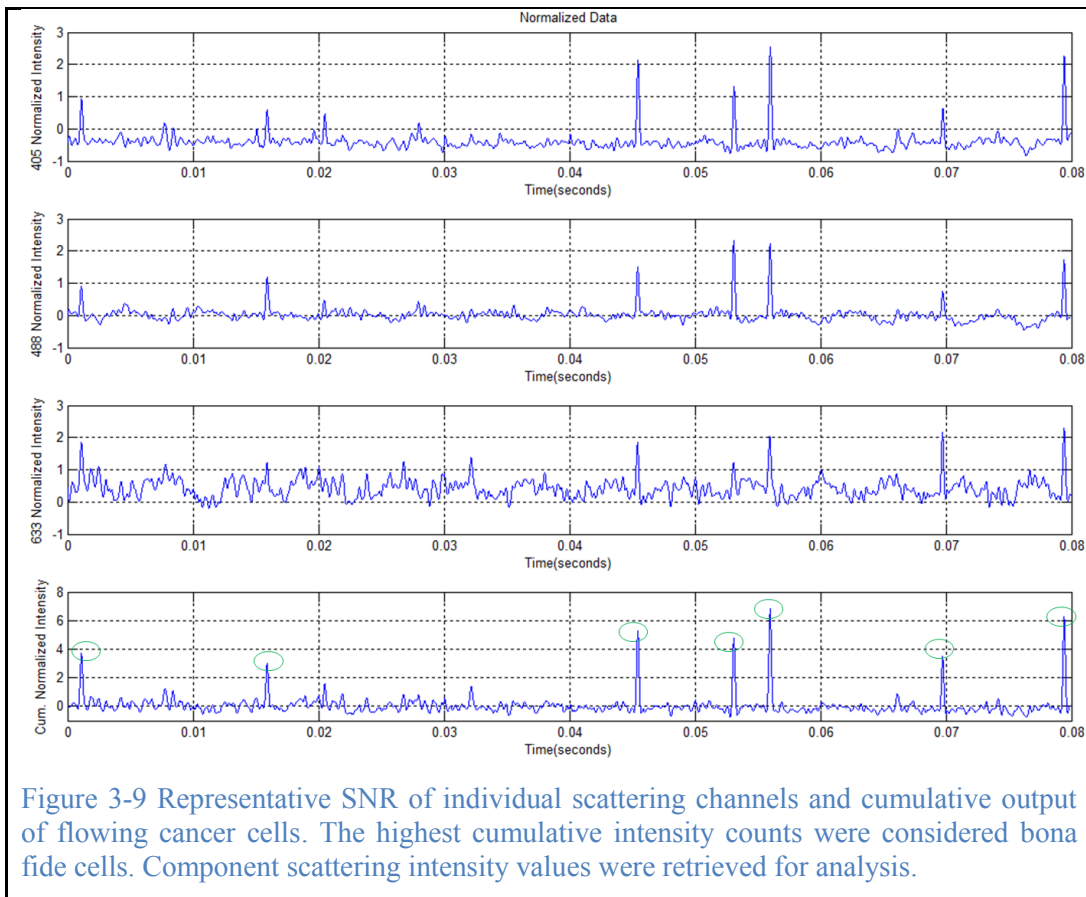
Equation 3-2 Cumulative peak threshold approach using the same nomenclature as Equation 3-1.

$$\sum I_{cells_{3\lambda(\parallel)}} = \sum_{\lambda}^{405,488,633} \frac{I_{measured_{\lambda(\parallel)}} - I_{media_{\lambda(\parallel)}}}{I_{spectralon_{\lambda(\parallel)}} \times \frac{P_{cells_{\lambda(\parallel)}}}{P_{spectralon_{\lambda(\parallel)}}}$$

As before in Equation 3-1,  $I_{cells_{\lambda(\parallel)}}$  were noise baseline-corrected and power normalized cell scattering intensities.  $I_{measured_{\lambda(\parallel)}}$  were the smoothed peak values from the acquired data stream.  $I_{media_{\lambda(\parallel)}}$  were the lower 99% of smoothed peak values from the acquired data stream.  $I_{spectralon_{\lambda(\parallel)}}$  was the average spectralon intensity value over 10 trials that provided a normalization parameter for day-to-day throughout variability.  $P_{cells_{\lambda(\parallel)}}$  was the illumination power value during cell flow measurements ( $\mu\text{W}$ ).  $P_{spectralon_{\lambda(\parallel)}}$  was the illumination power value during spectralon measurements, which was reduced relative to cell measurements to avoid PMT saturation due to the highly reflective (99%) surface the spectralon ( $\mu\text{W}$ ).

Assuming that cells were responsible for the highest cumulative peak intensities, the number of expected peaks then informed the single standard deviation threshold in the cumulative channel to create a vector of time indices. From the time indices, all individual channel intensities were retrieved for further analysis of cell scattering characteristics, thus increasing the detection rate to 100% of expected number of cells.

A sample SNR of the constitutive and cumulative channels of flowing cancer cells is shown in Figure 3-9. Joe Lyons, a fellow MS candidate, developed the cumulative peak-finding algorithm, and he continues to improve on the filtering parameters. For purposes of reproducibility and statistical analysis, component scattering intensity values corresponding to the time-correlated cell counts were mean normalized.

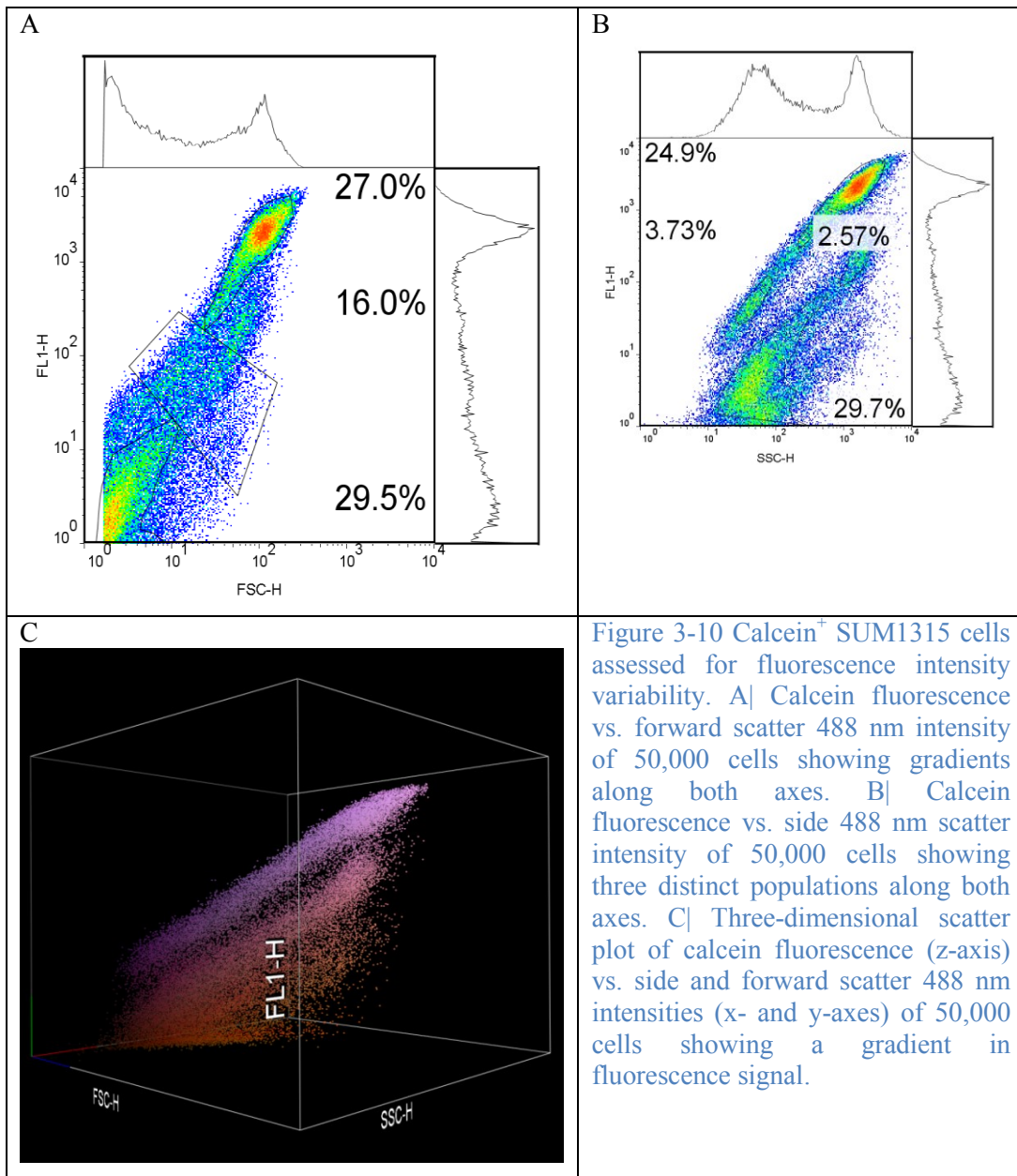


### 3.4.3 Fluorescence intensity as a standard marker in mixed populations

To visualize the light scattering signal distribution from the cells, the calibrated light scattering intensities at two wavelengths were displayed as density plots or as three-dimensional scattering plots, in RGB. Each cell type was assigned a particular color with the color intensity used to represent the signal distribution, analogous to a histogram, against the two wavelength parameters. In all our cell samples, fluorescence intensity was used as a standard for assessing the accuracy of the classification achieved based on the light scattering properties of the cells at 405, 488, and 633 nm. Specifically for these experiments, light scattering peaks correlated with a fluorescence peak were assumed to be emanating from cells that were truly cancer cells, while light scattering peaks that did not have a correlated fluorescence peak were assumed to result from normal white or red blood cells. Although helpful, fluorescence signal is not an ideal standard for three

reasons centering on varying levels of emission intensity, the presence of autofluorescent cells with overlapping emission spectra, and potential false positives from unintended dye leakage into purposefully unlabeled cells.

First, calcein and GFP fluorescence had varying levels of intensity. To assess variability of fluorescence intensity in calcein-stained SUM1315 cells, 50,000 cells were flowed in standard FACS (Figure 3-10). As indicated before in Figure 3-6, SUM1315 488 nm forward and side scatter intensities had bi-modal distributions, while fluorescence intensity, plotted along the ordinate, also showed a gradient. Three distinct bi-modal populations are visible in the fluorescence versus side scatter intensity plot (Figure 3-10 B) with 24.9 and 29.7% of the cells constituting dual low and high intensity regions, respectively. A three-dimensional plot with fluorescence along the z-axis and forward/side intensities along the x/y-axes illustrate the same three populations varying in fluorescence intensity (Figure 3-7 C).



In this way, the second limitation in using calcein as a marker for cancer cells involves cases of minimal fluorescence signal that overlapped in intensity with emission from rare autofluorescent cells. Whereas this inconsistency in fluorescence intensity had minimal impact on analyzing enriched cell populations, spiked and tumor-bearing murine samples contained autofluorescent cells whose presence inherently reduced sensitivity and specificity metrics by presenting false negatives in perceived CTC detection. The

presence of autofluorescent cells with overlapping emission spectra presented an interesting factor that will be further addressed in the context of GFP<sup>+</sup> CTC detection in 6.3.2.

Third and finally, although labelled cells were spiked into leukocyte suspensions immediately prior to data acquisition, the extended duration of some experiments allowed for false positive staining of leukocytes from residual calcein in solution.

### 3.5 Effect of Channel Depth

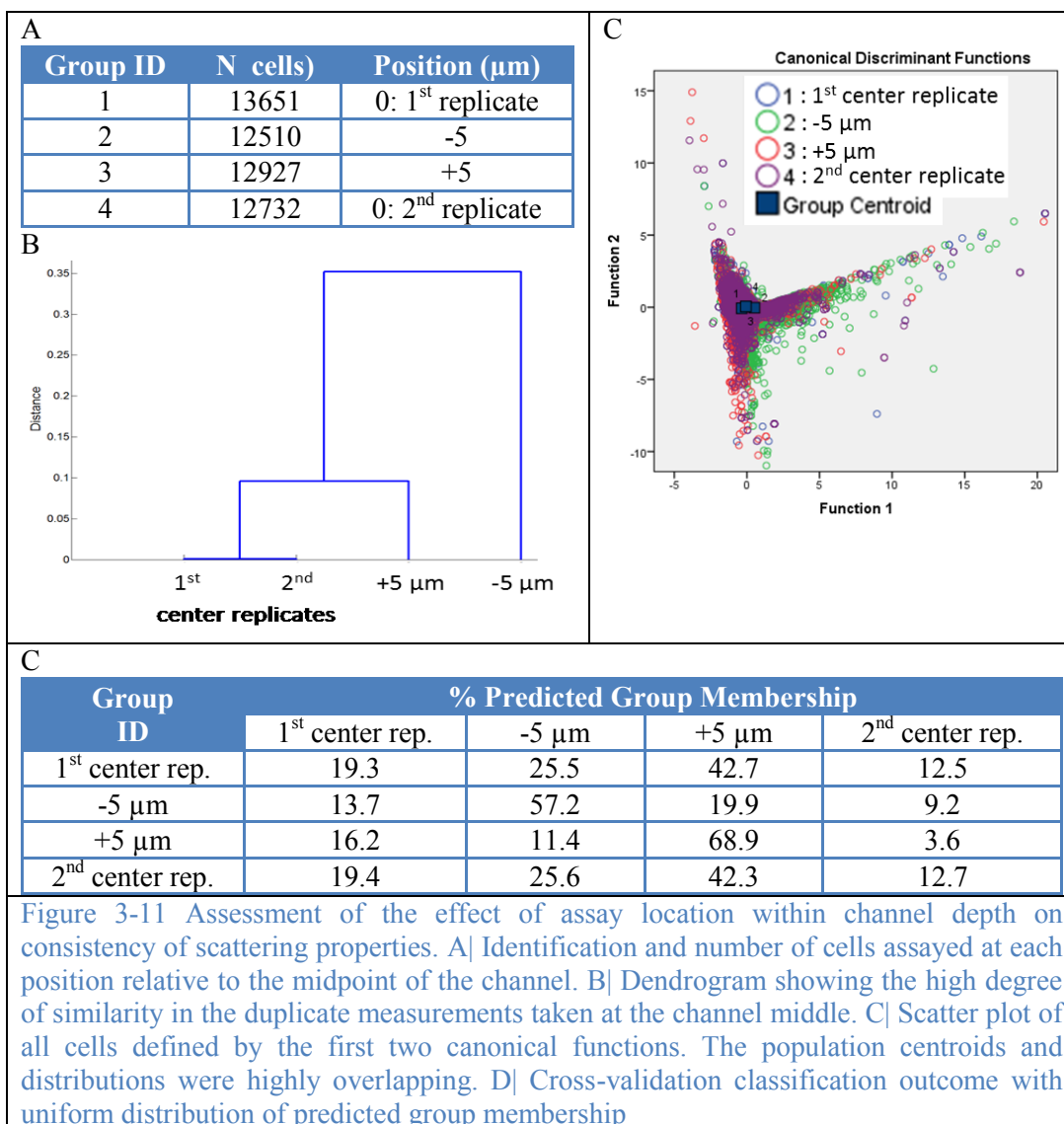
Scattering and fluorescence intensity values were acquired for flowing cells by illuminating a cross-section of the rectangular channel with a focused slit of three overlapping incident light wavelengths. The bottom surface of the channel, which equated to the top surface of the microscope slide, was found by imaging the reflection of the focused slit. The sample stage was then lowered half the height dimension of the channel, e.g. 15  $\mu\text{m}$  for a 30  $\mu\text{m}$  channel, to align the focal volume within the middle of the channel height. The slit widths extended beyond the channel width for a 30  $\mu\text{m}$  wide channel. At the focal point, the slit widths were approximately five  $\mu\text{m}$  and converge within a 3- $\mu\text{m}$  range of one another. Although the entire channel cross-section was illuminated, for a laminar flow regime within a rectangular channel, larger particles tend to flow along the channel periphery, especially in the corners<sup>165</sup>. The purpose of this experiment was to assess the reproducibility of manually aligning the focal volume of the incident lasers to the middle of the channel and the variability within a small height range of the channel midpoint. Scattering intensities at the channel middle (in duplicate) and  $\pm 5$   $\mu\text{m}$  were acquired for calcein-labelled SUM159 flowing at a rate of 3  $\mu\text{L}\cdot\text{min}^{-1}$  at a concentration of 50E4 cells $\cdot\text{mL}^{-1}$  in a 30x30  $\mu\text{m}^2$  channel. To determine whether the three positions yielded significantly different scattering characteristics, a MANOVA and discriminant classification were performed on the processed signals grouped by position



using the cumulative value of the scattering peak values and the three ratios thereof, i.e. 405/488, 405/633, and 488/633, as the four discriminant variables.

The high Wilks'  $\Lambda$  of 0.907, and low partial  $\eta^2$  of 0.032 suggested that there was only 3.2% variability among the channel positions. Although Box's M indicated that the assumption of equality of covariance matrices was violated, the large number of cells assayed and the consistently overlapping mean  $\pm \sigma$  intervals diminished concerns of non-normality. Supporting statistical analyses are provided in the Appendix section 9.3.

The duplicate measurements acquired at the channel middle were most similar, as indicated by the least significant difference (LSD) post hoc tests where all four discriminant variables were insignificantly different between the two groups (Figure 3-11 B). The +5 and -5  $\mu\text{m}$  positions were also predominantly insignificantly different among the four parameters with the exception of the first center replicate and -5  $\mu\text{m}$  positions in cumulative peak height and 488/633 and the -5  $\mu\text{m}$  and second center  $\mu\text{m}$  positions in cumulative peak height. The first two canonical functions (Figure 3-11 C) had minimal canonical correlations of 0.301 and 0.054, respectively, indicating that the functions failed to separate group means due to the high degree of similarity. The groups were predominantly classified uniformly, although the +5 and -5  $\mu\text{m}$  positions had larger percent correct classifications, which suggested that assaying at the channel middle minimized variability in measured light scattering intensity.



### 3.5.1 Conclusion and Discussion

A MANOVA revealed negligible variation between the duplicate measurements at the channel middle and minimal variation within the 10- $\mu\text{m}$  window centered on the middle of the channel. Moreover, the linear discriminant classifications yielded extensive overlap among the groups, thus suggesting that assaying within a 10- $\mu\text{m}$  window centered on the middle of the channel was reproducible. The increased consistency of the duplicate measurements taken at the channel middle was attributed to uniformity of cell flow and minimized channel edge effects at the channel middle. Therefore, this approach of assaying at the channel middle was employed for subsequent experiments.

## **4 Chapter: Light Scattering Measurements of Isolated Leukocyte Populations and In Vitro Breast Cancer Cells**

### **4.1 Introduction**

The first step in developing a peripheral blood CTC detection method entailed comparing scattering profiles among isolated samples of constitutive blood cell populations. The purposes of these experiments were to identify the backscattering space defined by the three interrogative wavelengths for mononuclear and granulocyte cells and to determine whether cancer cells scattered in a unique space. Due to the overlap in scattering characteristics of granulocytes and cancer cells, the previous leukemia work using this same laser-based backscattering system determined that specificity and sensitivity in cancer cell detection improved in the absence of granulocytes<sup>26</sup>. Therefore, the two major leukocyte sub-populations were analyzed individually to assess relative degrees of overlap with the scattering profile of cultured cancer cells.

### **4.2 Methods**

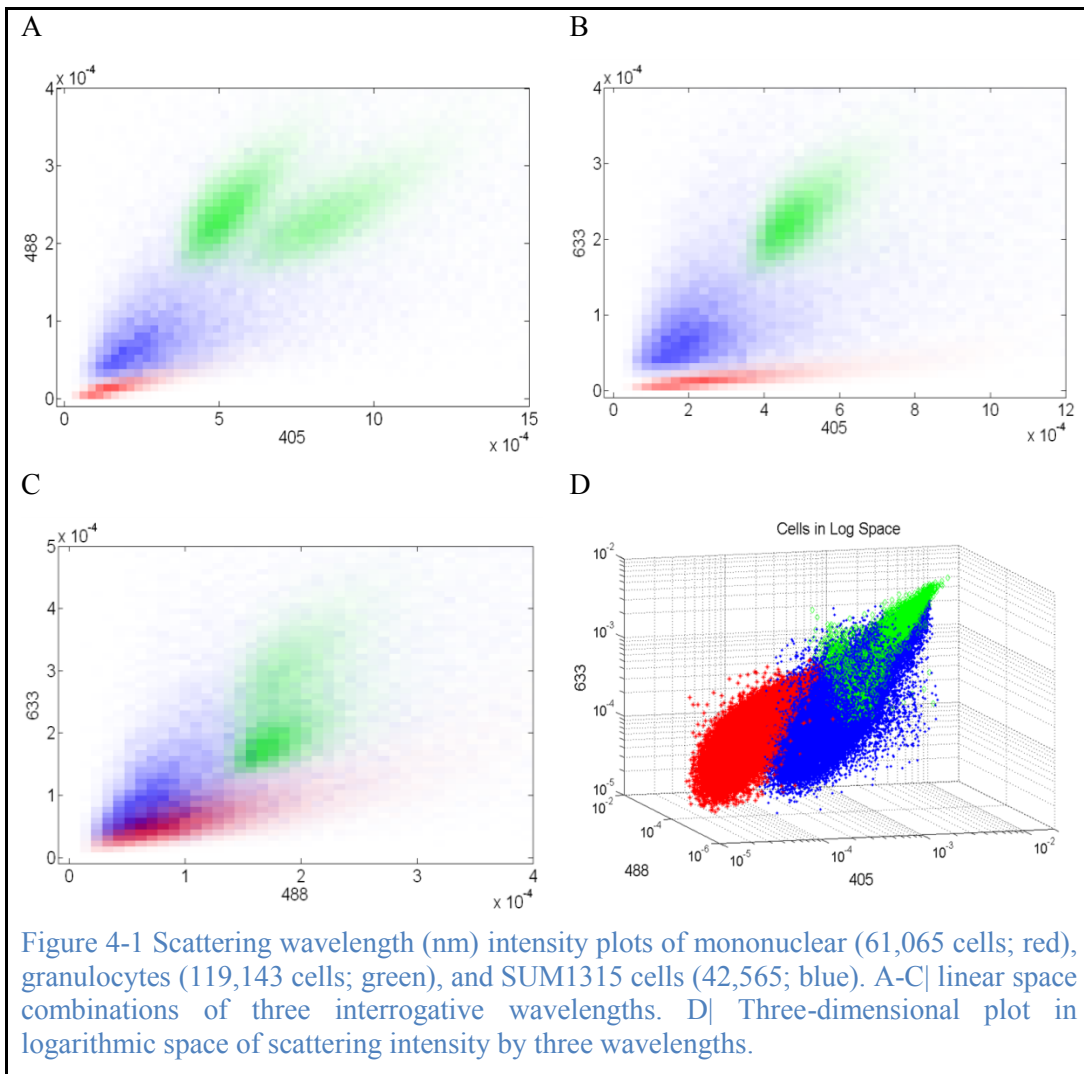
The experimental portion of this section centered on blood sample processing to isolate reliably granulocytes. Due to the close density values among granulocytes and erythrocytes, granulocytes sediment alongside abundant erythrocytes in standard density centrifugation, thus requiring additional erythrocyte-depletion steps to yield an enriched granulocyte population. The two explored methods were rosette sedimentation and erythrocyte-susceptible lysis. Conversely, mononuclear cells were readily enriched in the superficial layer above the intermediate density medium via density centrifugation.

Leukocytes were isolated from peripheral whole blood acquired from healthy human adults (20- to 50-years old) via venipuncture into vacutainers containing lithium heparin according to a protocol approved by the Tufts University Institutional Review Board (#07020146). PBMCs were isolated by a standard density gradient technique using Ficoll-Paque PLUS according to the manufacturer's instructions (GE Healthcare Life

Sciences, #17-1440-02). The density of the highly branched polysaccharide is 1.077 g/mL, which is an intermediate value between denser granulocytes and less dense mononuclear cells. First attempts to acquire granulocytes used a negative isolation rosette sedimentation technique<sup>26,166</sup>. The specific product, RosetteSep Human Granulocyte Enrichment Kit (StemCell Technologies, #15121/15161), yielded variable results, suffered from a high degree of donor inconsistency, and is no longer commercially available for these reasons. Nevertheless, three attempts were successful and provided granulocytes for flow experiments. The unsuccessful attempts resulted in low granulocyte yield by inadvertently sedimenting granulocytes within erythrocyte immune-rosettes. An alternative, more reproducible approach for granulocyte enrichment exploited an  $\text{NH}_4\text{Cl}$  (STEMCELL Technologies, #20110) erythrocyte lysis step following Ficoll-Paque gradient centrifugation and was performed according to the manufacturer's instructions. In all cases, after the final wash, isolated PBMCs, PMNs, and harvested cancer cells were resuspended in RPMI.

#### 4.3 Results

Three cell groups composed of cells from three different days were acquired to compare scattering characteristics. Scatter plots in Figure 4-1 show the spatial distribution of PBMC (61,064), PMN (119,143), and SUM1315 (42,565) cells. The 488 vs. 405 (Figure 4-1 A) and 633 vs. 405 nm (Figure 4-1 B) scatter plot histogram show the abundance of SUM1315 cells in an intermediate scattering space in between PBMCs and PMN. The three-dimensional scatter plot in logarithmic space (Figure 4-1 D) highlights the separation along the 405 nm axis with overlap on the low and high intensity ends of the SUM1315 population.



Two distinct PMN sub-populations were observed in the 488 vs. 405 and 633 vs. 488 plots; however, only a single cloud was visible in the 633 vs. 405 nm plot. SUM1315 cells were consistently concentrated in an intermediate space in between PBMCs and PMNs in the two-dimensional density plots. The three-dimensional plot did not denote population density and a subset of high-scattering SUM1315 cells visibly overlapped with the PMNs.

#### 4.4 Statistical Analysis

MANOVA and linear discriminant analysis were performed on the three enriched populations to determine the extent of overlap among scattering characteristics. Three cross-validation classifications were performed to ascertain similarities in planning for more targeted isolation approaches: (1) all three groups; (2) PMN vs. SUM1315; and (3) PBMC vs. SUM135. Discriminant variables were cumulative peak intensity (e.g. 405+488+633) and ratios of scattering intensities (e.g. 405/488, 405/633, and 488/633). The MANOVA among all three populations revealed significant differences in all four discriminant variables with overall significance ( $p < 0.0005$ ), which was supported by a low Wilks'  $\Lambda$  of 0.335 ( $F=40,493$ ,  $\eta^2=0.421$ ) and a low Pillai's Trace of 0.682 ( $F=28,849$ ,  $\eta^2=0.341$ ). The presence of high scattering cells in all three populations had minimal effect on the overall assumption of normality, and the covariance matrices contained just one value greater than four, which was 405/633 vs. 405/633<sup>167</sup>. A covariance value less than four is an accepted limit for minimal deviations from non-normality. Moreover, the more conservative Pillai's Trace, which accounted for minor deviations from normality, suggested a high degree of variance (34%) among the group centroids; therefore, linear discriminant analysis was appropriate. Complete classification outputs are provided in the Appendix section 9.4.

The case of all three populations modeled a lysis protocol where all cell types would have been retained for analysis. All discriminant variables were significant ( $p < 0.0005$ ) and the dendrogram and canonical scatter plot are provided in Figure 4-2. Based on the discriminant variables, SUM1315 cancer cells were more similar to granulocytes than mononuclear cells (Figure 4-2 A). Overlapping centroids of cancer cells (group 2, blue) and granulocytes (group 3, green) in Figure 4-2 B reflected this similarity. Moreover, both centroids were shifted toward higher values relative to mononuclear cells (group 1, red) due to higher cumulative scattering intensity.

Using accurate SUM1315 classification as a metric, the sensitivity, specificity, PPV, and NPV are shown in Table 4-1 for the three classification schemes. As expected from the dendrogram and population gradient in scattering intensity, SUM1315 cells were predominantly classified as PMNs (41.1%) and as a unique population from blood cells (42.9%) with the remainder classified as PBMCs (16.0%). Conversely, the blood cells exhibited less overlap, especially with one another. Due to the similarity in centroid functions, PMNs were primarily classified as their own population (61.1%) and as SUM1315 (38.2%) with a small minority being classified as PBMCs (0.7%). The vast majority of PBMCs were classified as being unique (99.3%) from SUM1315 (0.6%) and PMNs (0.1%). Overall, 68.1% of cells were classified correctly. The moderate sensitivity and specificity values of 42.9 and 74.6%, respectively, for the three-cell population case reflected the dispersed gradient of SUM1315 cells that overlapped with both blood cell populations. There was negligible improvement when discriminating SUM 1315 from PMNs; however, sensitivity and specificity increased to 92.7 and 82.8%, respectively, for the case of SUM1315 and PBMCs.

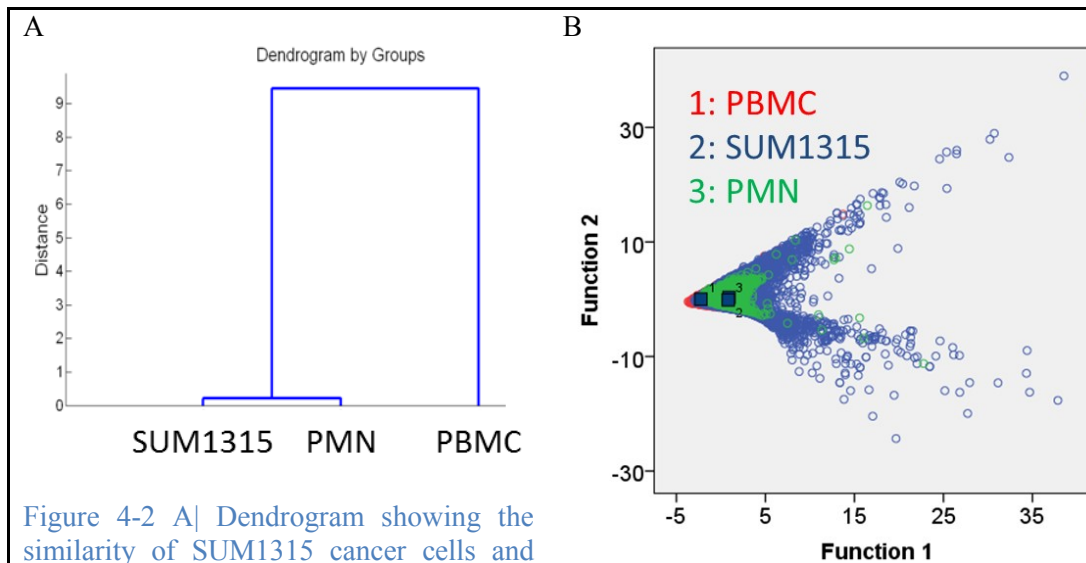


Figure 4-2 A| Dendrogram showing the similarity of SUM1315 cancer cells and granulocytes relative to mononuclear cells. B| Scatter plot of three isolated cell populations in canonical space, accounting for 100% of observed variance. Squares represent group centroids.

Table 4-1 Classification metrics of enriched cell populations showing the greater difference between cancer cells and mononuclear cells than granulocytes. Classification metrics refer to the detection of SUM1315 cells.

Test	Wilks' $\Lambda$	p-value	% Correct	Sensitivity	Specificity	PPV	NPV
PBMc vs. PMN vs. SUM1315	0.335	<0.0005	68.1	42.9	74.6	28.5	84.7
PMN vs. SUM1315	0.97	<0.0005	57.9	62.2	45.7	76.2	30.2
PBMc vs. SUM1315	0.43	<0.0005	92.7	82.8	99.5	99.2	89.2

## 4.5 Conclusion and Discussion

Reducing the experimental space to SUM1315 cells and either PBMCs or PMNs represented an outcome of an idealized blood processing protocol that did not account for yield losses of the rare cells nor bias toward enriching cancer cells with similar densities to those of the respective blood cells. Knowing that density centrifugation over Ficoll-Paque reliably separated PBMCs from PMNs and erythrocytes, an experiment was performed to assess the density and related yield of SUM1315 in the Ficoll-Paque protocol. Laying SUM1315 cells suspended in RPMI over Ficoll-Paque and adhering to



the same centrifugation and wash protocol resulted in a  $65.7 \pm 2.7\%$  cancer cell yield in what would have been the PBMC-enriched pellet from the supernatant above Ficoll-Paque. A logical extension of this approach would be to analyze the PBMC-enriched supernatant and PMN-enriched layer above the erythrocytes separately to increase CTC yield, albeit in two populations. However,  $\text{NH}_4\text{Cl}$  lysis is a necessary step in PMN isolation; therefore, with this moderate yield and the density of native CTCs being unknown, density centrifugation was replaced by  $\text{NH}_4\text{Cl}$  lysis for spiking experiments.

## **5 Chapter: Light Scattering Measurements of Lysed Leukocyte Populations Spiked With In Vitro Breast Cancer Cells**

### **5.1 Introduction**

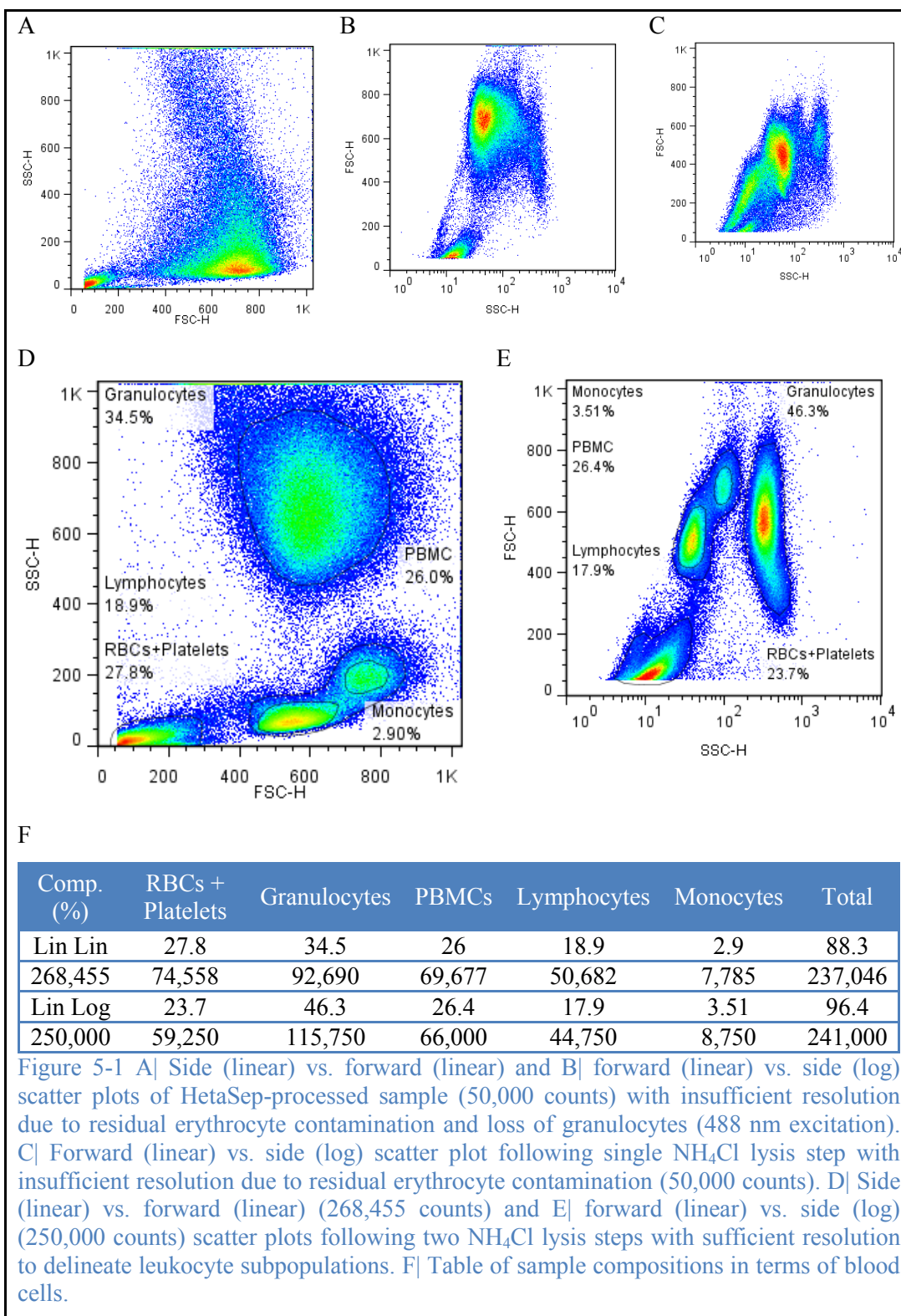
Having demonstrated that a subset of cultured breast cancer cells had unique scattering characteristics relative to isolated leukocyte sub-populations in enriched sample comparisons, the subsequent step focused on detecting cancer cells at low concentrations in mixed populations. The first aim was to develop a blood sample handling protocol in preparation for processing breast cancer patient samples without the advantage of fluorescently labelled cells. The second aim was to resolve the scattering characteristics of calcein-stained, cultured breast cancer cells spiked into leukocyte suspensions following erythrocyte and platelet depletion. Erythrocytes and platelets have significantly less scattering intensity than other blood cells; however, their relative small size and abundance necessitated removing them prior to flow analysis in an effort to mitigate confounding scattering and absorption effects at the assay point within a  $30 \times 30 \mu\text{m}^2$  cross-sectional area where erythrocytes and platelets could conceivably flow alongside cancer cells and leukocytes.

### **5.2 Methods – Leukocyte Preparations**

Leukocytes were isolated from peripheral whole blood acquired from healthy human adults (20- to 50-years old) via venipuncture into vacutainers containing lithium heparin. In an attempt to retain cancer cells in a blood sample, two erythrocyte depletion methods were investigated to enrich leukocytes, and  $\text{NH}_4\text{Cl}$  lysis was selected for labelled cancer cell spiking experiments. In all cases, after the final wash, enriched leukocytes and harvested cancer cells were resuspended in RPMI. Harvested SUM1315 and SUM159 cells were labelled with calcein and spiked into leukocyte suspensions at known concentrations as percentages of total cells immediately prior to flow.

Following erythrocyte depletion, both leukocyte enrichment methods contained multiple wash steps for platelet removal. Platelets are lighter, smaller, and less dense than other blood cells; therefore, the lower sedimentation rate retained platelets in the supernatant that was aspirated after each wash. Standard FACS (488 nm excitation) was used to assess rapidly erythrocyte depletion and forward-/side-scattering resolution of leukocyte sub-populations (Figure 5-1). Although theoretically less disruptive to leukocytes than  $\text{NH}_4\text{Cl}$ , the other option of erythrocyte-aggregation using HetaSep (STEMCELL Technologies, #07806) was less robust and required supplemental  $\text{NH}_4\text{Cl}$  lysis to achieve desirable scattering resolution of leukocyte sub-populations<sup>168</sup> (Figure 5-1 A,B). One  $\text{NH}_4\text{Cl}$  lysis step also yielded insufficient resolution due to a high level of residual erythrocytes (Figure 5-1 C). Although two  $\text{NH}_4\text{Cl}$  lysis steps resulted in a faintly pink cell pellet indicating trace erythrocytes, enhanced resolution allowed for the quantification of leukocyte sub-populations based on side and forward scatter intensity properties (Figure 5-1 D,E,F).

Both combinations of scatter plots (Figure 5-1 D, E) yielded comparable abundances of leukocyte sub-populations. Comparing the values in Figure 5-1 F to the physiological abundances in whole blood from Table 2-1, leukocytes constituted ~75% of the cell suspension, rather than ~0.1%, following two rounds of  $\text{NH}_4\text{Cl}$  lysis. As percentages of leukocytes, all sub-population abundances were within physiological ranges. Ammonium chloride lysis protocol is provided in the Appendix section 9.5.1.



### 5.3 Results

Calcein-stained cultured cancer cells were mixed into leukocyte suspensions following two rounds of  $\text{NH}_4\text{Cl}$  hemolysis. Eight experiments were conducted where SUM1315 cancer cells constituted one ( $n=2$ ), five ( $n=2$ ), and fifty ( $n=4$ ) percent of all cells in suspension, and the total cell concentration for flow analysis was  $50 \times 10^4$  cells  $\text{ml}^{-1}$ . Peaks were identified by the cumulative threshold approach where the expected number of cells based on leukocyte and SUM1315 concentration, flow rate, and assay time informed the final number of detected counts. These final counts had the highest cumulative scattering intensity (e.g.  $405+488+633$ ). Of these final counts, those with the highest 500-590 nm green fluorescence signal were considered to be calcein<sup>+</sup> SUM135 cells (“4 $\lambda$ -correlated”), and the remaining counts lacking green fluorescence signal were considered to be leukocytes (“3 $\lambda$ -correlated”). Aggregate scatter plots of SUM1315 ( $n=150,278$ ) and leukocytes ( $n=563,181$ ) of the individual experiments are shown in Figure 5-2.

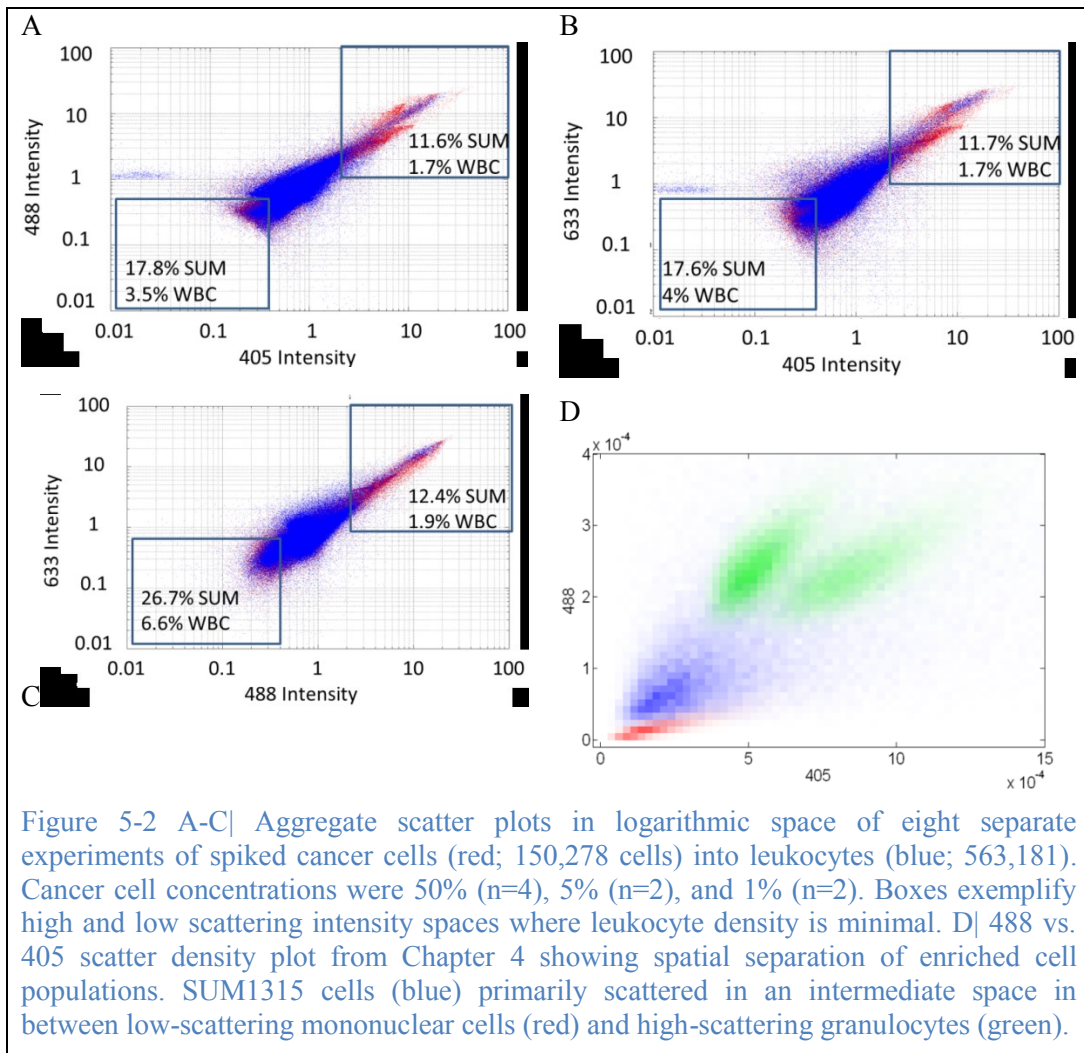


Figure 5-2 A-C| Aggregate scatter plots in logarithmic space of eight separate experiments of spiked cancer cells (red; 150,278 cells) into leukocytes (blue; 563,181). Cancer cell concentrations were 50% (n=4), 5% (n=2), and 1% (n=2). Boxes exemplify high and low scattering intensity spaces where leukocyte density is minimal. D| 488 vs. 405 scatter density plot from Chapter 4 showing spatial separation of enriched cell populations. SUM1315 cells (blue) primarily scattered in an intermediate space in between low-scattering mononuclear cells (red) and high-scattering granulocytes (green).

Both SUM1315 cancer cells and leukocytes scattered along an  $x=y$  intensity gradient in all three plots of the excitation wavelengths (Figure 5-2 A, B, C). In contrast with scattering characteristics acquired from enriched leukocyte sub-populations described in Chapter 4 and re-illustrated in Figure 5-2 D, lysed samples did not resolve into separate PBMC and PMN regions. Instead, sparsely-populated leukocyte scattering regions were observed at the extremes, as shown in the boxed regions of Figure 5-2 A, B, C. SUM159 cells spiked at one and fifty percent demonstrated the same continuous scattering intensity gradient. The lack of intermediate scattering intensity discrimination was attributed to a signal attenuation effect of residual erythrocytes flowing concurrently

with leukocytes and cancer cells in the lysed samples. A discussion on this effect concludes this chapter.

## 5.4 Statistical Analysis

Linear discriminant analysis was performed on the identified leukocyte and cancer populations to assess classification metrics. Calcein fluorescence emission demarcated spiked cancer cells. The first round of classification trials evaluated 4 $\lambda$ -correlated cancer cells and 3 $\lambda$ -correlated leukocytes from the same sample using scattering intensities and FWHM of detected peaks as discriminant variables in cross-validation (Experiments 1-10, Table 5-1)<sup>26</sup>. This approach minimized day-to-day variations in donor, blood sample lysis, and cell culture passaging. The second round of classifications combined three sets of data (Experiments 11-13, Table 5-1): (1) SUM159 spiked at one and fifty percent (n=2); (2) SUM1315 spiked at one percent (n=2); and (3) SUM1315 spiked at fifty percent (n=4).

Table 5-1 Classification statistics of cancer cell spiking experiments. Single-experiment basis analyses are above and combined data sets are presented below the solid black line. Exp: experiment number; TP: true positive; TN: true negative; FP: false positive; FN: false negative; Cannon Corr: canonical correlation.

Exp.	Cell Type	N (Cells)	Accuracy Correct (%)	Sensitivity TP (%)	Specificity TN (%)	PPV	NPV	Canon Corr.	Wilks Lambda
<b>Single Experiment Cross-Validation Classifications</b>									
<i>Cancer Cells Spiked at 1% of Total Cells</i>									
<b>1</b>	1315	1241	98.3	56.9	98.9	39.38	99.4	0.55	0.70
<b>2</b>	1315	1631	74.4	45.6	74.7	1.74	99.3	0.08	0.99
<b>3</b>	159	848	75.5	35.3	75.8	1.24	99.3	0.10	0.99
	Avg	<b>1240</b>	<b>82.7</b>	<b>45.9</b>	<b>83.1</b>	<b>14.1</b>	<b>99.3</b>	<b>0.2</b>	<b>0.9</b>
	StDev	<b>320</b>	<b>11.0</b>	<b>8.8</b>	<b>11.1</b>	<b>17.9</b>	<b>0.1</b>	<b>0.2</b>	<b>0.1</b>
<i>Cancer Cells Spiked at 5% of Total Cells</i>									
<b>4</b>	1315	3931	95.4	40.4	98.2	52.58	97.1	0.48	0.77
<b>5</b>	1315	4171	90.9	14.8	94.7	12.12	95.7	0.17	0.97
	Avg	<b>4051</b>	<b>93.2</b>	<b>27.6</b>	<b>96.4</b>	<b>32.3</b>	<b>96.4</b>	<b>0.3</b>	<b>0.9</b>
	StDev	<b>120</b>	<b>2.2</b>	<b>12.8</b>	<b>1.7</b>	<b>20.2</b>	<b>0.7</b>	<b>0.2</b>	<b>0.1</b>
<i>Cancer Cells Spiked at 50% of Total Cells</i>									
<b>6</b>	1315	56301	62.1	56.1	68.1	63.47	61.0	0.23	0.95
<b>7</b>	1315	33001	58.4	30.7	88.5	74.44	54.1	0.24	0.94
<b>8</b>	1315	25001	60.2	27.7	91.0	74.36	57.1	0.21	0.96
<b>9</b>	1315	25001	58.9	21.8	94.8	80.22	55.6	0.20	0.96
<b>10</b>	159	28101	51.1	38.0	64.7	52.83	50.1	0.11	0.99
	Avg	<b>33481</b>	<b>58.2</b>	<b>34.8</b>	<b>81.4</b>	<b>69.1</b>	<b>55.6</b>	<b>0.2</b>	<b>1.0</b>
	StDev	<b>11779</b>	<b>3.8</b>	<b>11.8</b>	<b>12.5</b>	<b>9.8</b>	<b>3.6</b>	<b>0.05</b>	<b>0.02</b>
<b>Combined Experiment Cross-Validation Classifications</b>									
<b>11</b>	159 (1&50%)	28949	79.0	96.7	74.9	47.13	99.0	0.513	0.737
<b>12</b>	1315 (All 1%)	2872	97.6	28.6	98.3	15.76	99.2	0.332	0.89
<b>13</b>	1315 (All 50%)	139304	55.1	35.4	74.6	58.22	53.7	0.164	0.973



Scattering characteristic differences among cancer cells and leukocytes were assessed based on the performance of the discrimination functions to correctly classify cell types. Distinct differences in scattering properties resulted in high percent accuracy reflected by high sensitivity, specificity, PPV, and NPV. Smaller Wilks Lambda values and higher canonical correlation values indicated enhanced sensitivity due to a greater separation of centroids in canonical space. There was a high degree of variability within each percentage spike category and across experiments, which was attributed to variability in lysis efficiency, donor variability, and cell culture passaging. For example, a more thorough hemolysis resulted in fewer residual erythrocytes, which minimized attenuation effects and enhanced cancer cell discrimination within the intermediate scatter intensity space between the two leukocyte sub-populations. The majority of experiments failed to achieve sensitivity and specificity values greater than 50 and 90%, respectively. The few exceptions, namely experiments 1 and 11, suggested that centroid separation existed in some circumstances of sample processing and cell passaging conditions. The other two combined trials, 12 and 13, had less robust classification performance, especially in sensitivity, than the component single-day experiments. This reduction in classification performance reflected the same variables of lysis efficiency, donor variability, and cell passaging conditions that increased detected scattering inconsistencies on a day-to-day basis. Moreover, instrument variability in terms of excitation and detection efficiencies inherently detracted from consistency in measured scattering intensities. Daily power and spectralon measurements reduced these sources of inconsistency in the final scattering intensity calculations (Equation 3-1, Equation 3-2); however, these steps are preliminary compared to the standardization controls available in commercial flow cytometers.

## 5.5 Conclusion and Discussion

Relatively high abundances of cancer cells on the low- and high-scattering intensity extremes of the aggregate population enabled some discrimination power; however, the overall approach was limited by the continuous gradient of leukocyte scatter intensity. The unique intermediate scattering intensity space between the two leukocyte sub-populations (Figure 4-1, Figure 5-2 D) was absent in the scatter plots of lysed samples. The population clouds of the high-scattering granulocytes and low-scattering mononuclear cells merged due to a signal attenuation effect of residual erythrocytes in the lysed samples. Whereas density centrifugation enhanced the extent of erythrocyte depletion in the isolated leukocyte sub-populations, residual erythrocytes constituted ~25% of cells in twice-lysed samples (Figure 5-1 D, E). The presence of residual erythrocytes in the cell suspensions attenuated scattering intensity as leukocytes or cancer cells were assayed within a focal volume that simultaneously contained erythrocytes, rather than the intended one-by-one cell assay approach. The net effect was that the two low- and high-scattering leukocyte sub-populations were a continuous distribution, thus diminishing an intermediate space that was previously shown in Chapter 4 to enhance sensitivity and specificity for cancer cell detection. This same erythrocyte attenuation effect was observed after a single lysis step using standard FACS (Figure 5-1 C); however, discrimination among leukocyte sub-populations based on 488 nm forward and side scatter intensity improved after a second lysis step (Figure 5-1 D, E). Additional lysis steps beyond the first two were not performed to mitigate deleterious effects to leukocyte viability with extended exposure to  $\text{NH}_4\text{Cl}$ .

Contrasting the flow regimes of a standard FACS flow cytometer and our custom system elucidated how lysed leukocyte sub-populations failed to resolve into separate scattering clouds in these experiments. Whereas FACS used hydrodynamic focusing to provide a more consistent one-by-one cell flow regime, the single-fluid flow regime in a

rigid cross-sectional microfluidic channel allowed for concurrent flow of two or more cells through the focal volume of the excitation slits. Within the  $30 \times 30 \mu\text{m}^2$  microfluidic channel, relatively small erythrocytes (6-8  $\mu\text{m}$  diameters, 2-2.5  $\mu\text{m}$  thickness) flowing alongside another cell of  $<20 \mu\text{m}$  in diameter (e.g. all leukocytes, smaller cancer cells) would have attenuated the scattering intensity.

## **6 Chapter: Fluorescence and Scattering Detection of Circulating Tumor Cells in Murine Model**

### **6.1 Introduction**

Recently, using microarray analysis, our collaborators Sonenshein et al., identified ADAM8 as a target of a multistep pathway downstream of NF- $\kappa$ B RelB, which is known to promote an aggressive phenotype in breast cancer<sup>169</sup>. An analysis of publicly available microarray databases indicated ADAM8 is overexpressed in aggressive breast cancers, including triple negative breast cancers (TNBC), and correlated with a poor patient outcome. The purpose of this collaborative project was to investigate the therapeutic potential of inhibiting ADAM8 in breast cancer. The specific objective within this thesis work was to enumerate CTCs in blood samples throughout the time course of tumor induction and immunotherapy studies.

ADAM8 promoted an aggressive phenotype of TNBC cells in culture<sup>93</sup>. In a mouse orthotopic model, tumors derived from TNBC cells with ADAM8 knockdown failed to grow beyond a palpable size and displayed poor vascularization. Brain metastases were also significantly reduced. Mechanistically, ADAM8 stimulated angiogenesis through release of VEGF-A and transendothelial cell migration via  $\beta$ 1-integrin activation. Similarly in vivo, treatment with an anti-ADAM8 antibody from the time of cell inoculation reduced primary tumor burden and metastases. Antibody treatment of established tumors profoundly decreased metastases in a resection model. As a non-essential protein under physiological conditions, ADAM8 represents a promising target for treatment of TNBCs, which currently lack targeted therapies and frequently progress with fatal dissemination.

### **6.2 Methods**

Three experiments were performed with cancer cells inoculated into the mammary fat pads (MFP) of female NOD/SCID (nonobese diabetic/severe combined

immunodeficiency) mice. Blood from wild type, non-tumor bearing, mice was also assessed. In all three experiments, GFP<sup>+</sup> clones of a known human metastatic cancer line, MDA-MB-231 were used. Therefore, cells with green fluorescence signal in the 500-590 nm detection channel were considered to be GFP<sup>+</sup> CTCs or green autofluorescent leukocytes.

### 6.2.1 Tumor Induction Studies

The first two experiments investigated the effect of knocking-down ADAM8 on tumor growth with the hypothesis that tumor cells expressing less ADAM8 would remain dormant while control tumor cells would proliferate, induce angiogenesis, and elicit metastatic spread. An ADAM8 knockdown cell line was created using an ADAM8 specific short hairpin (sh) RNA that reduced ADAM8 expression levels. The two mouse cohorts (n=6 each) in each of the two experiments were implanted with either a control clone (shCtrl-3) or an ADAM8 knockdown clone (shA8-20) of the MDA-MB-213 cell line according to a protocol approved by the Tufts University Institutional Animal Care and Use Committee (#M2011-51). Blood samples from four of the six samples in each cohort were analyzed. The means and motivation to detect GFP<sup>+</sup> cells occurred midway through the first experiment; therefore, a second experiment was conducted throughout a tumor induction time course. Blood samples from only one time point at 33 days post-inoculation were analyzed in the first experiment. All six mice in the control metastatic group developed brain metastases, whereas only one of the six mice in the ADAM8 knockdown group developed a metastatic lesion in the brain.

To assess CTC concentration over a tumor induction time course, a second experiment assayed blood samples drawn at 7, 14, and 21 days after inoculation. Blood was either collected at sacrifice (day 33) by cardiac puncture (~500 µl) or drawn from mice using the submandibular blood collection method (~100 µl) 7, 14 and 21 days after

inoculation of tumor cells into the MFP. In order to evaluate endogenous cell signals from non-tumor bearing mice, blood was also collected from NOD/SCID mice that were not injected with any tumor cells. All blood samples were collected in heparin (100 USP units/sample), diluted and processed the same day. Diluted with an equal volume of PBS, whole blood samples were flowed in microfluidic devices, each of which had five single 50  $\mu\text{m}$  (width) by 70  $\mu\text{m}$  (height) and 10 mm (length) channels. A dilution approach was taken to minimize sample disruption inherent to lysis and centrifugation protocols. Wider microfluidic channels were used to accommodate the increased viscosity of the diluted whole blood samples relative to hemolysed samples typically assayed in narrower 30x30  $\mu\text{m}^2$  channels.

The compromise with this approach was reduced scattering intensity resolution due to increased variability of assay location relative to focal volume within a larger cross-sectional area. To flow cells in a microfluidic channel for light scattering and fluorescence emission measurements, the outlet tubing was placed into Eppendorf tubes and a syringe pump at a flow rate of 6- $\mu\text{l min}^{-1}$  drew the heparinized blood suspension. Operating at a constant pressure, a 6- $\mu\text{l min}^{-1}$  set flow rate calibrated for water yielded an actual value of 4.5- $\mu\text{l min}^{-1}$  due to the increased viscosity of blood. Channels were pre-wetted by flowing PBS and the blood sample flow was allowed to stabilize prior to data acquisition. Of the initial ~100  $\mu\text{l}$  of whole blood collected, 34 $\pm$ 17, 55 $\pm$ 17, and 57 $\pm$ 9  $\mu\text{l}$  were analyzed for non-tumor bearing, shControl, and shADAM8 mice, respectively. One sample in each experimental cohort was discarded – shCtrl on Day 21 and shA8 on Day 14 – for coagulation issues that interrupted the flow protocol. For the final 33-day time point, 100  $\mu\text{l}$  of blood was analyzed.

Cells positive for GFP fluorescence were detected in the 500 to 590 nm “green” channel following excitation with 488 nm light and were time-correlated with 405 and

488 nm scattering peaks. Within the volume analyzed, leukocytes and CTCs constituted ~0.5% of the acquired backscattered and fluorescent light data stream. Using a 25 kHz sampling frequency, the lower 99.5% of the intensity values defined the mean and standard deviation of the background signal. Individual peaks were demarcated by 6 to 7 data points and the maximum value defined the intensity used to determine whether the cell had time-correlated scattering and fluorescence intensities values used for CTC identification. Within the previously developed Matlab program<sup>74</sup>, the intensity threshold was defined based on the number of standard deviations above the mean of the background signal. The number of standard deviations was 4, 4, and 5 for the 405, 488, and 500-590 nm channels, respectively. These thresholds retained leukocytes and CTCs while eliminating erythrocytes and platelets from further analysis.

#### **6.2.2 Tumor Induction, Resection and Antibody Treatment Study**

The purpose of the third experiment was to investigate ADAM8 as a target for immunotherapy in a more clinically relevant setting than a one-month tumor induction model. Two mouse cohorts were injected with the same metastatic control clone as in the first two experiments and were treated with a tumor resection and antibody treatment protocol. Twelve days after inoculation in the MFP, tumors became palpable, and treatment was initiated with either 1.5 mg/kg ADAM8 antibody Mab 1031 or isotype control IgG2B (R&D Systems) for the two groups. The Mab 1031 antibody was designed to bind to the metalloprotease and disintegrin domains of the extracellular part of ADAM8, thus inhibiting the catalytic and signaling functions of these domains. Antibody was further administered on day 15 and then on day 17 when tumors reached a volume of ~0.15 cm<sup>3</sup> and tumor resection was performed. Antibody treatment was continued twice weekly for a five-week period, and then organ metastasis was examined using fluorescence microscopy.

In the control group, metastases to the brain and lungs were seen in 8/8 and 7/8 mice, respectively, whereas in the anti-ADAM8-treated group only 2/9 and 1/9 mice showed metastases in these organs. Thus, treatment with an anti-ADAM8 antibody resulted in a profound reduction in the frequency of metastases to both the brain and lungs compared to the isotype control antibody.

Blood from four of the mice per group was drawn using the submandibular blood collection method (~200  $\mu$ l) 50 days after inoculation and 37 days after tumor resection. In order to evaluate the level of autofluorescence, blood was also collected from wild-type NOD/SCID mice that were not injected with tumor cells. All blood samples were collected in heparin (100 USP units/sample) and processed the same day. The blood volumes for each group were wild type (n=3)  $198 \pm 2$   $\mu$ l, isotype-treated (n=4)  $182 \pm 4$   $\mu$ l, and anti-A8 (n=4)  $232 \pm 65$   $\mu$ l.

Samples were hemolysed and flowed in narrower  $30 \times 30$   $\mu\text{m}^2$  channels to enhance scattering property discrimination relative to the first two experiments where diluted blood was assayed in wider channels. Blood cells were hemolysed with  $\text{NH}_4\text{Cl}$  and suspended in RPMI at a concentration of  $50 \times 10^4$  cells/ml. Samples were assayed at a flow rate of  $3\text{-}\mu\text{l min}^{-1}$ . Channels were pre-wetted by flowing PBS and the cell suspension flow was allowed to stabilize prior to data acquisition.

Cells positive for GFP fluorescence were detected in the 500-590 nm “green” channel following excitation with 488 nm light and were time-correlated with 405, 488, and 633 nm scattering peaks. Within the volume analyzed, leukocytes constituted ~1% of the acquired backscattered and fluorescent light data stream. Using a 25 kHz sampling frequency, the lower 99% of the intensity values defined the mean and standard deviation of the background signal. Individual peaks were demarcated by 6 to 7 data points, and the cumulative threshold approach was used to identify cells. The highest intensity time-

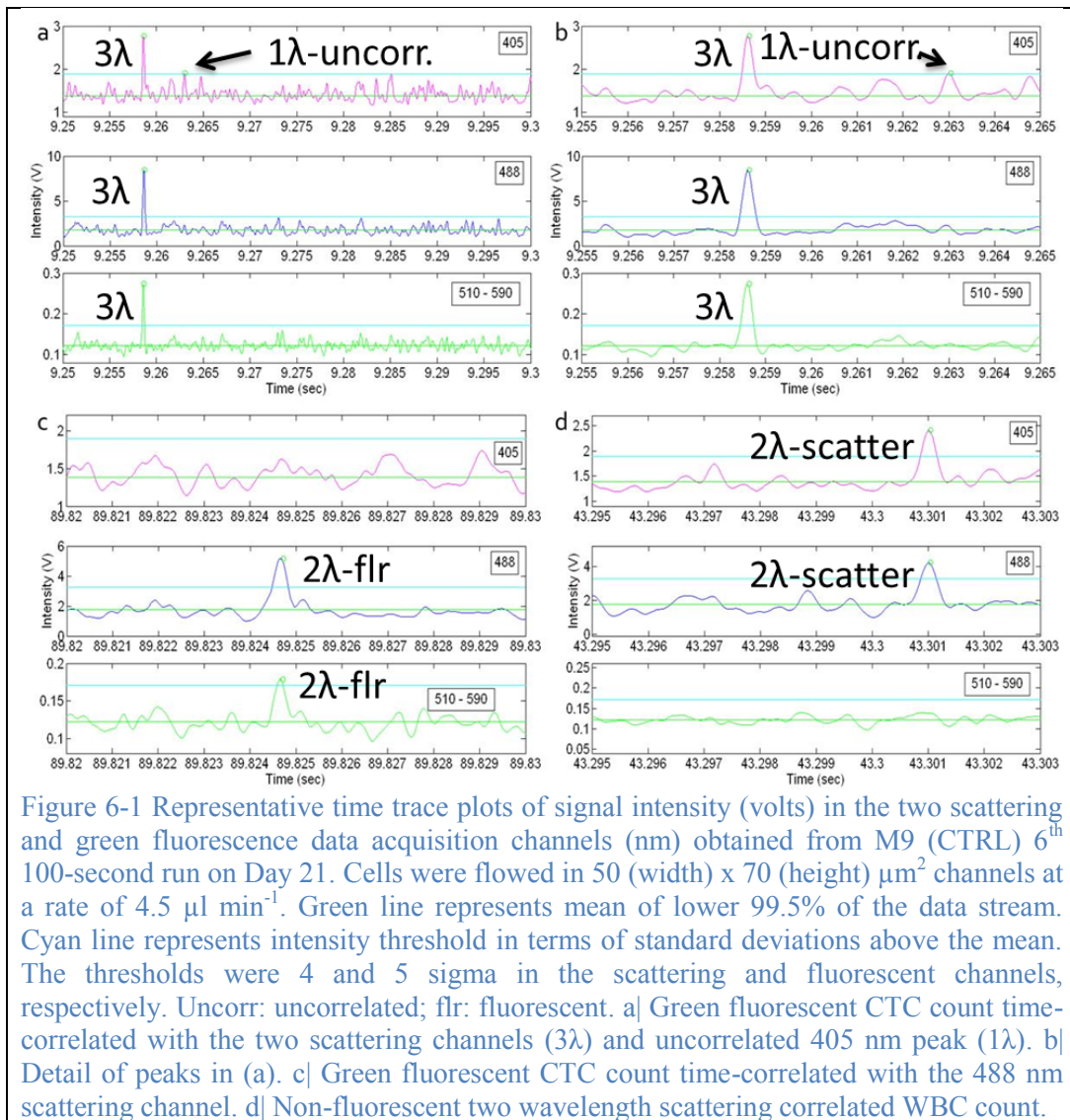


correlated peaks corresponding to the expected count based on concentration, assay time, and volumetric flow rate were used in discriminant analysis.

## **6.3 Results**

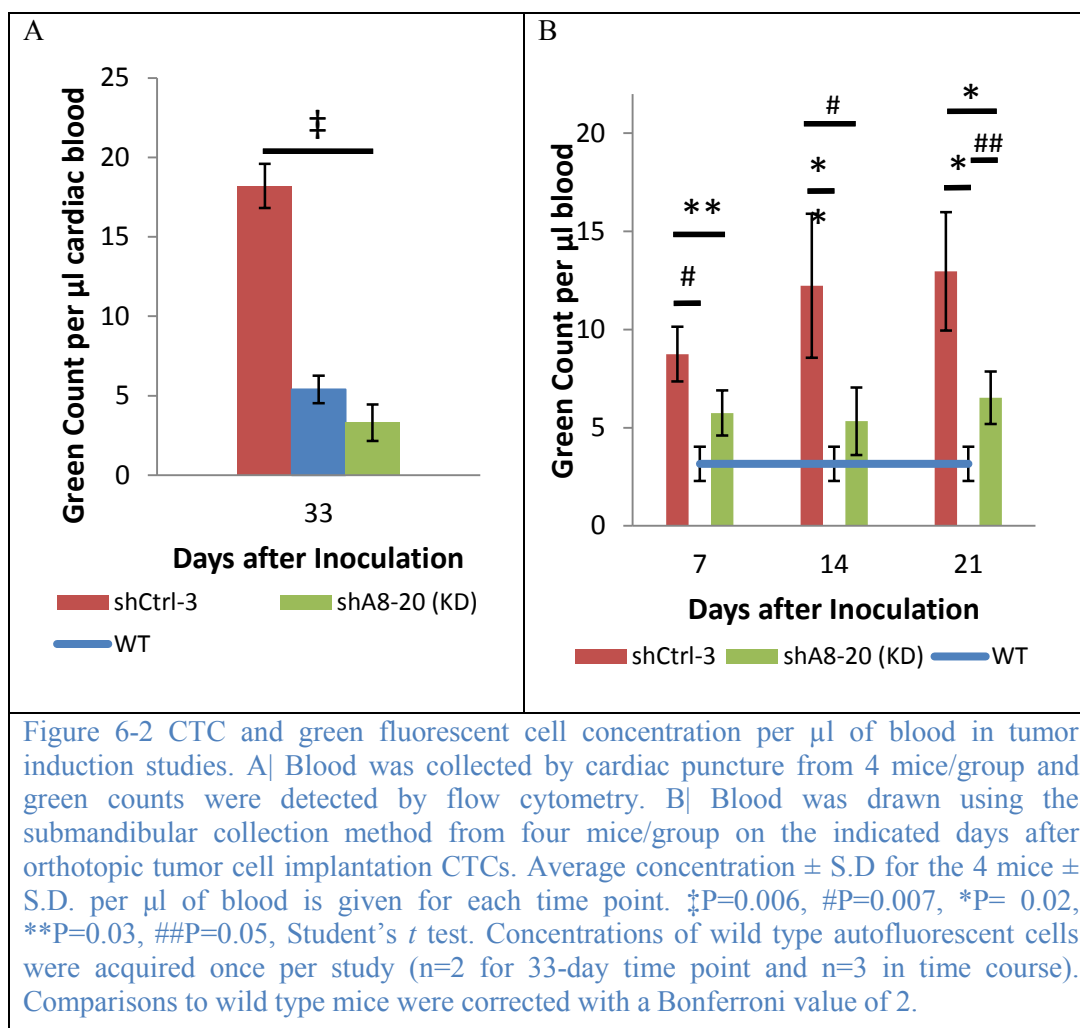
### **6.3.1 Tumor Induction**

Representative time traces of acquired scattering and fluorescence signal are illustrated in Figure 6-1 to show established standard deviation thresholds (cyan line) and the abundance of low scattering peaks, e.g. erythrocytes. Fluorescence signals were readily detected in these wider 50 (width) by 70 (height)  $\mu\text{m}^2$  channels.



Cells with a fluorescent peak and at least one time-correlated scattering peak were considered to be green fluorescent cells. Specifically, cells with 405 and 488 nm scattering peaks time-correlated with a fluorescence signal (Figure 6-1 A and B) were  $3\lambda$ . Cells with either a 405 or a 488 nm scattering peak time-correlated with a fluorescence peak (Figure 6-1 C) were fluorescent  $2\lambda$ . Non-fluorescent leukocytes were time-correlated in both the 405 and 488 nm scattering channels but lacked a fluorescent peak (Figure 6-1 D). Uncorrelated scattering peaks (Figure 6-1 A, B) were also non-fluorescent leukocytes.

The concentrations of green fluorescent cells detected in both tumor induction studies are shown in Figure 6-2. In both studies, the concentrations of CTCs were significantly lower in the mice injected with the ADAM8 knockdown shA8-20 cells than those injected with the known metastatic shCtrl-3 cells at each time point. In the second tumor induction time course study, CTCs were detected as early as seven days after cell implantation (Figure 6-2 B). This suggested a lower potential risk for developing metastases to distant organs when ADAM8 was knocked down, independent of tumor size.



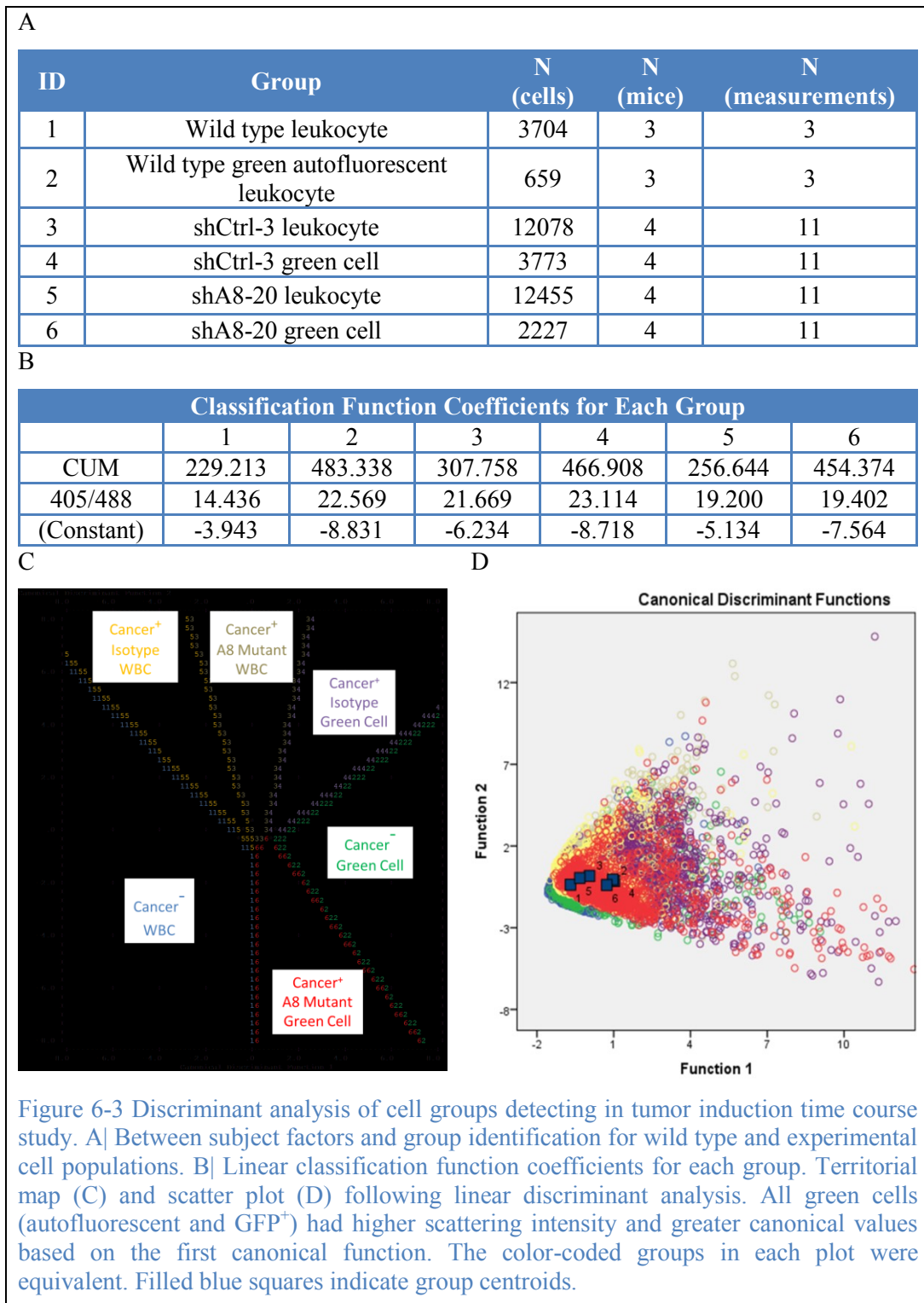
In wild type blood samples, autofluorescent leukocytes were detected in the green 500-590 nm PMT channel, thus indicating that green fluorescent cells detected in blood samples from the GFP<sup>+</sup> cancer-cell inoculated mice were potentially a heterogeneous population of autofluorescent leukocytes and GFP<sup>+</sup> CTCs. Of the wild type blood samples assayed, a concentration of  $3.2 \pm 1.1$  (submandibular blood collection, n = 3 mice) or  $5.4 \pm 3.4$  (cardiac puncture, n = 2 mice) green autofluorescent cells  $\mu\text{l}^{-1}$  blood was detected. Therefore, the presence of autofluorescent leukocytes was a limitation of using green fluorescent signal as an indicator of GFP<sup>+</sup> CTCs. The role of autofluorescent leukocytes in healthy and tumor-bearing mice is unknown. However, green fluorescent cells were consistently detected at higher concentrations in shCtrl-3-inoculated metastatic mice than in wild type mice. This observation was attributed to the presence of GFP<sup>+</sup> CTCs not found in wild type mice or an increase in green autofluorescent leukocytes as a response to metastatic cancer. Conversely, green fluorescent cell concentrations detected in shA8-20 ADAM8-knockdown mice were comparable to the wild type autofluorescent leukocytes abundances, except for the higher value at the day 21 time point. This similarity in green fluorescent cell concentrations was attributed to fewer GFP<sup>+</sup> CTCs or a minimal green autofluorescent leukocyte response to shA8-20 inoculation.

#### ***6.3.1.1 MANOVA and Linear Discriminant Analysis of Scattering Profiles – Six Groups of Leukocytes and Green Cells in Three Mouse Cohorts***

Although the primary aim of the study was to enumerate CTCs by GFP expression, the scattering intensities acquired in the 405 and 488 nm channels were used for discriminant analysis to characterize the scattering profiles of native CTCs and autofluorescent cells. Counts positive (green autofluorescent cells and CTCs) and negative (leukocytes) for 500-590 nm intensity were compared among the wild type control and experimental tumor-bearing groups. Whereas green counts from wild type

mice represented an autofluorescent population, green counts from tumor-bearing mice contained an unknown composition of green autofluorescent and GFP<sup>+</sup> CTCs. Therefore, MANOVA and linear discriminant analysis were used to discriminate cells types based on scattering properties. Cumulative scattering intensities (405+488) and the ratio thereof (405/488) were used as discriminant variables. Non-fluorescent and green fluorescent cell populations from each of the three mouse cohorts, e.g. wild type, aggregate shCtrl-3-inoculated, and aggregate shA8-20-inoculated, composed the six subject groups defined in Figure 6-3 A. One mouse in each experimental group, day 14 for shCtrl-3 and day 21 for shA8-20, were withheld for channel clogging and coagulation complications.

The MANOVA revealed significant differences in cumulative intensity between non-fluorescent leukocytes from all animals and both types of green fluorescent cells, e.g. autofluorescent leukocytes detected in wild type mice and green fluorescent cells detected in tumor-bearing mice. This difference was significant at  $P < 0.0005$  ( $F = 935$ ); however, a moderate Wilks'  $\Lambda$  of 0.778 and partial  $\eta^2$  of 0.118 suggested that this difference was attributed to a subset of green fluorescent cells. In contrast, entire population differences would have increased the observed variance among groups past the ~12% given by a partial  $\eta^2$  value of 0.118. The classification function coefficients are provided in Figure 6-3 B.



The consistently higher cumulative intensity coefficient values among the green fluorescent cell populations (groups 2, 4, and 6) corroborated the MANOVA finding. This classification outcome was illustrated in the higher values of the green fluorescent

cell population centroids in the territorial map (Figure 6-3 C) and scatter plot (Figure 6-3 D) in canonical space. Both autofluorescent green cells and potential GFP<sup>+</sup> CTCs identified in tumor-bearing were consistently similar with heightened scattering intensity weighted toward the 405 nm channel, as indicated by high 405/488 values relative to cumulative intensity. Dividing by a smaller 488 nm intensity value increased the 405/488 ratio. The full discriminant analysis is provided in the Appendix section 9.6.1. Classification results for unweighted prior probabilities are shown in Table 6-1.

Table 6-1 Classification results, by percent, of linear discriminant analysis following cross-validation. WT: wild type; Autoflr: autofluorescence; Flr: fluorescence; WBC: white blood cell, leukocyte

Group		Predicted Group Membership						Total	WBC	Green Flr Source	
		Wild Type		shCtrl-3		shA8-20				WT Autoflr Cancer <sup>-</sup>	Other Cancer <sup>+</sup>
		WBC	Green Autoflr WBC	WBC	Green Flr Cell	WBC	Green Flr Cell				
Wild Type	WBC	73.7	0.9	5.4	2.4	15.4	2.1	100	94.5	0.9	4.5
	Green Autoflr WBC	28.4	19	14.3	16	4.6	17.1	100	47.3	19.3	33.5
shCtrl-3	WBC	12.7	2.1	24.6	5.9	36.9	17.7	100	74.2	2.1	23.6
	Green Flr Cell	10.2	16	16.2	13	17.9	26.3	100	44.3	16.4	39.3
shA8-20	WBC	26.5	1.5	9.5	0.9	46.3	15.4	100	82.3	1.5	16.3
	Green Flr Cell	19.9	13	9.7	5.3	19.4	32.5	100	49	13.2	37.8



The classification results reflected the number of cells from each of the six populations that had scattering properties that aligned within the boundaries illustrated on the territorial map (Figure 6-3 C), thus yielding the net effect of overlaying the territorial map onto the canonical space scatter plot (Figure 6-3 D). As the scatter plot illustrated, green fluorescent cell population centroids were shifted toward higher values along the first canonical function relative to those of non-fluorescent leukocytes; however, there was extensive overlap among individual cells. The discriminant algorithm classifies a cell based on its proximity to a specific centroid. For example, if an individual wild type non-fluorescent leukocyte has scattering properties more alike to the centroid defined by all green fluorescent cells in a tumor-bearing mouse than its own group's centroid, then it will be classified as such a cell. Therefore, cross-classification among groups was expected based on visual inspection of the scatter plot.

The right side of Table 6-1 is a simplified representation where the six groups were reduced to three groups: leukocytes from all mice, green autofluorescent cells from wild type mice, and green counts from tumor-bearing mice. The average specificity for non-fluorescent leukocyte identification was  $83.7 \pm 8.3\%$  with  $1.5 \pm 0.5\%$  and  $14.8 \pm 7.9\%$  identified as green autofluorescent cells and green fluorescent counts deriving from tumor-bearing mice, respectively. Wild type green autofluorescent leukocytes with improbable epithelial origin, i.e. no GFP expression, were classified as 47.3% non-fluorescent leukocyte, 33.5% alike to green counts in tumor-bearing mice, and 19.3% unique. Green fluorescent cells from the two tumor-bearing mouse cohorts were classified similarly where  $46.7 \pm 2.35\%$  were considered to be non-fluorescent leukocytes,  $14.8 \pm 1.6\%$  were similar to green autofluorescent leukocytes, and  $38.6 \pm 0.8\%$  were classified uniquely. These results indicated that a subset of green fluorescent cells (<50%) had unique scattering properties relative to non-fluorescent leukocytes.

In an effort to distinguish autofluorescent cells from GFP<sup>+</sup> CTCs, a second MANOVA was performed on the green-correlated populations from the wild type, shCtrl, and shA8 mice. Using the same two parameters of cumulative intensity and 405/488 as discriminant variables, there was an insignificant difference among the three groups with  $P=0.071$  ( $F=2.16$ ), Wilks'  $\Lambda$  of 0.999, and partial  $\eta^2$  of 0.001. Therefore, it was hypothesized that additional discrimination parameters would be required to discern green autofluorescent cells from GFP<sup>+</sup> CTCs since fluorescent intensities were indistinguishable. With only two scattering detection channels used in the first scattering property analysis, a subsequent study was conducted with lysed blood samples, narrower microfluidic channels, and all three scattering wavelengths to potentially augment the discrimination power.

### **6.3.2 Scattering-Based Measurements in Tumor Resection Study**

In the tumor resection study, scattering and fluorescence (500-590 nm) intensities were acquired by flowing lysed samples in 30x30  $\mu\text{m}^2$  channels at three- $\mu\text{l min}^{-1}$  using all three interrogative wavelengths, i.e. 405, 488, and 633 nm. By flowing hemolysed leukocyte suspensions in narrower channels, relative to diluted whole blood in 50 (width) by 70 (height)  $\mu\text{m}^2$  channels, scattering signals were less attenuated by erythrocytes (Figure 6-4). Cells were detected using the cumulative threshold approach and fluorescent green cells are visible in the fluorescence detection channel (500-590 nm).

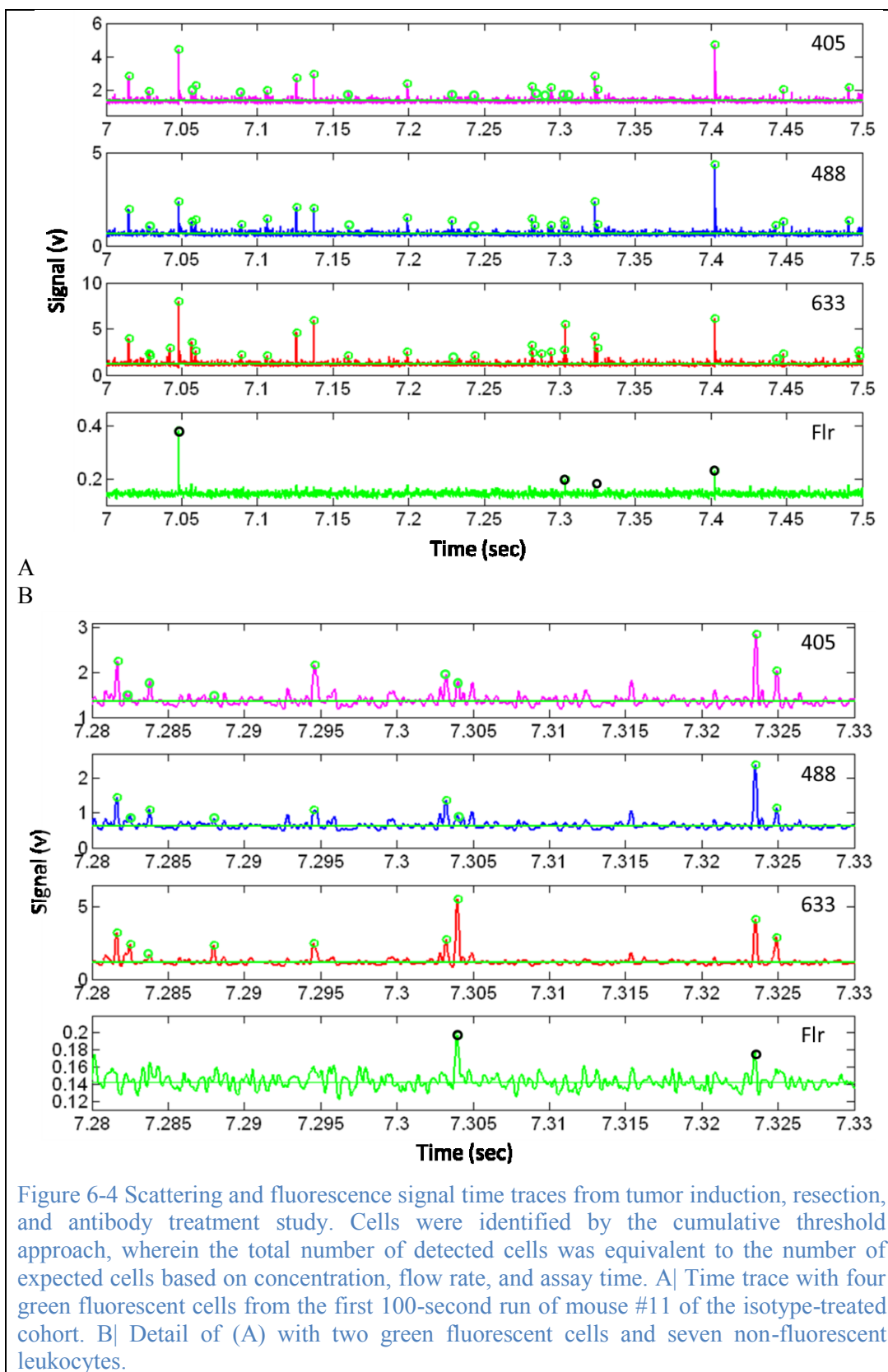


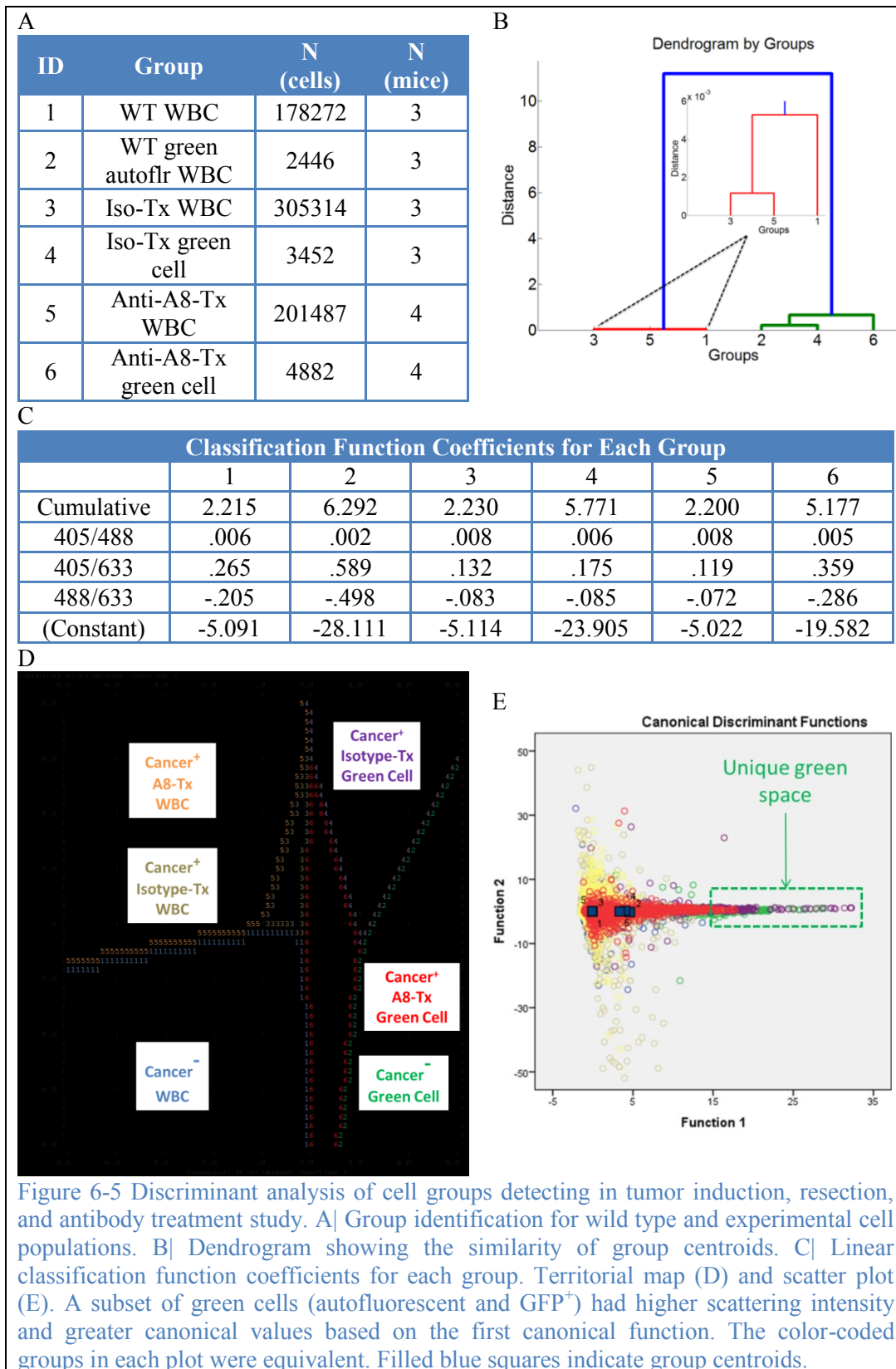
Figure 6-4 Scattering and fluorescence signal time traces from tumor induction, resection, and antibody treatment study. Cells were identified by the cumulative threshold approach, wherein the total number of detected cells was equivalent to the number of expected cells based on concentration, flow rate, and assay time. A| Time trace with four green fluorescent cells from the first 100-second run of mouse #11 of the isotype-treated cohort. B| Detail of (A) with two green fluorescent cells and seven non-fluorescent leukocytes.

Using the scattering intensities from the detected cells, two separate statistical analyses were performed with the following respective purposes:

1. Using MANOVA, define the canonical space occupied by non-fluorescent leukocytes and green fluorescent cells from all three cohorts to determine the general overlap between the two populations.
2. Using autofluorescent green cells from wild type mice as a reference population, determine the Mahalanobis distance for each correlated-green count acquired in each cohort of antibody-treated experimental groups to identify outliers representing improbable green autofluorescent leukocytes.

#### *6.3.2.1 MANOVA and Linear Discriminant Analysis of Scattering Profiles – Six Groups of Leukocytes and Green Cells in Three Mouse Cohorts*

Blood samples from each of the three mouse cohorts contained non-fluorescent leukocyte and green fluorescent cell populations. As before, green cells in cancer<sup>+</sup> mice consisted of unknown numbers of green autofluorescent cells and GFP<sup>+</sup> CTCs. All six groups of detected cells in this tumor resection and antibody treatment study were assessed via MANOVA and linear discriminant analysis (Figure 6-5). By acquiring scattering properties from all three interrogative wavelengths, cumulative intensity and ratios thereof were used as discriminant variables. One mouse in the isotype-treated cohort (#17) was withheld for blood coagulation complications prior to sample processing.



The MANOVA revealed significant differences in cumulative intensity between non-fluorescent leukocytes and both types of green fluorescent cells, e.g. autofluorescent leukocytes detected in wild type mice and green fluorescent cells detected in cancer<sup>+</sup> mice (Figure 6-5 B). This difference was significant at  $P < 0.0005$  ( $F = 7170$ ); however, a moderate Wilks'  $\Lambda$  of 0.805 and partial  $\eta^2$  of 0.053 suggested that this difference was attributed to only a subset of green fluorescent cells (Figure 6-5 E). In contrast, entire population differences would have increased the observed variance among groups past the ~5.3% given by a partial  $\eta^2$  value of 0.053. Cumulative intensity was the only discriminant variable among the four that significantly discriminated between non-fluorescent and fluorescent cell population properties. The primary finding was that green fluorescent cells (groups 2, 4, and 6) had greater cumulative scattering intensity than non-fluorescent leukocytes (groups 1, 3, and 5), which was reflected in the higher respective canonical function coefficients (Figure 6-5 C). This classification outcome was illustrated in the higher values of the green fluorescent cell population centroids in the territorial map (Figure 6-5 D) and scatter plot (Figure 6-5 E) in canonical space. The full discriminant analysis is provided in the Appendix section 9.6.2.1. Classification results for unweighted prior probabilities are shown in Table 6-2.

Table 6-2 Classification results, by percent, of linear discriminant analysis following cross-validation. WT: wild type; Autoflr: autofluorescence; Iso-Tx: isotype-treated; Anti-A8-Tx: anti-A8-treated; Flr: fluorescence; WBC: white blood cell, leukocyte

Group		Predicted Group Membership						Total	WBC	Green Flr Source	
		Wild Type		shCtrl-3		shA8-20				WT Autoflr Cancer <sup>-</sup>	Other Cancer <sup>+</sup>
		WBC	Green Autoflr WBC	WBC	Green Flr Cell	WBC	Green Flr Cell				
Wild Type	WBC	42.8	0.6	17.2	0.3	36.5	2.5	100	96.5	0.6	2.8
	Green Autoflr WBC	24.5	39.1	8.6	3.3	6.3	18.2	100	39.4	39.1	21.5
shCtrl-3	WBC	31.2	0.5	20.3	0.3	44.4	3.4	100	95.9	0.5	3.7
	Green Flr Cell	14.5	34.6	15.6	5.5	10.9	18.9	100	41	34.6	24.4
shA8-20	WBC	31.7	0.3	19.3	0.3	45.8	2.7	100	96.8	0.3	3
	Green Flr Cell	16.8	31.6	14.9	6.4	8.5	21.8	100	40.2	31.6	28.2

Relative to the previously described discrimination results from the tumor induction time course study, the primary improvements of using three rather than two scattering wavelengths were increased specificity for non-fluorescent leukocytes (Table 6-2) and increased sensitivity to a unique canonical space occupied exclusively by green fluorescent cells (Figure 6-5 E). The average specificity for non-fluorescent leukocyte identification was  $96.4 \pm 0.37\%$  with  $0.5 \pm 0.1\%$  and  $3.2 \pm 0.4\%$  identified as green autofluorescent cells and green fluorescent counts deriving from cancer<sup>+</sup> mice, respectively. In terms of reproducibility, all three non-fluorescent leukocyte populations were classified relatively equally, as corroborated by the small Mahalanobis distance among the group centroids (Figure 6-5 B).

Wild type green autofluorescent leukocytes with improbable epithelial origin, i.e. no GFP expression, were classified as 39.4% non-fluorescent leukocyte, 21.5% alike to green counts in cancer<sup>+</sup> mice, and 39.1% unique. Green fluorescent cells from the two cancer<sup>+</sup> mouse cohorts were classified similarly where  $40.6 \pm 0.4\%$  were considered to be non-fluorescent leukocytes,  $33.1 \pm 1.5\%$  were similar to green autofluorescent leukocytes, and  $26.3 \pm 1.9\%$  were classified uniquely. These results indicated that a subset of green fluorescent cells (<50%) had unique scattering properties, particularly cumulative intensity, relative to non-fluorescent leukocytes. These unique green fluorescent cells had first canonical function values greater than 15. Furthermore, overlapping classification among green fluorescent cells deriving from wild type and cancer<sup>+</sup> mice suggested that the majority of these cells had similar scattering characteristics. Narrower microfluidic channels and a decreased flow rate also enhanced signal quality by minimizing variability within the assay focal volume.



Having established a basis for discriminating non-fluorescent leukocytes from a subset of green counts, the next statistical analysis sought to distinguish the autofluorescent composition of green cells in each antibody-treated cohort.

#### ***6.3.2.2 Mahalanobis Distance of Each Green Count in Antibody-Treated Cohorts to Reference Wild Type Autofluorescent Population***

Without a GFP<sup>+</sup> CTC population to serve as a gold standard for classification, an alternative approach was developed to use the combined wild type autofluorescent cells as a reference population to detect outliers among the green counts identified in antibody-treated experimental cohorts. The outliers were hypothesized to indicate green fluorescent cells circulating in cancerous mice, e.g. GFP<sup>+</sup> CTCs or some other autofluorescent cells, not present in wild type mice.

Cumulative scattering intensity and the three ratios were again used as variables to define the global centroid and covariance of the reference autofluorescent leukocyte population and to characterize each green count in the experimental cohorts. A scatter plot of all green counts is shown in Figure 6-6 with marker size proportional to cumulative scattering intensity.

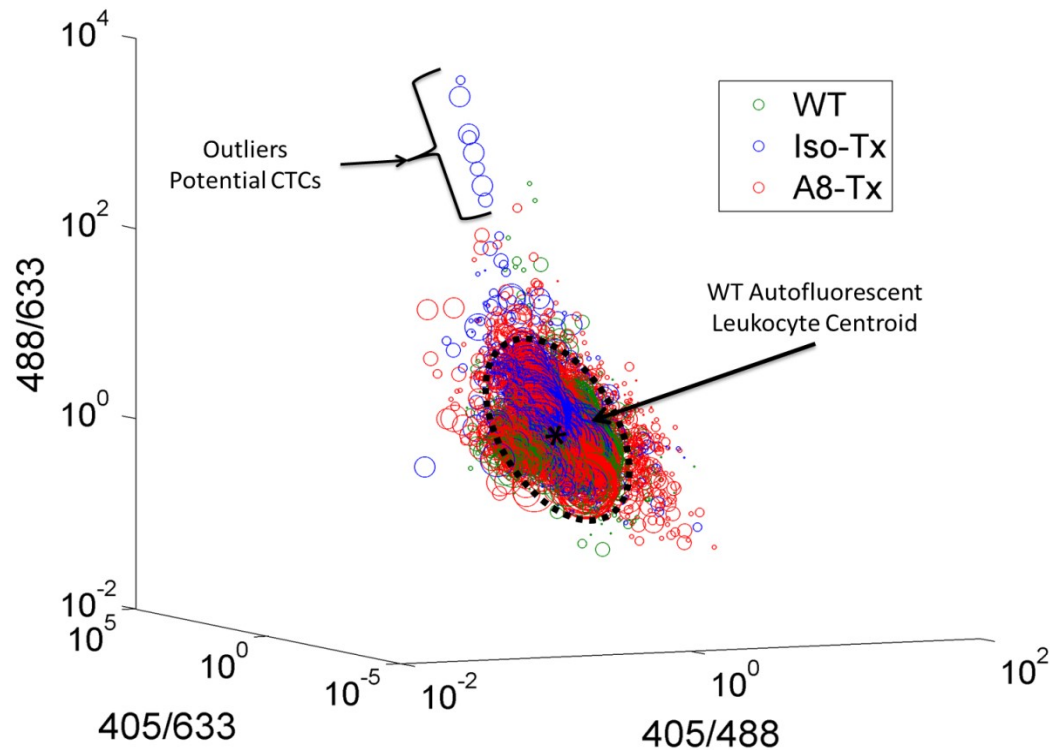
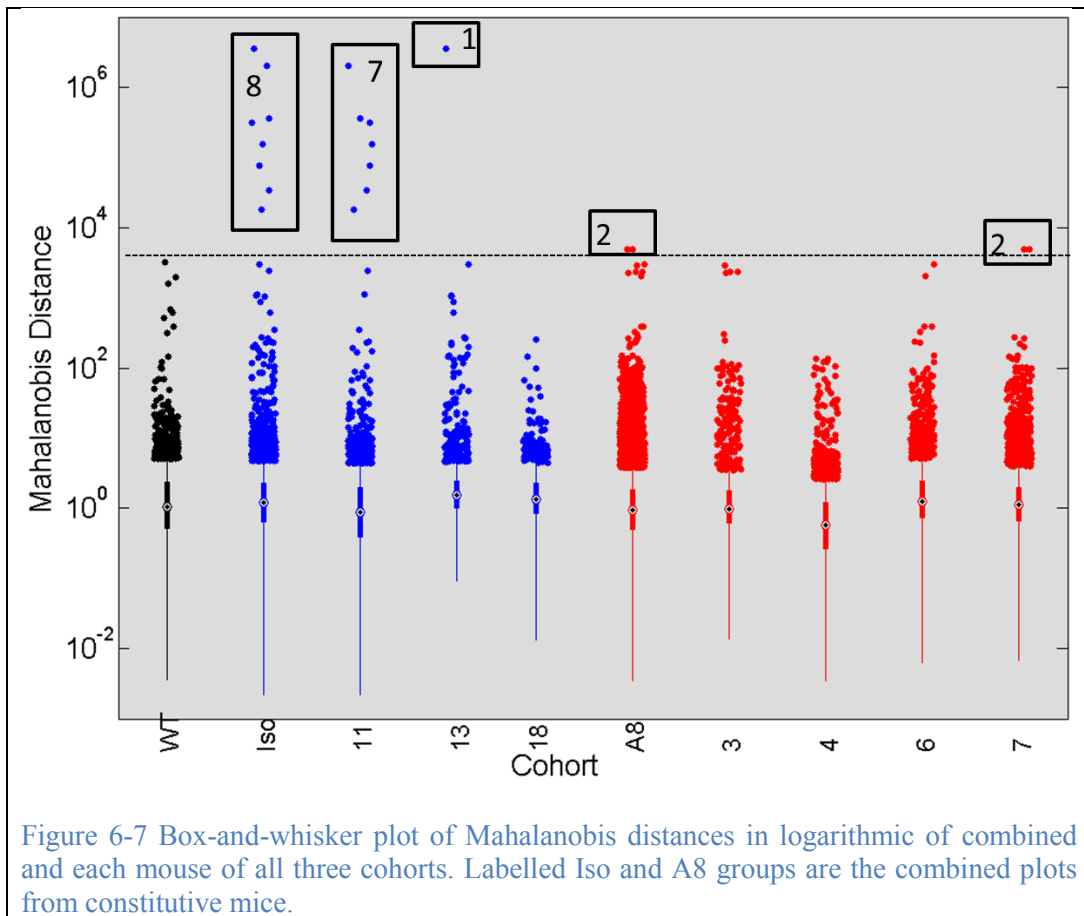


Figure 6-6 Scatter plot of all green counts in logarithmic 3-D scattering intensity ratio space. Marker size is proportional to cumulative scattering intensity to offer a fourth dimension to the plot.

The scatter plot illustrates the few outliers relative to predominantly overlapping majorities among the aggregate counts from the three mouse cohorts. In this way, the Mahalanobis distance of each cell, including wild type autofluorescent green cells, were calculated to the centroid of the reference wild type autofluorescent cell population. A box-and-whisker plot on a logarithmic scale illustrates the Mahalanobis distance dispersion of aggregate values from each treatment cohort and each mouse (Figure 6-7).



On each box, the central mark was the median, the edges of the box were the 25<sup>th</sup> and 75<sup>th</sup> percentiles, the whiskers extended to the most extreme data points not considered outliers, and outliers were plotted individually. The medians and interquartile ranges of all of mice predominantly overlapped. The preponderance of outliers on the upper end of the Mahalanobis distance range reflected the relatively small median of the distances relative to a minority of outlying cells. Strikingly, a majority of outlying cells in the experimental mice were within the range of Mahalanobis distances exhibited within the wild type autofluorescent group. Descriptive statistics are provided in Table 6-3).

Table 6-3 Descriptive statistics of Mahalanobis distances. Mets: observed metastases; B: brain; L: lungs

Cohort	Mouse	Mets	Cells	Mean	Median	Mode	Min	Max	StDev
<b>WT (n=3)</b>		None	4892	4.00	1.04	0.10	3.57E-03	3226.49	61.02
<b>Iso-Tx (n=3)</b>	11	B	1991	1489.52	0.87	1.15	2.24E-03	1.99E+06	4.61E+04
	13	B, L	1691	2125.44	1.52	1.02	9.33E-02	3.58E+06	8.71E+04
	18	B, L	1541	2.44	1.36	0.14	1.32E-02	257.38	8.61
<b>Average</b>			<b>1741</b>	<b>1205.80</b>	<b>1.25</b>	<b>0.77</b>	<b>0.04</b>	<b>1.86E+06</b>	<b>4.44E+04</b>
<b>StDev</b>			<b>187.08</b>	<b>889.63</b>	<b>0.27</b>	<b>0.45</b>	<b>0.04</b>	<b>1.46E+06</b>	<b>3.56E+04</b>
<b>A8-Tx (n=4)</b>	3	None	1491	10.58	0.98	1.11	1.40E-02	2934.28	128.48
	4	None	3071	1.66	0.58	0.29	3.51E-03	134.56	7.07
	6	None	1981	6.98	1.24	0.62	6.37E-03	3003.37	83.71
	7	B	3219	6.52	1.12	0.18	6.86E-03	4928.59	123.43
<b>Average</b>			<b>2440.50</b>	<b>6.43</b>	<b>0.98</b>	<b>0.55</b>	<b>7.68E-03</b>	<b>2750.20</b>	<b>85.67</b>
<b>StDev</b>			<b>727.37</b>	<b>3.17</b>	<b>0.25</b>	<b>0.36</b>	<b>3.85E-03</b>	<b>1709.16</b>	<b>48.58</b>
<b>T Test P-Value</b>			0.23	0.20	0.30	0.57	0.42	0.22	0.22

Without applying a Mahalanobis distance threshold, there was no significant difference between experimental cohorts via one-way ANOVAs (Appendix section 9.6.2.2). The majority of detected green cells in the experimental cohort groups exhibited scattering properties alike to those from wild type autofluorescent cells. Therefore, the majority of the heterogeneous population of green cells in the antibody-treated experimental cohorts was either green autofluorescent leukocytes or GFP<sup>+</sup> CTCs with similar light scattering properties. The few drastic outliers in isotype-treated mice #3 and #4 and anti-A8-treated mouse #7 represented the unique cells outside the dispersion range within the wild type autofluorescent population.

Having ascertained that the majority of green counts in the experimental cohorts were similar to autofluorescent cells detected in the wild type cohort, the next analysis sought to quantify green fluorescent cells as a percentage of total detected cells and to identify the unique attributes of the outliers (Table 6-4).

Table 6-4 Green cells as a percentage of all detected cells and extent of outliers beyond observed wild type dispersion. Mets: metastases. % Green: number of detected green fluorescent cells as a percentage of total detected cells. Exclude all WT: Mahalanobis distance threshold (Figure 6-7) that demarcates definitive outliers from the wild type autofluorescent leukocyte population.

Cohort	Mouse	Mets	Green Cells	All Cells	% Green	Green Cells /μl Blood	Exclude All WT			
							Count	% of Green	% of All	/ml Blood
WT (n=3)		None	4892	361437	1.35±0.7	9±4	0	0	0	0
Iso-Tx (n=3)	11	B	1991	177353	1.12	7	7	3.5E-01	3.9E-03	23
	13	B, L	1691	226116	0.75	4	1	5.9E-02	4.4E-04	3
	18	B, L	1541	126223	1.22	7	0	0	0	0
Average			1741	176564	1.03	6.1	2.67	0.14	1.46E-03	8.7
StDev			187.08	40785	0.20	1.2	3.09	0.15	1.77E-03	10.5
A8-Tx (n=4)	3	None	1491	10.58	1.64	10	0	0	0	0
	4	None	3071	1.66	2.31	14	0	0	0	0
	6	None	1981	6.98	3.13	19	0	0	0	0
	7	B	3219	6.52	2.56	15	2	6.2E-02	1.6E-03	9
Average			2440.50	103184	2.41	14.3	0.50	0.02	4.0E-04	2.4
StDev			727.37	28029	0.53	3.2	0.87	0.03	6.9E-04	4.1
T Test P-Value			0.23	0.06	0.02	0.02	0.31	0.38	0.40	0.40

As a percentage of total detected cells, mice treated with anti-A8 antibody contained  $2.41 \pm 0.53\%$  green cells, which was significantly more than isotype-treated mice with  $1.03 \pm 0.2\%$  ( $p=0.02$ ). Similarly, by assuming an average concentration of 595 leukocytes/ $\mu\text{l}$  of blood, mice treated with anti-A8 antibody contained  $14.3 \pm 3.2$  green cells/ $\mu\text{l}$  of blood, which was significantly more than isotype-treated mice with  $6.1 \pm 1.2$  green cells/ $\mu\text{l}$  of blood ( $p=0.02$ )<sup>170</sup>. The value of this finding centered on the unknown role of autofluorescent cells in cancer progression; however, the physiological evidence regarding metastatic burden was intriguing. Whereas, all mice in the isotype-treated cohort developed metastases, only mouse #7 in the anti-A8 cohort developed metastases. Seeing as mouse #7 was also the only subject in the anti-A8 cohort to contain definitive outliers, additional attributes of the scattering signals of these cells were investigated. As corroborated by Figure 6-6, the outliers had reduced 633 nm scattering intensity relative to the 405 and 488 nm intensities. Similarly, the FWHM and integrated area of each of the outlier peaks was 3.3 and 3.5 standard deviations greater than the mean value for wild type autofluorescent cells, respectively. This suggested that the outliers were larger cells with low scattering or high absorption characteristics of 633 nm.

## 6.4 Conclusions and Discussion

Green fluorescent cells representing either autofluorescent leukocytes or GFP<sup>+</sup> CTC populations were detected in all analyzed mouse peripheral blood samples. The number of detected fluorescent cells assayed weekly in a one-month tumor induction time course study correlated with prevalence of metastatic lesions. Green fluorescent cell concentrations were significantly higher in the cohort inoculated with a human metastatic cell line than in both the ADAM8-knockdown and wild type cohorts. The wild type cohort established a baseline green autofluorescent leukocyte concentration, which was significantly exceeded in two of the four time points by green fluorescent cell concentrations detected in the ADAM8-knockdown cohort. Fewer metastases were

observed in the ADAM8-knockdown cohort than in the metastatic control group, thus indicating that metastatic dissemination was reduced in the absence of ADAM8.

In the tumor induction and resection study, treatment with anti-ADAM8 antibody reduced the extent of metastases relative to mice treated with an isotype control antibody. Green fluorescent cell concentration assayed at a single time point 50 days after inoculation and 37 days after tumor resection was significantly increased in the anti-ADAM8-treated cohort relative to the isotype-treated control cohort. Linear discriminant analysis of backscattering properties determined that cumulative scattering intensity among a subset of green fluorescent cells was significantly greater than that of non-fluorescent leukocytes. Using all green autofluorescent leukocytes detected in wild type mice as a reference population, only ten green fluorescent cells detected in experimental mice were found to be outliers. These ten outlying cells were detected in three mice. Two of the mice were in the isotype-treated control group and both developed metastases. The other mouse was in the anti-A8 antibody treatment cohort and was the only mouse of its cohort to develop a metastatic lesion.

The majority of green fluorescent cells detected in antibody-treated mice had scattering characteristics similar to green autofluorescent leukocytes. Therefore, the significantly increased concentration of these cells detected in anti-ADAM8-treated mice implicated an immune response to cancer. The coincidental finding was that the ten definitive outliers occurred in mice that developed metastases, thus suggesting that these cells were GFP<sup>+</sup> CTCs or green autofluorescent cells that were unlike those detected in wild type mice.

Additional wild type samples are required to define the scattering properties of potential sub-populations of rare autofluorescent leukocytes to identify accurately outliers. The adaptive immune system of NOD/SCID mice is compromised due absent or



atypical T and B lymphocytes. Therefore, the green autofluorescent cells may be a heterogeneous, albeit limited, population of leukocytes. Separate studies involving GFP<sup>+</sup> and GFP<sup>-</sup> tumor induction would elucidate the relationship between CTC and autofluorescent leukocyte concentrations. Nevertheless, this general approach of using a reference population provided a library for negative selection of potential CTCs relative to autofluorescent leukocytes.

## 7 Chapter: Future Research Directions

### 7.1 Microfluidics

The current microfluidic channel design contains abrupt  $90^\circ$  angles and restrictions at the inlet and outlet sections of the rectangular channel. Channel clogs occurred at both ports but rarely within the channel length. Therefore, a future direction is to modify the height dimension of the SU-8 master to create a more gradual narrowing of the channel height, which would be similar to the present design of the width dimension on both ports. Other groups have incorporated this design by cross-linking a hemispherical droplet of SU-8 at the inlet and outlet ports following the initial UV-irradiation step<sup>171,172</sup>. One embodiment of the final design is illustrated in Figure 7-1.

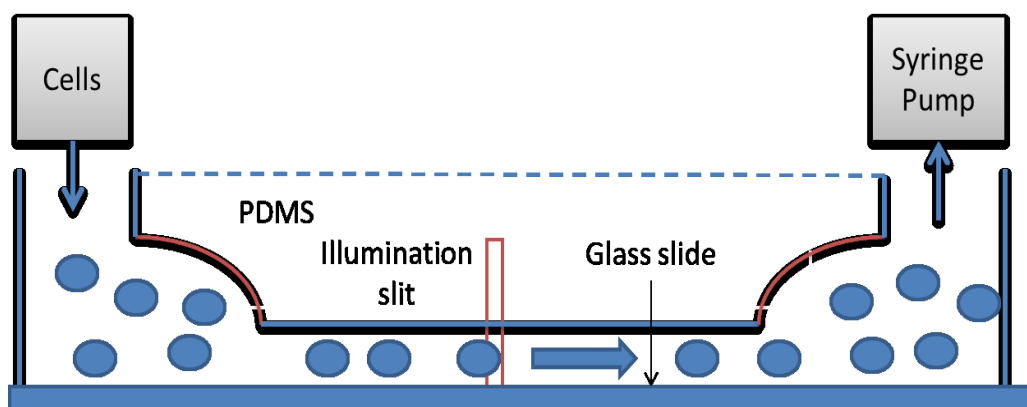


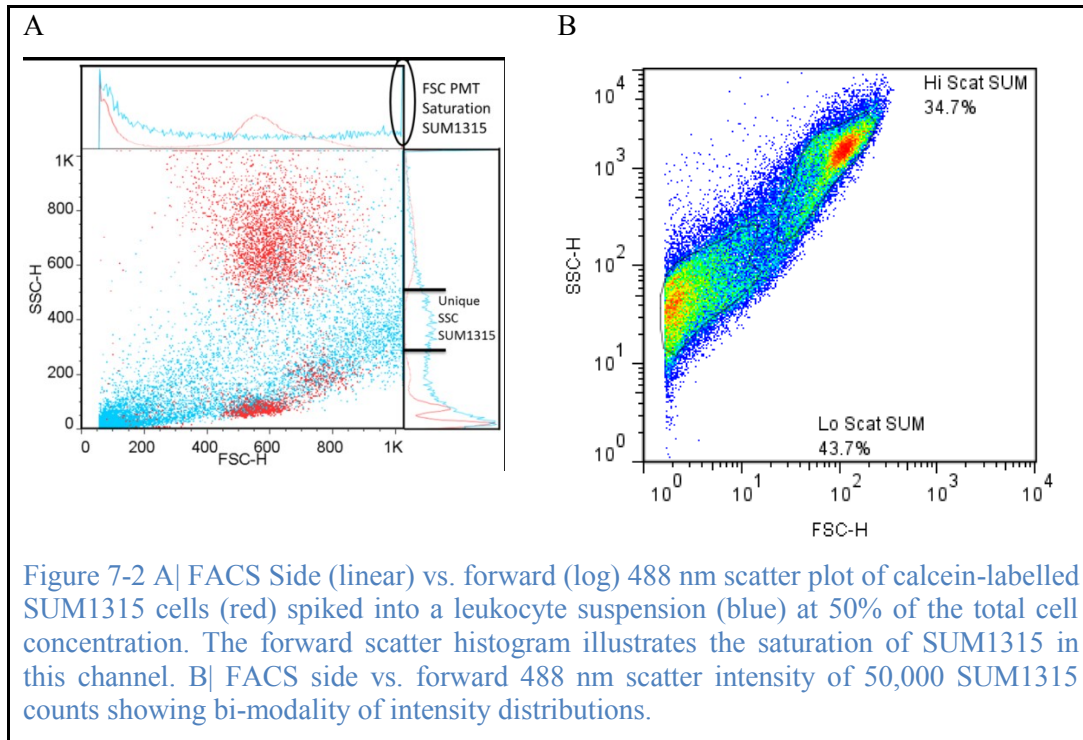
Figure 7-1 Rounded inlet and outlet ports to mitigate channel blockage during flow experiments.

A second future direction is to employ hydrodynamic focusing to the microfluidic platform. This approach is routinely used in commercial flow cytometers and is recently being used in microfluidics to vary flow rate and minimize assay channel clogging (10.1039/B708187A, 10.1063/1.2046729).

### 7.2 Forward and Side Scatter-Based Detection of Cancer Cells

Due to the rapid processing time and commercial amenities available in standard FACS analysis, forward and side scatter characteristics of calcein<sup>+</sup> SUM1315 cells spiked at a 50% concentration into twice-lysed leukocyte suspensions were acquired for a total

of 50,000 cells. Using the green fluorescence channel as a gold standard for SUM1315 cell identification, forward scatter intensity from a subset of SUM1315 cells saturated the acquisition window set to acquire leukocyte sub-populations (Figure 7-2).



Of the 25,000 cancer cells assayed, only a minority of the SUM1315 population was visible within the acquisition window; larger cells with higher forward scatter intensity saturated the PMT detectors set to acquire leukocytes that were entirely contained in the acquisition window (Figure 7-2 A). Therefore, standard FACS was not amenable to analyzing spiked samples with leukocyte sub-population resolution. However, based on an isolated SUM1315 flow analysis, large cancer cells may constitute ~35% of the population (Figure 7-2 B) that would be distinctly unique from leukocytes. A future direction in FACS analysis would be to reduce PMT voltage and gain settings to acquire the entire SUM1315 population. This is the opposite approach to that shown in Figure 7-2 A, and smaller blood and cancer cells would occupy the lower

forward intensity region of the acquisition window. Although discrimination of leukocyte sub-populations would decrease in response to lower PMT sensitivity to those scattering intensities, the benefit of enumerating large cancer cells would enhance cancer cell detection.

A related future direction would be to incorporate a forward scatter intensity detector into the custom microfluidic platform. Interestingly, the SUM1315 side scatter gradient exhibited a slight peak in the intermediate space between PBMCs and PMNs (Figure 7-2 A). Additional levels of cell type discrimination would be gained by modifying the microfluidic platform to acquire forward and side scatter intensity.

### **7.3 Density Centrifugation for Enhanced Erythrocyte Depletion**

The limitations of density centrifugation were first discussed in the concluding remarks of the Chapter 4 and included a bias to enrich cancer cells with similar densities to those of the two leukocyte sub-populations above and below  $1.077 \text{ g ml}^{-1}$  (e.g. Ficoll-Paque). However, the cell discrimination experiments of cancer cells spiked into lysed leukocytes presented in Chapter 5 yielded less than target sensitivity and specificity values. Therefore, further isolating leukocytes into sub-populations would recover the intermediate, relatively sparse scattering space that was observed in Chapter 4. The secondary benefit to these isolation steps would be generating two populations that would be more accurately defined by single mean and variance values that characterize MANOVA and linear discriminant analysis classification algorithms. Lysed samples contained both PBMCs and PMNs; however, the respective centroids of these two sub-populations could not be reproducibly defined due to the attenuating effects of erythrocytes within the focal volume of the excitation light. Attempting to define one bi-modal population with single mean and variance values undermined the classification performance of linear discriminant analysis.

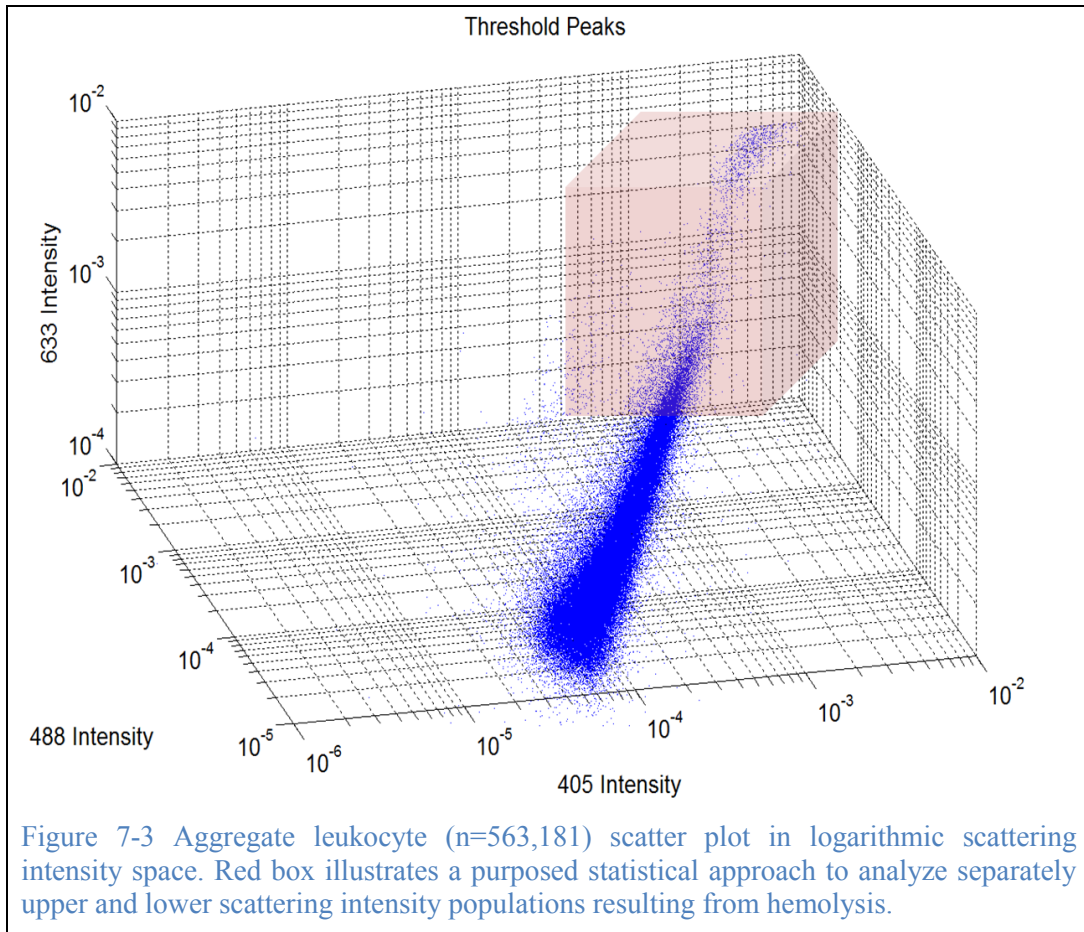
Future experiments using calcein-labeled cancer cells re-suspended into non-cancerous whole blood samples will validate the yield and efficacy of a density centrifugation approach. The purpose of these experiments is to validate that cancer cells that sediment within the upper PBMC- and lower PMN-enriched layers relative to Ficoll-Paque have distinct scattering properties despite their similarity in density. The number of detected cells in each layer will reflect the cumulative yield losses due to the isolation protocol and microfluidic-based flow cytometry detection approach. These experiments model a cancer patient blood sample where an unknown concentration of unlabeled cancer cells are suspended in whole blood.

#### **7.4 Leukocyte Library for Negative Selection of CTCs in Patient Samples**

In order to address the limitations in using cultured cancer cells as a gold standard for physiological CTC scattering properties, a different statistical approach beyond linear discriminant analysis is required to discriminate CTCs from blood cells. CTCs within cancer patient blood samples lack the experimental utility of GFP expression or an exogenous fluorescence marker (e.g. calcein) to demarcate these rare cells; therefore, an isolated CTC population does not exist for training set purposes. Moreover, by undergoing EMT, the most invasive of CTCs cease expression of epithelial-specific transcripts and antigens<sup>51</sup>. The ramifications of EMT on physical properties, e.g. light scattering via refractive organelles, are unknown. Consequently, a negative selection approach is useful to robustly define scattering spaces occupied by leukocytes obtained by either hemolysis or density centrifugation.

By leveraging the accumulated library of scattering properties from multiple donors analyzed over the course of multiple days, a reference population can be defined from which to exclude CTCs as outliers, i.e. via Mahalanobis distance. Similar to linear discriminant analysis, Mahalanobis distances are defined from the centroid of a reference

population; therefore, multiple clusters within a lysed reference population marginalize the approach. Instead, an example of an iterative approach is illustrated in Figure 7-3 where clusters of an overall population are analyzed separately to define accurately local centroids.

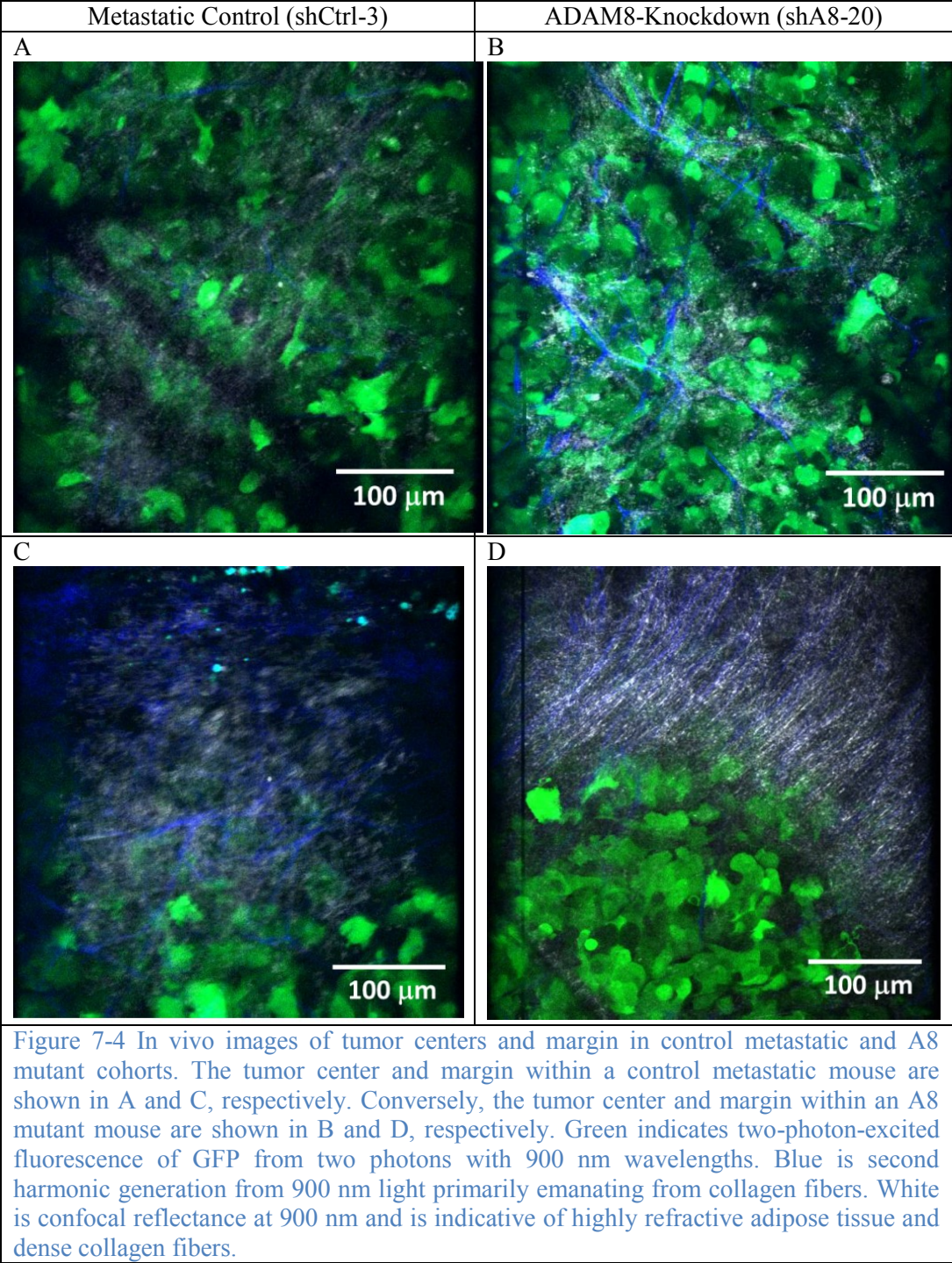


Although patient samples lack a fluorescent marker for positive identification, CTCs derived from fluorescent protein-expressing cancer cells implanted into mice could develop this detection method. Human cancer cells lacking fluorescent protein and exogenous dyes xenotransplanted into animal models would be the next development step in detecting physiological CTCs.

## 7.5 In Vivo Imaging of Tumor Body and Periphery

Following the hypothesis that the proteolytic capacity of ADAM8 augments invasiveness by interrupting the extracellular matrix (ECM), we pursued a pilot investigation to visualize the tumor and surrounding ECM in vivo. Two mice were anesthetized with ketamine/xylazine, MFPs were surgically exposed, and GFP<sup>+</sup> tumors were visualized with our group's custom two-photon microscope. Drs. Kyle Quinn and Carlo Alonzo conducted the imaging procedure. The noncentrosymmetric property of collagen elicited second-harmonic signal within the tumor body and border, which is illustrated in Figure 7-4.





Blood flow was also visualized via confocal reflectance. A future direction is to conduct a longitudinal study investigating changes in collagen morphology and blood flow within the tumor body and periphery in anti-A8 treated and metastatic control



isotype-treated mice. Such a study may elucidate anti-A8 antibody mechanisms to prevent tumor growth via hypoxia and inhibited intravasation capacity. Less neo-vascularization would minimize routes for metastatic dissemination. Furthermore, a higher degree of alignment of collagen fibers within the tumor volume and along the periphery ECM would suggest a less invasive capacity. The hypotheses would be that anti-ADAM8 antibody-treated tumors would have a reduced extent of vascularization and a higher degree of collagen fiber alignment in the ECM.

## 7.6 Leukocyte Autofluorescence

To date, a limited number of studies have been conducted on sources of autofluorescence in leukocytes. In brief, excitation of leukocytes at 466 nm light resulted in emission from 500-540 nm and was attributed to flavin and flavin coenzyme features<sup>173</sup>. Excitation/emission (nm) pairs for the following endogenous molecules were detected in isolated neutrophils: tryptophan at 290/330; NAD(P)H at 350/450; FAD at 450/530; and an unknown at 500/530<sup>174</sup>. Similar to PMNs, different investigators generated an excitation (260-500 nm) emission (280-700 nm) matrix for PBMCs and identified peaks attributed to tryptophan, NAD(P)H, and FAD<sup>175</sup>.

Autofluorescent cells played a dual role in this thesis work, and their identity and function in cancer merit further investigation. First and experimentally, endogenous autofluorescent green cells compromised our gold standard of calcein and GFP signal. In the first tumor induction study, the concentration of autofluorescent green cells was consistently less than the concentration of green counts detected in the metastatic mice, thus suggesting that GFP<sup>+</sup> CTCs constituted only a fraction of detected counts. However, autofluorescent cells had fluorescence emission and scattering intensities that overlapped with those of potential GFP<sup>+</sup> CTCs in metastatic mice. Flowing and analyzing an isolated population of cultured GFP<sup>+</sup> cancer cells to discern precisely scattering characteristics did

not recapitulate the flow conditions of lysed samples where residual blood cells and platelets attenuated measured scattering intensities.

Second, in any tumor induction study attempting to use GFP signal as a marker for CTCs, the green fluorescent cell population contained unknown numbers of autofluorescent cells and CTCs. These unknowns raised complementary questions on the roles of autofluorescent leukocytes, as components of the immune system, in cancer. For example, how does the abundance of autofluorescent leukocytes vary in wild type, cancer-bearing metastatic, or cancer-bearing mice in remission?

The GFP<sup>+</sup> tumor induction study referenced in section 1.2.4 conducted by Hwu et al. offered preliminary insight on red autofluorescent cell identity and their role in cancer progression<sup>61</sup>. Using tumor and metastatic lesion formation as discriminatory endpoints, the integral number of detected green cells less accurately predicted formation of metastases than the ratio of the number of green fluorescent peaks to the ratio of green to red fluorescent peaks. Therefore, mice with an increase in green counts coupled with a decrease in red autofluorescent counts had a greater prevalence of metastatic lesions. Using two separate detection channels and excitation sources of 488 and 633 nm, red autofluorescent cells correlated with FITC anti-mouse sca-1 or cd-31 antibodies in vivo in wild type mice. Sca-1 targeted multipotent hematopoietic stem cells<sup>176</sup>. CD-31 targeted precursor endothelial cells, as well as a range of hematopoietic cells including megakaryocytes, platelets, macrophages, granulocytes, and NK/T lymphocytes<sup>177</sup>. This range covered cells deriving from both myeloid and lymphoid progenitor cells, which corroborated the correlation results observed with sca-1 expression.

A preliminary follow-up study was conducted during this thesis work to more narrowly define the identities of red autofluorescent cells in human peripheral blood. The FACS-based study was performed on hemolysed samples using antibodies targeting a

range of leukocyte sub-population-specific markers conjugated to fluorescent phycoerythrin (PE) (peak excitation: 495; emission: 575 nm) (Table 7-1). The excitation sources were 488 and 633 nm.

Table 7-1 Target cell in lysed peripheral blood samples, excluding erythrocytes and platelets

CD Marker	Target Cell
<b>CD14</b> <sup>178</sup>	Monocytes
	Macrophages
<b>CD117 (cKit)</b> <sup>179</sup>	Hematopoietic stem cells (HSC)
	Multipotent progenitors (MPP)
	Mast cells
	Common myeloid progenitors (CMP)
<b>CD34</b> <sup>180</sup>	Hematopoietic stem cells (HSC)
	Mast cells
<b>CD44</b> <sup>181</sup>	Pan-leukocyte
<b>CD10</b> <sup>182</sup>	PreB cells
	PreT cells
	Granulocytes

The PE gate was established using an isotype antibody missing the fluorophore and excluded all but 0.085% of detected cells. This value approximated the abundance of green autofluorescent cells. The red autofluorescent intensity

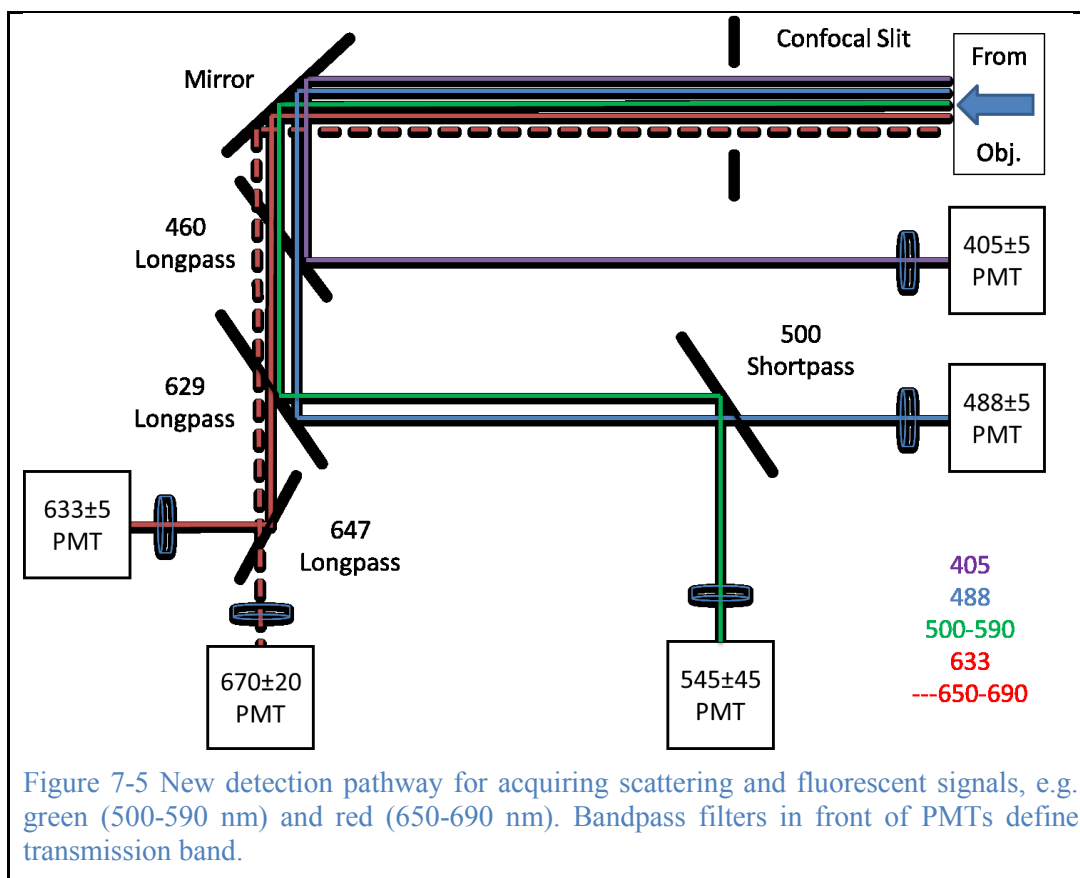
gate was established using an unstained sample and excluded all but 0.112±0.049% of detected cells across all samples. Table 7-2 includes the total number of cells detected and percentages that were positive for a (1) specific antibody; (2) red autofluorescent; (3) both antibody affinity and autofluorescent; (4) overlap within PE<sup>+</sup> population; and (5) overlap within autofluorescent population.

Table 7-2 Targeted antibody and red autofluorescence results.

	Cell Type	CD14		CD117		CD34		CD44		CD10	
	N (Cells)	38266	%N	40201	%N	41101	%N	38686	%N	20258	%N
1	PE <sup>+</sup>	64	0.167	19	0.047	88	0.214	38627	99.847	42	0.207
2	Red Autoflr	33	0.086	32	0.080	23	0.056	61	0.158	37	0.183
3	PE <sup>+</sup> /Autoflr	14	0.037	7	0.017	8	0.019	61	0.158	14	0.069
4	$\% \frac{\text{PE}^+/\text{Autoflr}}{\text{PE}^+}$	21.9		36.8		9.1		0.2		33.3	
5	$\% \frac{\text{PE}^+/\text{Autoflr}}{\text{Autoflr}}$	42.4		21.9		34.8		100.0		37.8	

Hematopoietic stem cells, myeloid progenitor cells, and differentiated cells were positive for red autofluorescence in non-cancerous human blood. Given these relative abundances, a future direction would be to investigate differences of the various red autofluorescent cell population concentrations in cancer patient blood. Reported by Hwu et al., red autofluorescent cell concentrations in circulation indicated an immune response and served as prognostic indicators of secondary metastasis development<sup>61</sup>. The specific cell identities (e.g. type of granulocytes or mononuclear) of upregulated cells in circulation would inform potential immunotherapy strategies to optimize a beneficial immune response. Future characterization directions include narrower identification schemes with anti-CD antibody combinations and cell sorting.

The detection pathway on the custom flow cytometer was improved to detect both red (650-690 nm) and green (500-590 nm) fluorescence signal (Figure 7-5). This improvement allows for two-color emission detection that would be useful in correlating fluorescently conjugated antibody signals with autofluorescence emission.



In addition to increasing sampling rate from 25 to 100 kHz, the new data acquisition (DAQ) board (National Instruments, USB-6341) integrates with LabView (National Instruments) for enhanced real-time monitoring capabilities. By monitoring the baseline in each PMT channel, the operator is able to empirically detect changes in flow rate that indicate clog formation within the microfluidic channel that adversely affect consistent scattering intensity acquisition.

## 7.7 Concluding Remarks

The confocal flow cytometry approach to cancer cell enumeration and light scattering characterization was useful in both in vitro method development and animal blood sample assessment. Fluorescence emission and backscattering intensity acquired by flowing cell suspensions in  $30 \times 30 \mu\text{m}^2$  microfluidic channels were the basis for cell type discrimination. The three interrogative wavelengths were 405, 488, and 633 nm.

Cultured cancer cells were significantly different from isolated mononuclear cells with encouragingly high sensitivity and specificity values of 92.7 and 82.8%, respectively. However, due to similarities in scattering properties between cancer cells and granulocytes, sensitivity and specificity values decreased to 42.9 and 74.6%, respectively, when all three cell populations were compared, e.g. cancer cells, mononuclear cells, and granulocytes. This same moderate classification performance was re-capitulated in a series of experiments where cancer cells were spiked into hemolysed leukocyte suspensions. Variability in classification performance was attributed multiple sources. Lysis efficiency, donor variability, and cell passaging conditions are inherent variables with limited potential for implementing engineering controls. However, advancements in real-time monitoring of flowing cell signal quality exemplify present standards in commercial flow cytometry and enhance control of day-to-day variations in system throughout.

Ammonium chloride hemolysis is not a recommended solitary blood sample-processing step due to the lack of discrimination among leukocyte sub-populations. Instead, the recommended cell enrichment objectives are maximal granulocyte- and erythrocyte-depletion and maximal retention of cancer cells. Recommended experiments include GFP<sup>+</sup> or fluorescently labelled cancer cells spiked into heparinized blood samples to determine the expected yield of cancer cells in each sedimentation layer of Ficoll-Paque density centrifugation.

Patient sample processing began at the conclusion of this work and was not presented within this thesis. Joe Lyons is continuing the project. The present approach involves analyzing the PBMC- and PMN-enriched layers via Ficoll-Paque density centrifugation. Normally distributed scattering property distributions obtained from erythrocyte-depleted leukocyte sub-populations optimizes the discrimination power of

MANOVA and linear discriminant analysis approaches. The purpose of these experiments is to validate that cancer cells that sediment within the upper PBMC- and lower PMN-enriched layers relative to Ficoll-Paque have distinct scattering properties despite their similarity in density. An enhanced enrichment approach would leverage the encouraging differences in light scattering properties of cultured cancer cells and PBMCs for clinical CTC detection and monitoring purposes.

The microfluidic platform is useful for assaying animal blood samples. Time-correlated fluorescence and scattering signals identified GFP<sup>+</sup> CTCs in metastatic mice. Preliminary results indicated that autofluorescent leukocytes and GFP<sup>+</sup> CTCs had unique scattering characteristics relative to non-fluorescent leukocytes, particularly in cumulative scattering intensity. The increased abundance of autofluorescent cells in anti-ADAM8-treated mice correlated with decreased metastatic burden and indicated a favorable immune response to cancer.

CTC enumeration remains a clinically relevant translational research thrust. Numerous ongoing clinical trials seek to identify CTCs as independent biomarkers of real-time cancer progression. Precise and accurate CTC detection platforms exemplify an improvement in diagnosis, prognosis, risk-adapted therapeutic strategies, and therapeutic monitoring.



## 8 References

1. Cristofanilli M, Budd GT, Ellis MJ, et al. Circulating tumor cells, disease progression, and survival in metastatic breast cancer. 2004;351:781-91.
2. Braun S, Vogl FD, Naume B, et al. A pooled analysis of bone marrow micrometastasis in breast cancer. The New England journal of medicine 2005;353:793-802.
3. Giuliano AE, Hawes D, Ballman KV, et al. Association of occult metastases in sentinel lymph nodes and bone marrow with survival among women with early-stage invasive breast cancer. JAMA : the journal of the American Medical Association 2011;306:385-93.
4. Siegel R, Ward E, Brawley O, Jemal A. Cancer statistics, 2011: the impact of eliminating socioeconomic and racial disparities on premature cancer deaths. CA: a cancer journal for clinicians 2011;61:212-36.
5. Mehlen P, Puisieux A. Metastasis: a question of life or death. Nature reviews Cancer 2006;6:449-58.
6. Alix-Panabieres C, Schwarzenbach H, Pantel K. Circulating tumor cells and circulating tumor DNA. Annual review of medicine 2012;63:199-215.
7. TR A. A case of cancer in which cells similar to those in the tumours were seen in the blood after death. Aust Med J 1869;14:146-9.
8. Yu M, Stott S, Toner M, Maheswaran S, Haber DA. Circulating tumor cells: approaches to isolation and characterization. J Cell Biol 2011;192:373-82.
9. Mostert B, Sleijfer S, Foekens JA, Gratama JW. Circulating tumor cells (CTCs): detection methods and their clinical relevance in breast cancer. Cancer treatment reviews 2009;35:463-74.
10. Cristofanilli M, Hayes DF, Budd GT, et al. Circulating tumor cells: a novel prognostic factor for newly diagnosed metastatic breast cancer. 2005;23:1420-30.
11. Pachmann K, Camara O, Kavallaris A, et al. Monitoring the response of circulating epithelial tumor cells to adjuvant chemotherapy in breast cancer allows detection of patients at risk of early relapse. J Clin Oncol 2008;26:1208-15.
12. Moreno JG, Miller MC, Gross S, Allard WJ, Gomella LG, Terstappen LWMM. Circulating tumor cells predict survival in patients with metastatic prostate cancer. Urology 2005;65:713-8.
13. de Bono JS, Scher HI, Montgomery RB, et al. Circulating Tumor Cells Predict Survival Benefit from Treatment in Metastatic Castration-Resistant Prostate Cancer. Clin Cancer Res 2008;14:6302-9.
14. Cohen SJ, Punt CJ, Iannotti N, et al. Prognostic significance of circulating tumor cells in patients with metastatic colorectal cancer. Annals of oncology : official journal of the European Society for Medical Oncology / ESMO 2009;20:1223-9.

15. Allard WJ, Matera J, Miller MC, et al. Tumor cells circulate in the peripheral blood of all major carcinomas but not in healthy subjects or patients with nonmalignant diseases. *Clin Cancer Res* 2004;10:6897-904.
16. Balic M, Lin H, Williams A, Datar RH, Cote RJ. Progress in circulating tumor cell capture and analysis: implications for cancer management. Expert review of molecular diagnostics 2012;12:303-12.
17. Riethdorf S, Fritsche H, Muller V, et al. Detection of circulating tumor cells in peripheral blood of patients with metastatic breast cancer: a validation study of the CellSearch system. *Clin Cancer Res* 2007;13:920-8.
18. Cohen SJ, Punt CJ, Iannotti N, et al. Relationship of circulating tumor cells to tumor response, progression-free survival, and overall survival in patients with metastatic colorectal cancer. *J Clin Oncol* 2008;26:3213-21.
19. Danila DC, Heller G, Gignac GA, et al. Circulating tumor cell number and prognosis in progressive castration-resistant prostate cancer. *Clin Cancer Res* 2007;13:7053-8.
20. Nole F, Munzone E, Zorzino L, et al. Variation of circulating tumor cell levels during treatment of metastatic breast cancer: prognostic and therapeutic implications. *Annals of oncology : official journal of the European Society for Medical Oncology / ESMO* 2008;19:891-7.
21. Hayes DF. A clinician's perspective on metastatic breast cancer: many diseases—we need to understand the biology. In: *Eur Breast Cancer Conf*; 2012 Mar. 21-24; Vienna, Austria; 2012.
22. Riethdorf S, Muller V, Zhang L, et al. Detection and HER2 expression of circulating tumor cells: prospective monitoring in breast cancer patients treated in the neoadjuvant GeparQuattro trial. *Clin Cancer Res* 2010;16:2634-45.
23. Nagrath S, Sequist LV, Maheswaran S, et al. Isolation of rare circulating tumour cells in cancer patients by microchip technology. *Nature* 2007;450:1235-U10.
24. Maheswaran S, Sequist LV, Nagrath S, et al. Detection of mutations in EGFR in circulating lung-cancer cells. *New Engl J Med* 2008;359:366-77.
25. Stott SL, Lee RJ, Nagrath S, et al. Isolation and Characterization of Circulating Tumor Cells from Patients with Localized and Metastatic Prostate Cancer. *Sci Transl Med* 2010;2.
26. Greiner C, Hunter M, Huang P, Rius F, Georgakoudi I. Confocal backscattering spectroscopy for leukemic and normal blood cell discrimination. *Cytometry Part A : the journal of the International Society for Analytical Cytology* 2011;79:866-73.
27. Chowdhury HH, Grilc S, Zorec R. Correlated ATP-induced changes in membrane area and membrane conductance in single rat adipocytes. *Annals of the New York Academy of Sciences* 2005;1048:281-6.

28. Gertler R, Rosenberg R, Fuehrer K, Dahm M, Nekarda H, Siewert JR. Detection of circulating tumor cells in blood using an optimized density gradient centrifugation. Recent results in cancer research Fortschritte der Krebsforschung Progres dans les recherches sur le cancer 2003;162:149-55.
29. Tan SJ, Lakshmi RL, Chen P, Lim WT, Yobas L, Lim CT. Versatile label free biochip for the detection of circulating tumor cells from peripheral blood in cancer patients. Biosensors & bioelectronics 2010;26:1701-5.
30. Moon HS, Kwon K, Kim SI, et al. Continuous separation of breast cancer cells from blood samples using multi-orifice flow fractionation (MOFF) and dielectrophoresis (DEP). Lab on a chip 2011;11:1118-25.
31. Pachmann K, Clement JH, Schneider CP, et al. Standardized quantification of circulating peripheral tumor cells from lung and breast cancer. Clin Chem Lab Med 2005;43:617-27.
32. Biocoll-Separating Solution, density 1.077 g/ml. 2014. (Accessed December 1, 2014, at <http://www.x-zell.co.th/product.php?productid=39574>.)
33. Vona G, Sabile A, Louha M, et al. Isolation by size of epithelial tumor cells : a new method for the immunomorphological and molecular characterization of circulating tumor cells. The American journal of pathology 2000;156:57-63.
34. Bhagat AA, Hou HW, Li LD, Lim CT, Han J. Pinched flow coupled shear-modulated inertial microfluidics for high-throughput rare blood cell separation. Lab on a chip 2011;11:1870-8.
35. Marrinucci D, Bethel K, Bruce RH, et al. Case study of the morphologic variation of circulating tumor cells. Human pathology 2007;38:514-9.
36. Gascoyne PR, Noshari J, Anderson TJ, Becker FF. Isolation of rare cells from cell mixtures by dielectrophoresis. Electrophoresis 2009;30:1388-98.
37. Krivacic RT, Ladanyi A, Curry DN, et al. A rare-cell detector for cancer. P Natl Acad Sci USA 2004;101:10501-4.
38. Ludwig JA, Weinstein JN. Biomarkers in cancer staging, prognosis and treatment selection. Nature reviews Cancer 2005;5:845-56.
39. Stott SL, Hsu CH, Tsukrov DI, et al. Isolation of circulating tumor cells using a microvortex-generating herringbone-chip. Proc Natl Acad Sci U S A 2010;107:18392-7.
40. Talasaz AH, Powell AA, Huber DE, et al. Isolating highly enriched populations of circulating epithelial cells and other rare cells from blood using a magnetic sweeper device. Proc Natl Acad Sci U S A 2009;106:3970-5.
41. Pachmann K, Camara O, Kavallaris A, et al. Monitoring the response of circulating epithelial tumor cells to adjuvant chemotherapy in breast cancer allows detection of patients at risk of early relapse. J Clin Oncol 2008;26:1208-15.

42. Wang S, Owens GE, Tseng HR. Nano "fly paper" technology for the capture of circulating tumor cells. *Methods in molecular biology* 2011;726:141-50.
43. Tibbe AG, Miller MC, Terstappen LW. Statistical considerations for enumeration of circulating tumor cells. *Cytometry Part A : the journal of the International Society for Analytical Cytology* 2007;71:154-62.
44. Ligthart ST, Coumans FA, Bidard FC, et al. Circulating Tumor Cells Count and Morphological Features in Breast, Colorectal and Prostate Cancer. *PloS one* 2013;8:e67148.
45. Attard G, Swennenhuis JF, Olmos D, et al. Characterization of ERG, AR and PTEN gene status in circulating tumor cells from patients with castration-resistant prostate cancer. *Cancer research* 2009;69:2912-8.
46. Saliba AE, Saias L, Psychari E, et al. Microfluidic sorting and multimodal typing of cancer cells in self-assembled magnetic arrays. *Proc Natl Acad Sci U S A* 2010;107:14524-9.
47. Alix-Panabieres C, Vendrell JP, Slijper M, et al. Full-length cytokeratin-19 is released by human tumor cells: a potential role in metastatic progression of breast cancer. *Breast cancer research : BCR* 2009;11:R39.
48. Alix-Panabieres C, Vendrell JP, Pelle O, et al. Detection and characterization of putative metastatic precursor cells in cancer patients. *Clinical chemistry* 2007;53:537-9.
49. Lu J, Fan T, Zhao Q, et al. Isolation of circulating epithelial and tumor progenitor cells with an invasive phenotype from breast cancer patients. *International journal of cancer Journal international du cancer* 2010;126:669-83.
50. Muller V, Alix-Panabieres C, Pantel K. Insights into minimal residual disease in cancer patients: implications for anti-cancer therapies. *European journal of cancer* 2010;46:1189-97.
51. Paterlini-Brechot P, Benali NL. Circulating tumor cells (CTC) detection: clinical impact and future directions. *Cancer letters* 2007;253:180-204.
52. Shaw JA, Brown J, Coombes RC, et al. Circulating tumor cells and plasma DNA analysis in patients with indeterminate early or metastatic breast cancer. *Biomarkers in medicine* 2011;5:87-91.
53. Papadopoulou E, Davilas E, Sotiriou V, et al. Cell-free DNA and RNA in plasma as a new molecular marker for prostate and breast cancer. *Annals of the New York Academy of Sciences* 2006;1075:235-43.
54. Pantel K, Brakenhoff RH, Brandt B. Detection, clinical relevance and specific biological properties of disseminating tumour cells. *Nature reviews Cancer* 2008;8:329-40.
55. Novak J, Georgakoudi I, Wei X, Prossin A, Lin CP. In vivo flow cytometer for real-time detection and quantification of circulating cells. *Optics letters* 2004;29:77-9.

56. Boutrus S, Greiner C, Hwu D, et al. Portable two-color in vivo flow cytometer for real-time detection of fluorescently-labeled circulating cells. *Journal of biomedical optics* 2007;12:020507.
57. Sipkins DA, Wei X, Wu JW, et al. In vivo imaging of specialized bone marrow endothelial microdomains for tumour engraftment. *Nature* 2005;435:969-73.
58. He W, Wang H, Hartmann LC, Cheng JX, Low PS. In vivo quantitation of rare circulating tumor cells by multiphoton intravital flow cytometry. *Proc Natl Acad Sci U S A* 2007;104:11760-5.
59. Tkaczyk ER, Tkaczyk AH, Katnik S, et al. Extended cavity laser enhanced two-photon flow cytometry. *Journal of biomedical optics* 2008;13:041319.
60. Georgakoudi I, Solban N, Novak J, et al. In vivo flow cytometry: a new method for enumerating circulating cancer cells. *Cancer research* 2004;64:5044-7.
61. Hwu D, Boutrus S, Greiner C, DiMeo T, Kuperwasser C, Georgakoudi I. Assessment of the role of circulating breast cancer cells in tumor formation and metastatic potential using in vivo flow cytometry. *Journal of biomedical optics* 2011;16:040501.
62. Le TT, Huff TB, Cheng JX. Coherent anti-Stokes Raman scattering imaging of lipids in cancer metastasis. *BMC cancer* 2009;9:42.
63. Nedosekin DA, Juratli MA, Sarimollaoglu M, et al. Photoacoustic and photothermal detection of circulating tumor cells, bacteria and nanoparticles in cerebrospinal fluid in vivo and ex vivo. *Journal of biophotonics* 2013;6:523-33.
64. Zharov VP, Galanzha EI, Tuchin VV. Integrated photothermal flow cytometry in vivo. *Journal of biomedical optics* 2005;10:051502.
65. Zharov VP, Galanzha EI, Tuchin VV. Photothermal flow cytometry in vitro for detection and imaging of individual moving cells. *Cytometry Part A : the journal of the International Society for Analytical Cytology* 2007;71:191-206.
66. Galanzha EI, Shashkov EV, Spring PM, Suen JY, Zharov VP. In vivo, noninvasive, label-free detection and eradication of circulating metastatic melanoma cells using two-color photoacoustic flow cytometry with a diode laser. *Cancer research* 2009;69:7926-34.
67. Collier T, Follen M, Malpica A, Richards-Kortum R. Sources of scattering in cervical tissue: determination of the scattering coefficient by confocal microscopy. *Applied optics* 2005;44:2072-81.
68. Golan L, Yeheskely-Hayon D, Minai L, Dann EJ, Yelin D. Noninvasive imaging of flowing blood cells using label-free spectrally encoded flow cytometry. *Biomedical optics express* 2012;3:1455-64.
69. Rubart M. Two-photon microscopy of cells and tissue. *Circulation research* 2004;95:1154-66.

70. Georgakoudi I, Rice WL, Hronik-Tupaj M, Kaplan DL. Optical spectroscopy and imaging for the noninvasive evaluation of engineered tissues. *Tissue engineering Part B, Reviews* 2008;14:321-40.
71. Rajadhyaksha M, Anderson RR, Webb RH. Video-rate confocal scanning laser microscope for imaging human tissues in vivo. *Applied optics* 1999;38:2105-15.
72. Zettergren E, Swamy T, Runnels J, Lin CP, Niedere M. Tomographic sensing and localization of fluorescently labeled circulating cells in mice in vivo. *Physics in medicine and biology* 2012;57:4627-41.
73. Georgakoudi I, Quinn KP. Optical imaging using endogenous contrast to assess metabolic state. *Annual review of biomedical engineering* 2012;14:351-67.
74. Greiner C, Hunter M, Rius F, Huang P, Georgakoudi I. Confocal backscattering-based detection of leukemic cells in flowing blood samples. *Cytometry Part A : the journal of the International Society for Analytical Cytology* 2011;79:874-83.
75. Forozan F, Veldman R, Ammerman CA, et al. Molecular cytogenetic analysis of 11 new breast cancer cell lines. *British journal of cancer* 1999;81:1328-34.
76. Boyle P. Triple-negative breast cancer: epidemiological considerations and recommendations. *Annals of oncology : official journal of the European Society for Medical Oncology / ESMO* 2012;23 Suppl 6:vi7-12.
77. Hanahan D, Weinberg RA. Hallmarks of cancer: the next generation. *Cell* 2011;144:646-74.
78. Harris AL. Hypoxia--a key regulatory factor in tumour growth. *Nature reviews Cancer* 2002;2:38-47.
79. Majmundar AJ, Wong WJ, Simon MC. Hypoxia-inducible factors and the response to hypoxic stress. *Molecular cell* 2010;40:294-309.
80. Adams RH, Alitalo K. Molecular regulation of angiogenesis and lymphangiogenesis. *Nature reviews Molecular cell biology* 2007;8:464-78.
81. Avraamides CJ, Garmy-Susini B, Varner JA. Integrins in angiogenesis and lymphangiogenesis. *Nature reviews Cancer* 2008;8:604-17.
82. Mierke CT. Role of the endothelium during tumor cell metastasis: is the endothelium a barrier or a promoter for cell invasion and metastasis? *Journal of biophysics* 2008;2008:183516.
83. Chambers AF, Groom AC, MacDonald IC. Dissemination and growth of cancer cells in metastatic sites. *Nature reviews Cancer* 2002;2:563-72.
84. Aguirre-Ghiso JA. Models, mechanisms and clinical evidence for cancer dormancy. *Nature reviews Cancer* 2007;7:834-46.
85. Pantel K, Alix-Panabieres C, Riethdorf S. Cancer micrometastases. *Nature reviews Clinical oncology* 2009;6:339-51.

86. Pantel K, Brakenhoff RH. Dissecting the metastatic cascade. *Nature reviews Cancer* 2004;4:448-56.
87. Koller G, Schlomann U, Golfi P, Ferdous T, Naus S, Bartsch JW. ADAM8/MS2/CD156, an emerging drug target in the treatment of inflammatory and invasive pathologies. *Current pharmaceutical design* 2009;15:2272-81.
88. Schlomann U, Wildeboer D, Webster A, et al. The metalloprotease disintegrin ADAM8. Processing by autocatalysis is required for proteolytic activity and cell adhesion. *The Journal of biological chemistry* 2002;277:48210-9.
89. Rao H, Lu G, Kajiya H, et al. Alpha9beta1: a novel osteoclast integrin that regulates osteoclast formation and function. *Journal of bone and mineral research : the official journal of the American Society for Bone and Mineral Research* 2006;21:1657-65.
90. Kelly K, Hutchinson G, Nebenius-Oosthuizen D, et al. Metalloprotease-disintegrin ADAM8: expression analysis and targeted deletion in mice. *Developmental dynamics : an official publication of the American Association of Anatomists* 2005;232:221-31.
91. Richens J, Fairclough L, Ghaemmaghani AM, Mahdavi J, Shakib F, Sewell HF. The detection of ADAM8 protein on cells of the human immune system and the demonstration of its expression on peripheral blood B cells, dendritic cells and monocyte subsets. *Immunobiology* 2007;212:29-38.
92. Yoshiyama K, Higuchi Y, Kataoka M, Matsuura K, Yamamoto S. CD156 (human ADAM8): expression, primary amino acid sequence, and gene location. *Genomics* 1997;41:56-62.
93. Romagnoli M, Mineva ND, Polmear M, et al. ADAM8 expression in invasive breast cancer promotes tumor dissemination and metastasis. *EMBO molecular medicine* 2013.
94. Young B. *Wheater's functional histology : a text and colour atlas*. 5th ed. Edinburgh?: Churchill Livingstone/Elsevier; 2006.
95. Roggan A, Friebel M, Do Rschel K, Hahn A, Müller G. Optical Properties of Circulating Human Blood in the Wavelength Range 400-2500 nm. *Journal of biomedical optics* 1999;4:36-46.
96. Darzynkiewicz ZR, M; Tanke, H.J., ed. *Cytometry: New Developments*. 4th ed. London, UK: Elsevier Academic Press; 2004.
97. Young B. *Wheater's functional histology a text and colour atlas*. In. 5th ed. Edinburgh?: Churchill Livingstone/Elsevier;; 2006:1 online resource (x, 437 p.).
98. Janeway C, Murphy KP, Travers P, Walport M, Janeway C. *Janeway's immunobiology*. 7th ed. New York: Garland Science; 2008.
99. Brinkmann V, Reichard U, Goosmann C, et al. Neutrophil extracellular traps kill bacteria. *Science* 2004;303:1532-5.

100. Lee LY, Gu Q, Gleich GJ. Effects of human eosinophil granule-derived cationic proteins on C-fiber afferents in the rat lung. *Journal of applied physiology* 2001;91:1318-26.
101. Nakanishi K. Basophils as APC in Th2 response in allergic inflammation and parasite infection. *Current opinion in immunology* 2010;22:814-20.
102. Dranoff G. Cytokines in cancer pathogenesis and cancer therapy. *Nature reviews Cancer* 2004;4:11-22.
103. Tuchin VV. *Advanced optical flow cytometry : methods and disease diagnoses*. Weinheim: Wiley-VCH; 2011.
104. Baba AI, Catoi C. In: *Comparative Oncology*. Bucharest; 2007.
105. Bannasch P. Sequential cellular changes during chemical carcinogenesis. *Journal of cancer research and clinical oncology* 1984;108:11-22.
106. Balkwill F, Mantovani A. Inflammation and cancer: back to Virchow? 2001;357.
107. Vesely MD, Kershaw MH, Schreiber RD, Smyth MJ. Natural Innate and Adaptive Immunity to Cancer. *Annu Rev Immunol* 2011;29:235-71.
108. Vesely M, Kershaw M, Schreiber R, Smyth M. Natural Innate and Adaptive. 2011;29.
109. de Visser K, Eichten A, Coussens L. Paradoxical roles of the immune system during cancer development. 2006;6.
110. Ishigami S. Prognostic value of intratumoral natural killer cells in gastric carcinoma. 2000;88.
111. Coca S. The prognostic significance of intratumoral natural killer cells in patients with colorectal carcinoma. 1997;79.
112. Imada S, Shijubo N, Kojima H, Abe S. Mast cells correlate with angiogenesis and poor outcome in stage I lung adenocarcinoma. 2000;15.
113. Gallagher B, Wang Z, Schymura M, Kahn A, Fordyce E. Cancer incidence in New York State acquired immunodeficiency syndrome patients. 2001;154.
114. Haagsma E. Increased cancer risk after liver transplantation: a population-based study. 2001;34.
115. Finke J. Where have all the T cells gone? Mechanisms of immune evasion by tumors. 1999;20.
116. Curiel T. Specific recruitment of regulatory T cells in ovarian carcinoma fosters immune privilege and predicts reduced survival. 2004;10.
117. Serafini P. Derangement of immune responses by myeloid suppressor cells. 2004;53.
118. Weiner LM, Surana R, Wang S. Monoclonal antibodies: versatile platforms for cancer immunotherapy. *Nature reviews Immunology* 2010;10:317-27.



119. Plosker GL. Sipuleucel-T: in metastatic castration-resistant prostate cancer. *Drugs* 2011;71:101-8.
120. Bass M, Optical Society of America. Handbook of optics. 2nd ed. New York: McGraw-Hill; 1995.
121. Bass M, Mahajan VN. Handbook of optics. Volume I, Geometrical and physical optics, polarized light, components and instruments. In. 3rd ed. New York: McGraw-Hill;; 2010:1 online resource ( v. (various pagings)).
122. Hulst HCvd. Light scattering by small particles. New York,: Wiley; 1957.
123. Dunn A, RichardsKortum R. Three-dimensional computation of light scattering from cells. *Ieee J Sel Top Quant* 1996;2:898-905.
124. Mourant JR, Freyer JP, Hielscher AH, Eick AA, Shen D, Johnson TM. Mechanisms of light scattering from biological cells relevant to noninvasive optical-tissue diagnostics. *Applied optics* 1998;37:3586-93.
125. Wilson JD, Cottrell WJ, Foster TH. Index-of-refraction-dependent subcellular light scattering observed with organelle-specific dyes. *Journal of biomedical optics* 2007;12:014010.
126. Yurkin MA, Semyanov KA, Maltsev VP, Hoekstra AG. Discrimination of granulocyte subtypes from light scattering: theoretical analysis using a granulated sphere model. *Optics express* 2007;15:16561-80.
127. Mourant JR, Johnson TM, Carpenter S, Guerra A, Aida T, Freyer JP. Polarized angular dependent spectroscopy of epithelial cells and epithelial cell nuclei to determine the size scale of scattering structures. *Journal of biomedical optics* 2002;7:378-87.
128. Ruban GI, Kosmacheva SM, Goncharova NV, Van Bockstaele D, Loiko VA. Investigation of morphometric parameters for granulocytes and lymphocytes as applied to a solution of direct and inverse light-scattering problems. *Journal of biomedical optics* 2007;12:044017.
129. Metcalf WK, Metcalf NF, Gould RN. Lymphocyte cytoplasmic refractive index (LCRI). *Antibiotics and chemotherapy* 1978;22:149-54.
130. Zharinov A, Tarasov P, Shvalov A, Semyanov K, van Bockstaele DR, Maltsev V. A study of light scattering of mononuclear blood cells with scanning flow cytometry. *J Quant Spectrosc Ra* 2006;102:121-8.
131. Ost V, Neukammer J, Rinneberg H. Flow cytometric differentiation of erythrocytes and leukocytes in dilute whole blood by light scattering. *Cytometry* 1998;32:191-7.
132. Backman V. Polarized Light Scattering Spectroscopy for Quantitative Measurement of Epithelial Cellular Structures. 1999;5.
133. Gouesbet G, Gréhan G. Generalized Lorenz-Mie Theories. In. Berlin, Heidelberg: Springer; 2011:310.

134. MiePlot. 2013. (Accessed October 20, 2013, at <http://www.philiplaven.com/mieplot.htm>.)
135. Mullaney PF, Van Dilla MA, Coulter JR, Dean PN. Cell sizing: a light scattering photometer for rapid volume determination. *The Review of scientific instruments* 1969;40:1029-32.
136. Kowaltowski AJ. Effect of Bcl-2 Overexpression on Mitochondrial Structure and Function. 2002;277.
137. Shapire HM. *Practical Flow Cytometry*: Wiley; 2003.
138. Mourant JR, Hielscher AH, Eick AA, Johnson TM, Freyer JP. Evidence of intrinsic differences in the light scattering properties of tumorigenic and nontumorigenic cells. *Cancer* 1998;84:366-74.
139. Backman V, Gopal V, Kalashnikov M, et al. Measuring cellular structure at submicrometer scale with light scattering spectroscopy. *Ieee J Sel Top Quant* 2001;7:887-93.
140. Wax A, Yang C, Backman V, et al. Cellular organization and substructure measured using angle-resolved low-coherence interferometry. *Biophysical journal* 2002;82:2256-64.
141. Hunter M, Backman V, Popescu G, et al. Tissue self-affinity and polarized light scattering in the born approximation: a new model for precancer detection. *Physical review letters* 2006;97:138102.
142. Mujat C, Greiner C, Baldwin A, et al. Endogenous optical biomarkers of normal and human papillomavirus immortalized epithelial cells. *International journal of cancer Journal international du cancer* 2008;122:363-71.
143. Drezek R, Guillaud M, Collier T, et al. Light scattering from cervical cells throughout neoplastic progression: influence of nuclear morphology, DNA content, and chromatin texture. *Journal of biomedical optics* 2003;8:7-16.
144. Roy HK, Iversen P, Hart J, et al. Down-regulation of SNAIL suppresses MIN mouse tumorigenesis: modulation of apoptosis, proliferation, and fractal dimension. *Molecular cancer therapeutics* 2004;3:1159-65.
145. Chalut KJ, Ostrander JH, Giacomelli MG, Wax A. Light scattering measurements of subcellular structure provide noninvasive early detection of chemotherapy-induced apoptosis. *Cancer research* 2009;69:1199-204.
146. Einstein AJ, Wu HS, Gil J. Self-affinity and lacunarity of chromatin texture in benign and malignant breast epithelial cell nuclei. *Physical review letters* 1998;80:397-400.
147. Xylas J, Quinn KP, Hunter M, Georgakoudi I. Improved Fourier-based characterization of intracellular fractal features. *Optics express* 2012;20:23442-55.

148. Pawley JB. Handbook of biological confocal microscopy. 3rd ed. New York: Springer; 2006.
149. Georgakoudi I, Hunter M. Fluorescence Spectroscopy Lab Notes. In: Lab 3. Medford, MA: Tufts University; 2012.
150. Tsien R. The green fluorescent protein. 1998;67.
151. Kaneshiro ES, Wyder MA, Wu Y-P, Cushion MT. Reliability of calcein acetoxymethyl ester and ethidium homodimer or propidium iodide for viability assessment of microbes. Journal of Microbiological Methods 1993;17:1-16.
152. Calcein, AM (C3099). Life Technologies, 2013. (Accessed 20 October, 2013, at <http://www.lifetechnologies.com/order/catalog/product/C3099?ICID=search-product>.)
153. Weibel DB, Diluzio WR, Whitesides GM. Microfabrication meets microbiology. Nature reviews Microbiology 2007;5:209-18.
154. Niemeyer CM, Mirkin CA. Nanobiotechnology concepts, applications, and perspectives. In. 1st ed. Weinheim: Wiley-VCH; 2004:1 online resource (xxii, 469 p.).
155. Zhan Y-H, Kuo J-N. Dimensions and capillary effects of microfluidic channel for blood plasma separation. In: Nano/Micro Engineered and Molecular Systems (NEMS), 2012 7th IEEE International Conference on; 2012; Kyoto: IEEE; 2012. p. 607-10.
156. Klecka WR. Discriminant analysis. In: Quantitative applications in the social sciences 19. Newbury Park, Calif. ; London: SAGE; 1980:1 online resource (71 p.).
157. O'Brien PC. Robust Procedures for Testing Equality of Covariance Matrices. Biometrics 1992;48:819-27.
158. Green SB, Salkind NJ. Using SPSS for Windows and Macintosh : analyzing and understanding data. 5th ed. Upper Saddle River, N.J.: Pearson/Prentice Hall; 2008.
159. DISCRIMINANT Algorithms. IBM, 2011. (Accessed 01 November 2013, 2013, at [http://pic.dhe.ibm.com/infocenter/spssstat/v20r0m0/index.jsp?topic=%2Fcom.ibm.spss.statistics.help%2Falg\\_discriminant\\_classification.htm](http://pic.dhe.ibm.com/infocenter/spssstat/v20r0m0/index.jsp?topic=%2Fcom.ibm.spss.statistics.help%2Falg_discriminant_classification.htm).)
160. DasGupta S. Pillai's Trace Test. In: Encyclopedia of Biostatistics: John Wiley & Sons, Ltd; 2005.
161. Cooley WW, Lohnes PR. Multivariate data analysis. New York;: Wiley; 1971.
162. Marshall GF, Stutz GE. Handbook of optical and laser scanning. 2nd ed. Boca Raton, FL: CRC Press; 2012.
163. Greiner C. Light Scattering Flow Cytometry for the Minimally Invasive Quantification of Circulating Leukemic Cells. Boston, MA: Tufts University; 2010.
164. Kuperwasser C, Dessain S, Bierbaum BE, et al. A mouse model of human breast cancer metastasis to human bone. Cancer research 2005;65:6130-8.

165. Yang X, Forouzan O, Burns JM, Shevkoplyas SS. Traffic of leukocytes in microfluidic channels with rectangular and rounded cross-sections. *Lab on a chip* 2011;11:3231-40.
166. Peters CE, Woodside SM, Eaves AC. Isolation of subsets of immune cells. *Methods in molecular biology* 2005;302:95-116.
167. Anderson TW. An introduction to multivariate statistical analysis. 2nd ed. New York: Wiley; 1984.
168. Kwant-Mitchell A, Ashkar AA, Rosenthal KL. Mucosal innate and adaptive immune responses against herpes simplex virus type 2 in a humanized mouse model. *Journal of virology* 2009;83:10664-76.
169. Wang X, Belguise K, Kersual N, et al. Oestrogen signalling inhibits invasive phenotype by repressing RelB and its target BCL2. *Nature cell biology* 2007;9:470-8.
170. Laboratory J. Physiological Data Summary – NOD.CB17-Prkdcscid/J (001303) In: Laboratory J, ed. Online; 2007.
171. Burns JM, Yang X, Forouzan O, Sosa JM, Shevkoplyas SS. Artificial microvascular network: a new tool for measuring rheologic properties of stored red blood cells. *Transfusion* 2012;52:1010-23.
172. Forouzan O, Burns JM, Robichaux JL, Murfee WL, Shevkoplyas SS. Passive recruitment of circulating leukocytes into capillary sprouts from existing capillaries in a microfluidic system. *Lab on a chip* 2011;11:1924-32.
173. Monici M, Pratesi R, Bernabei PA, et al. Natural fluorescence of white blood cells: spectroscopic and imaging study. *Journal of photochemistry and photobiology B, Biology* 1995;30:29-37.
174. Heintzelman DL, Lotan R, Richards-Kortum RR. Characterization of the autofluorescence of polymorphonuclear leukocytes, mononuclear leukocytes and cervical epithelial cancer cells for improved spectroscopic discrimination of inflammation from dysplasia. *Photochemistry and photobiology* 2000;71:327-32.
175. Xiao L, Liao X, Lin L, Huang H, Chen Y, Li B. Autofluorescence characteristics of human leukemia cells and mononuclear cells. In; 2010; 2010. p. 78452G-G-6.
176. Bradfute SB, Graubert TA, Goodell MA. Roles of Sca-1 in hematopoietic stem/progenitor cell function. *Experimental hematology* 2005;33:836-43.
177. Shaw JP, Basch R, Shamamian P. Hematopoietic stem cells and endothelial cell precursors express Tie-2, CD31 and CD45. *Blood cells, molecules & diseases* 2004;32:168-75.
178. Wright SD, Ramos RA, Tobias PS, Ulevitch RJ, Mathison JC. CD14, a receptor for complexes of lipopolysaccharide (LPS) and LPS binding protein. *Science* 1990;249:1431-3.

179. Hirota S, Isozaki K, Moriyama Y, et al. Gain-of-function mutations of c-kit in human gastrointestinal stromal tumors. *Science* 1998;279:577-80.
180. Mackie AR, Losordo DW. CD34-positive stem cells: in the treatment of heart and vascular disease in human beings. *Texas Heart Institute journal / from the Texas Heart Institute of St Luke's Episcopal Hospital, Texas Children's Hospital* 2011;38:474-85.
181. Hiraga T, Ito S, Nakamura H. Cancer stem-like cell marker CD44 promotes bone metastases by enhancing tumorigenicity, cell motility, and hyaluronan production. *Cancer research* 2013;73:4112-22.
182. Bilalovic N, Sandstad B, Golouh R, Nesland JM, Selak I, Torlakovic EE. CD10 protein expression in tumor and stromal cells of malignant melanoma is associated with tumor progression. *Modern pathology : an official journal of the United States and Canadian Academy of Pathology, Inc* 2004;17:1251-8.
183. Klecka WR. Discriminant analysis. Beverly Hills, Calif.: Sage Publications; 1980.
184. Tatsuoka MM. Multivariate analysis; techniques for educational and psychological research. New York,: Wiley; 1971.

## 9 Appendix

### 9.1 Chapter: Background

#### 9.1.1 Microfluidic Device Fabrication

#### Polydimethylsiloxane (PDMS) on SU-8 Mold

##### Standard Operating Procedure

(Modified by Michael Polmear from SOP provided by Prof. Robert White, Mechanical Engineering Dept.)

The microfluidic devices used in this work were created using soft lithography and fusion bonding techniques. This procedure begins with master fabrication that was performed at 200 Boston Ave. under the direction of Professor Robert White. Upon completion and passivation of the master mold, the procedure outlines the device fabrication steps using PDMS soft lithography.

##### 1. SU-B Master fabrication

The SU8 molds were manufactured at 200 Boston Ave. Two wafers were developed. Both starting substrates were <100> oriented, 100 mm diameter, 0.50-0.55 mm thick, single side polished silicon wafers. SU8-2025 spun on at 500 rpm for 10 seconds followed by 3000 rpm for 30 seconds. Softbake was three minutes at 80°C, six minutes at 110°C on hotplates. Exposure was 30 seconds at 20 mW cm<sup>-2</sup> (I-line intensity) with short pass UV filter. Post exposure bake was one minute at 75°C and six minutes at 105°C hotplates. Develop time was 7-10 minutes in SU8 developer (PM Acetate), followed by rinse with isopropyl alcohol (IPA), second 30-second develop in SU8 developer, rinse with IPA, blow dry. Then wafers were silanized using a few drops of tridecafluoro-1,1,2,2-tetrahydrooctyl trichlorosilane in a vacuum desiccator for two hours.

##### Measured Features

*SU8 thickness for channel height:*

- 7 min develop wafer: near center=26.0 microns, near edge= 32.1 microns
- 10 min develop wafer: near center=24.7 microns, near edge=33.0 microns

*Channel width (near wafer center) for channel width:*

- 7 min develop wafer: 22 microns
- 10 min develop wafer: 26 microns

##### 2. Material Requirements

###### 2.1. Equipment:

2.1.1.4" wafer tweezers, polystyrene Petri dish, plastic dish (Corning dish), plastic spoon/pipette tip, plastic cup, razor blade, aluminum foil, plasma O<sub>2</sub> asher, scale, vacuum desiccator, hot plate/oven, glass slides

2.1.2.Device: See appendix for design of 30 um channel and list of material suppliers

- 2.1.3. Chemicals: PDMS, and silanizing agent (tridecafluoro-1,1,2,2-tetrahydrooctyl trichlorosilane), hexane/heptane (organic solvent)
  - 2.2. Hazards associated with chemicals:
    - 2.2.1. PDMS: May cause eye and skin irritation. May cause respiratory and digestive tract irritation.
    - 2.2.2. Silanizing Agent: Corrosive. Causes severe irritation and burns.
    - 2.2.3. Harmful if ingested, inhaled, or absorbed through the skin.
    - 2.2.4. Lachrymator: Reacts violently with water releasing hydrogen chloride (HCL). Incompatible with oxidizing agents, acids, alcohols, and bases.
  - 2.3. Engineering Controls: Conduct procedure in ventilated fume hood. Store bottles of chemicals (sealed tightly) in cabinets with secondary containment. Work area should contain an eye wash and safety shower.
  - 2.4. Personal Protective Equipment: Nitrile gloves, apron, and goggles.
  - 3. SU-8 Silanization – passivation of surfaces to aid release from PDMS**
    - 3.1. Using wafer tweezers, place the SU-8 mold wafer along with 2-3 drops (use pipette) of the silanizing agent in a Petri dish and put in vacuum desiccator.
    - 3.2. Attach the desiccator to a vacuum hose on the hood vacuum port. Open the faucet-style vacuum valve. Leave the wafer under vacuum for at least 1 hour.
- The following steps are routinely performed once the master mold is created**
- 4. Mix and Degas PDMS**
    - 4.1. Silicone raw material is very sticky. Tape a piece of aluminum foil down inside the fume hood to act as a disposable work space. Place a piece of foil on top of the scale as well.
    - 4.2. On scale place a plastic cup. Reset weight to zero. Into the cup, pour the PDMS base then the curing agent (B) so the components are in a 9:1 (base:curing agent) ratio. The first master requires a total of 100 g, so 90 g base and 10 g curing agent. Sylgard 184 (PDMS) material is in the 225 lab above the sink or on the shelves next to the sink. Subsequent molds (by only cutting out the devices need a total of 30 g (27 g base, 3 g curing))
    - 4.3. Mix well with a plastic spoon or pipette tip (mix until mixture is milky due to air bubbles).
    - 4.4. Place cup on a petri dish in the vacuum oven to catch any overflow (make sure that it's not reserved). Close outlet port, open vacuum port, and let be for ~ 1 hour. Make sure that the heat is OFF - power switch light should be off and internal thermometer should be room temperature (~25°C). Otherwise, the PDMS will cure rapidly. Make sure the PDMS mixture does not foam out of the container. When large bubbles form at the surface, vent vacuum to pop bubbles.
  - 5. Pour PDMS**
    - 5.1. Carefully pour the PDMS over the SU-8 master wafer
    - 5.2. Try to minimize introduction of bubbles. Pop any lingering bubbles with a needle.
    - 5.3. Cure PDMS:
      - 5.3.1. PDMS will cure without heating in ~24 hours.
      - 5.3.2. To decrease cure time, place the Petri dish onto a hot plate/oven for 1-2 hrs at 65°C or 45 mins-1.5 hrs at 100°C. (If using oven in Room 285 set at setting 3 for ~ 65°C, ~ 4.5 for ~ 100°C)
    - 5.4. After curing, the wafer is stable and may be stored for months if necessary.
  - 6. Remove Mold and Punch Inlet/Outlet Ports**
    - 6.1. Cut out devices with scalpel

- 6.2. Punch ports with 1.5 mm biopsy punch starting from the bottom (side of the channel). Be careful to not touch the bottom surface. This will result in the cleanest cut at channel surface.
- 6.3. Use scotch tape to remove debris from device surface
- 7. Clean Glass slides (not needed for pre-cleaned slides)**
  - 7.1. Wear glove and work under chemical hood.
  - 7.2. In 50 ml graduated glass, put ~ 10 mls of hexane or heptane (organic solvent). Label glass if necessary.
  - 7.3. Put glass slide in hexane using tweezers. Treat both sides of slide surface for ~ 30 sec- 1 min in hexane solution.
  - 7.4. Using tweezers, remove glass slide. Air dry surface (can blow air on surface for faster drying).
- 8. Oxidize Surfaces for Bonding**
  - 8.1. Place new glass slide and device with to-be-bonded sides facing up in plasma cleaner (Rm 221)
  - 8.2. Close door to plasma cleaner, plug in pump, turn on plasma cleaner, set frequency to medium setting.
  - 8.3. Wait for plasma generation (~2-7 mins). Once you see purple plasma, let ash for no longer than 1 min. Over-ashing should be avoided due to a reduction in bond strength.
  - 8.4. Unplug pump and turn off plasma cleaner
  - 8.5. Merge channel surface of the device with upward facing surface of a glass slide. The bonding appears as a bubble escaping from the interface as the two surfaces come into permanent contact.
  - 8.6. Enhance bonding by placing devices on 65°C plate for 2 hrs
- 9. Storage**
  - 9.1. Store PDMS components in the photoresist storage cabinet.
  - 9.2. Store silanizing agent in solvents storage cabinet.
- 10. Waste Disposal**
  - 10.1. Cups, spoons, Petri dish, and wipes with PDMS on go in biohazard waste container.
  - 10.2. There should not be any silanizing agent left over; it should have evaporated away. If it has not, allow it to evaporate away in the hood and dispose of the container in solvent/photoresist trash.
  - 10.3. Razor blades, broken glass or broken silicon waste goes in the “sharps” waste.
- 11. Accident Procedures**
  - 11.1. Contact: Read MSDS prior to working with any chemical to familiarize yourself with the symptoms of exposure and recommendations for treatment.
  - 11.2. Skin contact: Flush with water.
  - 11.3. Eye contact: Flush with copious amounts of water for 15 minutes.
  - 11.4. Ingestion: Do not induce vomiting. If conscious and alert, rinse mouth and drink 2-4 cups of milk or water.
  - 11.5. Inhalation: Remove to fresh air. Resuscitate if necessary.
  - 11.6. Spill:
    - 11.6.1. Any small spills should be wiped up immediately with wipes. Dispose the wipes in the photoresist waste container.
    - 11.6.2. In case of large spill that you are not comfortable cleaning up, evacuate the lab and contact the lab manager and/or safety office.

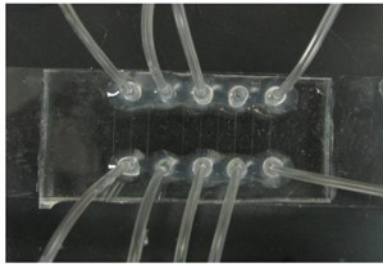
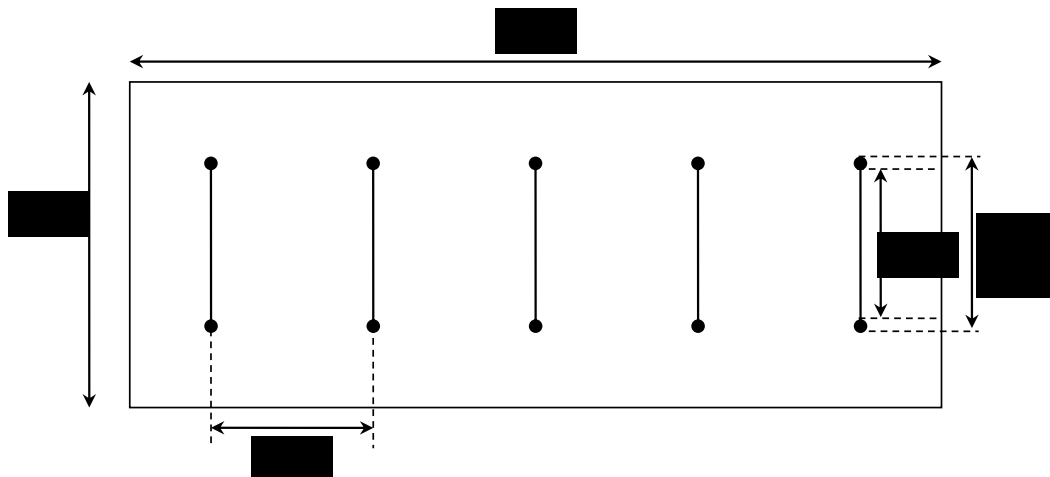
**For emergencies, call Tufts Emergency Services at x66911.**

## **Materials**

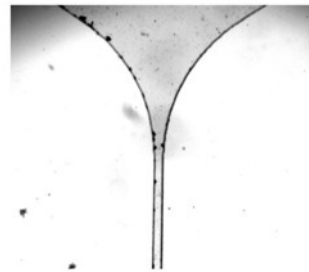


	P/N	Description
McMaster Carr	5114K11	50 ft. Beverage Clear Tygon PVC Tubing 1/16" ID, 1/8" OD, 1/32" Wall Thickness
McMaster Carr	75165A684	Type 304 SS Dispensing Needle 23 Gauge, .017" ID, .025" OD, 1/2" Long, packs of 50
Ellsworth	184 SIL ELAST KIT 0.5KG	Sylgard 184 kit

Current Channel dimensions: 30- $\mu$ m wide, 30- $\mu$ m high and 1-cm long with tapered inlet and outlet ports



Top view of PDMS microfluidic device with inlet and out tubings



Top view of tapered inlet or outlet port

### 9.1.2 Discriminant Analysis

Each discriminant variable has a global mean and variance defined by the entire data set and a local mean and variance within each group<sup>167</sup>. On a single case (e.g. cell) basis, the deviation between a particular case and the global mean of a given variable defines the dispersion of that variable. The total sum of squares and cross-products matrix (**T**) quantifies the global dispersion, defined by the individual cases and global means of the entire data set. The diagonal elements ( $i=j$ ) of the **T** matrix are the sum of the squares of the deviations from the global means. The off elements ( $i \neq j$ ) are the sum of the deviations on one variable multiplied by the deviation on another variable and indicate the covariance between two variables. The **T** matrix describes the variance of the entire data set. To define the variance within a group, the within-group sum of squares and cross-product matrix (**W**) is used. Rather than using the global mean, the value from each group is compared to the local mean of the defining group<sup>183</sup>.

If differences among group centroids exist, then the variance within a group will be less than that of the total. Therefore, the third and final comparison, the between-groups sum of squares and cross-products matrix (**B**) is the elemental difference between the **T** and **W** matrices. The **B** matrix is a final output of the MANOVA process and derived metrics quantify the extent of separation and overlap among the group centroids<sup>184</sup>.

Following characterization of the group and total spaces, discriminant analysis then derives a new variable, which is a linear combination of the discriminating variables. The driving property of the new variable is maximum centroid separation when the cases are plotted along the new axis. A schematic representation of this process is shown in Figure 9-1. For the simplified case of two groups and two discriminating variables,  $x$  and  $y$ , the groups predominantly overlap along the two intervals in the original axes. However, when the population distributions are compared along a different axis, then a greater degree of separation is possible.

The optimization problem maximizes between-groups variance and minimizes within-groups variance via a series of one-way analysis of variance tests<sup>183</sup>. The matrix  $\mathbf{W}^{-1}\mathbf{B}$  is the overall test statistic that indicates the maximum separation among different cell types (groups). By definition, multiplying a matrix by its eigenvalues results in a linear transformation of the matrix; therefore, coefficients of the discriminant function are the eigenvalues of corresponding eigenvectors of the matrix  $\mathbf{W}^{-1}\mathbf{B}$ . These linear combinations of discriminating variables are referred to as canonical discriminant functions. The number of eigenvalues of the eigenvector is equal to the number of discriminating variables<sup>167</sup>. The constraint is that within-group variance of the canonical variables is unity. Mean subtraction centers the cases about the origin in canonical space. Eigenvalues of the first eigenvector constitute the coefficients of the first canonical function, which accounts for the maximum amount of variability among the defined groups. Subsequent canonical functions contribute to discrimination power with diminishing extents<sup>167</sup>.

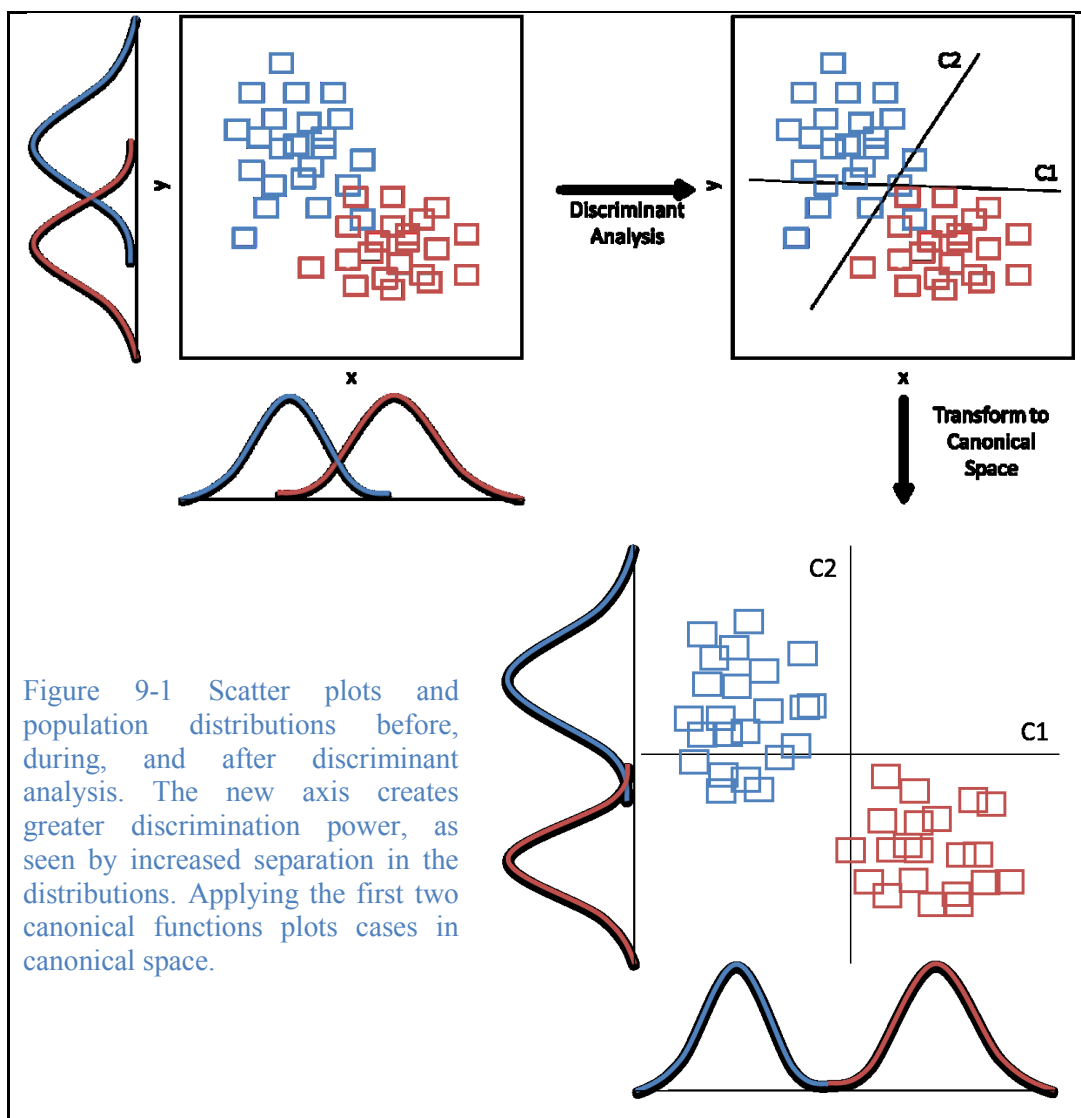


Figure 9-1 Scatter plots and population distributions before, during, and after discriminant analysis. The new axis creates greater discrimination power, as seen by increased separation in the distributions. Applying the first two canonical functions plots cases in canonical space.

Using increased fluorescence intensity as a unique standard for cancer cell identification, cross-validation analyses were conducted and their performance evaluated with the classification metrics found in Table 9-1.

Table 9-1 Contingency table and metrics of classification quality. PPV: positive predictive value; NPV: negative predictive value

		Classification Outcome		Metric
		Positive (Cancer/CTC)	Negative (Blood Cell)	
Condition Fluorescence Intensity (calcein <sup>+</sup> /GFP <sup>+</sup> )	Positive	True Positive (TP)	False Negative (FN, Type II error)	<i>Sensitivity</i> $= \frac{TP}{TP + FN}$
	Negative	False Positive (FP, Type I error)	True Negative (TN)	<i>Specificity</i> $= \frac{TN}{TN + FP}$
Metric		$PPV = \frac{TP}{TP + FP}$	$NPV = \frac{TN}{TN + FN}$	

Sensitivity is the probability of a correct classification of a positive condition, which would be correctly classifying a calcein<sup>+</sup> or GFP<sup>+</sup> cell as deriving from a separate population than fluorescence<sup>-</sup> blood cells. Specificity is the corollary and provides a probability of a correct classification of a negative condition. PPV is the precision rate of the method and provides a probability that the test is capable of detecting an existing condition; however, the metric is dependent on the prevalence of the condition. Therefore, the rarity of CTCs reduces the PPV. NPV indicates the probability that a negative test is accurate. However, like PPV, the NPV is reduced by a low prevalence. A contingency table and the previously described metrics apply to a test with an available “gold standard”, such as calcein or GFP fluorescence to identify positively an event for classification based on other variables, e.g. scattering characteristics.

## 9.2 Chapter: Flow Cytometry Instrumentation and Analytical Tools

### 9.2.1 Optical Components

<i>Illumination Path</i>			
Component	Description	Part Number	Supplier
405 nm laser	20 mW laser diode assembly	56ICS425	Melles Griot
488 nm laser	20 mW diode-pumped solid-state laser	PC13589	Spectra Physics
	Power supply	PC13302	
633 nm laser	20 mW HeNe	1144P	JDS Uniphase
	Power supply	1218-1	
Dichroic filter (D1)	Combines 488 and 633 nm	620DCXXR	Chroma
Dichroic filter (D2)	Combines 405, 488, and 633 nm	465DCXR	Chroma
Telescope lens (for 405 nm, L1-2)	2, plano-convex lenses, f=35mm	LA1027-A	Thorlabs
Polarizer (Pol1)	Input linear polarizer	03FPG021	Melles Griot
Iris	For alignment	SM2D25	Thorlabs
Cylindrical lens (Cyl Lens)	f=150mm	NT48-367	Edmund Optics
Achromatic lens (L3)	f=150mm	NT32-494	Edmund Optics

Beam splitter	R50/T50	50/50 Beam Splitter	Chroma
Mirrors (M1-5)		BB1-E02	Thorlabs
Objective	40x (NA=0.60)	LUCPLFLN	Olympus

<b><i>Trans-Illumination Imaging</i></b>			
<b>Component</b>	<b>Description</b>	<b>Part Number</b>	<b>Supplier</b>
Beam splitter	R50/T50	50/50 Beam Splitter	Chroma
Achromatic lens (L6)	f=150mm	NT32-494	Edmund Optics
LED	Green LED	LXHL-LM5C	Luxen V
CCD Camera	Watec monochrome camera	NT39-224	Edmund Optics

<b><i>Detection Path</i></b>			
<b>Component</b>	<b>Description</b>	<b>Part Number</b>	<b>Supplier</b>
Mirrors (M6-7)		BB1-E02	Thorlabs
Polarizer (Pol2)	Linear analyzer	03FPG021	Melles Griot
Achromatic lens (L4-5)	2, f=150mm	NT32-494	Edmund Optics
Mechanical slit (Confocal slit)	150 x 3000 $\mu\text{m}^2$	S15OR	Thorlabs
Dichroic filter (D3)	Split 405 from 488, 633, and 500-590 nm	460DCXRU	Chroma
Dichroic filter (D4)	Split 633 from 488 and 500-590 nm	629DXR	Chroma
Dichroic filter (D5)	Split 488 from 500-590 nm	500DXR	Chroma
Bandpass filter (BF1)	CWL=405, BW=10 nm	Z405/10x	Chroma
Bandpass filter (BF2)	CWL=488, BW=10 nm	Z488/10x	Chroma
Bandpass filter (BF3)	CWL=633, BW=10 nm	Z633/10x	Chroma
Bandpass filter (BF4)	CWL=545, BW=45 nm	545DF90	Omega
PMT (PMT1-4)	Detection area: 8x4 mm, WL range: 185-900 nm	R3896	Hamamatsu
PMT socket assembly		C6271	Hamamatsu
*CWL: center wavelength, BW: full-width at half-maximum bandwidth			

<b><i>Trans-Illumination Imaging</i></b>			
<b>Component</b>	<b>Description</b>	<b>Part Number</b>	<b>Supplier</b>
DAQ board	USB DAQ, 16-bit, 1 kHz total	DT9094	Data Translation
Computer			
Not included are optomechanical hardware			

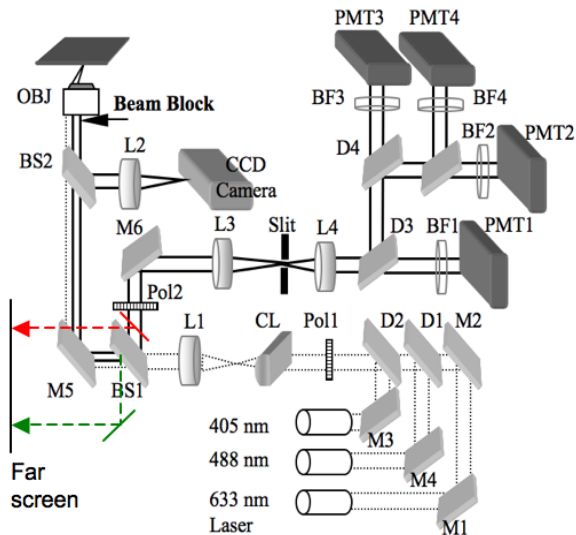
### 9.2.2 System Alignment Procedure

#### Protocol: Aligning Slit Illumination IVFC

##### Procedure

##### *Aligning critical parts of the system*

1. Warm up system. Turn on lasers for 15 minutes prior to continuing with alignment.
2. Using irises, determine that the incident beam is straight for the 405 laser first, then the 488 and 633 nm laser. To check, light from the 50/50 splitter is directed unto a mirror (shown in green in Figure 1) to project laser beams to a far screen. Check that the lasers beams are on top of each other.
3. Determine the achromat position relative to the objective. Beam in one direction is collimated while the other is focused. Adjust the achromat position along the rail -- correct position is when the collimated direction is as collimated as possible.
4. Adjust the cylindrical lens relative to the achromat. Similarly beam in on direction is collimated with the other is focused. Adjust the cylindrical lens position along the rail such that the collimated part of the beam is as collimated as possible. You may need to steer the beam and project it to a far enough screen to determine best position or remove M5 (mirror that steers beam up to objective).
5. Determine the focus position at the sample. Place a mirror upside down on a microscope slide. Make sure that the microscope collar is set for 1 mm slide. Place a mirror after the 50/50 beam splitter to project the image of the focus unto a far screen (shown in red in Figure 1). Check the z position of the 633 nm laser by blocking the 488 and 405 nm laser. Move the z micrometer up and down until you see a focused image of the 633 nm slit (again since half of beam is focused the other is collimated). Note the focus z position for the 633 nm laser. Check the z position of the 488 nm laser. Record the focus z position for the 488 nm laser – this is typically the same as the 633 nm laser. Check the z position of the 405 nm laser and record the position. If the z position is not the same as that from 488/633 lasers, return to the focus z position for the 488/633 and adjust the distance between the two lens in front of the 405 nm laser, until you see a focused image of the 405 nm slit in the far screen. Check that the 405 nm beam still follows the optic axis as the 488 and 633. Verify focus z position of 405 nm is the same as 488 and 633.
6. Determine the detection slit position relative to achromat lens in detection path. At the focus z position, the signal from the PMT should be maximize. Move the PMT position relative to the achromat until you get maximum signal from PMT.
7. Verify focus z position of lasers. Move the axial position above and below the focus. The PMT signal should go up and down accordingly in all three lasers for the same z position. If not check optic axis for all 3 lasers then verify focus z position for all 3 lasers again and re-adjust detection slit position if necessary.



Schematic of system. Note: light paths in red and green are used only during alignments and system checks.

### *System checks for Experiments*

1. Warm up system. Turn on lasers for 30 minutes prior to continuing with alignment.
2. Using irises, determine that the beam from all the lasers are following the optic axis starting with the 405 nm laser then the 488 and 633 nm lasers. To check, light from the 50/50 splitter is directed unto a mirror (shown in green in Figure 1) to project laser beams to a far screen. Check that the lasers beams are on top of each other.
3. Place a mirror upside down on microscope slide at the sample plane. Intercept light at red position in Figure 1 with a mirror to image slit in far field. Adjust z position until the slit at far screen is sharp (shown in red in Figure 1).
4. Verify z position with PMT.
5. Place microscope slide with dried 2.5  $\mu\text{m}$  beads at the sample plane. Intercept light in front of L3 with a card to image bead.
6. Steer the beam at the back of the objective for angled illumination.
  - a. Move M5 using micrometer until you just see the 633 nm slit being cropped (look at the projected image on top of the system) or
  - b. Move M5 using micrometer until you see the reflected light move outside the bead profile
  - c. Typically move the beam  $\sim 2.5$  mm laterally from straight or zero angle illumination position or

Block the back of the objective with beam block. Move beam block laterally until you see the specular reflection from the mirror being blocked.

### 9.2.3 Cell Suspension Flow Protocol

#### Protocol: Flow Measurement

##### Procedure

1. Isolate cells if necessary. Prepare cells according to desired concentration. Cells should be suspended in media with  $\leq 2\%$  FBS to minimize cell adhesion along the channel walls and/or cell clumping. Transfer cell sample for measurements into a 1.5 - 2 mL Eppendorf tube.
2. Warm-up the system. Turn on lasers for at least 15 minutes prior to measurement. Check alignment.
3. Obtain clean microfluidic device. Orient the device so that the slit length is oriented perpendicular to the flow direction. Tape device.
4. Adjust z position so that flow measurements are obtained at middle of channel (in axial direction). Determine the bottom of channel, which is the z position such that the slit is sharpest. With the micrometer, adjust the z position to  $\frac{1}{2}$  of channel height. For example, for 30 microns x 30 microns channel, flow measurements are typically obtained  $\sim 10 - 15$  microns above the slide.
5. Adjust lateral position so that measurements are obtained near the middle of the channel length, i.e. not by the inlet or outlet ports.
6. Place the cell sample in a post holder on the stage near the microfluidic device. Place inlet tubing in the sample, making sure the tubing is covered entirely with liquid to prevent bubbles from forming and entering the microfluidic channel.
7. Pre-fill inlet tubing with cell suspension and outlet tubing with filtered PBS to facilitate flow.
8. Connect outlet tubing to a syringe using a luer lock blunt needle. Carefully, pull liquid into the device by hand or using the pump at a higher flow rate than desired (which is required to cause enough pressure drop to draw the liquid into the channel). Once liquid enters the channel, place syringe in pump (if pulling by hand) then run pump at desired flow rate.
9. Wait for at least 20 minutes for the flow to stabilize before taking measurements.
10. Constantly mix cell solution to prevent clumping and to ensure homogenous cell solution. You may use magnetic stirrer to constantly mix the cell sample.

##### Notes:

- You may push the cell solution (reverse direction of flow) but it is harder to ensure that the cell solution is homogenous due to cell sedimentation.
- If using a magnetic stirrer, it may be necessary to use longer inlet tubing. Sample maybe placed in a small glass vial, such as a scintillation vial, instead of Eppendorf tubes.
- It is not recommended that channels be re-used, to minimize contamination. If channel must be re-used, clean the channel by flowing RPMI into the channel for 30 minutes at high flow rate using a clean syringe and needle.

### 9.2.4 Instructions for Individual Channel Threshold Approach in MATLAB

Data and instrumentation/experimental parameters from all experiments are organized by acquisition date and are located on ODDT: MichaelPolmear\FlowData

1. Flow experiment



- a. Yields four .dcf files – one from each PMT channel
- b. Convert .dcf files to .mat files using GUI
  - i. Access from ‘guide’ in MATLAB
  - ii. Lab computer: C:\MichaelPolmear\GUI from Derrick
    1. Start time: 0
    2. End time: Total number of seconds per run
    3. Smoothing: 1
    4. Size of Int: 10,000
    5. No. of Int: 250
  - iii. Output files are \_parameters and \_smoothed
    1. Smoothed is a misnomer because smoothing occurs later
2. Place the following .m files in a folder eg. “FlowMfiles”. The files are located on ODDT: Michael\Polmear\FlowMfiles
  1. run1file
  2. runall\_v2
  3. runall\_v3
  4. smoothfile\_sctfl\_v6
  5. smoothfile\_sctfl\_v7
  6. smoothfile\_sctfl\_1file
  7. peakrun\_auto\_sctfl5
  8. peakrun\_auto\_sctfl\_1file
  9. peakfindsf4
  10. photopeak
  11. multi\_peaksizesf4
  12. findcorrp\_k\_photosf
  13. cmbine\_width\_v3
  14. mean\_arclsr\_files\_btch
  15. normcells\_spec\_wflr\_v1
  16. testscattercloud
3. Put your experiment data in directory eg. sum092011
  - a. Ideally you should name your files as
    - i. “celltype#\_20xpar\_f405” for 405
    - ii. “celltype#\_20xpar\_f488” for 488
    - iii. “celltype#\_20xpar\_f633” for 633
    - iv. “celltype#\_20xpar\_fflr” for fluorescence
  - b. # pertains to the trial number, e.g. first 3 minutes is #1, 2<sup>nd</sup> 3 minutes of data is #2
  - c. For slit system, the objective is 40x but most of our measurements before that used the 20x. I hard-coded the filename in smoothfile\*.m file. Feel free to change this if you really want to match the name of the file to the objective used
  - d. .txt files to be included in data directory
    - i. cellnormalize
    - ii. file1
    - iii. filepar
    - iv. meanfiles
    - v. specfiles
    - vi. specnormalize
  - e. .mat files to be included in data directory
    - i. ph\_20xpar\_f405
    - ii. ph\_20xpar\_f488

- iii. `ph_20xpar_f633`
  - iv. `ph_20xpar_fflr`
    - 1. All must be same length as cell data
- f. .m files to be included in data directory
  - i. `calc_spec`
  - ii. `plt#script`, where # corresponds to the number of cell type to be plotted
- 4. To be able to run the mfiles from folder FlowMfiles
  - a. In Matlab, add FlowMfiles in the Matlab path by using “addpath” command, e.g. “addpath Z:\MikePolmear\FlowMfiles”
- 5. To test out threshold for 1 file in an experiment:
  - a. In Matlab type in “run1file”
    - i. % opens file1.txt which contains the file to open & threshold values for peak detection.
    - ii. Example: `mx 1 0.02 8 5 5 8 50 50 50 50`
    - iii. `mx`: cell type flowed, used in filename of saved data
    - iv. `1`: filename, e.g. first file for cell type
    - v. `0.02`: time sequence is analyzed in divided in this time for analysis in sec
    - vi. `8 5 5 8`: peak threshold for 405, 488, 633, Flr channels as determined by standard deviation increment
    - vii. `50 50 50 50`: ignore: intended for photodiode data that are no longer used
    - viii. Transfers information to next mfile
  - b. `smoothfile_sctfl_1file`
    - i. % opens files and smooths data; sampling freq is hard-coded; transfers data and threshold values to next `peakrun_auto_scfl_1file.m`. Output of `run1file.m` is “Correlated\_cellname#” which has all the peaks counted including correlated and uncorrelated peaks, time & widths of peaks.
  - c. `peakrun_auto_scfl_1file`
    - i. % calls `peakfindsf4.m` and `findcorrpk_photosf`. Concatenates peaks from each interval.
  - d. `peakfindsf4`
    - i. % calls `multi_peaksizesf4`
  - e. `multi_peaksizesf4`
    - i. % finds peaks within time interval above threshold based on mean and stdev. Mean is based on 95% of data (see variable “percent”). Outputs are peak time, height and fwhm.
  - f. `findcorrpk_photosf`
    - i. % finds correlated peaks from peaks counted
  - g. When you run `run1file`, you get a figure with threshold boundaries and peaks found at each time interval analyzed. Press enter to view next time interval result. Keep pressing until you viewed enough time interval to determine if threshold is OK. To stop, press Cntrl-C to Stop.
  - h. Adjust the threshold if necessary. Re-run `run1file` to check threshold again. Optimal method for determining threshold? Peaks above horizontal light blue circled in green.

6. Once you're satisfied with the threshold, you may run all the data for same cells taken at the same condition with the same threshold. You can now runall\_v2 analyze a batch of files. Type runall\_v2 on Matlab command line to run.
  - a. runall\_v2.m
    - i. %reads filepar.txt and must have threshold values that match those in file1.txt
  - b. smoothfile\_sctfl\_v6
    - i. % opens files and smooths data; sampling freq is hard-coded; transfers data and threshold values to next peakrun\_auto\_sctfl\_v6.m. Output of same as in 1 file version
  - c. peakrun\_auto\_sctfl5
    - i. % calls peakfindsf4.m and findcorrpk\_photosf. Concatenates peaks from each interval.
    - ii. Define time tolerance (tlrnce) in between peaks
      1. 8e-4 sec
  - d. peakfindsf4
    - i. % calls multi\_peaksizesf4
  - e. multi\_peaksizesf4
    - i. % finds peaks within time interval above threshold based on mean and stdev. Mean is based on 95% of data (see variable "percent"). Outputs are peak time, height and fwhm.
  - f. findcorrpk\_photosfn
    - i. % finds correlated peaks from peaks counted
  - g. Produces correlated .mat files for each data file trial
7. runall\_v2
  - a. Called files
    - i. smoothfile\_sctfl\_v6
      1. peakrun\_auto\_sctfl5
        - a. peakfindsf4
          - i. multi\_peaksizesf4
      2. findcorrpk\_photosfn
  - b. Original process: baseline subtraction (medium contribution)
  - c. Need to normalize to spectralon with normcells\_spec\_wflr\_v1 to generate denominator for normalization
8. runall\_v3
  - a. Called files
    - i. smoothfile\_sctfl\_v7
      1. peakrun\_auto\_sctfl5
        - a. peakfindsf4
          - i. multi\_peaksizesf4
        - b. findcorrpk\_photosfn
    - b. Baseline correction followed automatically by spectralon normalization
    - c. No need for normcells\_spec\_wflr\_v1
    - d. Must run mean\_arclsr\_files\_btch and calc\_spec.m first
  9. run cmbine\_wdth\_v3
    - a. % Program combines files together. Width threshold can be applied – used to remove wide widths that can be from bubbles. File output is named "Correlated\_wdth\_cellname\_all.mat"
    - b. User inputs:
      - i. Enter cell type:
      - ii. Enter first trial (t1):

- iii. Enter last trial (t2):
  - iv. Enter total time for each trial (sec):
  - v. Enter width threshold (sec):
    - 1. 1 sec for bubbles
  - vi. Enter percent for background
    - 1. E.g. 95 for 95%
  - c. Produces “Correlated\_wdth\_cellname\_all”
- 10. Run `plot_matrix_compile_07312012`
  - a. Produces 1, 2, 3 and 4  $\lambda$  matrices
    - i. Use these subpopulations for analysis if intensity values are final according to normalization requirements
    - ii. Change file to be loaded and prefix to the output files in the workspace
    - iii. Append threshold information to file name for bookkeeping purposes
    - iv. Otherwise, continue to `mean_arclsr_files_btch`
- 11. Run `export_workspace_07052012.m` to transfer length of subpopulations to Excel
  - a. Change file to be loaded
- 12. Run `ksdensity_FWHM_05212013.m` to visualize FWHM peak distribution of subpopulation of choice and obtain mean and standard deviation parameter of distribution for calculating flow rate in Excel
  - a. Change file to be loaded and specific subpopulation, i.e. 3 $\lambda$  or 4 $\lambda$
- 13. Run `mean_arclsr_files_btch`
  - a. Reads `meanfiles.txt`, which must match the number of spectralon files
  - b. Calculates the avg of each spectralon time trace
  - c. Produces `mean_spec#par`, where # is the file number
- 14. run `calc_spec.m`
  - a. Put this mfile in specific measurement data directory
  - b. % Opens avg of each spectralon time trace. Eventually concatenates the all the spectralon data to calculate single spectralon avg value at 405, 488 and 633. Name of avg spectralon files listed in `specfiles.txt` in measurement data directory. Includes the pwr factor taking into account difference in power used during spectralon and cell measurements.
  - c. You must change the following variable values:
    - i. `pwrcells` = power at sample during cell or bead measurements for 405, 488, and 633 nm wavelengths in  $\mu\text{W}$
    - ii. `pwrspec` = power at sample during spectralon measurements for 405, 488, and 633 nm wavelengths in  $\mu\text{W}$
    - iii. Also change the filename that spectralon data will be saved to
      - 1. For example, see last line in code: `save specpar_OD6 specpar mspecpar`
        - a. In this case filename w/ the avg spectralon data including pwr factor is saved as “`specpar_OD6.mat`” in current directory
- 15. run `normcells_spec_wflr_v1` → can put in mfile directory
  - a. % Normalizes cell data with spectralon data. Opens `cellnormalize.txt` and `specnormalize.txt` Note: `normcells_spec_wflr` uses data from “`Correlated_wdth_cellname_all.mat`”. Output file will be saved into one file “`celldata_spec.mat`” which contains all the spectralon normalized cell data. Data from this file is what you use for scatter or density plots
  - b. Example
    - i. `cellnormalize.txt` has the following lines

1. sum1315
  2. du4465
  - ii. specnormalize.txt has the following lines (based on step 7)
    1. specpar\_OD6
    2. specpar\_OD3
  - iii. \*\* In this example, sum1315 was taken with OD6 filter and du4465 was taken with OD3 filter. You must match the line number in the cellnormalize.txt with the corresponding power used for cell measurements relative to the spectralon in the specnormalize.txt file
16. Create your scattering figures either scatterplot or testscattercloud.m
- a. cherry\_histogram\_FACS.m
    - i. I usually make a script file within the directory that opens celldata\_spec.mat and calls testscattercloud so I have a record of figures I've ran.
    - ii. Example: sum1315 vs. lym vs grn data the script lines can look like this: %%%%%%%%%%
 

```
load celldata_spec.mat

Sctr = testscattercloud(lymspec(:,1), lymspec(:,2), sum1315spec(:,1),
sum1315spec(:,2),      grnspec(:,1),  grnspec(:,2),  250,250).
xlabel('405'); ylabel('488');

%%%%%%%%%%%%%
```

In the above:

lym = assigned color Red

sum1315 = assigned color Green

grn = assigned color Blue

If you want to assign color red to sum1315 you must put it in place of lymspec in the above example. If you only want to plot one cell type, you have to create zero arrays for the other 2 color.

#### Data Analysis Flow

- 1) Acquire data from cells and spectralon at same PMT gain setting
  - a) Output is ASCII
- 2) Measure power at sample and spectralon plane
  - a) Output is ASCII
- 3) Convert ASCII files to .mat files using Matlab GUI – no smoothing
- 4) Apply Butterworth filter (smooth) data
- 5) Calculate mean and standard deviation of lower *percent* of data (baseline)
- 6) Determine standard deviation threshold above base mean to identify peaks
- 7) Examine each channel in each trial individually
- 8) Find correlated and uncorrelated peaks among channels in single trial
- 9) Vertically concatenate correlated and uncorrelated peaks from batch
  - a) Outputs are peak center (s), peak intensity, and FWHM (s)
- 10) Calculate mean signal from individual spectralon trials
- 11) Calculate  $Power\ factor = \frac{power\ at\ cells}{power\ at\ spectralon}$

- 12) Multiply averages of each spectralon trial by the power factor
- 13) Calculate the average of each of these normalized values (mspecpar) over all trials
- 14) Divide smoothed peak intensity by averages from spectralon data –or–
- 15) Divide smoothed peak intensity by averages from bead data

### 9.3 Effect of Channel Depth Statistical Analysis - 10- $\mu$ m Window Centered on the Middle of the Channel

The purpose of this experiment was to assess the reproducibility of manually aligning the focal volume of the incident lasers to the middle of the channel and the variability within a small height range of the channel midpoint. Scattering intensities at the channel middle (in duplicate) and  $\pm 5 \mu\text{m}$  were acquired for calcein-labelled SUM159 flowing at a rate of  $3 \mu\text{L}\cdot\text{min}^{-1}$  at a concentration of  $50\text{E}4 \text{ cells}\cdot\text{mL}^{-1}$  in a  $30\times 30 \mu\text{m}^2$  channel. All tables were generated using SPSS and interpretations of key findings are provided beneath each table.

ID	N	Position ( $\mu\text{m}$ )
1	13651	0
2	12510	-5
3	12927	+5
4	12732	0

Interpretation: group identities, cell numbers, and positions for focal volume placements for channel depth analysis.

Group Statistics			
ID		Mean	Std. Deviation
1	CUM	0.677	1.025
	r405to488	0.441	0.229
	r405to633	1.571	9.841
	r488to633	3.884	15.350
2	CUM	0.697	1.241
	r405to488	0.586	0.342
	r405to633	1.971	1.272
	r488to633	3.723	2.388
3	CUM	0.767	1.248
	r405to488	0.367	0.215
	r405to633	1.108	2.056
	r488to633	3.225	6.218
4	CUM	0.691	1.076
	r405to488	0.439	0.210
	r405to633	1.706	5.121
	r488to633	4.128	10.947
Total	CUM	0.708	1.150
	r405to488	0.457	0.266
	r405to633	1.585	5.787
	r488to633	3.741	10.131

Interpretation: all means  $\pm \sigma$  overlapped, thus suggesting negligible differences in centroid characteristics within the four-dimensional discriminant space. Consistently higher standard deviation values for the 405/633 and 488/633 variables relative to cumulative peak intensity and 405/488 values indicated potential inequality of covariance matrices. Therefore, the next step was to consult the Pooled Within-Groups Matrices table.

Tests of Equality of Group Means					
	Wilks' Lambda	F	df1	df2	Sig.
CUM	.999	16.139	3	51816	.000
r405to488	.913	1651.328	3	51816	.000
r405to633	.997	49.793	3	51816	.000
r488to633	.999	18.301	3	51816	.000

Interpretation: The consistently high Wilks' Lambda values (near 1) suggested minimal variation in group means. The significant results ( $p < 0.0005$ , F-Test) were less meaningful than the Wilks' Lambda values due to the high number of assayed cells, as shown by the high number of degrees of freedom of the second component of the F statistic (df2). The first degrees of freedom value (df1) was one minus the number of groups, of which there were four in this analysis.

Pooled Within-Groups Matrices					
		CUM	r405to488	r405to633	r488to633
Covariance	CUM	1.322	-.008	.045	.118
	r405to488	-.008	.064	.049	-.134
	r405to633	.045	.049	33.400	56.766
	r488to633	.118	-.134	56.766	102.533

Interpretation: As noted in the Group Statistics table, the 405/633 and 488/633 variables had higher standard deviation values, which were reflected in the higher covariance values in this table. This result indicated that the 405/633 and 488/633 distributions among all groups had non-normal characteristics. Considering the large number of cells assayed, the effect of these non-normal characteristics were best understood by interpreting the canonical functions and classification results. In other words, a consistently small deviation from normality would still warrant using MANOVA to assess scattering property differences as a function of assay location within the channel.

### Summary of Canonical Discriminant Functions

Eigenvalues				
Function	Eigenvalue	% of Variance	Cumulative %	Canonical Correlation
1	.099	97.1	97.1	.301
2	.003	2.8	99.9	.054
3	.000	.1	100.0	.009

Interpretation: The first canonical function accounted for vast majority of observed variance (97.1%) but had minimal discrimination power, as demonstrated by a low canonical correlation ( $\ll 1$ ). The second and third discriminant functions had diminishing power.

Wilks' Lambda				
Test of Function(s)	Wilks' Lambda	Chi-square	df	Sig.
1 through 3	.907	5061.357	12	.000
2 through 3	.997	154.093	6	.000
3	1.000	4.659	2	.097

Interpretation: Wilks' lambda is a measure of how well each function separated cases into groups. It is equal to the proportion of the total variance in the discriminant scores not explained by differences among the groups. Smaller values of Wilks' lambda indicates greater discriminatory ability of the function. Although the associated chi-square test statistics were significant, the high Wilks' Lambda values ( $\sim 1$ ) indicated that the functions yielded a maximum of  $\sim 10\%$  ( $1 - 0.907$ ) variance among the group centroids.



<b>Standardized Canonical Discriminant Function Coefficients</b>			
	Function		
	1	2	3
CUM	-.025	-.482	.547
r405to488	.921	.323	-.140
r405to633	.756	-2.958	1.133
r488to633	-.651	3.446	-.317

Interpretation: Larger absolute values of coefficients corresponded to variables with greater discriminating ability. As noted in the previous Wilks' Lambda table, the first discriminant function was more powerful, albeit with minimal effect, than the other two functions. In the case of the first function, the ratio variables were weighted more heavily than the cumulative intensity value, thus suggesting that cumulative intensity did not vary throughout the assay window.

<b>Classification Function Coefficients</b>				
	id			
	1	2	3	4
CUM	.545	.573	.607	.555
r405to488	8.579	10.595	7.373	8.551
r405to633	-.823	-.701	-.797	-.821
r488to633	.504	.437	.482	.506
(Constant)	-3.797	-4.815	-3.309	-3.800

Interpretation: the classification functions were used to assign cases to groups. Each group had a separate function that yielded maximum coverage a given group's centroid and dispersion. The discriminant model assigned each cell during cross-validation to the group whose classification function obtained the highest score.

#### 9.4 Chapter: Light Scattering Measurements of Isolated Leukocyte Populations and In Vitro Breast Cancer Cells

The purposes of these experiments were to identify the backscattering space defined by the three interrogative wavelengths for mononuclear and granulocyte cells and to determine whether cancer cells scattered in a unique space. Discriminant variables were cumulative peak intensity (e.g. 405+488+633) and ratios of scattering intensities (e.g. 405/488, 405/633, and 488/633). Statistical tests were performed in SPSS.

The dates of data sets analyzed were:

PBMC: 03/28/2012, 05/16/2012, and 07/16/2012

SUM1315: 03/25/2012, 04/05/2012, and 04/18/2012

PMN: 05/16/2012, 07/16/2012, and 08/02/2012

#### 9.4.1 All Three Enriched Cell Populations – PBMC, PMN, and SUM1315

##### 9.4.1.1 MANOVA

##### General Linear Model

##### Between-Subjects Factors

	N
id 1: PBMC	61064
2: SUM1315	42565
3: PMN	119143

##### Descriptive Statistics

	id	Mean	Std. Deviation	N (cells)
CUM	1	2.91E-04	1.64E-04	61064
	2	1.54E-03	2.20E-03	42565
	3	1.32E-03	1.13E-03	119143
	Total	1.08E-03	1.36E-03	222772
r405to488	1	7.95E-01	2.58E-01	61064
	2	2.37E+00	1.65E+00	42565
	3	2.64E+00	7.49E-01	119143
	Total	2.08E+00	1.21E+00	222772
r405to633	1	5.43E-01	2.14E-01	61064
	2	3.45E+00	2.74E+00	42565
	3	3.49E+00	6.55E-01	119143
	Total	2.67E+00	1.84E+00	222772
r488to633	1	7.21E-01	3.00E-01	61064
	2	1.61E+00	1.03E+00	42565
	3	1.40E+00	3.95E-01	119143
	Total	1.26E+00	6.53E-01	222772

**Multivariate Tests**

Effect	Value	F	Hypothesis df	Error df	Sig.	Partial Eta Squared
Pillai's Trace	.682	28848.688	8.000	445534.000	.000	.341
id Wilks' Lambda	.335	40493.114	8.000	445532.000	.000	.421

Interpretation: The small test statistic values ( $\ll 1$ ) and large partial eta squared values ( $\gg 0$ ) suggested that differences among the four discriminant were of sufficient magnitude to discriminate separate cell populations. Pillai's trace is more conservative than Wilks' Lambda but still observed 42% variance among the three cell types.

**Tests of Between-Subjects Effects**

Source	Dependent Variable	Partial Eta Squared	Sig.
id	CUM	.130	.000
	r405to488	.431	.000
	r405to633	.505	.000
	r488to633	.267	.000

Interpretation: Higher partial eta squared values denoted variables with greater discrimination power; therefore, 405/633 was the most powerful, but all were significant ( $p < 0.0005$ , F-test).

**Post Hoc Tests****Multiple Comparisons LSD**

Dependent Variable	(I) id	(J) id	Mean Difference (I-J)	Std. Error	Sig.	95% Confidence Interval	
						Lower Bound	Upper Bound
CUM	1	2	-1.25E-03	8.03E-06	.000	-1.27E-03	-1.23E-03
		3	-1.03E-03	6.33E-06	.000	-1.04E-03	-1.02E-03
	2	1	1.25E-03	8.03E-06	.000	1.23E-03	1.27E-03
		3	2.22E-04	7.18E-06	.000	2.08E-04	2.36E-04
	3	1	1.03E-03	6.33E-06	.000	1.02E-03	1.04E-03
		2	-2.22E-04	7.18E-06	.000	-2.36E-04	-2.08E-04
r405to488	1	2	-1.58E+00	5.77E-03	.000	-1.59E+00	-1.56E+00
		3	-1.84E+00	4.55E-03	.000	-1.85E+00	-1.83E+00
	2	1	1.58E+00	5.77E-03	.000	1.56E+00	1.59E+00
		3	-2.65E-01	5.16E-03	.000	-2.75E-01	-2.55E-01
	3	1	1.84E+00	4.55E-03	.000	1.83E+00	1.85E+00
		2	2.65E-01	5.16E-03	.000	2.55E-01	2.75E-01
r405to633	1	2	-2.91E+00	8.18E-03	.000	-2.92E+00	-2.89E+00
		3	-2.94E+00	6.45E-03	.000	-2.96E+00	-2.93E+00
	2	1	2.91E+00	8.18E-03	.000	2.89E+00	2.92E+00
		3	-3.76E-02	7.32E-03	.000	-5.20E-02	-2.33E-02
	3	1	2.94E+00	6.45E-03	.000	2.93E+00	2.96E+00
		2	3.76E-02	7.32E-03	.000	2.33E-02	5.20E-02
r488to633	1	2	-8.89E-01	3.53E-03	.000	-8.95E-01	-8.82E-01
		3	-6.83E-01	2.78E-03	.000	-6.88E-01	-6.77E-01
	2	1	8.89E-01	3.53E-03	.000	8.82E-01	8.95E-01
		3	2.06E-01	3.16E-03	.000	2.00E-01	2.12E-01
	3	1	6.83E-01	2.78E-03	.000	6.77E-01	6.88E-01
		2	-2.06E-01	3.16E-03	.000	-2.12E-01	-2.00E-01

Interpretation: significant differences in all four discriminant variables were observed among all three groups. SUM1315 cells (ID 2, blue) had significantly greater cumulative intensity and 488/633 than both leukocyte sub-populations. SUM1315 cells had significantly greater and lower 405/488 and 405/633 than PBMCs and PMNs, respectively.

#### 9.4.1.2 Linear Discriminant Analysis

##### Between-Subjects Factors

	N
1: PBMC	61064
id 2: SUM1315	42565
3: PMN	119143

##### Discriminant

##### Tests of Equality of Group Means

	Wilks' Lambda	F	df1	df2	Sig.
CUM	.870	16674.179	2	222769	.000
r405to488	.569	84412.680	2	222769	.000
r405to633	.495	113627.801	2	222769	.000
r488to633	.733	40586.257	2	222769	.000

Interpretation: Low Wilks' Lambda values ( $\ll 1$ ) suggested appreciable variation among group means, and 405/633 elicited the most discrimination potential.

**Covariance Matrices**

id		CUM	r405to488	r405to633	r488to633
1	CUM	2.678E-8	-1.619E-6	-3.560E-6	-4.588E-6
	r405to488	-1.619E-6	.067	.019	-.031
	r405to633	-3.560E-6	.019	.046	.042
	r488to633	-4.588E-6	-.031	.042	.090
2	CUM	4.835E-6	1.543E-5	.001	.000
	r405to488	1.543E-5	2.713	2.559	-.367
	r405to633	.001	2.559	7.527	1.319
	r488to633	.000	-.367	1.319	1.071
3	CUM	1.281E-6	-7.009E-5	.000	-5.440E-5
	r405to488	-7.009E-5	.560	.210	-.213
	r405to633	.000	.210	.429	.069
	r488to633	-5.440E-5	-.213	.069	.156
Total	CUM	1.858E-6	.000	.001	.000
	r405to488	.000	1.470	1.642	.060
	r405to633	.001	1.642	3.394	.730
	r488to633	.000	.060	.730	.427

Interpretation: Only one covariance value greater than 4 (in the SUM1315 group) was observed, thus suggesting that deviations from normality were not expected to affect test significance.

**Summary of Canonical Discriminant Functions****Eigenvalues**

Function	Eigenvalue	% of Variance	Cumulative %	Canonical Correlation
1	1.902 <sup>a</sup>	98.6	98.6	.810
2	.028 <sup>a</sup>	1.4	100.0	.164

a. First 2 canonical discriminant functions were used in the analysis.

Interpretation: A high % of variance and canonical correlation value (near 1) indicated that the first discriminant function effectively discriminated among the groups, i.e. the discriminant scores correlated with the actual group membership.

**Wilks' Lambda**

Test of Function(s)	Wilks' Lambda	Chi-square	df	Sig.
1 through 2	.335	243458.980	8	.000
2	.973	6109.392	3	.000

Interpretation: The associated chi-square test statistics were significant, and the low Wilks' Lambda values ( $<<1$ ) of the first two functions indicated that the functions yielded a maximum of 66.5% (1-0.335) variance among the group centroids.

**Standardized Canonical Discriminant Function  
Coefficients**

	Function	
	1	2
CUM	.298	.326
r405to488	1.076	-.203
r405to633	-.197	-.451
r488to633	.910	.857

Interpretation: Larger absolute values of coefficients corresponded to variables with greater discriminating ability. As noted in the previous Wilks' Lambda table, the first discriminant function was more powerful than the second function. In the case of the first function, the 405/488 and 488/633 were weighted more heavily than the cumulative intensity and 405/633 values.

**Classification Statistics****Classification Function Coefficients**

	id		
	1	2	3
CUM	249.312	1069.924	937.122
r405to488	4.960	8.597	8.601
r405to633	-2.928	-3.519	-3.352
r488to633	8.157	13.774	12.962
(Constant)	-5.254	-17.130	-16.304

**Classification Results<sup>c</sup>**

	id	Predicted Group Membership			Total
		1	2	3	
Cross-validated <sup>b</sup>	Count	1	2	3	
		60635	386	43	61064
		6820	18267	17478	42565
		842	45462	72839	119143
	%	1	2	3	
		99.3	.6	.1	100.0
		16.0	42.9	41.1	100.0
		.7	38.2	61.1	100.0

b. Cross validation is done only for those cases in the analysis. In cross validation, each case is classified by the functions derived from all cases other than that case.

c. 68.1% of cross-validated grouped cases correctly classified.

**9.4.2 PMN vs. SUM1315****Discriminant****Between-Subjects Factors**

	N
id 2: SUM1315	42565
3: PMN	119143

**Tests of Equality of Group Means**

	Wilks' Lambda	F	df1	df2	Sig.
CUM	.996	695.254	1	161706	.000
r405to488	.988	1953.910	1	161706	.000
r405to633	1.000	19.323	1	161706	.000
r488to633	.980	3350.667	1	161706	.000

Interpretation: High Wilks' Lambda values (near 1) suggested minimal variation among group means.



**Summary of Canonical Discriminant Functions****Eigenvalues**

Function	Eigenvalue	% of Variance	Cumulative %	Canonical Correlation
1	.031 <sup>a</sup>	100.0	100.0	.173

Interpretation: A low canonical correlation ( $\ll 1$ ) indicated that the discriminant scores yielded by the classification function did not correlate with actual group membership.

**Wilks' Lambda**

Test of Function(s)	Wilks' Lambda	Chi-square	df	Sig.
1	.970	4911.740	4	.000

Interpretation: The associated chi-square test statistics was significant; however, the high Wilks' Lambda value (near 1) suggested that there was only 3% variance between group means.

**Standardized Canonical Discriminant Function Coefficients**

	Function
	1
CUM	.361
r405to488	.069
r405to633	-.545
r488to633	1.067

Interpretation: Although the overall function lacked discriminatory power, 488/633 was the most weighted variable.

**Classification Statistics****Classification Function Coefficients**

	id	
	2	3
CUM	777.495	680.920
r405to488	6.832	6.806
r405to633	-2.929	-2.785
r488to633	11.320	10.644
(Constant)	-13.450	-12.726

**Classification Results<sup>c</sup>**

	id	Predicted Group Membership		Total
		2	3	
Cross-validated <sup>b</sup>	Count 2	19450	23115	42565
	3	45028	74115	119143
	% 2	45.7	54.3	100.0
	3	37.8	62.2	100.0

b. Cross validation is done only for those cases in the analysis. In cross validation, each case is classified by the functions derived from all cases other than that case.

c. 57.9% of cross-validated grouped cases correctly classified.

**9.4.3 PBMC vs. SUM135****Discriminant****Between-Subjects Factors**

	N
id 1: PBMC	61064
2: SUM1315	42565

**Tests of Equality of Group Means**

	Wilks' Lambda	F	df1	df2	Sig.
CUM	.841	19584.015	1	103627	.000
r405to488	.658	53978.425	1	103627	.000
r405to633	.604	67957.756	1	103627	.000
r488to633	.721	40163.716	1	103627	.000

Interpretation: Low Wilks' Lambda values ( $\ll 1$ ) suggested appreciable variation among group means, and cumulative intensity elicited the most discrimination potential.

**Summary of Canonical Discriminant Functions****Eigenvalues**

Function	Eigenvalue	% of Variance	Cumulative %	Canonical Correlation
1	1.325 <sup>a</sup>	100.0	100.0	.755

Interpretation: A high canonical correlation (near 1) indicated that the discriminant scores yielded by the classification function correlated with actual group membership.

**Wilks' Lambda**

Test of Function(s)	Wilks' Lambda	Chi-square	df	Sig.
1	.430	87451.197	4	.000

Interpretation: The associated chi-square test statistics was significant, and the low Wilks' Lambda value ( $< 1$ ) suggested that there was 57% variance between group means.

#### Standardized Canonical Discriminant Function Coefficients

	Function
	1
CUM	.328
r405to488	.948
r405to633	-.242
r488to633	.836

Interpretation: 405/488 and 488/633 were the most weighted variables in the discriminant function.

#### Classification Statistics

##### Classification Function Coefficients

	id	
	1	2
CUM	151.153	693.575
r405to488	2.616	4.681
r405to633	-1.456	-1.776
r488to633	4.004	6.789
(Constant)	-2.804	-9.177

Fisher's linear discriminant functions

**Classification Results**

		Predicted Group Membership		Total
		1	2	
Cross-validated	Count			
	1	60788	276	61064
	2	7337	35228	42565
	%			
	1	99.5	.5	100.0
	2	17.2	82.8	100.0

b. Cross validation is done only for those cases in the analysis. In cross validation, each case is classified by the functions derived from all cases other than that case.

c. 92.7% of cross-validated grouped cases correctly classified.

## 9.5 Appendix – Chapter: Light Scattering Measurements of Lysed Leukocyte Populations Spiked With In Vitro Breast Cancer Cells

### 9.5.1 Ammonium Chloride Lysis Protocol

For heparinized blood (Li<sup>+</sup> green top tube)

1. Prepare 1x lysis buffer from 10x stock (StemCell Technologies #20110)
  - a. 1 mL 10x into 9 mL DI H<sub>2</sub>O
2. Transfer 1 mL whole blood into 15 mL conical tube
3. Mix 1x lysis buffer into blood at 1:1
  - a. 1 mL blood = 1 mL 1x lysis buffer
4. Incubate for 10 min at RT
5. Dilute with 10 mL 1x PBS
6. Spin 600xg (1200 RPM in Rm 273) for 5 min at RT
7. Aspirate pink supernatant down to cell red cell pellet
8. Mix 1x lysis buffer into blood at 2:1
  - a. 1 mL blood originally = 0.5 mL 1x lysis buffer
9. Dilute with 10 mL 1x PBS
10. Spin 600xg RPM for 5 min at RT
11. Aspirate pink supernatant down to cell red cell pellet
12. Re-suspend in RPMI
  - a. Start with 4 mL of RPMI for 1 mL blood
13. Count. Want 30-50 e4 cells/mL
14. Re-adjust concentration using RPMI
15. Store samples on ice for flow analysis

## 9.6 Chapter: Fluorescence and Scattering Detection of Circulating Tumor Cells in Murine Model

### 9.6.1 Tumor Induction Time Course Study Discriminant Analysis

MANOVA and linear discriminant analysis were used to discriminate cells types based on scattering properties. Cumulative scattering intensities ( $I_{405}+I_{488}$ ) and the ratio thereof ( $I_{405}/I_{488}$ ) were used as discriminant variables. Non-fluorescent and green fluorescent cell populations from each of the three mouse cohorts, e.g. wild type, aggregate shCtrl-3-inoculated, and aggregate shA8-20-inoculated, composed the six subject groups. One mouse in each experimental group, day 14 for shCtrl-3 and day 21 for shA8-20, were withheld for channel clogging and coagulation complications. Analyses were performed in SPSS.

#### Group Identification

ID	Group	N (cells)	N (mice)	N (measurements)
1	Wild type leukocyte	3704	3	3
2	Wild type green autofluorescent leukocyte	659	3	3
3	shCtrl-3 leukocyte	12078	4	11
4	shCtrl-3 green cell	3773	4	11
5	shA8-20 leukocyte	12455	4	11
6	shA8-20 green cell	2227	4	11

**Group Statistics**

id		Mean	Std. Deviation
1	CUM	7.80E-03	3.89E-03
	r405to488	1.74E-01	1.09E-01
2	CUM	1.63E-02	1.01E-02
	r405to488	2.74E-01	1.84E-01
3	CUM	1.05E-02	4.27E-03
	r405to488	2.61E-01	1.07E-01
4	CUM	1.58E-02	9.28E-03
	r405to488	2.80E-01	1.62E-01
5	CUM	8.79E-03	4.21E-03
	r405to488	2.31E-01	7.37E-02
6	CUM	1.53E-02	1.08E-02
	r405to488	2.36E-01	1.33E-01
Total	CUM	1.06E-02	6.32E-03
	r405to488	2.42E-01	1.12E-01

Interpretation: All groups means $\pm\sigma$  overlapped, thus suggesting that overall population differences were negligible; however, scattering properties of sub-populations were not elucidated in this table.

**Tests of Equality of Group Means**

	Wilks' Lambda	F	df1	df2	Sig.
CUM	.826	1470.921	5	34890	.000
r405to488	.934	495.574	5	34890	.000

Interpretation: Relatively high Wilks' Lambda values (near 1) suggested some variation among group means, and cumulative peak intensity elicited the most discrimination potential.

**Covariance Matrices<sup>a</sup>**

id		CUM	r405to488
1	CUM	1.516E-5	6.022E-5
	r405to488	6.022E-5	.012
2	CUM	.000	.001
	r405to488	.001	.034
3	CUM	1.826E-5	-4.395E-5
	r405to488	-4.395E-5	.012
4	CUM	8.606E-5	.000
	r405to488	.000	.026
5	CUM	1.775E-5	-7.508E-5
	r405to488	-7.508E-5	.005
6	CUM	.000	.000
	r405to488	.000	.018
Total	CUM	3.992E-5	6.735E-5
	r405to488	6.735E-5	.013

a. The total covariance matrix has 34895 degrees of freedom.

Interpretation: Uniformly small covariance values suggested that the individual groups and the combined variable distributions were normal.

**Summary of Canonical Discriminant Functions****Eigenvalues**

Function	Eigenvalue	% of Variance	Cumulative %	Canonical Correlation
1	.243 <sup>a</sup>	87.4	87.4	.442
2	.035 <sup>a</sup>	12.6	100.0	.184

Interpretation: A moderate % of variance and moderate canonical correlation value (<0.5) indicated that the discriminant functions discriminated somewhat among the groups.

**Wilks' Lambda**

Test of Function(s)	Wilks' Lambda	Chi-square	df	Sig.
1 through 2	.778	8778.351	10	.000
2	.966	1196.297	4	.000

Interpretation: The associated chi-square test statistics were significant, and the moderate Wilks' Lambda values ( $<<1$ ) of the first two functions indicated that the functions yielded a maximum of 22.2% (1-0.778) variance among the group centroids.

**Standardized Canonical Discriminant Function Coefficients**

	Function	
	1	2
CUM	.909	-.417
r405to488	.392	.920

Interpretation: Larger absolute values of coefficients corresponded to variables with greater discriminating ability. As noted in the previous Wilks' Lambda table, the first discriminant function was more powerful than the second function. In the case of the first function, the cumulative intensity was weighted more heavily than the 405/488 values.

**9.6.2 Tumor Induction, Resection, and Antibody Treatment Study**

Each of the three mouse cohorts yielded a leukocyte and green fluorescent population. As before, green counts in tumor-bearing mice consisted of unknown numbers of green autofluorescent cells and GFP<sup>+</sup> CTCs. All six groups of identified cells in this tumor resection and antibody treatment study were assessed via MANOVA and linear discriminant analysis. By acquiring scattering properties from all three interrogative wavelengths, cumulative intensity and ratios thereof were used as discriminant variables. One mouse in the isotype-treated cohort (#17) was withheld for blood coagulation complications prior to sample processing. Analysis was performed in SPSS.

**9.6.2.1 Analysis of Non-Fluorescent Leukocytes and Green Fluorescent Cells among Three Mouse Cohorts****9.6.2.1.1 MANOVA**

ID	Group	N (cells)	N (mice)
1	Wild type leukocyte	178272	3
2	Wild type green autofluorescent leukocyte	2446	3
3	Isotype-treated leukocyte	305314	2
4	Isotype-treated green cell	3452	2
5	Anti-A8-treated leukocyte	201487	4
6	Anti-A8-treated green cell	4882	4



**General Linear Model****Descriptive Statistics**

	id	Mean	Std. Deviation
CUM	1	2.926	1.031
	2	8.314	6.099
	3	2.947	0.988
	4	7.628	5.548
	5	2.907	0.888
	6	6.842	3.968
	Total	3.000	1.279
r405to488	1	1.055	0.554
	2	1.295	0.476
	3	1.076	14.507
	4	1.091	0.485
	5	1.056	0.385
	6	1.195	0.659
	Total	1.067	9.616
r405to633	1	1.426	1.101
	2	1.620	1.940
	3	1.295	6.210
	4	2.406	53.156
	5	1.267	0.968
	6	1.530	10.758
	Total	1.329	5.688
r488to633	1	1.311	0.782
	2	1.261	1.523
	3	1.296	6.530
	4	2.512	58.283
	5	1.278	1.069
	6	1.371	13.272
	Total	1.301	6.107

Interpretation: All groups means $\pm\sigma$  overlapped, thus suggesting that overall population differences were negligible; however, consistently high cumulative scattering intensities means among the three green fluorescent cell groups suggested that sub-populations had markedly higher cumulative intensity values.

### Multivariate Tests

Effect	Value	F	Hypothesis df	Error df	Sig.	Partial Eta Squared
id Pillai's Trace	.196	7169.761	20.000	2783388.000	.000	.049
Wilks' Lambda	.805	7812.125	20.000	2307854.410	.000	.053

Interpretation: The discrepancy between a small Pillai's Trace and small Partial Eta Squared suggested that this test statistic was not appropriate for this analysis, which was attributed to non-normal aspects of the population, e.g. outliers, high covariance values, and scattering variables that did not contribute to mean differences.

### Tests of Between-Subjects Effects

Source	Dependent Variable	Sig.	Partial Squared Eta	Observed Power
id	CUM	.000	.192	1.000
	r405to488	.690	.000	.227
	r405to633	.000	.000	1.000
	r488to633	.000	.000	1.000

Interpretation: As observed in the descriptive statistics table with predominantly overlapping mean $\pm\sigma$  intervals among discriminant variables, only the cumulative intensity variable provided meaningful discrimination among the groups (~19.2%).

### Post Hoc Tests - Multiple Comparisons, LSD

Dependent Variable	(I) id	(J) id	Mean Difference (I-J)	Std. Error	Sig.	95% Confidence Interval	
						Lower Bound	Upper Bound
CUM	1	2	-5.39E+00	2.34E-02	0	-5.43E+00	-5.34E+00
		3	-2.12E-02	3.43E-03	0	-2.79E-02	-1.45E-02
		4	-4.70E+00	1.98E-02	0	-4.74E+00	-4.66E+00
		5	1.92E-02	3.74E-03	0	1.19E-02	2.65E-02
	2	6	-3.92E+00	1.67E-02	0	-3.95E+00	-3.88E+00
		1	5.39E+00	2.34E-02	0	5.34E+00	5.43E+00
		3	5.37E+00	2.34E-02	0	5.32E+00	5.41E+00
		4	6.86E-01	3.04E-02	0	6.27E-01	7.46E-01
		5	5.41E+00	2.34E-02	0	5.36E+00	5.45E+00
		6	1.47E+00	2.85E-02	0	1.42E+00	1.53E+00

	3	1	2.12E-02	3.43E-03	0	1.45E-02	2.79E-02
		2	-5.37E+00	2.34E-02	0	-5.41E+00	-5.32E+00
		4	-4.68E+00	1.97E-02	0	-4.72E+00	-4.64E+00
		5	4.04E-02	3.30E-03	0	3.39E-02	4.68E-02
		6	-3.89E+00	1.66E-02	0	-3.93E+00	-3.86E+00
		1	4.70E+00	1.98E-02	0	4.66E+00	4.74E+00
	4	2	-6.86E-01	3.04E-02	0	-7.46E-01	-6.27E-01
		3	4.68E+00	1.97E-02	0	4.64E+00	4.72E+00
		5	4.72E+00	1.97E-02	0	4.68E+00	4.76E+00
		6	7.86E-01	2.56E-02	0	7.36E-01	8.36E-01
		1	-1.92E-02	3.74E-03	0	-2.65E-02	-1.19E-02
	5	2	-5.41E+00	2.34E-02	0	-5.45E+00	-5.36E+00
		3	-4.04E-02	3.30E-03	0	-4.68E-02	-3.39E-02
		4	-4.72E+00	1.97E-02	0	-4.76E+00	-4.68E+00
		6	-3.93E+00	1.67E-02	0	-3.97E+00	-3.90E+00
		1	3.92E+00	1.67E-02	0	3.88E+00	3.95E+00
	6	2	-1.47E+00	2.85E-02	0	-1.53E+00	-1.42E+00
		3	3.89E+00	1.66E-02	0	3.86E+00	3.93E+00
		4	-7.86E-01	2.56E-02	0	-8.36E-01	-7.36E-01
		5	3.93E+00	1.67E-02	0	3.90E+00	3.97E+00
		2	-2.40E-01	1.96E-01	0.22	-6.24E-01	1.44E-01
r405to488	1	3	-2.12E-02	2.87E-02	0.46	-7.74E-02	3.50E-02
		4	-3.59E-02	1.65E-01	0.83	-3.60E-01	2.88E-01
		5	-1.30E-03	3.13E-02	0.97	-6.26E-02	6.00E-02
		6	-1.40E-01	1.39E-01	0.32	-4.13E-01	1.34E-01
		1	2.40E-01	1.96E-01	0.22	-1.44E-01	6.24E-01
	2	3	2.19E-01	1.95E-01	0.26	-1.64E-01	6.01E-01
		4	2.04E-01	2.54E-01	0.42	-2.94E-01	7.02E-01
		5	2.39E-01	1.96E-01	0.22	-1.45E-01	6.22E-01
		6	1.00E-01	2.38E-01	0.67	-3.67E-01	5.67E-01
		1	2.12E-02	2.87E-02	0.46	-3.50E-02	7.74E-02
	3	2	-2.19E-01	1.95E-01	0.26	-6.01E-01	1.64E-01
		4	-1.47E-02	1.65E-01	0.93	-3.37E-01	3.08E-01
		5	1.99E-02	2.76E-02	0.47	-3.42E-02	7.40E-02
		6	-1.19E-01	1.39E-01	0.39	-3.90E-01	1.53E-01
		1	3.59E-02	1.65E-01	0.83	-2.88E-01	3.60E-01
	4	2	-2.04E-01	2.54E-01	0.42	-7.02E-01	2.94E-01
		3	1.47E-02	1.65E-01	0.93	-3.08E-01	3.37E-01
		5	3.46E-02	1.65E-01	0.83	-2.89E-01	3.58E-01

	6	-1.04E-01	2.14E-01	0.63	-5.23E-01	3.15E-01	
	5	1	1.30E-03	3.13E-02	0.97	-6.00E-02	6.26E-02
		2	-2.39E-01	1.96E-01	0.22	-6.22E-01	1.45E-01
		3	-1.99E-02	2.76E-02	0.47	-7.40E-02	3.42E-02
		4	-3.46E-02	1.65E-01	0.83	-3.58E-01	2.89E-01
		6	-1.38E-01	1.39E-01	0.32	-4.11E-01	1.35E-01
	6	1	1.40E-01	1.39E-01	0.32	-1.34E-01	4.13E-01
		2	-1.00E-01	2.38E-01	0.67	-5.67E-01	3.67E-01
		3	1.19E-01	1.39E-01	0.39	-1.53E-01	3.90E-01
		4	1.04E-01	2.14E-01	0.63	-3.15E-01	5.23E-01
5		1.38E-01	1.39E-01	0.32	-1.35E-01	4.11E-01	
r405to633	1	2	-1.94E-01	1.16E-01	0.09	-4.21E-01	3.29E-02
		3	1.31E-01	1.70E-02	0	9.80E-02	1.64E-01
		4	-9.80E-01	9.77E-02	0	-1.17E+00	-7.88E-01
		5	1.59E-01	1.85E-02	0	1.23E-01	1.95E-01
		6	-1.04E-01	8.25E-02	0.21	-2.66E-01	5.74E-02
	2	1	1.94E-01	1.16E-01	0.09	-3.29E-02	4.21E-01
		3	3.25E-01	1.15E-01	0.01	9.90E-02	5.52E-01
		4	-7.86E-01	1.50E-01	0	-1.08E+00	-4.91E-01
		5	3.53E-01	1.16E-01	0	1.26E-01	5.80E-01
		6	8.98E-02	1.41E-01	0.52	-1.86E-01	3.66E-01
	3	1	-1.31E-01	1.70E-02	0	-1.64E-01	-9.80E-02
		2	-3.25E-01	1.15E-01	0.01	-5.52E-01	-9.90E-02
		4	-1.11E+00	9.73E-02	0	-1.30E+00	-9.20E-01
		5	2.76E-02	1.63E-02	0.09	-4.38E-03	5.96E-02
		6	-2.35E-01	8.20E-02	0	-3.96E-01	-7.47E-02
	4	1	9.80E-01	9.77E-02	0	7.88E-01	1.17E+00
		2	7.86E-01	1.50E-01	0	4.91E-01	1.08E+00
		3	1.11E+00	9.73E-02	0	9.20E-01	1.30E+00
		5	1.14E+00	9.76E-02	0	9.47E-01	1.33E+00
		6	8.76E-01	1.26E-01	0	6.28E-01	1.12E+00
	5	1	-1.59E-01	1.85E-02	0	-1.95E-01	-1.23E-01
		2	-3.53E-01	1.16E-01	0	-5.80E-01	-1.26E-01
		3	-2.76E-02	1.63E-02	0.09	-5.96E-02	4.38E-03
		4	-1.14E+00	9.76E-02	0	-1.33E+00	-9.47E-01
6		-2.63E-01	8.24E-02	0	-4.25E-01	-1.02E-01	
6	1	1.04E-01	8.25E-02	0.21	-5.74E-02	2.66E-01	
	2	-8.98E-02	1.41E-01	0.52	-3.66E-01	1.86E-01	
	3	2.35E-01	8.20E-02	0	7.47E-02	3.96E-01	
	4	-8.76E-01	1.26E-01	0	-1.12E+00	-6.28E-01	

	5	2.63E-01	8.24E-02	0	1.02E-01	4.25E-01
	2	5.03E-02	1.24E-01	0.69	-1.93E-01	2.94E-01
	3	1.49E-02	1.82E-02	0.41	-2.08E-02	5.06E-02
1	4	-1.20E+00	1.05E-01	0	-1.41E+00	-9.95E-01
	5	3.28E-02	1.99E-02	0.1	-6.08E-03	7.18E-02
	6	-6.06E-02	8.86E-02	0.49	-2.34E-01	1.13E-01
	1	-5.03E-02	1.24E-01	0.69	-2.94E-01	1.93E-01
	3	-3.54E-02	1.24E-01	0.78	-2.78E-01	2.08E-01
2	4	-1.25E+00	1.61E-01	0	-1.57E+00	-9.35E-01
	5	-1.74E-02	1.24E-01	0.89	-2.61E-01	2.26E-01
	6	-1.11E-01	1.51E-01	0.46	-4.07E-01	1.86E-01
	1	-1.49E-02	1.82E-02	0.41	-5.06E-02	2.08E-02
	2	3.54E-02	1.24E-01	0.78	-2.08E-01	2.78E-01
3	4	-1.22E+00	1.05E-01	0	-1.42E+00	-1.01E+00
	5	1.79E-02	1.75E-02	0.31	-1.64E-02	5.23E-02
	6	-7.55E-02	8.81E-02	0.39	-2.48E-01	9.72E-02
r488to633	1	1.20E+00	1.05E-01	0	9.95E-01	1.41E+00
	2	1.25E+00	1.61E-01	0	9.35E-01	1.57E+00
4	3	1.22E+00	1.05E-01	0	1.01E+00	1.42E+00
	5	1.23E+00	1.05E-01	0	1.03E+00	1.44E+00
	6	1.14E+00	1.36E-01	0	8.74E-01	1.41E+00
	1	-3.28E-02	1.99E-02	0.1	-7.18E-02	6.08E-03
	2	1.74E-02	1.24E-01	0.89	-2.26E-01	2.61E-01
5	3	-1.79E-02	1.75E-02	0.31	-5.23E-02	1.64E-02
	4	-1.23E+00	1.05E-01	0	-1.44E+00	-1.03E+00
	6	-9.34E-02	8.84E-02	0.29	-2.67E-01	7.99E-02
	1	6.06E-02	8.86E-02	0.49	-1.13E-01	2.34E-01
	2	1.11E-01	1.51E-01	0.46	-1.86E-01	4.07E-01
6	3	7.55E-02	8.81E-02	0.39	-9.72E-02	2.48E-01
	4	-1.14E+00	1.36E-01	0	-1.41E+00	-8.74E-01
	5	9.34E-02	8.84E-02	0.29	-7.99E-02	2.67E-01

Interpretation: The least significance difference (LSD) post hoc provided the most detailed insight into similarities and differences based on scattering properties among the six groups. Cumulative intensity was the only discriminant variable that provided consistent differences among the six groups, and the primary finding was that green fluorescent cells had greater cumulative intensity than non-fluorescent leukocytes. In contrast, 405/488 values failed to provide any discrimination power. The other variables of 405/633 and 488/633 suggested that non-fluorescent leukocytes (groups 1, 3, and 5) were consistently similar, whereas green fluorescent cells (groups 2, 4, and 6) were variably similar and distinct from the other groups.

## 9.6.2.1.2 Linear Discriminant Analysis

**Tests of Equality of Group Means**

	Wilks' Lambda	F	df1	df2	Sig.
CUM	.808	33055.338	5	695847	.000
r405to488	1.000	.613	5	695847	.690
r405to633	1.000	44.607	5	695847	.000
r488to633	1.000	28.001	5	695847	.000

Interpretation: High Wilks' Lambda values (1) suggested negligible variation among group means, except for cumulative intensity with ~20% variance (1-0.808) variance among the groups.

**Covariance Matrices<sup>a</sup>**

id		CUM	r405to488	r405to633	r488to633
1	CUM	1.062	-.067	-.207	-.142
	r405to488	-.067	.307	.271	.043
	r405to633	-.207	.271	1.213	.718
	r488to633	-.142	.043	.718	.611
2	CUM	37.198	.099	-1.176	-1.038
	r405to488	.099	.226	.236	-.012
	r405to633	-1.176	.236	3.762	2.730
	r488to633	-1.038	-.012	2.730	2.318
3	CUM	.976	.178	.013	-.032
	r405to488	.178	210.450	2.634	-.100
	r405to633	.013	2.634	38.560	39.760
	r488to633	-.032	-.100	39.760	42.637
4	CUM	30.781	-.033	.057	.371
	r405to488	-.033	.236	-.078	-.334
	r405to633	.057	-.078	2825.532	3096.907
	r488to633	.371	-.334	3096.907	3396.863
5	CUM	.789	-.009	.015	.042
	r405to488	-.009	.148	.055	-.083
	r405to633	.015	.055	.937	.865
	r488to633	.042	-.083	.865	1.142
6	CUM	15.749	-.207	-1.396	-1.303
	r405to488	-.207	.434	.290	-.108
	r405to633	-1.396	.290	115.725	140.756
	r488to633	-1.303	-.108	140.756	176.144
Total	CUM	1.637	.066	-.020	-.020
	r405to488	.066	92.464	1.244	-.059
	r405to633	-.020	1.244	32.349	34.243
	r488to633	-.020	-.059	34.243	37.293

a. The total covariance matrix has 695852 degrees of freedom.

Interpretation: Consistently high covariance values in the 405/633 and 488/633 distributions suggested high deviations from normality, which was attributed to individual cell outliers that were illustrated in Figure 6-6.

### Summary of Canonical Discriminant Functions

#### Eigenvalues

Function	Eigenvalue	% of Variance	Cumulative %	Canonical Correlation
1	.238 <sup>a</sup>	98.5	98.5	.439
2	.003 <sup>a</sup>	1.4	99.9	.059
3	.000 <sup>a</sup>	.1	100.0	.011
4	.000 <sup>a</sup>	.0	100.0	.001

a. First 4 canonical discriminant functions were used in the analysis.

Interpretation: The first canonical function accounted for the majority of variance among the six groups; however, <50% of discriminant scores correlated with the actual group membership. This moderation performance was attributed to the non-normal population characteristics and the lack of discrimination power among the scattering intensity ratio variables.

#### Standardized Canonical Discriminant Function Coefficients

	Function			
	1	2	3	4
CUM	.999	.035	-.018	-.005
r405to488	-.009	.147	-.089	.995
r405to633	.284	-6.036	.146	.038
r488to633	-.255	5.977	.851	.049

Interpretation: Larger absolute values of coefficients corresponded to variables with greater discriminating ability. As noted in the previous Wilks' Lambda table, the first discriminant function was the most powerful. In the case of the first function, the cumulative intensity was weighted more heavily than the scattering intensity ratios.

#### 9.6.2.2 One-way ANOVAs of Scattering Intensities of Tumor-Bearing Green Counts and Aggregate Wild Type Green Autofluorescent Cells as a Reference Population

Without a GFP<sup>+</sup> CTC population to serve as a gold standard for classification, an alternative approach was developed to use the combined wild type autofluorescent cells as a reference population to detect outliers among the green counts identified in antibody-treated experimental cohorts. The outliers were hypothesized to indicate green fluorescent cells circulating in cancerous mice, e.g. GFP<sup>+</sup> CTCs or some other autofluorescent cells, not present in wild type mice. A one-way ANOVA was performed



using scattering light intensities as discriminant variables to investigate population differences.

### Descriptives

	N	Mean	Std. Deviation	Std. Error	95% Confidence Interval for Mean		
					Lower Bound	Upper Bound	
i405	WT	4892	3.16	2.42	0.035	3.09	3.23
	Isotype-Tx	5363	2.84	2.04	0.028	2.78	2.89
	Anti-A8-TX	9762	2.40	1.42	0.014	2.37	2.43
	Total	20017	2.70	1.91	0.013	2.68	2.73
i488	WT	4892	2.52	1.76	0.025	2.47	2.57
	Isotype-Tx	5363	2.74	2.02	0.028	2.69	2.80
	Anti-A8-TX	9762	2.25	1.40	0.014	2.22	2.28
	Total	20017	2.45	1.69	0.012	2.43	2.47
i633	WT	4892	2.54	2.43	0.035	2.47	2.61
	Isotype-Tx	5363	2.53	2.24	0.031	2.47	2.59
	Anti-A8-TX	9762	2.14	1.74	0.018	2.10	2.17
	Total	20017	2.34	2.07	0.015	2.31	2.37

Interpretation: Overlapping mean $\pm\sigma$  ranges and 95% confidence intervals suggested that the three scattering intensities among the three groups were not remarkably different.

**Multiple Comparisons – Bonferroni**

Dependent Variable	(I) Mice Group	(J) Mice Group	Mean Diff. (I-J)	Std. Error	Sig.	95% CI for Mean	
						Lower Bound	Upper Bound
i405	WT	Iso-Tx	0.324	0.037	.000	0.235	0.413
		Anti-A8-Tx	0.757	0.033	.000	0.678	0.836
	Iso-Tx	WT	-0.324	0.037	.000	-0.413	-0.235
		Anti-A8-Tx	0.433	0.032	.000	0.356	0.509
	Anti-A8-Tx	WT	-0.757	0.033	.000	-0.836	-0.678
		Iso-Tx	-0.433	0.032	.000	-0.509	-0.356
i488	WT	Iso-Tx	-0.221	0.033	.000	-0.300	-0.142
		Anti-A8-Tx	0.271	0.029	.000	0.200	0.341
	Iso-Tx	WT	0.221	0.033	.000	0.142	0.300
		Anti-A8-Tx	0.492	0.028	.000	0.424	0.560
	Anti-A8-Tx	WT	-0.271	0.029	.000	-0.341	-0.200
		Iso-Tx	-0.492	0.028	.000	-0.560	-0.424
i633	WT	Iso-Tx	0.012	0.041	1.000	-0.086	0.109
		Anti-A8-Tx	0.402	0.036	.000	0.315	0.488
	Iso-Tx	WT	-0.012	0.041	1.000	-0.109	0.086
		Anti-A8-Tx	0.390	0.035	.000	0.306	0.474
	Anti-A8-Tx	WT	-0.402	0.036	.000	-0.488	-0.315
		Iso-Tx	-0.390	0.035	.000	-0.474	-0.306

Interpretation: Although each comparison was significant ( $p < 0.0005$ ), the presence of outliers (Figure 6-6) undermined this finding by violating a key assumption of normality. Instead, the high degree of overlap of interquartile ranges in the Mahalanobis distance distributions suggested predominantly similar scattering characteristics among the groups (Figure 6-7).